NUMERICAL SIMULATIONS OF DISK-PLANET INTERACTIONS

DISSERTATION

ZUR ERLANGUNG DES GRADES EINES DOKTORS

DER NATURWISSENSCHAFTEN

DER FAKULTÄT FÜR MATHEMATIK UND PHYSIK

DER EBERHARD-KARLS-UNIVERSITÄT ZU TÜBINGEN

VORGELEGT VON

GENNARO D'ANGELO

AUS POZZUOLI (ITALIA)

2003

Tag der mündlichen Prüfung: 4. Juni 2003

Dekan: Prof. Dr. Herbert Müther

1. Berichterstatter: Prof. Dr. Wilhelm Kley

2. Berichterstatter: Prof. Dr. Klaus Werner

NOTICE

Persons attempting to find a motive
in this narrative will be prosecuted;
persons attempting to find a moral in it
will be banished; persons attempting
to find a plot in it will be shot.

MARK TWAIN,
THE ADVENTURES OF HUCKLEBERRY FINN,
1885

Thesis advisors
Prof. Willy Kley
Prof. Thomas Henning

Author
Gennaro D'Angelo

NUMERICAL SIMULATIONS OF DISK-PLANET INTERACTIONS

ABSTRACT

The aim of this dissertation is to study the dynamical interactions occurring between a forming planet and its surrounding protostellar environment. This task is accomplished by means of both two- and three-dimensional numerical simulations. In order to render the proper development of the work, results from such calculations are presented according to the same temporal order they were achieved.

The first part of my research plan concerned global simulations in three dimensions. These were intended to investigate the large-scale effects caused by a Jupiter-size body still in the process of accreting matter from its neighborhood. For the first time, this problem was tackled in a three-dimensional space. The computations are global in the sense that they embrace a whole portion of circumstellar disk, extending over a radial distance interval of eleven astronomical units. For computational reasons, we relied on a local-isothermal equation of state to describe the thermal properties of disk material. Simulations show that, despite a density gap forms along the orbital path, Jupiter-mass protoplanets still accrete at a rate on the order of 0.01 Earth's masses per year when they are embedded in a disk whose mass, inside twenty-six astronomical units, is 0.01 solar masses. In the same conditions, the migration time scale due to gravitational torques by the disk is around one hundred thousand years. These outcomes are in good agreement with previous assessments obtained from two-dimensional calculations of infinitesimally thin disks as well as from linearized analytical theories of disk-planet interaction.

The global approach is the most rigorous way of treating planets in disks because it avoids making simplified assumptions on the propagation of the perturbations induced by the embedded body. Yet, this approach usually prevents from attaining numerical resolutions necessary to inquire into the local effects of disk-planet interactions and to handle those arising from Earth-mass objects. The second part of my work was dedicated to overcome this restriction by employing a nested-grid technique within the frame of the two-dimensional approximation. The method allows to perform global simulations of planets orbiting in disks and, at the same time, to resolve in great detail the dynamics of the flow inside the Roche lobe of both massive and low-mass planets. Therefore, it was applied to planetary masses ranging from one Jupiter-mass to one Earth-mass. In each case, the high resolution supplied by the nested-grid technique permits an evaluation of the torques, resulting from short and very short range gravitational interactions, more reliable than the one previously estimated with the aid of numerical methods. Likewise, the mass flow onto the planet is computed in a more accurate fashion. Resulting migration time scales are in the range from roughly twenty thousand years, for intermediate mass planets, to a million years, for very low as well as high-mass planets. Growth time scales depend strongly on

the protoplanet's mass. Above 64 Earth-masses, this time scale increases as the 4/3-power of the planet's mass. Otherwise it raises as the 2/3-power, occasionally yielding short lengths of time because of the two-dimensional geometry. Circumplanetary disks form inside of the Roche lobe of Jupiter-size secondaries. Its azimuthally-averaged rotational velocity is nearly Keplerian, though it becomes sub-Keplerian as the mass of the perturber is decreased. In contrast, a hydrostatic envelope builds up around a one Earth-mass object.

As a natural evolution, the nested-grid strategy was implemented in three dimensions. In order to evaluate the consequences of the flat geometry on the local flow structure around planets, simulations were carried out to investigate a range of planetary masses spanning from 1.5 Earth's masses to one Jupiter's mass. Furthermore, in such calculations protoplanets were modeled as extended structure and their envelopes were taken into account through physically realistic gravitational potentials of forming planets. Outcomes show that migration rates are relatively constant when perturbing masses lie above approximately a tenth of the Jupiter's mass, as prescribed by Type II migration regime. In a range between seven and fifteen Earth's masses, it is found a dependency of the migration speed on the planetary mass that yields time scales considerably longer than those predicted by linear analytical theories. Type I migration regime is well reproduced outside of such mass interval. The growth time scale is minimum around twenty Earth-masses, but it rapidly increases for both smaller and larger mass values. With respect to accretion and migration rates, significant differences between two- and three-dimensional calculations are found in particular for objects with masses smaller than ten Earth-masses. The flow inside the Roche lobe of the planet is rather complex, generating spiral perturbations in the disk midplane and vertical shocks in the meridional direction. Recirculation is also observed in many instances.

The final part of this work was dedicated to the simulation of non-local isothermal (i.e., radiative) models. Hence, with such calculations the locally isothermal hypothesis was relaxed and for the first time the full thermo-dynamics evolution of the system could be modeled. Since the complexity of the problem does not allow a detailed description of all the energy transport mechanisms, we use a simplified but physically significant form of the energy equation, by restricting to two-dimensional computations. Different temperature regimes are examined, according to the magnitude of the fluid kinematic viscosity. The gap structure was found to depend on the viscosity regime, and only cold environments offer the right conditions for a wide and deep gap to be carved in. The temperature profile inside the circumplanetary disk falls off as the inverse of the distance from the planet. Clockwise rotation is established around low-mass non-accreting planets, because of large pressure gradients. As for migration and accretion, estimates are generally on the same order of magnitude as those acquired with the aid of local isothermal models. Since the gap is generally filled in the high-viscosity case, Type I migration regime might extend to larger planetary masses.

CONTENTS

LIST OF FIGURES

LIST OF TABLES

ACKNOWLEDGMENTS

How can we live without our lives?
How will we know it's us without our past?

JOHN STEINBECK,
THE GRAPES OF WRATH,
1939

I arrived in Jena on the 15th of November 1999. The train dropped me off at the "Paradise" station with the burden of my luggage and my fears.

It was late afternoon when I got to Jena.

I soon put down the cumbersome part of my burden, but I could not get rid of the rest so quickly and easily. When the memory of that Monday afternoon runs through my mind, I can't help thinking of the life that followed; I can't help thinking of what I was looking for and of what I found. This thought brings to my mind a passage from the famous lyrics: "*You can't always get what you want, but if you try sometimes you may find that you get what you need*".

I firmly believe that events and people can leave a profound sign in a person's life. I reckon that in my case, people more than events have played a role. From them I "grabbed" the motivation that has sustained me during this period. I am not sure whether these people could get from me as much as I got from them: this is hard to tell. Yet, I have tried to be myself through good and bad. And good and bad cannot be separated without mistaking.

Maria Teresa Gomez is the one person whose commitment made everything start. She made my dream come true. I sincerely thank her for all she has done.

I should pay a tribute to my "colleagues" at AIU-Jena: Ilaria and Rainer. Both brought me up when the water got too deep and I was tired of swimming. The memory of their smiley faces will never vanish from my mind.

In my opinion, true people are the best, for they are scared neither of themselves nor of the others. Dorothea and Klaus tried to teach me how to look in the eyes of who sits next to you and reach his soul. They did it to me while I was sitting on the bench of a place where people go seeking. And on that very day I found. I could write a thousand PhD theses and still we would not be even.

Thomas and Willy gave me the chance to earn this PhD title. I know that I have been a pain in the neck for them, but everybody has to bear his own cross...

Lots of thanks go to my friend Enrico, world-wide known as *Krukkettone*. I met him in Jena. We spent a great deal of time laughing, playing jokes on each other, loitering, and hanging around. He reminded me of what friendship is. Our paths crossed there and I hope they will cross again.

I really appreciated the support of all my friends at OAC Naples: they were always present when I needed.

I repute myself fortunate, for I had the pleasure of meeting and spending long hours with (King) Guenther: I still do not know whether I should admire more the scientist or the man. Probably both.

There finally come the special persons, those who deserve special thanks. They are placed here at the end because they are responsible for having carried me to the finish line. I can't see any other chance: if it is not their merit, it's their fault.

Martin, Maria, Elisabeth, and Konrad: it would take me other three years to thank you in a decent way. You never saved a smile; you never denied support. You showed me what are the fundamental things in life and how to place persons over everything else. From the very beginning to the very end, you were just priceless to me. I cannot even conceive how I could have gone through the ordeals of this adventure without all of you.

Milena and I made the fortune of phone companies both in Germany and in the United States. I guess now they are quite disappointed. For long periods we were like overlapping souls over a phone line. Whatever it took, she has been always by my side, even when the whole Atlantic ocean happened to fall between us. I recognize that it has been a tough job, but she accomplished it as only she could have done.

My family (Pasquale, Elena, Rosaria, Sara, and Charlie) has been next to me for all these years, making everything easy for me to bear. I wished I could give to them what they have given me during all this period.

If I left anyone out of this list or I was unfair, please do not get resented: there is always time to acknowledge.

From the deepest of my heart, I thank this place where I never missed the sun, the ocean, and the second half of me.

Miami, September 2002

Dedicated to whom
I am indebted the most:
my father Pasquale,
and my mother Elena.

I have no data yet. It is a capital mistake to theorise before one has data. Insensibly one begins to twist facts to suit theories, instead of theories to suit facts.

SIR ARTHUR CONAN DOYLE,
THE ADVENTURES OF SHERLOCK HOLMES,
1892

CHAPTER 1

EXTRASOLAR PLANETS: OBSERVATIONS, STATISTICS, AND THEORY

This first chapter intends to summarize our present knowledge on extrasolar planets. We will briefly discuss what we have learned so far from observations and what is the status of the theories on planet formation.

1.1 Introduction

There are many billions of stars in the Galaxy and a similar number of galaxies populate the universe. Billions of Billions of stars are around us, though their distance is often hardly conceivable. Billions of Billions of chances that there are other "Worlds" in the universe, besides our own. Speculations on the existence of other planetary systems have accompanied the history of mankind thinking, starting from the great Greek philosophers, such as Epicurus and Aristotle.

It is doubtless, however, that more than the mere presence of planets beyond the Solar System, the real aim of human beings is the search for extraterrestrial "life", as we can conceive it. Although the former issue may be now considered a new topic of research, the latter still remains at the frontiers between science and philosophy. The ancestral enigma about whether or not we are just an anomaly in the universe is far from been solved.

Since the beginning of the last century, scientists have started to discuss, on physical basis, about the existence and formation of extrasolar planets (see, e.g., Spitzer 1939). Premature announcements of detections were also made but subsequently declared to be false.

Years had to pass for this intriguing field to achieve significant steps forward. In fact, the last two decades have been witness to rapid scientific advances. Our understanding of planetary formation has improved a lot. New methods for detecting extrasolar planets have been developed. Observational campaigns for targeted searches have been initiated. Starting from the middle of the past decade, all these efforts have produced strong and

convincing evidences for the existence of a number of planets outside the Solar System.

Extrasolar bodies should be typically billions of times as faint as their host stars and separated from them by less than one second of arc. At optical wavelengths, this combination makes direct detection extremely demanding, especially from the ground. For this reason alternative techniques have been developed in order to observe the dynamical perturbations induced on the star by an orbiting planet.

From the historical viewpoint, radio pulsar timing provided the first detection of an extrasolar planetary-mass body orbiting a neutron star (Wolszczan and Frail 1992). This offers an extraordinary example of how robust the process of planet formation is, since that object must have been born from a post super-nova explosion environment. High-precision radial velocity measurements resulted in the detection of the first planetary body surrounding main-sequence stars in 1995. Few years later, in 1998, gravitational microlensing provided evidences of a low-mass planet orbiting a star near the center of our Galaxy, $30\,000$ light years away from us.

An always update list of extrasolar planet detections, with relevant information and details about each of the single entries, can be found on the Web pages of the *Extrasolar Planet Encyclopedia* (`http://www.obspm.fr/planets`), and of the *California & Carnegie Planet Search* (`http://exoplanets.org/`). These sites can give an immediate idea of the human resources actively involved in the field.

All of the extrasolar planets discovered so far, by means of radial velocity measurements, have masses between 0.2 and $11\ M_{♃}$ ($M_{♃}$ is the mass of Jupiter), orbital periods in the range 3–1700 days, and semi-major axis comprised between 0.04 and 2.8 AU. Bodies with masses considerably lower than Jupiter's cannot be detected with current radial velocity techniques, whereas longer-period planets have likely escaped detection due to the short observational coverage period. However, most of these newly discovered systems[1] have orbital properties which do not match those measured in our Solar System. Over one-third of them have orbital eccentricities larger than 0.3 and two-thirds orbit the host star within the Sun-Mercury distance. Although Doppler measurements preferentially select planets in tight orbits, these findings are surprising anyway. Theoretical and observational progresses in understanding planet formation and evolution have been fast, but the solution of this puzzling scenario is far from been complete. Based on these data, around 5% of all solar-type star in the Galaxy may host massive planets and an even larger percentage may harbor lower mass planets. Extrapolating these numbers, one could expect that the Milky Way is crowded with the presence of one billion planets (Perryman 2000). Though not many planetary systems are known to have more than one planet (only 12% of them are multiple), it is likely, according to the current knowledge, that giant planets have companions, yet to be discovered.

Section 1.2 is a short review of the detection methods. Since this is only an introductory chapter, it is meant to give just the basic information regarding the treated issues. Interested readers should refer to the cited papers, which are more specific. Section 1.3 describes current efforts and future projects, intended for new discoveries and for characterizing already known extrasolar planets. Then, in § 1.4, we summarize the statistical information which can be gathered from observations. Finally, in § 1.5, we present the

[1] With the term "system" one generally refers to the parent star and the orbiting planet(s).

current status of theories on planet formation.

The rest of this dissertation deals primarily with the late stages of the evolution of protoplanets. It will be rather technical, therefore a general introduction to the topic seems necessary in order to realize the context which this work enters. With the aid of numerical calculations we intend to inquire the advanced stages of planetary formation.In particular we focus on the phase when the material, from which they generated, can either influence and actually determine their final characteristics, or rather destroy them.

1.2 Detection Techniques

Over the past one and a half decades, new techniques have emerged that enable the detection of planets around stars. Although almost all of the currently known extrasolar planets, which are generally classified as *giant planets*, have been detected via high-precision radial velocity measurements, it appears rather improbable that the same method might be applicable to the detection of planets with mass significantly lower than Jupiter's. Hence other techniques have to be refined in order to pursue the goal of discovering objects in the "habitable zone", i.e., in that distance range where liquid water can exist on the planet's surface.

We begin by describing the so called "indirect techniques", which have provided all of the apparent detections of Jupiter-like planets around solar-type stars. Direct imaging of extrasolar objects is still the major challenge in the field. We also mention about evidences of circumstellar disks, since they are intimately connected with planet formation.

Further details on detection of extrasolar planets can be found, for example, in Woolf and Angel (1998), Marcy and Butler (1998), and Perryman (2000).

1.2.1 Doppler Technique

Stellar displacements about a fixed point are caused by gravitational interaction with a massive companion, such as another star or a giant planet. This happens to our Sun, which moves at a speed of $\sim 13\ \mathrm{m\,s^{-1}}$ around the Solar System barycenter. If we consider a star of mass $M_\star$, around which a body of mass M_p revolves with an orbital period P, then the amplitude of the stellar radial velocity, induced by the companion is (Marcy and Butler 1998)

$$K = \left(\frac{2\,\pi\,G}{P}\right)^{1/3} \frac{M_\mathrm{p}\,\sin i}{(M_\star + M_\mathrm{p})^{2/3}} \frac{1}{\sqrt{1-e^2}}, \tag{1.1}$$

where e and i are the orbital eccentricity and inclination, respectively. The orbit's period is given by Kepler's third law. If the orbit is circular and $M_\mathrm{p} \ll M_\star$, then the amplitude reduces to

$$K = 28.4 \left(\frac{P}{1\ \mathrm{year}}\right)^{-1/3} \left(\frac{M_\mathrm{p}\,\sin i}{M_\mathrm{Jupiter}}\right) \left(\frac{M_\star}{M_\odot}\right)^{-2/3}, \tag{1.2}$$

A Jupiter mass at 1 AU causes a reflex amplitude of $28.4\,\sin i\ \mathrm{m\,s^{-1}}$, which is easily detectable. A confident detection requires that the amplitude be at least four times as large as the Doppler error. Thus, a Doppler precision of $3\ \mathrm{m\,s^{-1}}$ enables minimum amplitude

detections of $12\ \mathrm{m\,s^{-1}}$. Therefore, a Jupiter-mass companion, orbiting a Sun-like star at 5.2 AU ($K = 12.5 \sin i\ \mathrm{m\,s^{-1}}$), would be on the limit. A Saturn-mass companion would be detected only within one astronomical unit. For an Earth-mass object the reflex amplitude would be far below the limit ($K = 0.1 \sin i\ \mathrm{m\,s^{-1}}$). The $\sin i$ dependency implies that systems seen face-on ($i = 0°$) provide no measurable Doppler effect. Additionally, radial velocity measurements can only determine $M_\mathrm{p} \sin i$, rather than M_p. Thus, since the system inclination is usually not known, they furnish a lower limit to the planetary mass. Though the amplitude K is not related to the distance between the star and the observer, signal-to-noise considerations set an upper magnitude limit, which is typically around the magnitude $V = 8$. From the above relations one can realize that Doppler measurements favor the detection of large bodies orbiting at short distance from the primary.

In order for the Doppler technique to be effective, stellar surfaces are required to have stable velocities. Surface turbulence, rotation, and pulsation can prevent planet detections or produce false ones. Based on studies of velocity stability of late-type dwarfs, the limit to the Doppler technique resides around $3\ \mathrm{m\,s^{-1}}$, which has been already achieved (Butler et al. 1996).

1.2.2 Astrometric Detections

The path followed by a star orbiting the star-planet barycenter appears as an ellipse when projected on the plane of the sky, whose angular semi-major axis α is given by

$$\alpha = \left(\frac{M_\mathrm{p}}{M_\star}\right)\left(\frac{a}{d}\right), \tag{1.3}$$

where a and d represent the semi-major axis of the orbit and the system distance, respectively. In the above relation α is in arcseconds when a is in astronomical units and d in parsecs. Hence, the astrometric signature of a planet is proportional to both its mass and its orbital distance.

A Jupiter planet orbiting the Sun would result in an angular amplitude $\alpha = 500\ \mu\mathrm{as}$, when viewed from $10\ \mathrm{pc}$, which would lower to $0.1\ \mu\mathrm{as}$ for the Earth. Therefore, the required astrometric accuracy to detect planets typically ranges from micro to milli-arcseconds. This method is particularly sensitive to orbital periods longer than a year, thus it is complementary to radial velocity measurements. Moreover, it can be applied to hot and rapidly rotating stars for which the Doppler technique is not so appropriate. In the lucky event that a is already known from spectroscopic observations, d from the parallax of the star, and $M_\star$ form the spectral type, then astrometry yields directly the planetary mass, instead of $M_\mathrm{p} \sin i$. Furthermore, a single epoch astrometric observation can constrain the system inclination. For multi-planet systems, astrometric observations are able to determine the relative orbital inclination of the various components.

Astrometric detections demand extremely accurate positional measurements over a long period of time. For example, unconfirmed reports of small astrometric displacements, consistent with planetary-mass bodies, have been made for Barnard's star ($M_\mathrm{p} = 0.7$ and $0.5\ M_{♃}$, with $P = 12$ and 20 years respectively, van de Kamp 1982) and for Lalande 21185 ($M_\mathrm{p} = 0.9\ M_{♃}$ and a period of 5.8 years, Gatewood 1996).

1.2.3 Photometric Technique

The first observations of extrasolar planets impressed the scientific community with a striking evidence: the presence of Jupiter-size bodies orbiting the parent star at some tenths of astronomical unit (Mayor and Queloz 1995). This discovery implies that transits of planets, in front of stellar disk, should commonly occur.

Actually, O. Struve, back in 1952, was the first to conceive detections of extrasolar planets by means of eclipse signatures of the star by the planet.

The fractional drop in the measured light from the star can be quantified by the factor

$$f = \frac{\Delta L_\star}{L_\star} = \left(\frac{S_\mathrm{p}}{R_\star}\right)^2, \tag{1.4}$$

in which we indicated as $S_\mathrm{p}/R_\star$, the planet-to-star radius ratio and as $L_\star$, the star luminosity. A Jupiter-size object would obscure 1% of the solar disk. The percentage would lower to 0.008% in case of an Earth-size body. The occultation duration depends on the orbital distance a of the planet (via its period) as well as on the stellar radius:

$$\Delta t \simeq 13 \left(\frac{M_\star}{M_\odot}\right)^{-1/2} \left(\frac{a}{1\ \mathrm{AU}}\right)^{1/2} \left(\frac{R_\star}{R_\odot}\right) \ \mathrm{hours}. \tag{1.5}$$

Jupiter transits the Sun in 29 hours, while the Earth takes 13 hours.

A photometric variation of 1% is easily measurable from the ground with automated wide-field telescopes that can acquire CCD images of thousands of stars simultaneously. Moreover, such 1% dimming is distinguishable from other effects, like star spots and photospheric granulation fluctuations. This can be accomplished with small class telescopes, permitting the establishment of large observational campaigns.

Yet, for a transit to occur, the orbital inclination i must be such that

$$\tan i > \left(\frac{a}{R_\star}\right). \tag{1.6}$$

Equation (1.6) implies that the orbit needs to be nearly edge-on ($i = 90°$). In fact, if $a = 0.1$ AU and $S_\mathrm{p} = R_\mathrm{Q}$, the inclination angle $i \in [87.3°, 90°]$. Its well-known from galactic astronomy that, for randomly oriented planes in the sky, the probability $\mathcal{P}$ that the inclination angle falls between i' and $90°$ is $\mathcal{P}[i', 90°] = \cos i'$. Thus, 4.7% of all Jupiter-like planets, orbiting at a tenth of astronomical unit, are expected to transit.

Charbonneau et al. (2000) observed the first transit of an extrasolar planet (HD 209458) which had been discovered in a radial velocity survey.

Planetary transits are extremely precious since they can provide a great wealth of information. Planet radii can be directly measured by the fractional reduction of star light during the transit. Transits also allow to measure the orbital inclination, once a and $R_\star$ are known. Hence, they permit to determine the planet's mass from $M_\mathrm{p} \sin i$. When M_p and S_p are known, the density can be evaluated. As a consequence, distinctions can be made between gaseous giants and rocky planets and constraints are yielded on their chemical composition.

1.2.4 Gravitational Microlensing

Gravitational lensing is the amplification of light rays from a distant source by an intervening object. It was first considered by Einstein in 1936. The relative motion between the background source, the interposed lens, and the observer leads to apparent brightening and subsequent dimming of the resulting image. This may occur over a time scale of hours.

The essential formulas used to analyze gravitational lensing have been reported by many authors (see, e.g., Refsdal and Surdej 1994). Investigations have been carried out and it has been found that, when one or more planets orbit the primary lens, detectable fine structures in the photospheric signature of the background object occurs relatively frequently, even for low-mass planets. The probability of observing such fine structures are estimated to be around 17% for Jupiter-like and 3% for Saturn-like systems.

Bennett et al. (1999) reported of a microlensing event as the first convincing example of planet's discovery with this technique, though it was contested afterward (Albrow et al. 2000).

The advantages of microlensing for planet detection are the high sensitivity, even for low-mass objects and its effectiveness out to very large distances because it requires no photons from either the planet or the parent star. In fact it represents the only technique capable of detecting interstellar planetary-mass bodies. However, the major disadvantage is that specific systems cannot be selected for study. Once a microlensing event occurs, it is quite unlikely that another recurs, for the same system, on a relevant time scale.

1.2.5 Direct Imaging

A future class of techniques involves direct imaging of planets around their host stars. This is by far the most intriguing goal of extrasolar planet finders, since it represents the only way to actually "see" a planet.

Lately, a lot of effort has been directed toward the issue. However, the prospect is made complicated by the small fluxes expected from the planets, compared to those emitted by the stars. Confining to the visible wavelength range, a Jupiter-like planet would appear 10^{-9} times as luminous as its parent star. A solar-type star, at 10 parsecs, would have a magnitude $V = 5$, whereas its Jupiter, at 5 AU, would have a magnitude $V = 27$, and would be separated by 0.5 arcsec. In the range from 20 to 100 μm, the brightness contrast increases to $\sim 10^{-5}$.

Direct imaging of planets requires that the noise in the point spread function (PSF) wings is less than 4 (for the IR range) and 9 (for the visible range) orders of magnitudes with respect to the brightness peak of the star. Had one only to consider light diffraction, the minimum aperture, or baseline, D to fulfill the above requirement would be:

$$D > 0.4 \left(\frac{\lambda}{1\ \mu\mathrm{m}}\right) \left(\frac{d}{10\ \mathrm{pc}}\right) \left(\frac{5\ \mathrm{AU}}{a}\right) \mathrm{m}, \tag{1.7}$$

where λ is the observing wave length, d is the distance to the star, and a is the separation between the planet and the star. Thus, provided that enough light is gathered, diffraction is not a real issue. Besides diffraction, PSF wings are caused also by atmospheric seeing and exo-zodiacal light, which actually pose the biggest challenges to detect planets.

Specific instruments are being developed to work in the infra-red range, such as the coronographic adaptive optics and the ground-based interferometric imaging, and planned to be attached to the largest observational facilities on Earth: the Keck, the Very Large Telescope, and the Large Binocular Telescope.

1.2.6 Circumstellar Disks

In contrast to the observational difficulties for planets, it is now relatively easy to observe disks (Beckwith and Sargent 1996). They are extremely large (extending over hundreds of astronomical units from the star); they both emit and reflect light very efficiently. Additionally, disks appear to be long-lived, between 10^6 and 10^7 years, and robust against disruption caused by events accompanying early stellar evolution. They are surprisingly common in our Galaxy and resemble the picture of our primitive solar nebula. Disks are particularly evident due to the strong emission in the infrared wavelength range, between $2\,\mu\mathrm{m}$ and $1\ \mathrm{mm}$. Their spectra are much broader than any single-temperature black body. In fact, they originate from thermal emission over a wide range of temperatures: from ~ 1000 K, nearby the star, to ~ 10 K toward the outer disk edges.

The star β *Pictoris* represents a famous example of debris disk (see, e.g., Artymowicz 1997). The disk was discovered from observations of the infrared satellite IRAS. The innermost parts seem to be depleted of gas and dust, suggesting the presence of planets.

Most disks are observed around young T *Tauri* stars, which are close to star-forming regions. Calculations imply that the disk phase, and thus planetary formation, only lasts for a small fraction of the system's total life time. In spite of this, some stars may maintain disks around them for billions of years, without forming any planet (Perryman 2000).

A number of disks have been imaged by the Hubble Space Telescope. One of them, namely HD 141569, apparently shows a dark band which could be ascribed to the presence of a $1.3\ M_{♃}$ planet that has carved a gap in it (Weinberger et al. 1999). The system is old enough (10^6–10^7 years), so disk material is supposedly cool enough. This is a necessary condition for the gap to be wide and deep and thus observable.

1.3 Observations of Extrasolar Planets

Already at the end of the eighties, early radial velocity surveys targeted some stars in order to determine the brown dwarf mass function. This was done by searching for low-mass ($M_{\star} < 1\ M_{\odot}$) binary companions of main-sequence stars (see, e.g., Campbell et al. 1988). As accuracy passed the threshold of $15\ \mathrm{m\,s^{-1}}$, moving toward the expected planetary signals, groups working in the field intensified their efforts starting new observational campaigns and monitoring many more stars. The number of institutions presently involved in this "planet hunt" is impressive. An incomplete list (from Perryman 2000) includes: University of British Columbia; University of Arizona; McDonald Observatory Planetary Search, Texas; Lick Observatory; Advanced Fibre-Optic Echelle at the Whipple Telescope in Arizona; ESO Planet Search at the European Southern Observatory; the Observatoire de Haute Provence with the Elodie spectrometer; the Keck I 10-meter telescope with the HIRES spectrometer; the Anglo-Australian Telescope; the Swiss 1.2-meter Euler

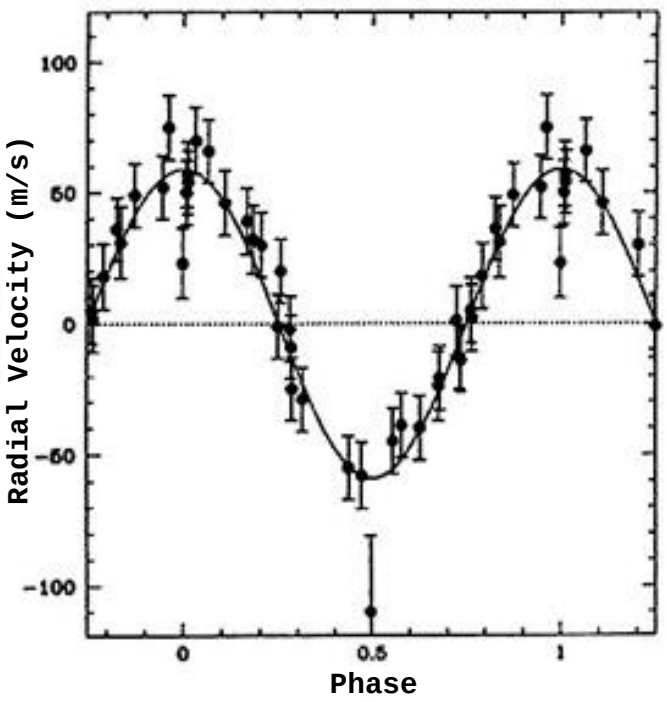

Figure 1.1: Radial velocity measurements of 51 *Pegasi* by Mayor & Queloz (*Extrasolar Planet Encyclopedia*). The periodic variation of the radial velocity has been confirmed to be due to a giant planet orbiting the star very closely. This was the first detection of a giant planet around main-sequence star.

telescope at La Silla with Coralie spectrometer; the 10-meter Texas Hobby-Eberly Telescope. Within each program, between one and three hundred late-type stars (with a visual magnitude $V < 7.5$) are being monitored in a systematic manner. The Coralie instrument alone is surveying 1600 stars.

The first observation of a low-mass companion ($11\ M_{\mathrm{Jup}}$), orbiting the star HD 114762, was achieved in 1989. Yet, prior to 1995, no representative of a planetary Jupiter-mass population had been found.

After one year of quiet study and careful examination, Mayor and Queloz (1995) announced the discovery of the first planetary candidate around the star 51 *Pegasi* (Fig. 1.1). This detection was soon confirmed by the group at the Lick Observatory, who also reported two new planetary systems that they had been surveying: 70 *Virginis* (Marcy and Butler 1996) and 47 *Ursae Majoris* (Butler and Marcy 1996). Table 1.1 contains the Keplerian orbital parameters of the first ten planetary candidate detections, along with some details of the parent stars.

The short period of 51 *Peg* companion raised many controversies. In fact, besides the unexpected short period, some proposed that the measured Doppler shifts arose from non-linear radial stellar pulsations. Subsequent studies eventually proved that the planet hypothesis was the most reasonable one.

New discoveries have followed at an amazing fast rate. It suffices to mention that the planet candidate population has risen from 8, in 1998 (Marcy and Butler 1998) to 34, in March 2000 (Perryman 2000). At the present date, October 2002, the number has increased to 101 candidates, eleven of them belonging to multi-planetary systems. (*Extrasolar Planet Encyclopedia*). All of them have been discovered by means of radial velocity measurements.

Table 1.1: Orbital elements and host star properties of the first ten candidates as planetary systems (from Perryman 2000). Entries are chronologically arranged, according to the publication date of the the announcement. Actually, the first case lies somewhat on the limit between very massive planets and low-mass brown dwarfs. The various symbols are those introduced in the previous section.

Star Name	Spectral Type	$M_\star$ $[M_\odot]$	d [pc]	K $[\mathrm{m\,s^{-1}}]$	$M_\mathrm{p}\sin i$ $[M_\oplus]$	P [days]	a [AU]	e
HD 114762	F7V	0.82	40.6	615	10.96	84.03	0.351	0.33
51 *Peg*	G5V	0.98	15.4	55	0.46	4.231	0.052	0.01
47 *UMa*	G0V	1.03	14.1	51	2.60	1084.0	2.09	0.13
70 *Vir*	G2.5V	1.10	18.1	316	7.42	116.7	0.482	0.40
τ *Boo*	F7V	1.20	15.6	474	4.14	3.313	0.047	0.02
16 *Cyg* B	G2.5	1.00	21.6	50	1.68	796.7	1.69	0.68
ρ *CrB*	G2V	1.00	17.4	61	0.99	39.81	0.224	0.07
HD 187123	G3V	1.00	47.9	72	0.54	3.097	0.042	0.01
Gliese 876	M4	0.32	4.7	235	2.07	60.90	0.207	0.24
HD 217107	G7V	0.96	19.7	140	1.29	7.130	0.072	0.14

Other techniques have not been successful yet. However, for each of them, the hope of many researchers relies on future ground-based and, above all, space programs.

Astrometric observations suffer many limitations when conducted from the ground, which prevent attaining a precision better than milliseconds. They are by far more accurate when made from outside the Earth's atmosphere. Measurements from the space mission Hipparcos, the only carried out so far, have been employed for detection of brown dwarfs. Moreover, Hipparcos has provided constraints on planetary masses of known systems. Future space astrometry experiments will try to reach accuracies around a micro-arcsecond, like NASA's SIM and ESA's GAIA missions. The former will be dedicated to the detailed orbit determination of systems detected from ground-based facilities. The latter will monitor approximately a billion stars, up to the magnitude $V \simeq 20$, as part of a census of the galactic stellar population.

Ground-based photometry achieving an accuracy better than 0.1% is complicated by variable atmospheric extinction. The situation would improve if detectors were operating above the atmosphere. Eddington mission was planned by ESA. It includes a 1-meter telescope with a wide field of view. After the first couple of years, to be dedicated to study stellar seismology, the mission should be dedicated to planetary transit detections in up to $700\,000$ stars. The expected precision is about 10^{-6}, therefore it should capable of revealing transits of Earth-mass objects orbiting main-sequence stars. US Kepler mission was specifically designed to find Earth-mass bodies in the habitable zone, for a variety of stellar types. Unfortunately, it was not selected as part of the NASA's Discovery Program. Another space project, COROT, is led by the French Space Agency and is scheduled for launch in 2004. It will reach a photometric accuracy between 7×10^{-4} and 5×10^{-3}. These values will not probably allow detection of Earth-class planets, but slightly larger

(and closer to the central star) objects might be targeted. Two similar projects (MONS and MOST) have been planned by the Danish and Canadian Space Agencies.

Also in the case of gravitational microlensing, there are plans for space programs. NASA's SIM is planned for launch in 2005 and it is going to observe lensing events announced by ground-based facilities. GAIA mission, by ESA, could offer good opportunities as well.

Direct imaging would offer promising prospects to detect and characterize terrestrial planets with an infrared space interferometer having a baseline on the order of 50 meters. In fact, such facility would greatly improve the flux contrast between the planet and the star. Besides, it would make accessible the spectral window 6–17 μm, which contains signatures of molecular species, like H_2O, CO_2, O_3, and CH_4, considered indicators of life. Both ESA and NASA plan to launch satellites (Darwin and TPF, respectively), equipped with instruments of this kind, sometime after 2010. Additionally, the Hubble Space Telescope, NASA's SIRTF (a 0.85-meter infrared observatory), and the Next Generation Space Telescope (to be launched in 2010) might also be capable of planet imaging.

1.4 Statistics of Extrasolar Planets

After a couple of years of discoveries, the depicted scenario turned out to be quite bizarre and very different from what the general opinion expected: all of the planets were revolving on either extremely close or extremely eccentric orbits. It was not clear, and still it is not, whether the anomalies reside in the properties of our Solar System or those objects just represent the tail of the brown dwarf distribution. It is almost certain that selection effects have played a role. In fact, even with the highest Doppler precision measurements of $3\ \mathrm{m\,s^{-1}}$, only minimum masses of $0.5\ M_{♃}$ can be detected at 2 AU .

The statistical properties that we will discuss are based on a sample of 101 candidates.

1.4.1 Planetary Mass Function

The mass function[2] of low-mass stellar companions starts to steepen below $10\ M_{♃}$ and continues to rise down to the detection limit, as shown in Figure 1.2. The data are extracted from surveys which would have easily detected any sub-stellar companions with $M_{\mathrm{p}} \sin i \gtrsim 3\ M_{♃}$, orbiting at distances shorter than 2 AU. But great incompleteness is likely to exist for $M_{\mathrm{p}} \sin i \lesssim 1\ M_{♃}$, over the same range of distances. However, restricting to objects of shorter periods, with an accuracy of $3\ \mathrm{m\,s^{-1}}$, a Saturn-mass planet can be revealed within 1 AU, and a Neptune-mass planet can be observed inside 0.1 AU. As a result, the true mass function might be even steeper toward lower masses than that illustrated in Figure 1.2.

The scarcity of sub-stellar mass representatives having $M_{\mathrm{p}} \sin i \gtrsim 10\ M_{♃}$ is quite striking, since they would be easily detected by the monitoring campaigns conducted so far. Apparently, less than 0.3% of the stars, with masses between 0.3 and $1.1\ M_{\odot}$, have companions in the range from 10 to $80\ M_{♃}$ orbiting inside 3 AU. This characteristic is now

[2]The integral of mass function between M_1 and M_2 yields the total number of objects in that mass range.

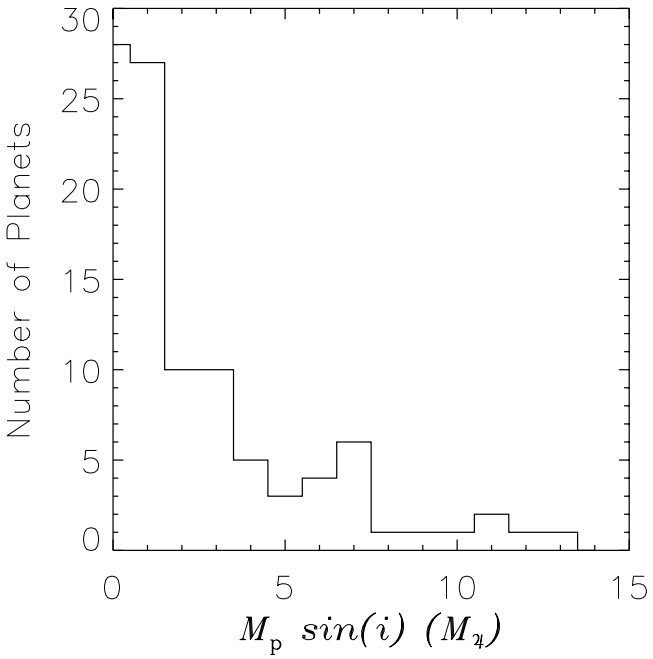

Figure 1.2: Sub-stellar mass function obtained from planetary candidates listed on the Web site of the *Extrasolar Planet Encyclopedia*. The sample should be complete for companions more massive than $3\ M_\oplus$, within 2 AU.

known as "brown dwarf desert". A possible mechanism, which might have caused it, is orbital migration due to gravitational interaction with circumstellar disk material.

1.4.2 Orbital Distances

As mentioned before, all the radial velocity observation with high precision are biased toward the discovery of planets in tight orbits, since short period bodies yield larger Doppler signals (and over shorter times) relative to long period ones. This selection effect could explain the excess of planets found within 0.2 AU, with respect to those revolving outside 2 AU (see Fig. 1.3, left panel). However, it does not definitely offer any convincing argument about the evidence that the range of distances $a \leq 0.2$ AU is so greatly preferred to the range from 0.2 to 0.7 AU.

Standard theories would predict giant planet formation only beyond ~ 4 AU (Lissauer 1993; Hubbard et al. 2002). Then, orbital migration by a gaseous circumstellar disk would drive them all the way down to the small orbits that we observe today. This phenomenon is one of the major topics of the present dissertation. Since the migration time scale $\tau_{\rm M}$ is proportional to the semi-major axis a, the larger a the longer $\tau_{\rm M}$ results. Therefore, one would expect that more planets should be observed at larger orbital distances. Yet, as we will see in the next chapters, migration velocity may depend on various, poorly known, parameters characterizing the protostellar disk, as well as on the planetary mass. The piling up of objects at 0.05 AU may be due either to some types of halting mechanism or, once again, to some intrinsic limitations of the observations.

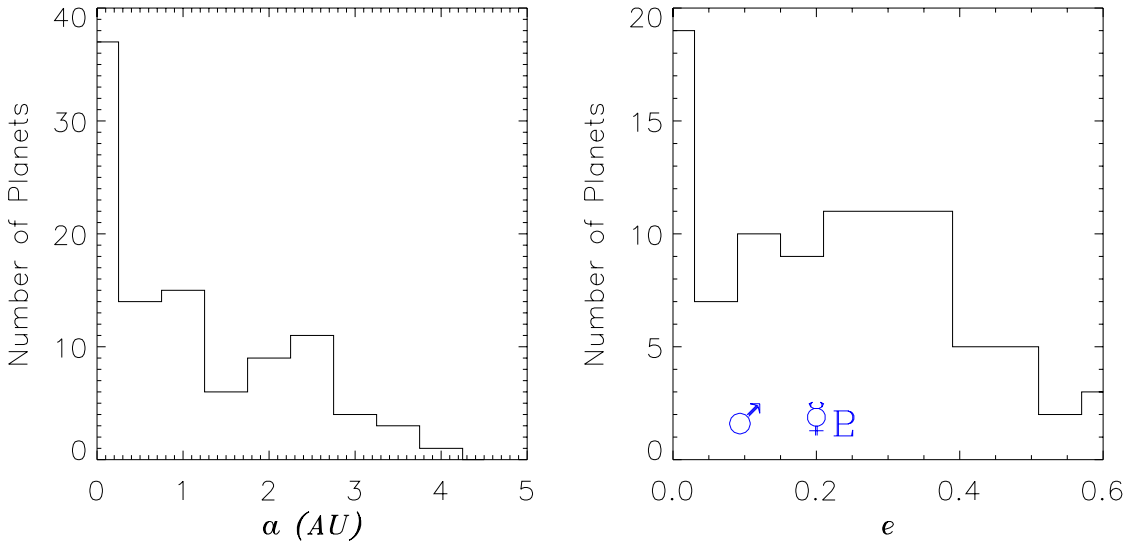

Figure 1.3: Orbital semi-major axis (**left panel**) and eccentricity (**right panel**) of planetary candidates listed on the Web site of the *Extrasolar Planet Encyclopedia.* Symbols in the right panel refer to the Solar System planets with the most eccentric orbits (Pluto, Mercury, and Mars).

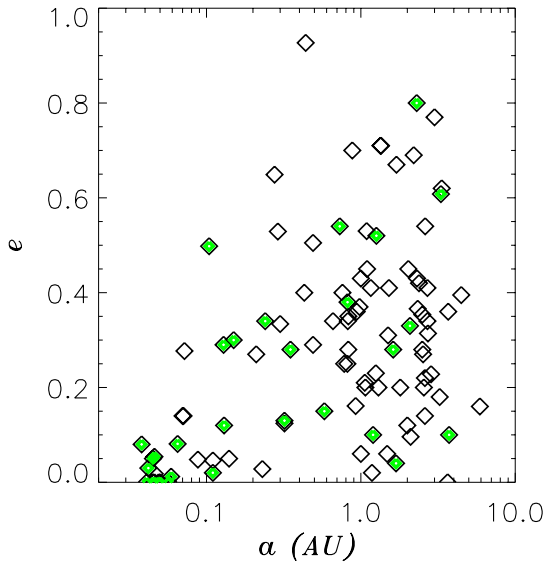

Figure 1.4: Eccentricity plotted versus the semi-major axis of extrasolar planet candidates. Tight orbits tend to be more circular whereas large eccentricities are found for distant planets. Green filled diamonds represents objects less massive than one Jupiter's mass.

1.4.3 Orbital Eccentricities

In the right panel of Figure 1.3 there is reported the histogram of the eccentricities of the planet candidates, detected so far. It shows that a numerous ensemble of planets

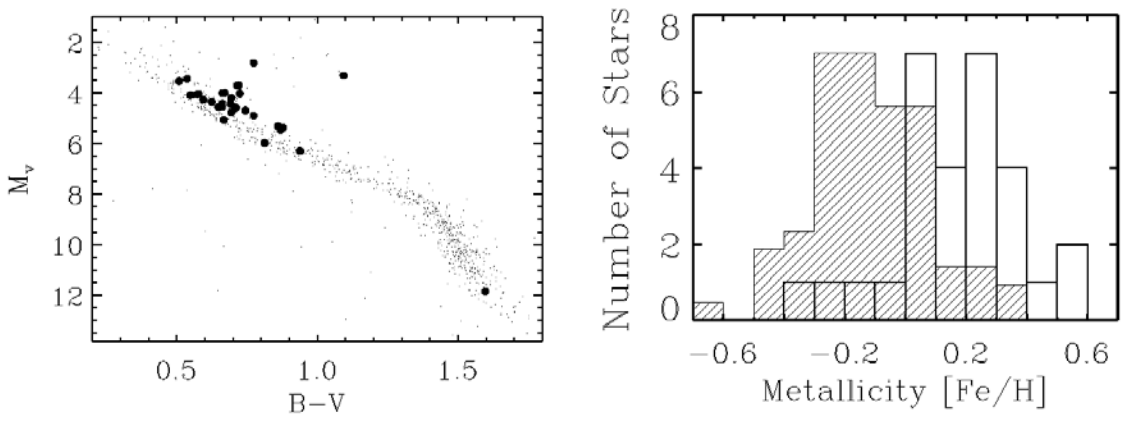

Figure 1.5: **Left panel**. Color-magnitude diagram of main-sequence stars with spectral type extending from F0 to M7. Small dots represents stars nearer than 20 pc. Larger dots indicate the positions occupied in the diagram by stars with planets. **Right panel**. Metallicity histogram of the stars hosting planets (empty boxes) compared to that of the nearest field stars (hatched region). It is evident that all of the star harboring planets are metal-rich relative to the Sun, which is itself metal-rich compared to nearby field stars. From Butler et al. (2000).

has very eccentric orbits ($e > 0.2$). Moreover, there seems to be a correlation between orbital eccentricity and semi-major axis, favoring close circularized trajectories and more elliptical distant ones (see Fig. 1.4). In the standard scenario of planet formation, orbits should remain nearly circular. Yet, eccentricities can be easily driven away from zero via gravitational perturbations in multi-planetary systems. Furthermore, in some cases high orbital eccentricities may be related to the circumstance that the parent star belongs to a binary system (Mazeh et al. 1997).

Recent investigations, on solar-type stars, indicate that extrasolar planets and brown dwarfs have in common the same distribution of probability for orbital periods and eccentricities (Stepinski and Black 2000). Additionally, they share very a similar correlation between periods and eccentricities and a similar lack of correlation between masses and eccentricities. Thus, as some researchers have already suggested, the properties of the present sample of extrasolar planets could appear more "natural" in the context of a broader populations which included all low-mass stellar companions. As a matter of fact, without enlarging the ensemble of planetary candidates, such an issue cannot be addressed properly.

1.4.4 Properties of the Host Stars

Figure 1.5 (left panel) shows the color-magnitude diagram centered on the main sequence star with spectral type from F0 and M7. Types earlier that F5 do not offer those sharp spectral features necessary for accurate Doppler measurements, because of their fast rotation. The small dots, which indicate stars within 20 pc from the Hipparcos catalog,

well define the main sequence. The vast majority of the stars harboring planets (larger dots) lie on the main sequence and have a color index $B-V$ in the interval $[0.5, 1.0]$. Many of these stars are also naked-eye stars. Except for dwarf M and K stars, stellar masses are all around the solar mass value. Because of their faint luminosity, only since recently both dwarf M and K stars are being monitored.

Another interesting characteristic of the stars that host planets is that they have significantly higher metal content (elements heavier than helium), as demonstrated by the histogram in Figure 1.5 (right panel). The comparison sample is constituted by G dwarfs residing within 20 pc from the Sun. In some cases, like ρ^1 55 *Cnc* and 14 *Her*, planet bearing stars are among the most metal-rich stars in the solar neighborhood. Two possible scenarios have been proposed to explain such an occurrence. In the first, high metallicity environments would facilitate the birth of both metal-rich stars and rocky cores (and thus, giant planets). This hypothesis is essentially based on the assumption the metals make condensation easier. In the second, stars would be "polluted" or "enriched" by the capture of migrating bodies. Of course, in this last circumstance, the impact could have the desired consequence only if the convective zone of the outer stellar envelope were sufficiently small. Otherwise, the addition of heavy elements would be barely significant. We have seen that most of the stars hosting planets are main-sequence solar-mass stars, hence they are likely to have radiative cores with relatively small outer convection envelope.

1.5 Theory of Extrasolar Planet Formation

Formation theories concerning extrasolar planets generally follow the same arguments as formation theories of planets in our Solar System. Since a couple of hundred years, this has represented one of the most fundamental problems of science. An incredible amount of work has been dedicated to it, which has resulted in different theories, yet no final conclusions have been reached. Many reviews have been written on the topic (e.g., Pollack 1984; Lissauer 1993; Wuchterl et al. 2000; Hubbard et al. 2002), which can give an idea of our present-day knowledge on the issue.

The scenario of planetary formation is far from being complete, therefore only a rough picture of it can be painted. This often has its foundations on the common physical knowledge, observational, and experimental constraints collected from the Solar System. When investigation must be based on available traces rather than on the necessary data, it happens that some implications cannot be demonstrated, and then they are just assumed for the sake of the "common sense".

In what we may call a "standard disk" picture, formation proceeds through several stages (Lissauer 1993). Circumstellar material is made out of a mixture of gas and dust. Because of sedimentation, dust particles settle into the midplane of the disk, generating a dense layer. Grains are likely to collide and stick together, producing larger particles whose size may range from 0.01 and 10 m (Beckwith et al. 2000). Afterward, collisions lead to the formation kilometer-size bodies, also named "planetesimals", over a period between 10^4 to 10^5 years. Planetesimals gravitationally interact with each other and possibly settle on preferential Keplerian orbits, with gaps among them. In a third phase, complex N-body interactions change the orbital paths of planetesimals so that there may be close

encounters. As a result, some of these objects can be disrupted, or scattered away. Yet, if encounters happen at low relative velocities, larger bodies may form, which are usually referred to as "planet's embryos". Embryos have masses around 10^{23} km, though this value is quite uncertain and depends on the distance from the central star and certain properties of the local environment. At this point of planet formation, a runaway growth sets in. Over 10^7 to 10^8 years, terrestrial-size planets may generate. Actually, the length of time is connected to the details of encounters between planetesimals. The growth should end when the reservoir of planetesimals between planetary cores empties. If planet's cores grow large enough ($\sim$ 10–30 $M_{\oplus}$), their gravitational attraction leads to the accretion of residual gas from the surrounding environment. Such process gives birth to giant gas planets (Bodenheimer and Pollack 1986). In the popular picture, these planets happen to be generated in the outer parts of the Solar System because the initial debris density might have been higher there, due to lower temperatures and better conditions for condensation. Gas accretion would then greatly reduce when disk-planet interactions eventually lead to the carving of a density gap (Lin and Papaloizou 1993). Contrary to what initially argued, simulations show that a Jupiter-mass planet can still accrete material through the gap (e.g., Kley 1999, and next chapters). But, with masses of a few Jupiter's, accretion drastically decreases and becomes negligible.

An alternative proposal for giant planet formation proceeds via gravitational instabilities in a massive cool protostar nebula and subsequent fragmentation (Pollack 1984; Boss 2000). This mechanism would also accelerate giant planet formation.

This possible scenario has been shaped on the evidences offered by our Solar System. Data furnished by extrasolar planets have brought new evidences some of which, unfortunately, do not match to the aforementioned theory. These new evidences suggest that three categories can be identified: Jupiter analogues (such as 47 *UMa*), planets on highly eccentric orbits (such as 70 *Vir*), and "hot Jupiters" (such as 51 *Peg*) with small circular orbits. A reliable planet formation theory should encompass all of them and explain not only the mass distribution but also the observed eccentricity and semi-major axis distributions. Apparently, the standard picture depicted before only applies to the first category.

As a matter of fact, even the definition of planet should probably be revised since planet-size free-floating bodies are observed and some stars may harbor both brown dwarfs and giant planets (Hubbard et al. 2002). If brown dwarfs and extrasolar planets have a common origin, in the broader framework of stellar companions' formation, as pointed out by Stepinski and Black (2000), then something needs to be changed in the standard scenario.

Migration of planets (Goldreich and Tremaine 1980) may play a major role to reconcile the standard theory with new evidences provided by extrasolar planets. In fact, giant planets could as well form farther away from the star and then been moved inward by gravitational torques, due to disk material (see, e.g., Lubow et al. 1999; Kley et al. 2001). Yet, many open issues still remain on this topic, among the most important ones are how to efficiently halt migration and whether it unconditionally happens to be inward. Various mechanisms have been proposed to stop migration, such as the disruption of the disk near the star by the stellar magnetosphere. Perturbations by stellar encounters have been also considered, as a possible source of orbital eccentricity. Another mechanism heavily relies

on the imperative of fast inward migration. Giant planets would continuously form and then be accreted by the star, until the disk material would be diluted enough to allow longer viscous evolution times. It is beyond doubts that massive disks ($M_{\rm D} > 0.01\ M_{\odot}$) would offer a few chances, if any, to a massive body to survive. Thereby, many heavy planets should form and be destroyed before one (or more) could eventually have a long-lasting life.

Very recently, Trilling et al. (2002) conducted a numerical statistical study on the survival of giant protoplanets, for a variety of initial conditions. They conclude that, because of fast inward migration, surviving planets have relatively large semi-major axes (several astronomical units). Hence, the planets observed to this date only represent a small fraction (25% to 33%) of the giant planet population around solar-type stars. Many undetected objects must exist, orbiting at large distances ($d \gtrsim 2$ AU) from the parent stars. Furthermore, they find that the efficiency of giant planet formation is very high and that between 10% and 80% of all solar-type stars should host a giant planet during their pre-main sequence phase.

But probably both semi-major axis and eccentricity distribution must be inserted in a larger context in which multiple-planet formation and / or interaction is contemplated. Attempts to numerically study these situations have already been initiated (Kley 2000; Snellgrove et al. 2001). Unfortunately, multi-planet systems do not provide the wealth of information required to tackle this problem yet. Too many degrees of freedom are still present. Future observational programs could hopefully eliminate some of them and clarify some aspects of this puzzling problem. In only a few years many steps forward have been made and many others are likely to be taken in the near future.

1.5.1 Interaction between Disks and Embedded Planets

Regardless of the precise mechanisms which lead to the formation of planets, once an Earth-like object has formed, it affects the surrounding medium via gravitational perturbations. As a consequence, particular locations (Lindblad resonances) are excited and spiral density waves emanate from around L1 and L2 Lagrangian points. When the mass of the perturber is large enough, the perturbation regime becomes non-linear. The planet removes angular momentum from material inside of its orbit and transfers it to material outside of the orbit, eventually opening a density gap along the orbital path. Yet, the perturbed disk environment reacts to the planet. As a result, the planetary orbit has to adjust to the gain or loss of energy and angular momentum. Therefore semi-major axis, the eccentricity, and the inclination change in time and the way they change eventually determines the planet survival.

The problem of disk-planet interaction has been approached by means of analytical studies as well as of local and global numerical simulations.

The first evaluation of the exchange of angular momentum and energy between a disk and an embedded body was performed by Goldreich and Tremaine (1980). By using a linear perturbation theory for thin disks they concluded that the time scale over which the semi-major axis of a Jupiter-type planet would change is around 10^4 years. Yet, because of their approximations, they could not estimate the direction of the drifting motion. Papaloizou and Lin (1984) found that, due to the balance of viscosity and tidal angular mo-

mentum transfer, a density gap is generated and that a Jupiter-mass planet would open a gap even in a disk whose aspect ratio is ≈ 0.05. Ward (1986) conducted an analytical study of the Lindblad torques, taking into account density, pressure, and sound speed gradients inside the disk. He showed that the direction of the radial migration is usually toward the central star and that Earth-mass planets migrate on a time scale much shorter than the disk life time. Only if the mass is large enough to open a deep and wide gap, migration slows down (Ward 1997). Recently, Tanaka et al. (2002) analyzed both Lindblad and corotation torques arising from a three-dimensional isothermal disk. They found that torques exerted at corotation locations can reduce the migration speed of low-mass planets. The same conclusion was reached by Masset (2001).

From the numerical point of view, this problem was tackled for the first time by Miki (1982), who carried out two-dimensional hydrodynamic simulations of the gas flow around a planet embedded in a disk with a local linearized shearing sheet method. Within the framework of local simulations, Miyoshi et al. (1999) modeled disks with planets in both two and three dimensions in order to determine gravitational torques in the linear regime, i.e., for protoplanets with masses smaller than roughly a tenth of Jupiter's. More recently, following a similar strategy, Tanigawa and Watanabe (2002) inquired into the details of the two-dimensional flow structure around protoplanets, evaluating the mass accretion rate. Local simulations have the asset of better resolving the flow and density structures around protoplanets, because only a small portion of disk is taken into account. However, they do not allow to compute directly the torque balance onto the protoplanet. Moreover, they are more sensitive to the chosen boundary conditions. Additionally, it is not certain whether, in the absence of large scale features, the local flow is correctly reproduced. For example, local computations cannot account for the gap formation. For this reason the global description, where the domain covers an entire disk ring, should always be preferred to the local one. Global and fully non-linear simulations were performed by Kley (1999), Bryden et al. (1999), Lubow et al. (1999), and Masset (2002), assuming the planet on a circular orbit, and by Kley (2000) and Nelson et al. (2000), following the planet's orbital decay. Both gravitational torques and mass accretion could be estimated.

The present work proceeds with this line of research, attempting to move ahead on unexplored grounds. Via global computations, we simulate Jupiter-size planets in three-dimensional disks, analyzing both planet's migration and accretion. The lack of simulations accounting for all the three dimensions is a sign of the difficulties posed by them. But they are necessary because only comparing outcomes from computations in two- and three-dimensions one can be reasonably sure of the limitations and the applicability range of (more affordable) models in two dimensions. Unfortunately, global simulations have the disadvantage of not allowing an appropriate resolution in the Roche lobe of the perturber. Yet, the flow in the vicinity of a protoplanet is fundamental for the determination of some of its final properties, such as mass and rotation rate. Furthermore, the fluid dynamics inside of the Roche lobe gives indications concerning satellite formation. By means of an appropriate numerical tool, though still treating the disk globally, we resolve all the determinant length scales of the problem in a very accurate manner. We therefrom achieve an accurate representation of the flow around protoplanets with masses as large as Jupiter's and as small as the Earth's, in both two and three dimensions. In this context it should be

pointed out that a thorough investigation of planet formation has to include not only local aspects but also global ones. All of the studies conducted so far (see, e.g., Bodenheimer and Pollack 1986; Wuchterl 1991, 1993; Tajima and Nakagawa 1997) have used physically detailed (one-dimensional) models but have neglected the interaction of the forming planet with the surrounding medium. Finally, in order to have a more realistic and faithful picture of disk-planet interactions, we attempt to tackle the outstanding issue of coupling the thermal part to the dynamics evolution of the system.

For as to what we have heard you affirm, that there are other Kingdoms and States in the World inhabited by human Creatures as large as yourself, our Philosophers are in much doubt, and would rather conjecture that you dropt from the Moon, or one of the Stars; because it is certain, that a hundred Mortals of your Bulk would, in a short time, destroy all the Fruits and Cattle of his Majesty's Dominions.

JONATHAN SWIFT,
GULLIVER'S TRAVELS,
1726

CHAPTER 2

GLOBAL SIMULATIONS IN THREE DIMENSIONS

This chapter will mostly deal with global computations of embedded Jupiter-mass planets in three dimensions. Therefore, unlike all the calculations performed so far, also the vertical structure of the disk will be resolved. This will allow to evaluate the global effects that the vertical dimension may have on disk-planet interactions and the differences existing between global models in two and three dimensions.

2.1 Introduction

The only global and non-linear numerical computations of planets embedded in disks have been performed by relying on the two-dimensional approximation, as anticipated in § 1.5.1. The need of approaching this problem by employing a full three-dimensional description resides in the nature of the planet's perturbations. In fact, the perturbing effects due to the gravitational force exerted by the planet are largest around its Roche lobe. Even though accretion disks are geometrically thin, when considered from the global point of view, they might be not as such when considered from the length scales over which planet perturbations are strongest. Although theoretical arguments can be invoked to justify the validity range of the flat geometry, only 3D calculations can give the final proof.

In § 2.2, we introduce the physical model and we also state all the assumptions and approximations. In § 2.3, we present a test calculation analyzing the ability of the code to describe disks in three dimensions. Sections 2.4 and 2.5 contain the results for the complete cases including the planet. The conclusions are given in the last § 2.6.

2.2 Model Description

In calculating the dynamical evolution of an accretion disk, it is usually assumed that the mean free path between individual particles is small compared to the overall extent of the disk. Thus, the evolution is described best by the hydrodynamic approximation including viscosity, i.e., the Navier-Stokes equations. Here, we consider a full three-dimensional

model which includes the vertical extension of the disk.

The disk is non-self-gravitating and is orbiting a protostar having a mass of $1\ M_\odot$. The total mass of the disk M_D within the simulated region, 2.08 to 13 AU, is $3.5 \times 10^{-3}\ M_\odot$. Embedded in this disk there is a massive protoplanet of typically $1\ M_\mathrm{J}$ but a smaller mass of $0.5\ M_\mathrm{J}$ has been considered as well. The planet is assumed to be on a fixed circular orbit throughout the evolution.

2.2.1 Basic Equations

Suited best for this problem are spherical polar coordinates $(O; R, \theta, \varphi)$ where R denotes the radial distance from the origin, θ the polar angle measured from the z-axis, and φ denotes the azimuthal coordinate starting from the x-axis.

In this coordinate system, the mid-plane of the disk coincides with the equator ($\theta = \pi/2$), and the origin of the coordinate system, $R = 0$, lies in the center of mass of the star and planet. Sometimes we will need the radial distance from the polar (i.e., the rotational) axis which we denote by a lower case $r = R \sin\theta$, which is the radial coordinate in cylindrical coordinates.

For a better resolution of the flow in the vicinity of the planet, we work in a rotating coordinate system which rotates with the orbital angular velocity Ω, which is identical to the orbital angular velocity of the planet

$$\Omega_\mathrm{p} = \sqrt{\frac{G\,(M_\star + M_\mathrm{p})}{a^3}} \tag{2.1}$$

where $M_\star$ is the mass of the star, M_p the mass of the planet, and a is the distance of the star from the planet. For the sake of comparison, we calculated additional models in the inertial frame.

The full hydrodynamic equations, including the viscous terms, spelled out in spherical polar coordinates can be found for example in Tassoul (1978) or Mihalas and Weibel Mihalas (1999). However, as we use here a more conservative variant of the momentum equations including a rotating frame of reference we quote them explicitly.

The radial momentum equation reads

$$\frac{\partial \rho\, u_R}{\partial t} + \nabla \cdot (\rho\, u_R\, \mathbf{u}) = \rho\, \frac{u_\theta^2}{R} + \rho\, (\omega + \Omega)^2\, R\, \sin^2\theta - \frac{\partial p}{\partial R} - \rho\, \frac{\partial \Phi}{\partial R} + f_\mathrm{R}, \tag{2.2}$$

where ρ denotes the density of the gas, $\mathbf{u} = (u_R, u_\theta, u_\varphi)$ is the velocity of the gas, ω is the azimuthal angular velocity as measured in the rotating frame, p is the gas pressure, and Φ denotes the gravitational potential due to the star and the planet.

The meridional momentum equation is

$$\frac{\partial (\rho\, R\, u_\theta)}{\partial t} + \nabla \cdot (\rho\, R\, u_\theta\, \mathbf{u}) = \rho\, (\omega + \Omega)^2\, R^2\, \sin\theta\, \cos\theta - \frac{\partial p}{\partial \theta} - \rho\, \frac{\partial \Phi}{\partial \theta} + f_\theta. \tag{2.3}$$

The angular momentum equation reads

$$\frac{\partial \rho\, h_t}{\partial t} + \nabla \cdot (\rho\, h_t\, \mathbf{u}) = -\frac{\partial p}{\partial \varphi} - \rho\, \frac{\partial \Phi}{\partial \varphi} + f_\varphi, \tag{2.4}$$

where we defined the *total* specific angular momentum

$$h_t = (\omega + \Omega)\ R^2\ \sin^2\theta, \tag{2.5}$$

i.e. the azimuthal velocity in the rotating frame is given by $u_\varphi = \omega\, R\, \sin\theta$.

The Coriolis force of the last equation for u_φ has been incorporated into the left hand side. Thus, it is written in such a way as to conserve total angular momentum best. This conservative treatment is necessary to obtain an accurate solution of the embedded planet problem, as demonstrated by Kley (1998).

The vector $\boldsymbol{f}$ includes the viscous forces and it has the following components: $f_R = \rho\,[\nabla\cdot\mathbf{S}]_R$, $f_\theta = \rho\, R\,[\nabla\cdot\mathbf{S}]_\theta$, and $f_\varphi = \rho\, R\,\sin\theta\,[\nabla\cdot\mathbf{S}]_\varphi$. The components of the divergence of the stress tensor $\mathbf{S}$, in spherical polar coordinates, are explicitly stated in Mihalas and Weibel Mihalas (1999). For the description of the viscosity we assume a Reynolds stress-tensor approach with a constant kinematic viscosity coefficient ν having the value 10^{-5} in dimensionless units (see next section for an explanation), which translates into a Reynolds number of 10^5. For the given vertical thickness of the disk ($H/r = 0.05$) this value for ν is equivalent to $\alpha \approx 4\times 10^{-3}$ at the planet location.

For simplicity, to avoid any complications due to internal heating and radiative transport, we treat here only disks with a specified temperature distribution (see below).

2.2.2 Numerical Issues

The calculation are performed using the three-dimensional nested grid MHD-code NIRVANA, whose details will be explained in the next chapter.

For computing convenience, we use dimensionless units where all the lengths are normalized the distance of the planet to the star, i.e., $r_0 = 5.2$ AU. The unit of time is the inverse orbital frequency of the planet $t_0 = 1/\Omega_\mathrm{p}$. The evolutionary times as quoted in the result sections are typically given in units of the orbital period $P = 2\pi/\Omega_\mathrm{p}$ of the planet. The density ρ_0 is normalized such that the total mass of the disk is $3.5\times 10^{-3}\ M_\odot$.

The computational domain consists of a spherical polar section of the disk, extending radially from $R_\mathrm{min} = 0.4$ to $R_\mathrm{max} = 2.5$, meridionally from $\theta_\mathrm{min} = 80^\circ$ to $\theta_\mathrm{max} = 90^\circ$, and azimuthally from 0 to $2\,\pi$. Vertically, the computational domain has an extension of 10° measured from the equatorial plane, which is sufficient to include the whole disk. For the standard case, the domain is covered by $(N_R, N_\theta, N_\varphi) = (128, 20, 128)$ grid cells, which are distributed equidistantly in R, θ, and φ. For the higher resolution cases the number of azimuthal grid cells is increased to 384. Some additional simulations required different grid resolutions which will be explicitly given when such computations are discussed.

We have assumed reflection symmetry with respect to the equatorial plane, and simulate only the upper half of the disk, as mentioned above. In the azimuthal direction, we use periodic boundary conditions, and in the radial direction we chose closed inner and outer boundaries. For a more detailed discussion on the boundary conditions, along with some effects ascribable to them, see CHAPTER 5.

2.2.3 Initial Setup

The initial disk is assumed to be axi-symmetric with respect to the polar axis, $\theta = 0$, of the coordinate system. The gas moves with Keplerian velocity around the central star and has no radial and vertical motion; that means the velocity at $t = 0$ is $\mathbf{u} = [0, 0, (\Omega_{\rm K} - \Omega)\, R]$, where $\Omega_{\rm K}$ is the Keplerian angular velocity of the gas, $\Omega_{\rm K} = (G\, M_\star / r^3)^{1/2}$, and we have included the correction caused by the rotating coordinate frame. For simplicity we neglect any vertical dependence of u_φ in the initial conditions because the vertical thickness H of protoplanetary disks at a given distance r from the center is typically very small compared to the radius.

Here we assume that the disk has a *constant* relative thickness $h = H/r$ at all radii. This is usually a good approximation for accretion disks since detailed vertical models give, for regions which are not flared, a very weak dependence of H/r with radius, typically $H/r \propto r^{0.1}$. Here we choose three different values ranging from $H/r = 0.05$ up to $H/r = 0.15$. A thin Keplerian disk is radially in equilibrium as gravitational and centrifugal forces approximately balance because pressure effects are small. The vertical structure can be obtained from the equation of hydrostatic equilibrium (in cylindrical coordinates). If one assumes that the disk is thin and is locally isothermal, $T = T(r)$, one finds easily that the local vertical density profile is given by a Gaussian (Frank et al. 1992). Hence, neglecting again geometry effects, we use as initial density

$$\rho(t = 0) = \frac{\rho_0}{(r/r_0)^{3/2}} \exp\left[-\left(\frac{\vartheta}{h} \right)^2 \right], \tag{2.6}$$

where $\vartheta = \pi/2 - \theta$ is the polar angle measured from the mid-plane of the disk. The constant ρ_0, which sets the total mass of the disk, is arbitrary as long as no back-reaction of the disk onto the orbit of the planet or self gravity is taken into account. Here we adjust ρ_0 such that the total mass of the disk within the computational domain (from 2.08 to 13.0 AU) is $M_{\rm D} = 3.5 \times 10^{-3} M_\odot$. The radial dependence has been chosen such that the vertically averaged density $\Sigma(r) = \int_{-\infty}^{+\infty} \rho {\rm d}z$, i.e., the surface density, falls off as $r^{-1/2}$. This allows a direct comparison of the new three-dimensional results with previous two-dimensional computations by Kley (1999). The constant r_0 is some reference radius which we may choose to coincide with the present-day Jupiter orbital radius. The temperature law follows from the constancy of h, and is given by

$$T = h^2 \left(\frac{\mu\, m_{\rm H}}{k} \right) \left(\frac{G\, M_\star}{r} \right), \tag{2.7}$$

where μ is the mean molecular weight, $m_{\rm H}$ is the hydrogen mass, and k is the Boltzmann constant. Since only the gas pressure p enters the momentum equations written before and $p \propto T/\mu$, these calculations are independent of the specific value of the mean molecular weight.

In general we consider that a planet with mass $1\ M_{♃} = 0.001\ M_\odot$ is located at $R = 5.2$ AU and, since we are working in the corotating frame, at the fixed azimuthal angle $\varphi = \pi$. Yet, lower planetary masses will be also simulated.

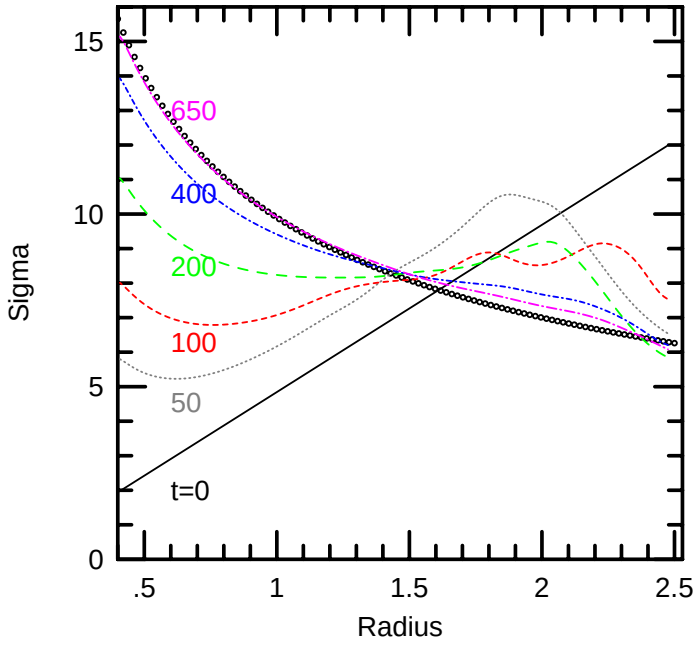

Figure 2.1: Vertically averaged density Σ, as function of the distance r from the rotational axis, at different times for the test model with no planet and an initially constant three-dimensional density. At late times Σ approaches the analytic profile (circles).

The standard model (§ 2.4) refers to a modest resolution of $(N_R, N_\theta, N_\varphi) = 128 \times 20 \times 128$) grid-cells. However, to test the reliability of this apparently low resolution concerning the accretion and migration rate (that is gravitational torques) we also considered higher resolution models with with different physical parameters, as given in Table 1 below. We note that, using the standard resolution, there are about 4.5 radial and only 1.7 azimuthal grid-cells within the Roche lobe of a Jupiter-mass planet. However, since mass is taken out continuously from the middle of the Roche lobe we believe that this resolution may be sufficient to yield reliable results. This is tested by higher resolution cases, which give in fact essentially the same outcomes for the mass accretion and the migration rate.

2.3 A Test Case

As this is the first application of the code to three-dimensional disks we present, in the beginning, results of a test calculation where we study the evolution of a section of a disk, without a planet, toward dynamical equilibrium. Then we describe our results obtained for the full embedded planet case.

We start with an initially constant density $\rho = \text{constant}$ configuration rotating with Keplerian speed around the star. The radial and vertical velocities have been set to zero initially. For the given temperature profile, which is constant on $\theta = \text{constant}$-surfaces, we expect the vertical density profile to become Gaussian (see above) and for the surface density Σ the final radial distribution should follow the law $\Sigma \propto r^{-1/2}$.

In Figure 2.1 we display the radial dependence of the azimuthally averaged surface density at different times. We note that during the whole time evolution, that is during

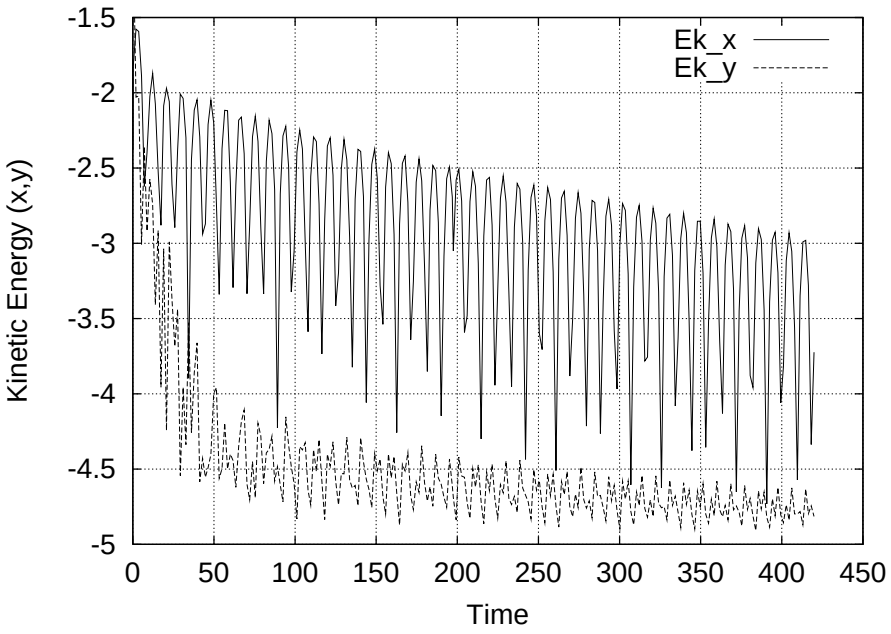

Figure 2.2: Time evolution of the total kinetic energies in the radial (x) and meridional (y) direction.

500 orbits or 200000 time steps, the azimuthal asymmetry did not grow beyond 10^{-13}. At $t = 0$, the constant three dimensional density yields a profile $\Sigma_0 \propto r$. During the evolution toward equilibrium sound waves are generated which are slowly damped by the viscosity, and finally the density profile approaches the analytic solution.

The viscous damping is illustrated in Figure 2.2, where the time evolution of the total kinetic energy of the radial and vertical velocity components are displayed. After a brief and fast initial decline due to non-linear effects, the decay proceeds on the long viscous time scale.

The evolution toward vertical equilibrium is displayed in Figure 2.3 where we plot the vertical density distribution at $r = 1$, at different evolutionary times. As expected from hydrostatic equilibrium, the vertical structure settles to a Gaussian distribution, because of the vertical constant temperature.

2.4 Planet Embedded in a Disk: Standard Model

Now we first consider our standard case of a $M_{\rm p} = 1\ M_{\sun}$ planet embedded in a disk with the constant vertical height $H/r = 0.05$, equivalent to a Mach number of 20 throughout the disk. As described above we start from an initially axi-symmetric configuration with a gap imposed (see also Fig. 2.7 below). Gravitational interaction of the planet with the disk leads to the creation of tightly wound trailing spiral density waves.

In Figure 2.4 the overall structure of the surface density Σ is displayed after 150 or-

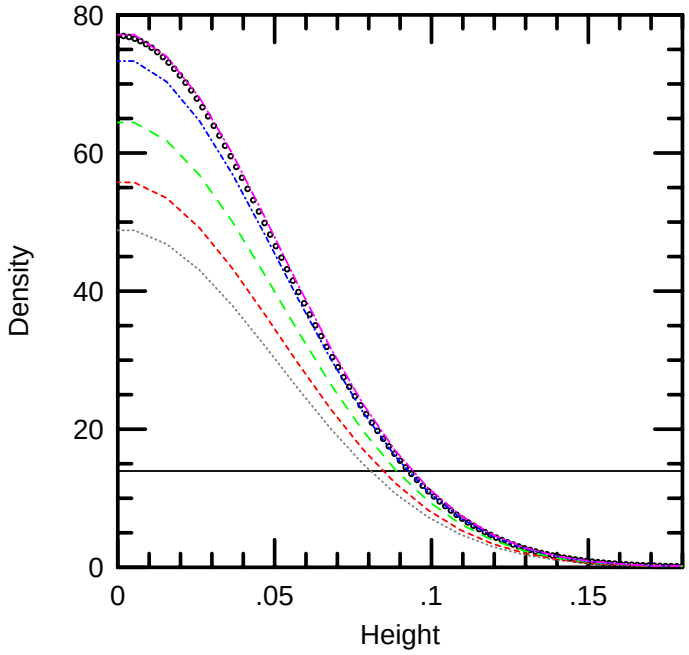

Figure 2.3: Vertical dependence of the density at $r = 1$, at various times. Starting from the initial constant density configuration, the final distribution becomes Gaussian (circles) as expected (circles). The evolutionary times are identical to Figure 2.1

bits of the planet. The spirals emanate from the vicinity of the planet and reach the outer boundary. Since the radial outer border is closed to mass flow, there the waves are reflected, which is more clearly seen in the right panel of Figure 2.4. This reflection is somewhat larger for the computations performed here than that observed in previous calculations executed by Kley (1999) (with the code RH2D) because the computational domain is smaller.

In the region outside of the planet two spirals are inter-twined and in the inner region three. This difference is caused by the location of the appropriate Lindblad resonances in comparison to the radial extent of the gap. Only resonances which are located farther away from the planet than the gap size can be excited effectively.

In Figure 2.5 the density slice $\rho(R, \theta, \pi)$ is shown at $t = 150$ orbits. In addition, the two-component velocity field (u_R, u_θ) is shown. Inside the gap, around $R = 1$, the flow field is definitely directed toward the mid-plane of the disk, onto the planet. Even from the farthermost grid cells, at $R \approx 1$, the velocity points to the position of the planet. This implies that all the fluid elements, along the vertical direction, are involved in the planet accretion process as it is assumed when adopting a 2D approximation. This can be attributed to the fact that, because of the continuous mass extraction from within the Roche lobe, the vertical hydrostatic balance is lost which allows material from all heights to fall down onto the planet. Clearly seen in Figure 2.5 are also the locations of the spiral waves which show up as density enhancements reaching from the mid-plane of the disk all the way down to the surface. At all heights the arms are at the same radial position because in case of the isothermal assumption the wave propagation speed is the same at all heights. Caused by the closed inner boundary conditions, the density becomes very large near $R_{min} = 0.4$

At each side of the planet, a column of material is also visible, it extends from $\theta = 0$

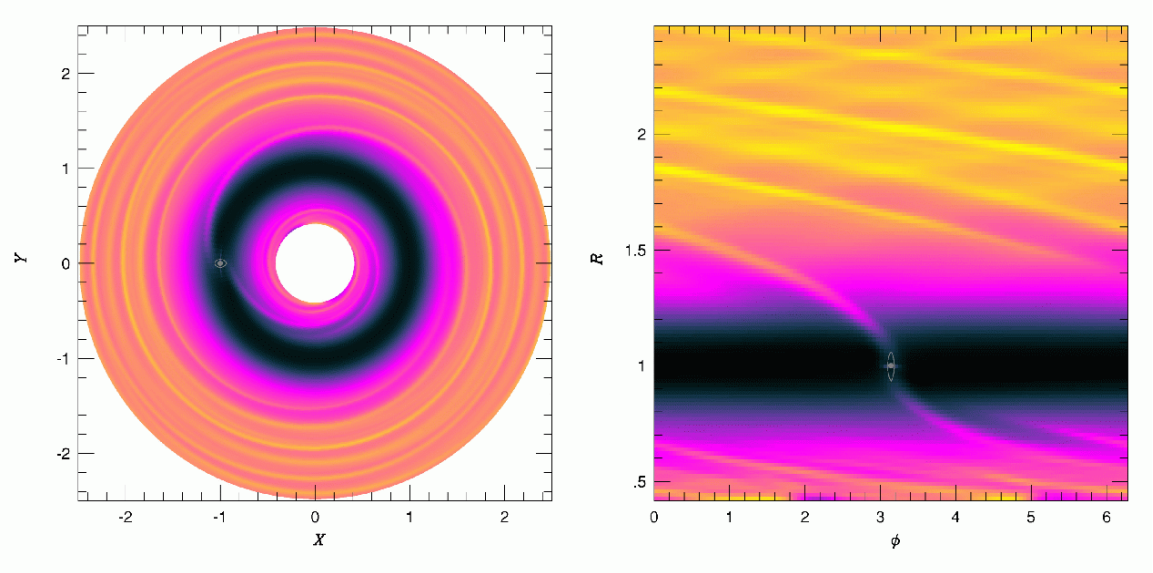

Figure 2.4: The surface density distribution at $t = 150$ orbits. Left in Cartesian $x - y$ coordinates, right in radial and azimuthal coordinates ($r - \varphi$ plane).

to $\theta \simeq 0.05$. Though not very well resolved in the radial direction, this material might be contained within the Hill sphere of the planet which, in the present case, has a radius of $\simeq 0.069$ in dimensionless units. From the velocity field, it seems that the fluid elements belonging to these structures, move toward the planet according to bow-shape stream lines. High-resolution computations, presented in CHAPTER 5, indicate that those are signatures of shock fronts, where the laminar flow is disrupted.

In Figure 2.6 we plot the density structure in the $\theta - \varphi$ plane at the planet's location $R = 1$ for the same model. Also here the loss of vertical hydrostatic equilibrium is reflected by the vertically downward motion of the gas.

The radial dependence of the surface density is shown in Figure 2.7 together with other simulations using always identical *physical* parameters. The initial density profile is given by the dark dotted line. We use two different codes RH2D (labeled 2D: solid lines) and NIRVANA (labeled N2D: dashed lines; N3D: dashed-dotted lines) where we use the latter one in a 2D setup and in the previously described 3D setup. Each of the three models is run in the inertial and the corotating frame. The initial total matter content of the models has been adjusted to agree in all cases. Clearly the overall agreement of all models is very good, the shape of the gap is identical for all models. The only difference is that the models run with NIRVANA show a larger variation at the outer radial boundary (at $R = 2.5$) which is an indication of a stronger wave reflection in the NIRVANA-code, possibly due to slightly different boundary conditions.

The good agreement of the different models is corroborated in Figure 2.8 where we plot the obtained total mass accretion rate $\dot{M}_{\rm p}$ onto the planet for the different models. Only for the corotating 3D cases the obtained $\dot{M}_{\rm p}$ appears to be slightly but not significantly

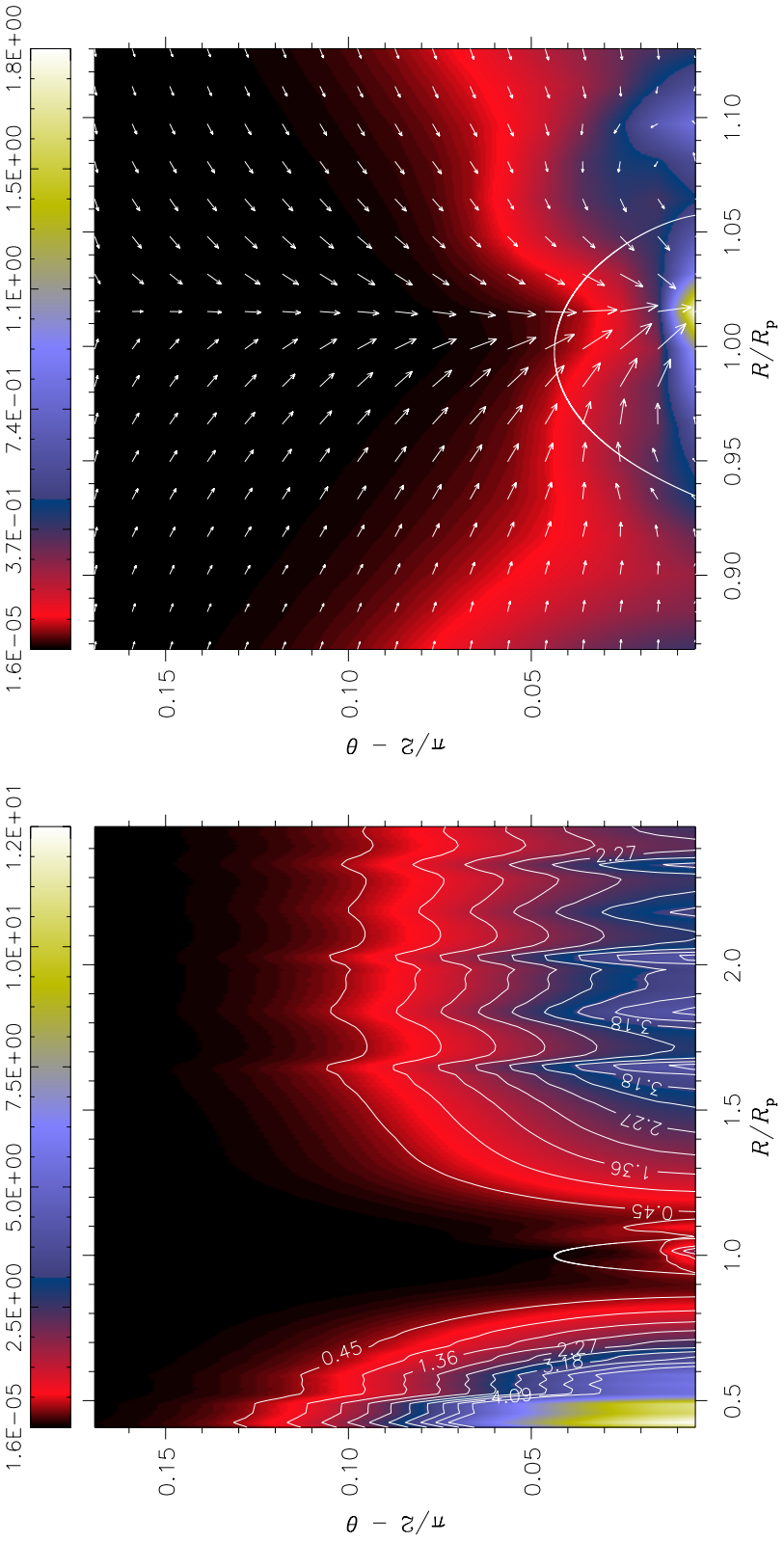

Figure 2.5: Density distribution with isodensity lines and velocity field in the $r-\theta$ plane at $\varphi = \pi$ (where the planet is located) after 150 orbits. **Left:** Larger domain. **Right:** Enlargement of the region near the planet.

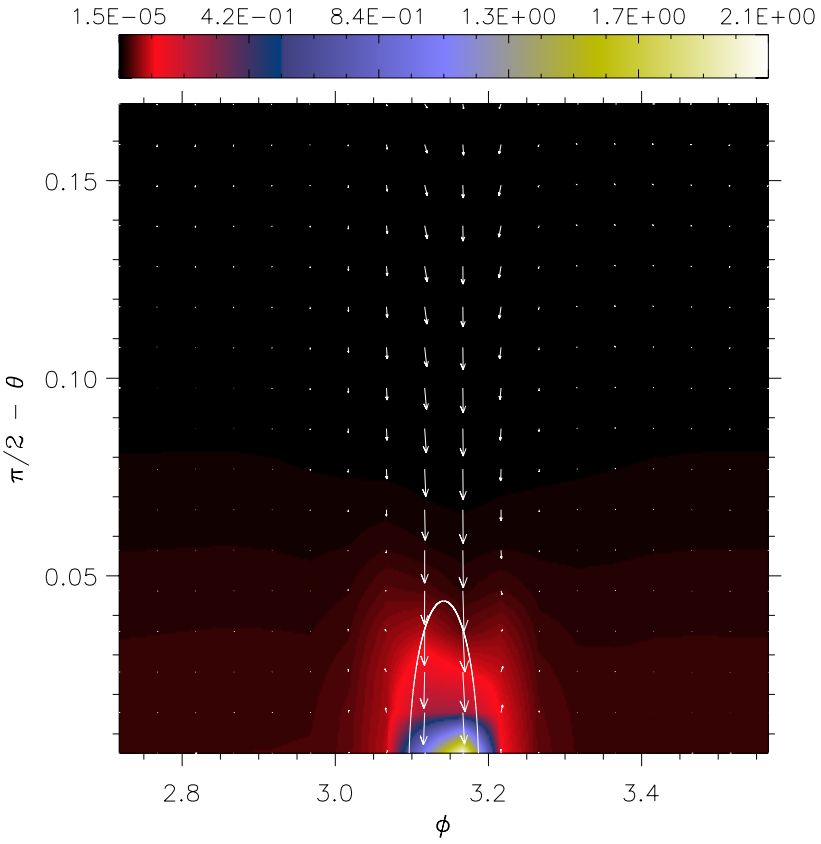

Figure 2.6: Density distribution and velocity field in the $\theta - \varphi$ plane at $R = 1$ (where the planet is located) after 150 orbits.

higher. The accretion rate does not depend on the chosen resolution as is shown by the higher resolution model (384 azimuthal grid-cells, otherwise identical to N3d rot.) which has been run only until $t \approx 100$ due to limited computational resources.

2.4.1 Gravitational Torques

The gravitational force $\boldsymbol{F}$ of the disturbed non-axi-symmetric density distribution of the disk creates a torque $\boldsymbol{T} = \boldsymbol{r} \times \boldsymbol{F}$ on the planet, which eventually alters its orbital elements. For the present work however, these changes have no dynamical influence, because we assume that the planet remains on a fixed circular orbit. The resulting radial distribution of the vertical z-component of the torque is shown, as a solid line, for the standard 3D-model (N3D rot.) in Figure 2.9. It shows a strong variation (spikes) with radius that is caused by the spiral density structure. The Figure shows also the same quantity as obtained from the N2D rot. model. As one can see, the two curves have slightly different shapes only close to the planet (at $R \approx 0.9$ and $R \approx 1.1$), where the 3D result is less

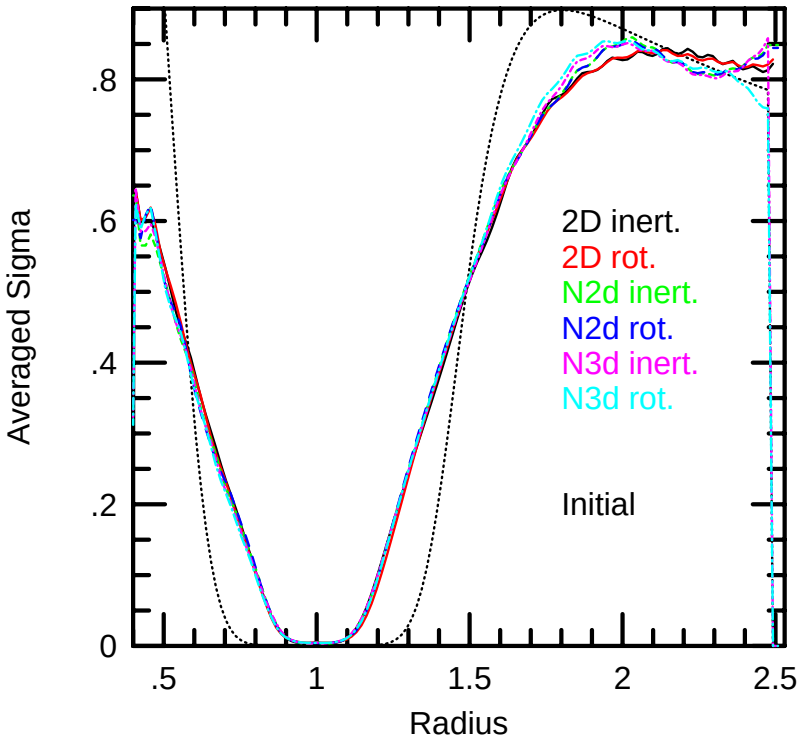

Figure 2.7: Azimuthally averaged surface density $\Sigma(r)$ after 150 orbital periods of the planet for three different models: 2D (code RH2D) solid lines, N2d (NIRVANA in 2D) dashed lines, and N3d (NIRVANA in 3D) dashed-dotted lines, each run in the inertial and corotating frame. The dark dotted line denotes the initial density profile.

variable.

The total torque $T_\perp$ can be obtained by integrating $T_z(r)$ over all radii. An applied torque on the planet changes its angular momentum $L_p = m\,a^2\,\Omega_\mathrm{p}$ and leads to a change in its orbital distance

$$\dot{a} = \frac{2}{a\,M_\mathrm{p}\,\Omega_\mathrm{p}}\,T_\perp. \tag{2.8}$$

As the direction of the motion is determined by the sign of the total torque, it is clear already from Figure 2.9 that the planet will migrate inward. The main contribution to this lowering of a comes from the density in the trailing spiral arm near the outer edge of the gap. The deep minimum at $r \approx 1.7$ refers to the $2:1$ outer Lindblad resonance. It has been demonstrated already (Lubow et al. 1999; Nelson et al. 2000) that the material lying at radii larger than the planet's semi-major axis tend to move the planet inward while inner material has the opposite effect. As there is typically more mass (larger area) in the outer region the net effect will be an inward migration of the planet. For the time scale of this

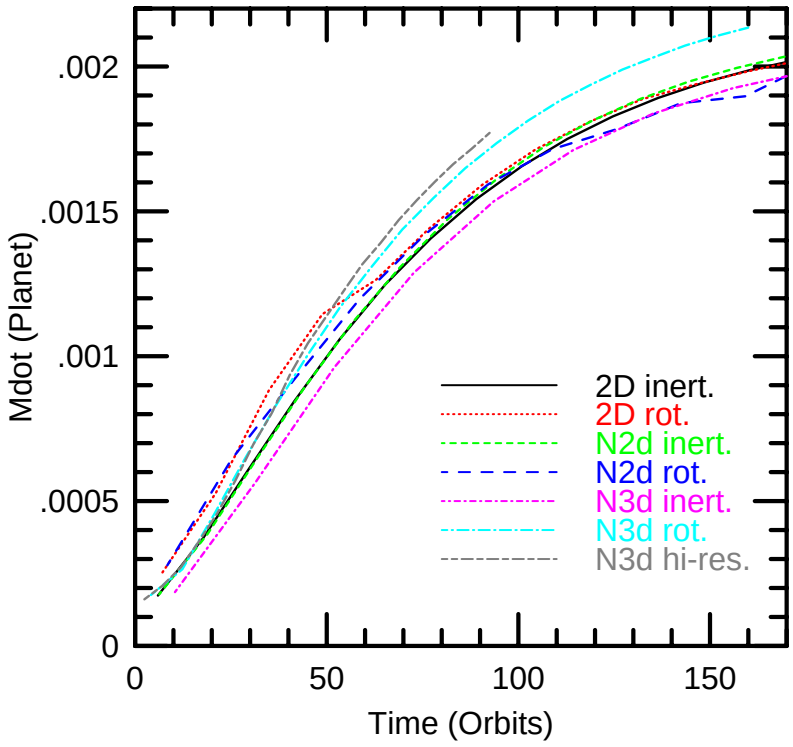

Figure 2.8: Mass accretion rate onto the planet in dimensionless units versus time for the models shown in Figure 2.7. One high-resolution model (with 384 azimuthal grid-cells) run in the rotating frame has been added.

migration

$$\tau_{\rm M} = \frac{a}{|\dot{a}|}$$

we find for *all* the models $\tau_{\rm M} \approx 10^5$ years if we assume a total disk mass within $[r_{\rm min}, r_{\rm max}]$ of $3.5 \times 10^{-3}\ M_\odot$. This compares favorably with the analytic results of Goldreich and Tremaine (1980) based on a linear analysis which results for the same disk density also in a time scale of about 10^5 years. The dynamical evolution of migrating planets has been studied in detail, in a two-dimensional framework, by Nelson et al. (2000).

2.5 Varying the Disk Height and the Planetary Mass

We have also run models with smaller planet masses and higher H/r ratios. The parameters of some of such models are listed in Table 2.1. For all of them the boundary conditions at inner radial border are such that they allow matter to outflow from the computational domain but not to inflow. For each set of physical parameters we have performed

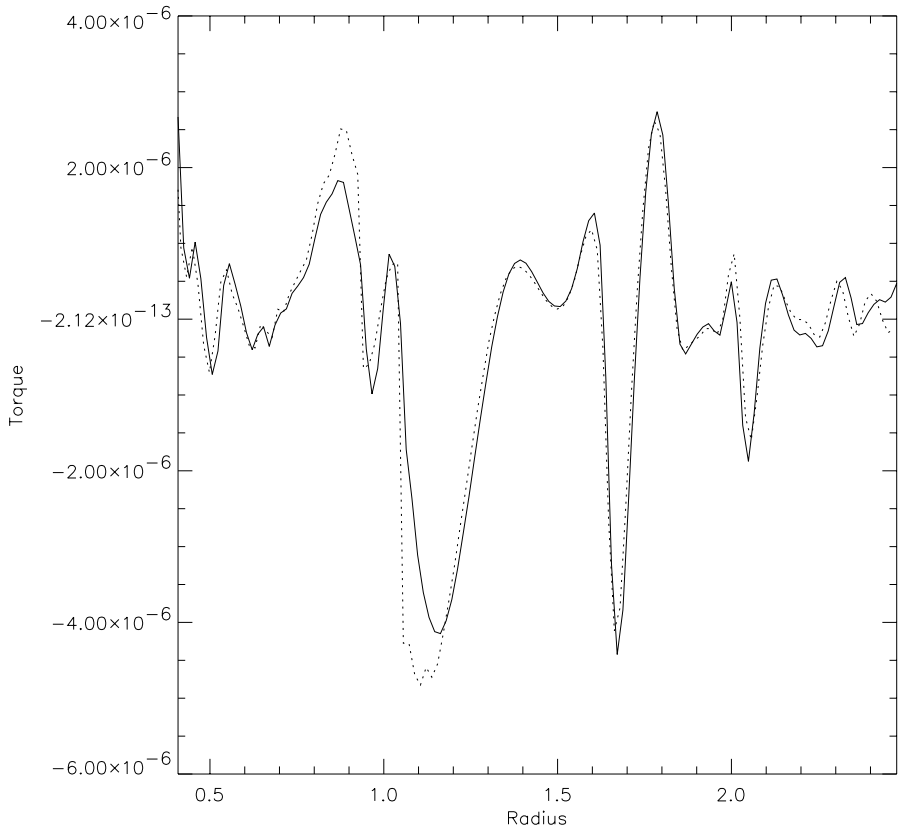

Figure 2.9: Radial distribution of the torque component T_z on the planet at time $t = 150$ orbits for the models N3D rot. (solid line) and N2D rot. (dotted line).

two- and three-dimensional calculations at much higher resolution than the standard test case discussed in the previous section. As can be seen from the Table we have chosen the number of grid-cell in the azimuthal φ-direction such as to make the grid-cells approximately square shaped, which required $N_\varphi = 384$ grid-cells. The number of grid-cells in the vertical direction was higher for the model P3 ($N_\theta = 30$) because of the larger H/r.

In order to illustrate how the density wave pattern varies with the thickness of the disk, the density for model L is plotted in Figure 2.10. That relative to models C and P3 is shown in Figure 2.11. To intensify the contrast between high densities in the outer part of the disk and the low densities in the gap and the inner disk regions, a logarithm scaling of Σ is used in some panels (see Figure captions for details). Since the propagation of the spiral perturbations is governed by the sound speed, we must expect that the thicker the disk the wider the spiral waves are. One can clearly observe such occurrence in Figure 2.10 and the right panels of Figure 2.11. On the other hand, waves can propagate in the vertical direction. There are resonances which lie above the disk mid-plane and therefore, if the disk is thick enough to enclose those locations, the intensity of spiral perturbations is re-

Table 2.1: Parameters of the 2D (A, D, P2a, P2b) and 3D (B, C, P3) models used to compare the planet mass accretion rate. Model L simulates a very thin disk.

Model	$M_{\rm p}^{a}$	H/r^{b}	R-Range^{c}	θ-Range	ΔR	$\Delta\theta^{d}$	$\Delta\varphi^{e}$
B	0.50	5.0×10^{-2}	$[0.4, 2.5]$	$[80°, 90°]$	0.01640	0.01027	0.01653
A	0.50	5.0×10^{-2}	$[0.4, 2.5]$		0.01640		0.01653
L	1.00	2.5×10^{-2}	$[0.4, 2.5]$	$[85°, 90°]$	0.01640	0.00969	0.01653
C	1.00	1.0×10^{-1}	$[0.4, 2.5]$	$[70°, 90°]$	0.01640	0.00997	0.01653
D	1.00	1.0×10^{-1}	$[0.4, 2.5]$		0.01640		0.01653
P3	1.00	1.5×10^{-1}	$[0.4, 6.5]$	$[60°, 90°]$	0.04766	0.01939	0.04987
P2a	1.00	1.5×10^{-1}	$[0.4, 6.5]$		0.04766		0.04987
P2b	1.00	1.5×10^{-1}	$[0.4, 6.5]$		0.04766		0.01653

$^{(a)}$ The planet mass is normalized to the mass of Jupiter.
$^{(b)}$ r represents the distance from the rotational axis.
$^{(c)}$ The radial extent is given in units of the orbital radius $R_{\rm p}$.
$^{(d)}$ The resolution is expressed in radians.
$^{(e)}$ $\varphi \in [0, 2\,\pi]$.

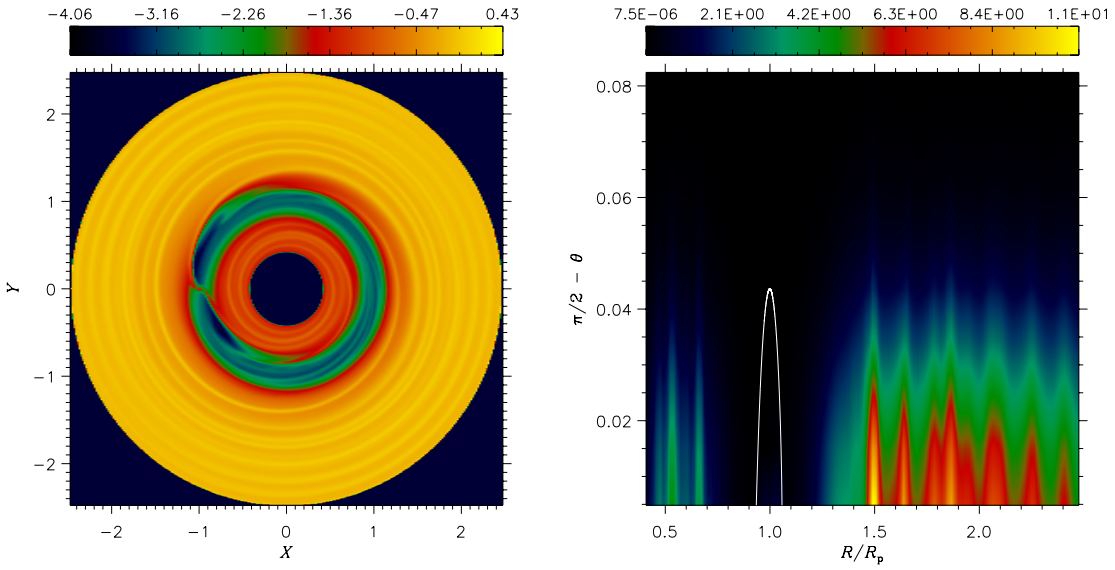

Figure 2.10: **Left**. Surface density for the additional model L (see Table 2.1) which simulates a Jupiter-mass object in a disk with $h = 0.025$. The color scaling is logarithmic. **Right**. Mass density in a vertical slice containing the planet. The section of the Roche lobe is also indicated. Note how sharp the spiral perturbations appear.

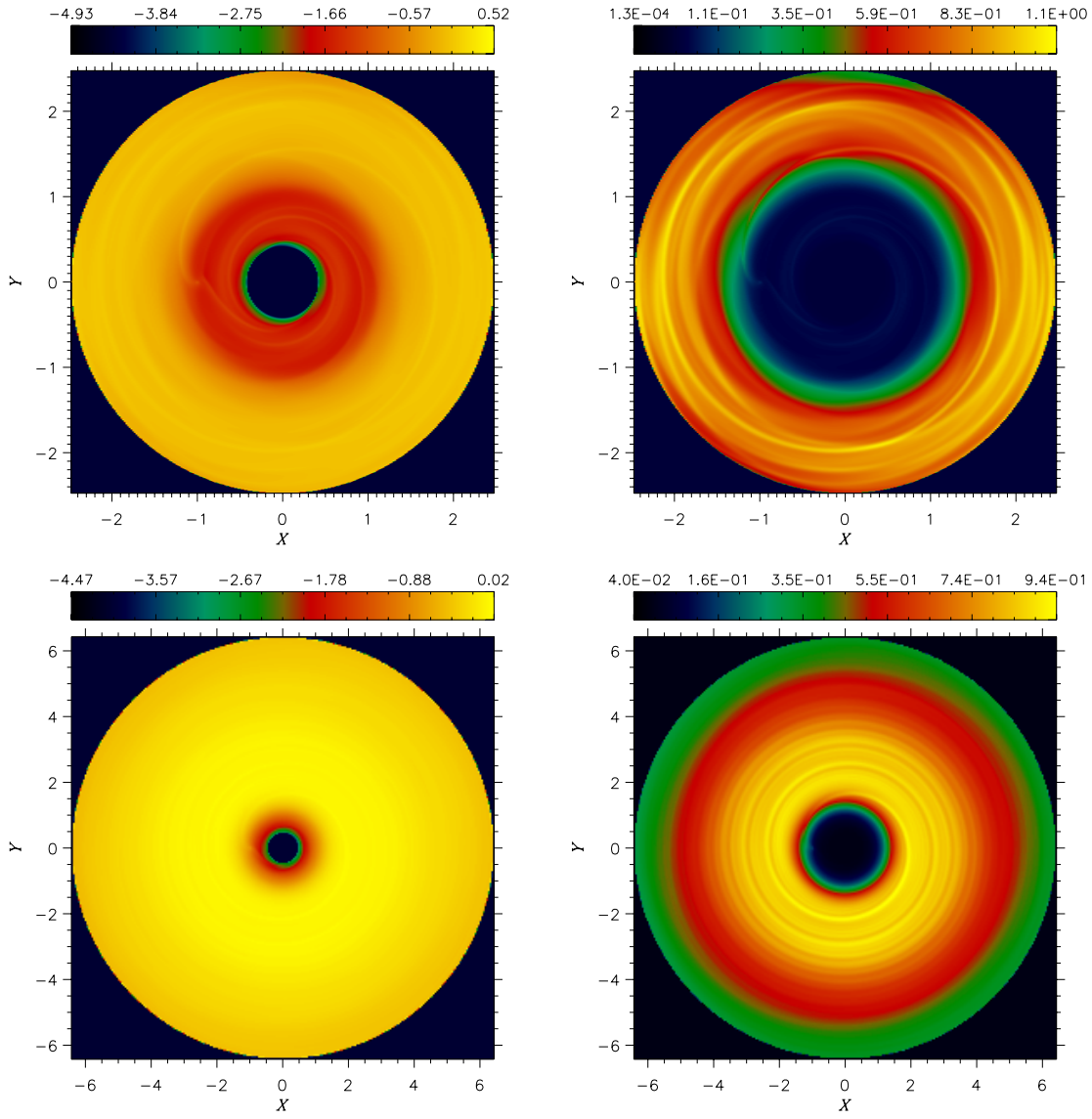

Figure 2.11: Surface density for two additional models (see Table 2.1). The color scaling is logarithmic in the left panels, linear in the right panels. **Top**. Model C has $M_{\rm p} = 1\ M_{\rm J}$ and $h = 0.1$. **Bottom**. In model P3 the disk is quite thick ($h = 0.15$) and therefore the radial extent of the domain was enlarged. The central hollow observed in the right panels is due to the combined effects of the gap and the depletion of the inner disk.

duced and the density appears smoother. This effect is visible in Figure 2.11 in the panels regarding the surface density.

For the sake of completeness, we also show the surface density and the mass density for a model which has $M_{\rm p} = 0.5\ M_{\rm J}$ and a standard pressure scale height $H/r = 0.05$. The

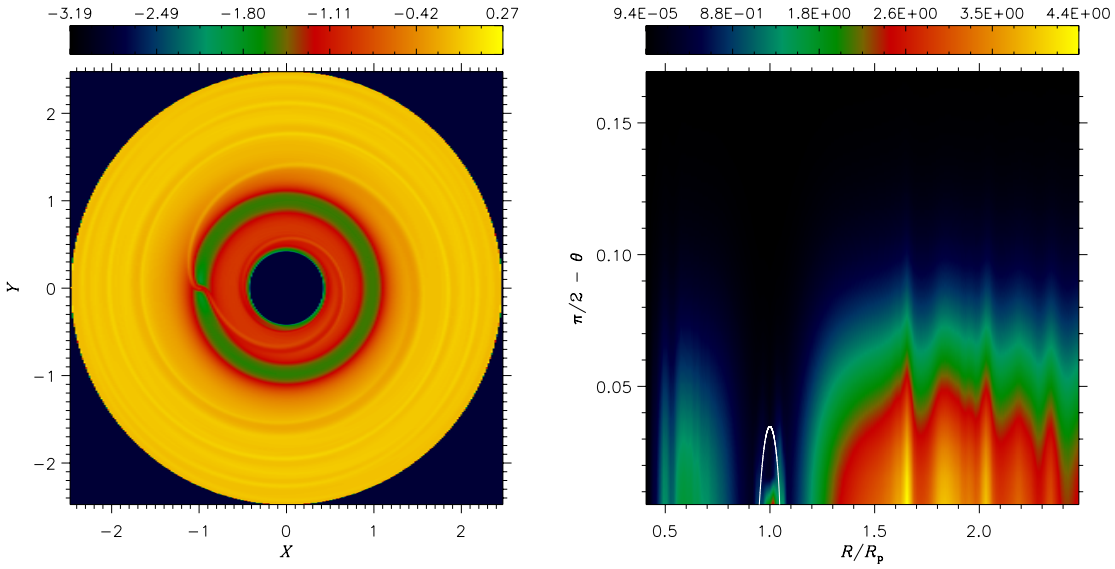

Figure 2.12: **Left**. Surface density for the additional model B (see Table 2.1) which simulates a 0.5 Jupiter-mass object in a disk with $h = 0.05$. The color scaling is logarithmic. **Right**. Mass density in a vertical slice containing the planet. The section of the Roche lobe is also indicated for comparison.

gap and perturbation pattern scale as the sphere of influence of the planet and therefore as $M_{\rm p}^{1/3}$. Thus, not much difference is expected to be seen between model B and our standard model discussed in § 2.4.

In case of the Models A and B the ratio of the Hill radius ($R_{\rm H}$) to the local thickness of the disk is almost unity. One can see that, after 200 orbits, the 3D model accretion rate (Fig. 2.13, upper-left panel) is 12% less than that of the corresponding 2D model. For Models C and D (Fig. 2.13, upper-right panel) the ratio $R_{\rm H}/H$ decreases to 0.7 and the two curves show a difference of 10%. In the lower-left panel of the same Figure one can clearly see that, despite the difference in azimuthal resolution, the 2D model (P2a and P2b) results differ very little, while the 3D one lies almost the 30% below. These comparisons show that whenever $R_{\rm H}/H \leq 1$, the 2D approximation starts to break down and the 2D accretion rates lie consistently above the 3D values.

2.6 Conclusions

We have performed 3D simulations of embedded Jupiter type planets in a protostellar disk of mass $M_{\rm D} = 10^{-2}\ M_{\odot}$. We have shown that for a fully three-dimensional standard model, having the vertical disk thickness $H/r = 0.05$ and the constant (dimensionless) viscosity $\nu = 10^{-5}$, the obtained mass accretion rate $\dot{M}_{\rm p} \approx 6 \times 10^{-5}\ M_{\earth}/{\rm yr}$ and migration time scale of $\tau_{\rm M} \approx 10^5$ yr are in very good agreement with corresponding 2D calculations.

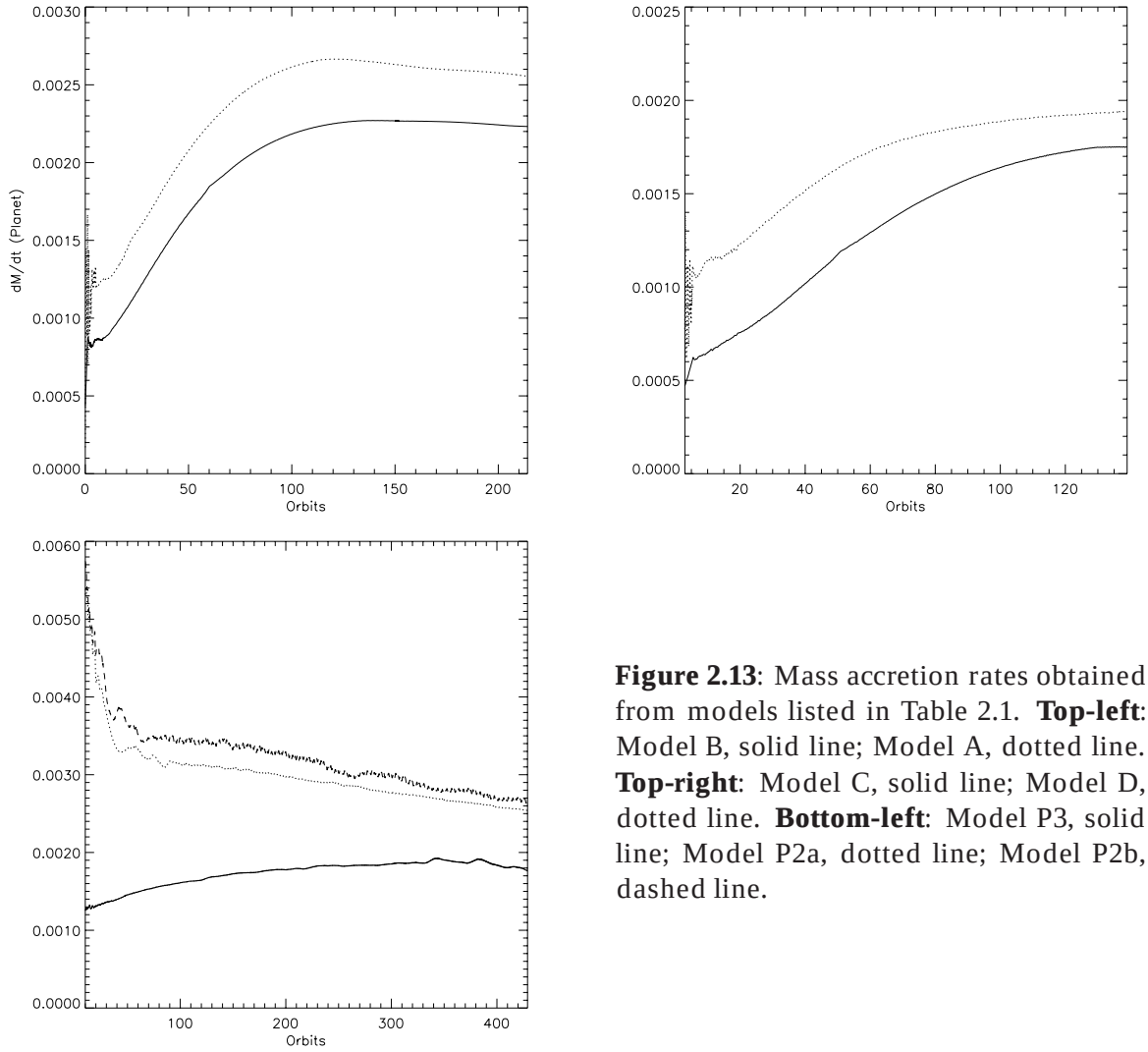

Figure 2.13: Mass accretion rates obtained from models listed in Table 2.1. **Top-left**: Model B, solid line; Model A, dotted line. **Top-right**: Model C, solid line; Model D, dotted line. **Bottom-left**: Model P3, solid line; Model P2a, dotted line; Model P2b, dashed line.

The value for the accretion rate $\dot{M}_{\rm p}$ quoted in Kley (1999) is lower than the value obtained in this work because here we take into account the accretion from both sides of the disk while previously we considered only accretion from outside. Hence, we conclude that in this standard case the two-dimensional (r–φ) calculations give an adequate representation of the evolution of planets in disks.

However, this agreement between 2D and 3D calculations can only be expected if the vertical extent of the Roche lobe of the planet is comparable to the disk thickness or larger, that is for high planetary masses. If the Roche lobe is much smaller than the disk thickness the gap will not be opened fully, and one may expect that some of the disk material will flow across the gap, which is not fully cleared in these circumstances, and does not end up onto the planet. This situation has been addressed with lower q and higher H/r models, and indeed we find a slightly reduced mass accretion onto the planet in these cases.

The present results and those previously published concerning mass accretion and

planet migration by ourselves and others, although in rough agreement with each other, may nevertheless suffer from insufficient resolution of the flow within and around the Roche lobe of the planet. Once within the Roche lobe the gas will form a miniaturized accretion disk around the planet. The question on how fast the accretion flow will be depends on the local viscosity within this sub-disk. If the disk is able to transport all the incoming material rapidly enough, the mass removal scheme used here will be satisfactory.

To address these questions much higher numerical resolutions possibly by applying methods of grid refinement will have to be used. Very interesting first results have been presented by Ciecieląg et al. (2000b) but this issue definitely requires more work. Next chapters are devoted to computations executed with a grid refinement method known as *Nested-Grid Technique*. It will allow us to overcome all resolution restrictions and investigate in great detail what happens nearby a protoplanet, while maintaining a global treatment of the disk.

George said:

'You know we are on the wrong track altogether. We must not think of the things we could do with, but only of the things that we can't do without.'

JEROME K. JEROME,
THREE MEN IN A BOAT,
1889

CHAPTER 3

NUMERICAL METHOD AND NESTED-GRID TECHNIQUE

This chapter is devoted to a generic description of the numerical method we have adopted to solve the equations of magneto-hydrodynamics, though we work in a purely hydrodynamics context. However, since there exists an extensive literature on the subject, this chapter is not meant to be a complete overview of such a method. In fact we will mostly focus on a particular strategy to gain local resolution and accuracy in the calculations we aim at.

3.1 Introduction

The variety of astrophysical systems which can be approximated as either magneto--hydrodynamical (MHD) or hydrodynamical (HD) flows is a proof of the importance that fluid dynamics modeling has in this field. The applicability range of MHD and HD descriptions spans from processes occurring in the intergalactic and interstellar media to those taking place in the nuclei of galaxies and stars. The assumptions required to analytically solve HD equations are so restrictive to make analytic solutions of no practice use. Therefore, theoretical astrophysicists have broadly relied on numerical solutions of these equations. As consequence of the growing interest in the field and the extensive use of this approach, many numerical methods have been developed to solve the HD equations. One of the most straightforward and well-tested is the method of the finite differences, a so called *grid-based method*. In finite differencing, physical quantities, such as density and momenta, are discretized over a grid of points and derivatives are approximated to the ratio of finite differences. The assets of such a scheme are so many that it represents, by far, the most used numerical method in theoretical astrophysics.

The distinctive property of the systems of astronomical interest is that many physical effects have to be included in order to have a realistic model. These effects usually involve time scales which may differ by many order of magnitudes. Hence, each of them must be handled appropriately. Moreover, very often also the length scales of the various physical phenomena may be significantly different. These may lead to not accurate results if the spatial resolution, i.e., the distribution and the number of the points is not sufficient all

over the investigated region. Thus, even a numerical approach to the problem is not at all an easy task.

The resolution issue can be addressed by a mesh refinement technique. The followed strategy is to increase the number of the grid points in regions where the spatial gradient of the physical quantities is large. Several of such techniques have been worked out and they can be broadly divided in two categories: adaptive refinements and static refinements. In the first category the grid structure evolves with time whereas in the second it is static and does not change in time. Adaptivity usually implies a complexity in coding which may be very difficult to implement. Furthermore, astrophysical applications have proved that it is very powerful for some problems but not so useful for others.

Adaptive mesh refinement techniques are basically characterized either by redistributing a fixed number of grid cells or by generating finer cells whenever necessary. In the first case grid cells are allowed to move and therefore even an initial simple mesh becomes topologically very distorted as time goes by. Mesh distortion has two undesired consequences: discretization errors, different in each coordinate direction, are introduced and the formal convergence rate of the finite differences scheme is generally restricted to the first order for fully adaptive 2D and 3D problems. However, this strategy has been applied successfully in 1D problems (e.g. Dorfi and Drury 1987). The second case of adaptive mesh refinement has been elaborated by Berger and Oliger (1984) and is based on structured grid patches. Patches are made out of a fixed number of grid points and can be generated or destroyed wherever some criteria are met. Patches may be laid over pre-existing patches up to a selected level, allowing a very fine resolution in confined regions. Some numerical codes have been implemented based on this technique and applied to astrophysical problems (Ziegler 1998; Plewa and Müller 2001) but mainly in Cartesian coordinates.

However, in order to avoid adding the complexity of a numerical procedure to the complexity of the physical nature of the problem, we rely on a static refinement strategy based on the use of multiple nested grids. Static methods are simpler to code and to handle, they are more robust and easy to control. Yet, contrary to adaptive methods they are less general and successfully applicable only to a more restricted class of problems.

The nested grid technique is represented by a hierarchical sequence of grids where, starting from a basic grid, successively finer resolution grids, called also subgrids, are ”nested” within coarser ones. For the sake of simplicity we will refer to equidistant grids in the coordinate space. This will assure also a higher convergence rate of the finite difference scheme. The level of nesting can be arbitrarily high and as many subgrids as desired can be comprised in a particular grid level, provided that no subgrid overlapping occurs.

In contrast to the adaptive mesh refinement technique, the topological character of the grid is conserved during the computation. The integration of the HD equations proceeds, whatever the hierarchy level, on a simple equidistant mesh. To preserve the conservative nature of the underlying hyperbolic equations, neighboring subgrids interacts with each other.

In the next section we briefly describe the numerical procedure used to solve the HD equations and in § 3.3 we introduce the nested grid technique as implemented here. Sections 3.4, 3.5, and 3.6 are specifically devoted to those aspects of this technique which have been modified and improved in order to make the scheme more stable with respect to

the type of computations that we intended to perform. In the final section, we give some remarks on the performances of this method.

3.2 Numerical Method

In order to study the planet-disk interaction, we utilize a finite difference method to solve the standard hydrodynamic equations,i.e., those outlined in the previous chapter for the 3D problem and those presented in the next chapter for the 2D one. As we intend to achieve a very high resolution around the planet, we can use a static refinement technique, as the multiple nested grids. This is possible since, as already stated in CHAPTER 2, we can choose a rotating basic grid and assume that the planet orbital eccentricity is zero. Thereby, the position of the planet remains fixed within the grid hierarchy.

The above requirements are provided by an early FORTRAN-Version of NIRVANA (Ziegler and Yorke 1997), which is a 3D, nested-grid, MHD code, based on a covariant Eulerian formalism. The relevant equations are solved on a mesh structure having a constant spacing in each coordinate direction. When the code is applied to three-dimensional disks, it is natural to use a spherical polar coordinate system. However, when it is applied to a two-dimensional geometry, i.e., to an infinitesimally thin disk, the natural choice becomes a cylindrical reference frame where the z-dimension is switched off.

For our purposes, the code is used in a pure hydrodynamics mode. This is indeed a good approximation in our case because, at the planet distance, circumstellar material has temperatures around ~ 100 K. Thus matter is not ionized, i.e., no plasma effects arise and magnetic field are so weak that can be neglected.

Fluid advection and source terms (right-hand side of equations, see § 2.2 and § 4.2) are treated via an operator splitting technique with a time explicit multi-step solution procedure. This can be sketched as follows. If we let $\boldsymbol{w}$ be the vector of the physical quantities[1] $(\rho, e, \rho\boldsymbol{u})$, then the equations can be formally written in a very compact way:

$$\frac{\partial \boldsymbol{w}}{\partial t} = \mathcal{L}_1[\boldsymbol{w}] + \mathcal{L}_2[\boldsymbol{w}] + \mathcal{L}_3[\boldsymbol{w}] + \cdots + \mathcal{L}_P[\boldsymbol{w}]. \tag{3.1}$$

Each of the operators $\mathcal{L}_1, \mathcal{L}_2, \ldots, \mathcal{L}_P$ is the mathematical representation of a term (e.g., advection, pressure gradient, gravitational force, viscous force, etc.) in the HD equations. The finite-difference multi-step procedure can be formulated as

$$\begin{aligned}
\frac{W^{(1)} - W^{(0)}}{\Delta t} &= L_1[W^{(0)}], \\
\frac{W^{(2)} - W^{(1)}}{\Delta t} &= L_1[W^{(1)}], \\
\frac{W^{(3)} - W^{(2)}}{\Delta t} &= L_1[W^{(2)}], \\
\frac{W^{(P)} - W^{(P-1)}}{\Delta t} &= L_1[W^{(P-1)}],
\end{aligned} \tag{3.2}$$

[1] Here we indicate with ρ the mass density (and with "Σ" the surface density), with "e" the specific energy, and with $\boldsymbol{u}$ the velocity vector.

where $\Delta t = t_{n+1} - t_n$ is the time interval and $t = t_n$ the starting time. Operators $L_{(1,...,P)}$ and quantities W are discrete approximations of $\mathcal{L}_{(1,...,P)}$ and w, respectively. Starting from $W^{(0)} = W(t_n)$ one gets $W^{(1)}$, which is used in the successive sub-step. Eventually, one ends up with $W^{(P)} = W(t_{n+1})$. The order of the operators $L_{(1,...,P)}$ generally has little effect on the numerical solution. Such procedure is formally first-order accurate in time. However, in some cases, the order arrangement can improve the accuracy order of the solution.

A detailed description about how the complete procedure can be actually coded, including also magnetic fields and radiation transfer, can be found in the famous trilogy of papers by Stone and Norman (1992a,b) and Stone et al. (1992). These three papers represent an excellent reference and constitute the core of the famous ZEUS code, a widely employed numerical tool in astrophysics. NIRVANA is a ZEUS-type code.

As for the fluid advection, NIRVANA uses a second-order monotonic transport algorithm, introduced by van Leer (1977), which guarantees global conservation of mass and angular momentum. In order to maintain the second-order accuracy, the directional splitting of the three advection operators must be symmetric. A strict symmetric splitting would add, however, extra computational time, for which reason symmetry is improved by simply alternating the splitting order between successive cycles. Higher orders schemes, such as the *Piecewise Parabolic Algorithm* (PPA) (Colella and Woodward 1984), have been lately used for astrophysical purposes. Yet, though PPA is unrivaled in its ability to keep sharp contact discontinuities, it is computationally very expensive. For many multi-dimensional applications, such as ours, it is not clear whether this high cost generates significantly better solutions than those provided by van Leer's algorithm, when it is run at finer resolutions.

The viscosity part was added to the original implementation and is treated explicitly (Kley 1999). The full form of the viscous stress tensor has been implemented for a *Newtonian fluid* according to the *Stokes hypothesis*, i.e. with a bulk viscosity $\zeta = 0$ (see Mihalas and Weibel Mihalas 1999).

3.3 Nested-Grid Technique

This technique is particularly useful when very high local resolution is required at specific and predefined points of the computational domain. In our situation, this allows us to simulate both the overall behavior of the disk and the immediate surroundings of the planet. Since this kind of numerical approach is quite new for the calculation of disk-planet interaction, we describe the method to some extent, but *only* referring to our particular and specific case.

A similar numerical scheme has been adopted, for astrophysical simulations, by a number of authors. Ruffert (1992) used this approach to investigate the collision between a white dwarf and a main-sequence star. In his paper the numerical method is explained in detail. Yorke et al. (1993) and Burkert and Bodenheimer (1993) simulated the collapse of a protostellar cloud. An application to flux-limited radiation hydrodynamics can be found in Yorke and Kaisig (1995). Lately, Yorke and Sonnhalter (2002) has used such strategy, with a frequency-dependent radiation transport to study the early stages of star formation. Applications have been made also to other fields. For example, Skamarock et al. (1989)

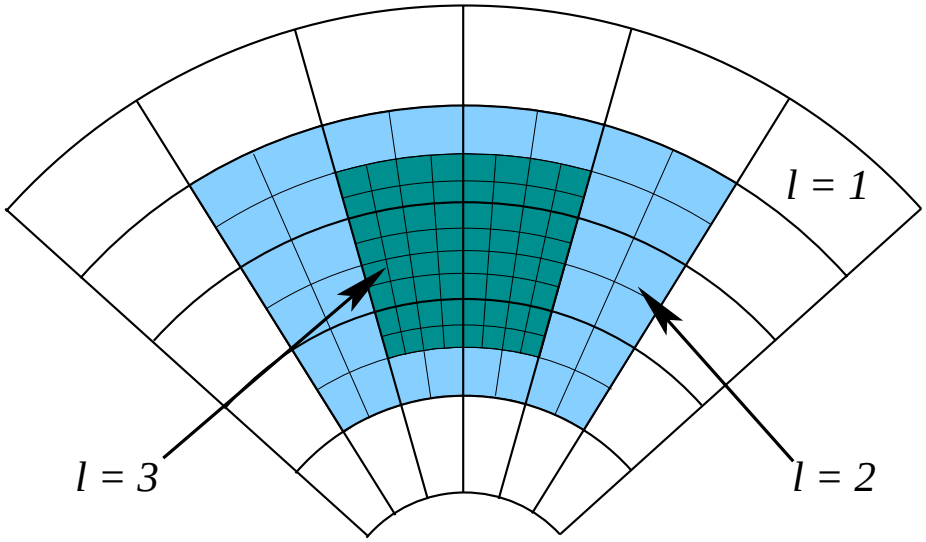

Figure 3.1: Face-up projection of a three-level grid system in two-dimensional cylindrical coordinates. On the finest subgrid ($l = 3$) the linear spatial resolution is four times as large as it is on the main grid ($l = 1$).

employed it for numerical weather prediction.

The method relies on the basic idea that, whenever a greater resolution is needed in a designated region, a finer subgrid is located inside the main grid (i.e., the one covering the whole computational domain). If the resolution is not high enough yet, another subgrid may be placed on the underlying one. Since any subgrid can host a finer subgrid structure, a grid hierarchy is generated, also called "system of nested grids". In principle there is no limit to the degree of nesting. A three-level hierarchy, in 2D cylindrical coordinates, is shown in Figure 3.1 whereas one in 3D Cartesian coordinates appears in Figure 3.2.

The necessary equations are then integrated, *independently*, on every grid level. However, two neighbor subgrids must exchange the necessary information whenever the integration proceeds from one grid level to another.

Since the scheme is time-explicit, restrictions are imposed on the time step because, for stability reasons, the Courant-Friedrichs-Lewy (CFL) condition must be fulfilled during each integration, on each level.

In order to avoid lengthy formulas and incomprehensible pictures, we will generally illustrate how a nested system of grids works in 2D cylindrical coordinates $(O; r, \varphi)$, because this is one of the two cases that we are interested in (i.e., to represent an infinitesimally thin disk). The hydrodynamical unknowns are the density and the velocity components (see Fig. 3.5 and 3.7, or § 3.5.1, for the definition of such quantities on the computational grid). To depict disks with thickness, 3D spherical polar coordinates $(O; R, \theta, \varphi)$ are used (as done in CHAPTER 2). Thus, what we say for the 2D case directly applies to the radial and azimuthal coordinates of the 3D case, provided that the cylindrical radius r coincides with the polar radius R. Thereupon, we mention how they must be extended to

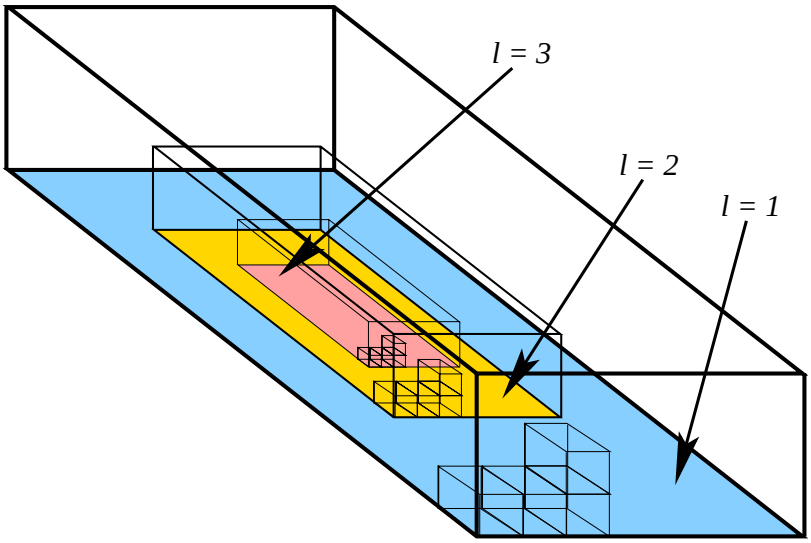

Figure 3.2: Three-level grid system in three-dimensional Cartesian coordinates. Each volume cell on the main grid ($l = 1$) is divided into 4^3 volume cells on the the finest subgrid ($l = 3$).

include the co-latitude coordinate, by using similarity arguments. Yet, complete formulas will be also presented in an explicit form, for the 3D case, since the interpolation procedure may be somewhat more complex.

3.4 Basic Integration Cycle

Although any refinement ratio would be possible, the risk of numerical instabilities and inaccuracies at the interfaces between two neighboring grids increases as this ratio grows. Since we are interested in keeping the algorithm as stable as possible, in our calculations we use the smallest possible refinement ratio:

$$\frac{\Delta r(l+1)}{\Delta r(l)} = \frac{\Delta \theta(l+1)}{\Delta \theta(l)} = \frac{\Delta \varphi(l+1)}{\Delta \varphi(l)} = \frac{1}{2}, \tag{3.3}$$

where $\Delta r(l)$, $\Delta \theta(l)$, and $\Delta \varphi(l)$ represent the mesh discretization, along each direction, on the grid level l (here $l = 1$ identifies the main grid). In order to analyze a complete integration cycle, let's suppose that we have a three-level hierarchy at an evolutionary time t. The cycle will be completed when on each grid the system has evolved for the same time:

1. We always start the integration from the finest level. During the first step of the cycle, this grid is evolved for a time interval

$$\Delta t_1(3) = \min\left[\Delta t_1^{\mathrm{CFL}}(3), \frac{1}{2}\Delta t_1^{\mathrm{CFL}}(2), \frac{1}{4}\Delta t_1^{\mathrm{CFL}}(1)\right], \tag{3.4}$$

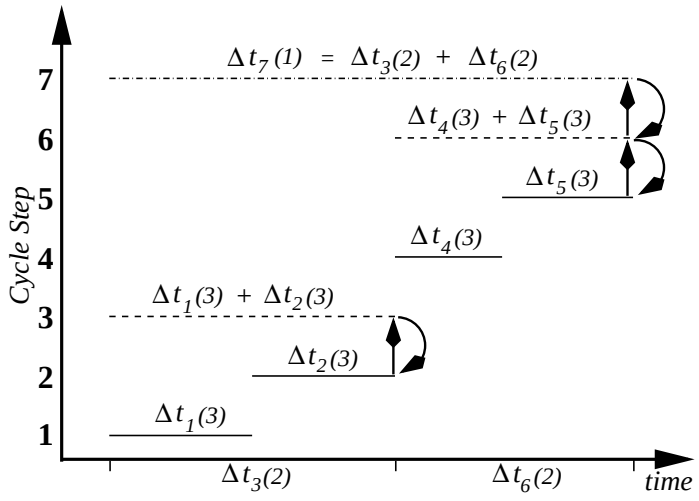

Figure 3.3: Scheme of a complete integration cycle for a three-level grid system. Arrows indicate the direction of information transfer when integration proceeds from a level to the next lower one. Straight arrows stand for the solution updating process on the levels 2 and 1 (i.e., form fine to coarse grids). Bow-arrows indicate the data transfer for setting the boundary quantities on the levels 3 and 2 (i.e., form coarse to fine grids).

where $\Delta t_1^{\mathrm{CFL}}(l)$ represents the time step resulting from the CFL criterion applied to the level l (see, e.g., Ziegler 1998; Kley 1999), after its latest integration. Thus, $\Delta t_1(3)$ accounts for the CFL stability criterion on the whole set of grids.

2. The third grid has to be integrated once more because of equation (3.3). Since after the first step this was the only level to evolve, we only have to check the new CFL time step for this grid, $\Delta t_2^{\mathrm{CFL}}(3)$. Then it can move further in time for an interval

$$\Delta t_2(3) = \min\left[\Delta t_2^{\mathrm{CFL}}(3), \frac{1}{2}\,\Delta t_1^{\mathrm{CFL}}(2), \frac{1}{4}\,\Delta t_1^{\mathrm{CFL}}(1)\right]. \tag{3.5}$$

3. Now level 2 can be integrated for a time

$$\Delta t_3(2) = \Delta t_1(3) + \Delta t_2(3) \leq \Delta t_1^{\mathrm{CFL}}(2), \tag{3.6}$$

so that numerical stability is automatically assured. At this point of the cycle the first information exchange takes place: the solution on the level 2 is corrected via the more accurate solution of the level 3; the boundary values of the level 3 are updated by using the solution of the level 2, which covers a larger domain. These fundamental interactions will be described later.

We have just seen that a level $l+1$ has to be visited two times as often as the level l. Then the next two cycle steps will be similar to the first two, provided that the appropriate CFL time steps are employed to compute $\Delta t_4(3)$ and $\Delta t_5(3)$. During the sixth step, the level 2 evolves for $\Delta t_6(2) = \Delta t_4(3) + \Delta t_5(3)$. Eventually, during the seventh step, the integration of the level 1 is performed using a time step $\Delta t_7(1) = \Delta t_3(2) + \Delta t_6(2)$ which is, by construction, smaller than $\Delta t_1^{\mathrm{CFL}}(1)$. The cycle is now complete and each grid level has evolved for the same amount of time $\Delta t_7(1)$. The entire cycle sequence is schematically sketched in Figure 3.3.

In general, within this kind of cycle, a level l is integrated 2^{l-1} times.

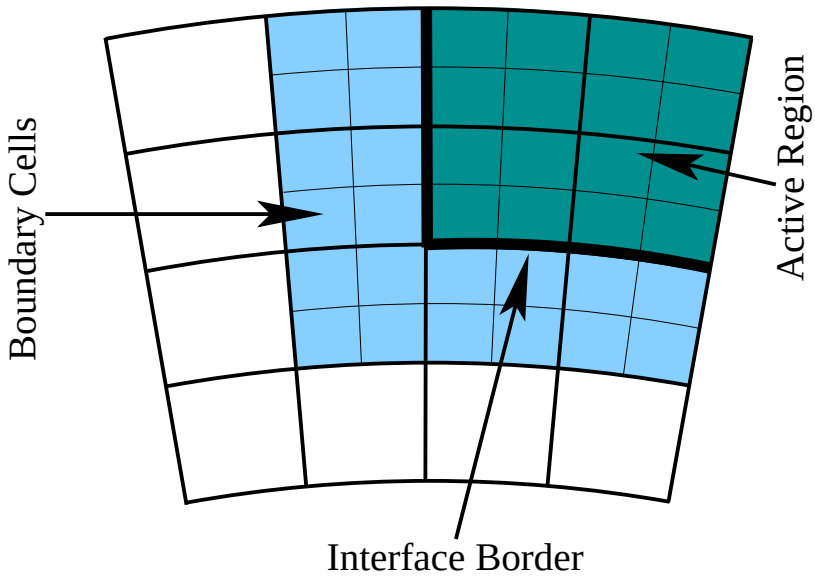

Figure 3.4: Interface between a subgrid and its host in 2D cylindrical coordinates. The light-colored zone marks those cells containing boundary values needed for the subgrid integration, the "ghost cells". The darker region refers to the so-called "active zone", where values are effectively computed on the subgrid. The thick line, which separates the previous regions, encloses the grid cells on the coarse grid whose content is replaced by the more accurate one coming from the subgrid.

3.5 Downward Information Transfer

We already mentioned that after the third step of the iteration cycle, grids 3 and 2 have to exchange some information. In general, this exchange must occur every time the grid level l evolves to the same time as the level $l+1$. Because of the higher resolution, we assume the solution of the level $l+1$ to be more accurate than that of the level l. Therefore, the fine-grid solution replaces the coarse one on the common computational domain. Whatever the level in the hierarchy is, the frame formed by the first and the last two grid cells are ghost cells (see Fig. 3.4). This indicates that they contain the boundary values necessary to perform the algorithm integration. Ghost cells of level $l+1$ do not contribute to the updating process of the solution of level l.

The replacement procedure is straightforward: in 2D a surface-weighted average, using the nearest fine values, substitutes the coarse quantity. For example, referring to Figure 3.5, the averaged coarse density (Σ^{C}) is

$$\Sigma^{\mathrm{C}} = \frac{\sum_i \Sigma_i^{\mathrm{F}} A_i}{\sum_i A_i} = \frac{(\Sigma_1^{\mathrm{F}} + \Sigma_4^{\mathrm{F}})\, A_1 + (\Sigma_2^{\mathrm{F}} + \Sigma_3^{\mathrm{F}})\, A_2}{2\,(A_1 + A_2)}. \tag{3.7}$$

In this geometry, since the advected quantities are the radial momentum density $\Sigma\, u_r$ and the angular momentum density $\Sigma\, r^2\, \omega$, these are the interpolated quantities, along with Σ.

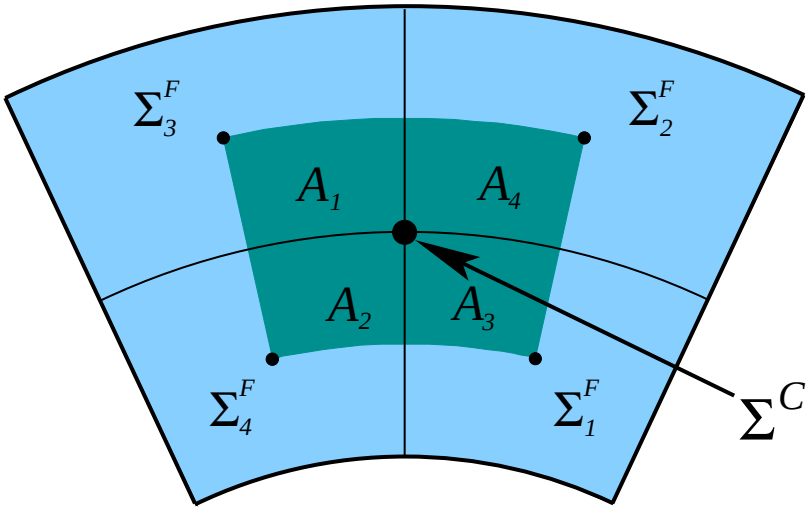

Figure 3.5: Surface weighted average of the surface density. A *coarse* cell is shown along with the four *fine* cells it comprises. As a scalar, the surface density is cell-centered within the appropriate refinement (dots). $\Sigma^{\rm C}$ represents the new, interpolated, value of the coarse cell; $\Sigma_i^{\rm F}$ are the fine interpolating quantities. Because of the fixed value of $\Delta\varphi(l)$, $A_1 = A_4$ and $A_2 = A_3$.

In three-dimensional spherical coordinates, the surface-weighted average turns into a volume-weighted average, which involves 8 fine cells. Similarly to the surface elements, volume elements are azimuthally independent. Therefore, in the 3D-geometry the equivalent of equation (3.7) only requires four independent volume sectors.

Interpolation of scalars can be easily figured out by considering the 2D area elements as the projection of a set of volume elements onto the plane $\theta = \pi/2$. Then, a second set of four volumes must be added on the top of it. The upper set is located at the co-latitude $\theta(l+1)$ whereas the lower set is located at latitude $\theta(l+1) + \Delta\theta(l+1)$.

In three dimensions, the other interpolated quantities are the linear momentum density $\rho\, u_R$, and the angular momenta in the meridional and azimuthal directions: $R\,\rho\, u_\theta$ and $R\,\sin\theta\rho\, u_\varphi$ (strictly speaking, these are angular momentum densities). As vectors' interpolation might appear not so trivial as the one yielding the updated values of scalar quantities, we will also propose explicit algorithms, employing grid-related quantities in spherical polar coordinates (see § 3.5.1).

Since velocities are centered at the sides of a cell (see Figs. 3.6 and 3.7 for the cylindrical geometry), this average is a little more complex than the previous one and requires six terms in two dimensions. Indicating with $u^{\rm C}$ the coarse value of the linear (i.e., radial) momentum density to be interpolated and with $u_i^{\rm F}$ the surrounding fine grid values, we have:

$$u^{\rm C} = \frac{(u_1^{\rm F} + u_6^{\rm F})\, A_1 + (u_2^{\rm F} + u_5^{\rm F})\, A_2 + (u_3^{\rm F} + u_4^{\rm F})\, A_3}{2\,(A_1 + A_2 + A_3)}. \tag{3.8}$$

The angular momentum can be handled accordingly by using the appropriate finer-grid

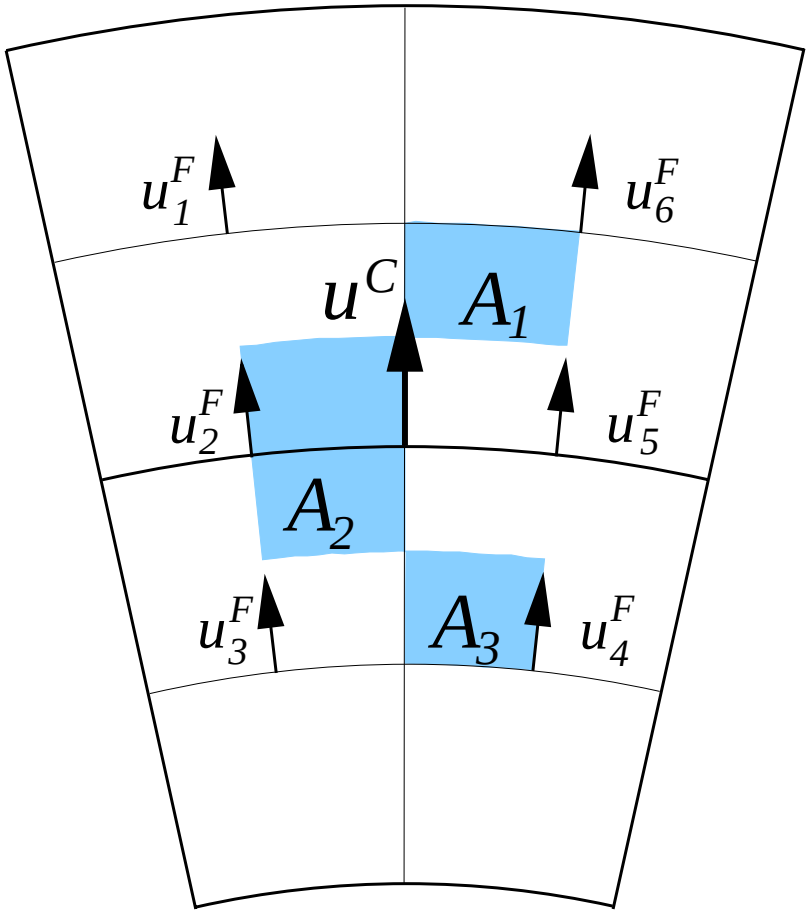

Figure 3.6: Surface weighted average of the radial momentum density $u = \Sigma u_r$. Two coarse cells are drawn (thick lines). Fine cells are delimited by thin lines. Because of the staggered structure of the grid, vectors are face-centered within the cell.

quantities and area patches. Both can be easily identified by drawing a picture similar to Figure 3.6.

In three dimensions, interpolation of momenta take 12 file cells to be accomplished. Following similarity arguments, a formula for the updated linear momentum can be written down without much effort (see § 3.5.1). Azimuthal and meridional angular momenta are interpolated in a similar fashion once the correct fine-grid quantities and volume elements are identified. Unfortunately, 3D sketches in spherical polar coordinates do not help much. In contrast, 2D projections may result more useful to the goal.

In a successive step, velocities are retrieved, both in 2D and 3D. Since the gravitational potential is assigned, it doesn't need to be transferred from a finer level to a coarser one. The same is valid for the energy density in the circumstance that no energy equation is solved. However, if the energy transport is accounted for and an energy equation has to be solved, as a scalar, energy density receives the same treatment as the mass density.

3.5.1 Interpolation Formulas in Three Dimensions

The aim of this section is to furnish some algorithms useful for updating the values of scalars and momenta on a coarse grid with those computed on the hosted (finer) one, in spherical polar coordinates.

For such purpose, we indicate with ρ^{C} the mass density to be interpolated on the level l. The interpolating values, on the finer subgrid level $l+1$, are indicated simply as $\rho(i,j,k)$. For the density average, the i-index varies between i and $i+1$ and so do the other two indexes.

Accordingly, u_R^{C}, u_θ^{C} and u_φ^{C} are the coarse radial, meridional and azimuthal angular momentum. The finer values from which they are reset will be denoted as $u_R(i,j,k)$, $u_\theta(i,j,k)$, and $u_\varphi(i,j,k)$, respectively[2]. For the average of the radial vector component, the i-index varies between $i-1$ and $i+1$, while the other two indexes vary between j (k) and $j+1$ ($k+1$). In case of the meridional angular momentum, the j-index ranges from $j-1$ to $j+1$, while the others are i (k) and $i+1$ ($k+1$). For the azimuthal angular momentum, it is the k-index to extend over the wider range. Such occurrence depends on the mesh locations where these vector components are defined.

The finer grid coordinates (on level $l+1$) are $(R_i, \theta_j, \varphi_k)$, and the grid spacing is $(\Delta R, \Delta\theta, \Delta\varphi)$. This is constant over the computing mesh. In all of the above quantities, we dropped the level index ($l+1$) to avoid being too cumbersome. Since the grid has a staggered structure, scalars are volume-centered, i.e., $\rho(i,j,k)$ lies at $(R_i + \Delta R/2, \theta_j + \Delta\theta/2, \varphi_k + \Delta\varphi/2)$, while ρ_R^{C} resides at $(R_i + \Delta R, \theta_j + \Delta\theta, \varphi_k + \Delta\varphi)$ (the linear resolution doubles from a grid to the hosted one). Instead, vector components are centered each on a different face of the volume element. For example, the radial component $u_R(i,j,k)$ is located at $(R_i, \theta_j + \Delta\theta/2, \varphi_k + \Delta\varphi/2)$, whereas the coarse radial momentum u_R^{C} is defined at $(R_i, \theta_j + \Delta\theta, \varphi_k + \Delta\varphi)$. The location of the other quantities follows by similarity.

The interpolation is basically a volume-weighted average, as already mentioned before. It is meant to refine the solution computed on the level l by means of that resulting from integration of the finer resolution level $l+1$. Eight volumes are necessary to carry out a scalar interpolation. Momentum interpolations require that twelve spherical sectors must be employed, one for each of the involved fine-grid quantities. Yet, since the metric in a spherical polar topology is independent of the azimuthal angle φ, some of them actually coincide. Hence, a smaller number of such elements are to be found. In order to distinguish among the four volume sets, we introduce the notations $V^{(\rho)}$, $V^{(R)}$, $V^{(\theta)}$ and $V^{(\varphi)}$, according to the quantity to average (ρ^{C}, u_R^{C}, u_θ^{C}, and u_φ^{C}). These four sets differ because of the space metric.

Once the correct elements have been chosen, the coarse mass density can be replaced by

$$\rho^{\mathrm{C}} = \frac{\sum_{ijk} \rho(i,j,k)\, V^{(\rho)}(i,j)}{2 \sum_{ij} V^{(\rho)}(i,j)}. \tag{3.9}$$

In fact, sectors $V^{(\rho)}$ are φ-independent, thus only four volumes enter this average. In a

[2] Note that these are momenta and not velocities.

similar manner, new momenta can be written, in a concise form, as

$$u_{\Xi}^{\mathrm{C}} = \frac{\sum_{ijk} u_{\Xi}(i,j,k)\, V^{(\Xi)}(i,j,k)}{\sum_{ijk} V^{(\Xi)}(i,j,k)}, \tag{3.10}$$

where $\Xi = (R, \theta, \varphi)$. For computational purposes, a volume element is preferentially cast into the form

$$V = \left(\Delta R^3/3\right)\, \left(-\Delta \cos\theta\right)\, \left(\Delta\varphi\right). \tag{3.11}$$

The set of sectors $V^{(\rho)}$ required in equation (3.9) is the following

$$\begin{aligned}
V^{(\rho)}(i,j) &= \frac{1}{3}\left(R_{i+1}^3 - R_i^3\right)\, \left[\cos\left(\theta_j\right) - \cos\left(\theta_{j+1}\right)\right]\, \Delta\varphi & (3.12)\\
V^{(\rho)}(i+1,j) &= \frac{1}{3}\left[\left(R_{i+1} + \Delta R\right)^3 - R_{i+1}^3\right]\, \left[\cos\left(\theta_j\right) - \cos\left(\theta_{j+1}\right)\right]\, \Delta\varphi & (3.13)\\
V^{(\rho)}(i,j+1) &= \frac{1}{3}\left(R_{i+1}^3 - R_i^3\right)\, \left[\cos\left(\theta_{j+1}\right) - \cos\left(\theta_{j+1} + \Delta\theta\right)\right]\, \Delta\varphi & (3.14)\\
V^{(\rho)}(i+1,j+1) &= \frac{1}{3}\left[\left(R_{i+1} + \Delta R\right)^3 - R_{i+1}^3\right] \\
&\quad \left[\cos\left(\theta_{j+1}\right) - \cos\left(\theta_{j+1} + \Delta\theta\right)\right]\, \Delta\varphi & (3.15)
\end{aligned}$$

Also for the radial and meridional directions, the denominator of equation (3.10) reduces to $2\sum_{ij} V^{(\Xi)}(i,j)$, though the summation includes six terms, this time. Therefore, the set of volume elements necessary for the interpolation of the radial momentum u_R^{C} are:

$$\begin{aligned}
V^{(R)}(i-1,j) &= \frac{1}{3}\left[\frac{1}{8}\left(R_{i-1} + R_i\right)^3 - R_{i-1}^3\right] \\
&\quad \left[\cos\left(\theta_j\right) - \cos\left(\theta_{j+1}\right)\right]\, \Delta\varphi & (3.16)\\
V^{(R)}(i,j) &= \frac{1}{24}\left[\left(R_i + R_{i+1}\right)^3 - \left(R_{i-1} + R_i\right)^3\right] \\
&\quad \left[\cos\left(\theta_j\right) - \cos\left(\theta_{j+1}\right)\right]\, \Delta\varphi & (3.17)\\
V^{(R)}(i+1,j) &= \frac{1}{3}\left[R_{i+1}^3 - \frac{1}{8}\left(R_i + R_{i+1}\right)^3\right] \\
&\quad \left[\cos\left(\theta_j\right) - \cos\left(\theta_{j+1}\right)\right]\, \Delta\varphi & (3.18)\\
V^{(R)}(i-1,j+1) &= \frac{1}{3}\left[\frac{1}{8}\left(R_{i-1} + R_i\right)^3 - R_{i-1}^3\right] \\
&\quad \left[\cos\left(\theta_{j+1}\right) - \cos\left(\theta_{j+1} + \Delta\theta\right)\right]\, \Delta\varphi & (3.19)\\
V^{(R)}(i,j+1) &= \frac{1}{24}\left[\left(R_i + R_{i+1}\right)^3 - \left(R_{i-1} + R_i\right)^3\right] \\
&\quad \left[\cos\left(\theta_{j+1}\right) - \cos\left(\theta_{j+1} + \Delta\theta\right)\right]\, \Delta\varphi & (3.20)\\
V^{(R)}(i+1,j+1) &= \frac{1}{3}\left[R_{i+1}^3 - \frac{1}{8}\left(R_i + R_{i+1}\right)^3\right] \\
&\quad \left[\cos\left(\theta_{j+1}\right) - \cos\left(\theta_{j+1} + \Delta\theta\right)\right]\, \Delta\varphi & (3.21)
\end{aligned}$$

The group of elements involved in the updating process of the meridional angular momentum u_θ^{C} is:

$$V^{(\theta)}(i,j-1) = \frac{1}{3}\left(R_{i+1}^3 - R_i^3\right)\left\{\cos\left(\theta_{j-1}\right) - \cos\left[(\theta_{j-1}+\theta_j)/2\right]\right\}\Delta\varphi \quad (3.22)$$

$$V^{(\theta)}(i,j) = \frac{1}{3}\left(R_{i+1}^3 - R_i^3\right) \left\{\cos\left[(\theta_{j-1}+\theta_j)/2\right] - \cos\left[(\theta_j+\theta_{j+1})/2\right]\right\}\Delta\varphi \quad (3.23)$$

$$V^{(\theta)}(i,j+1) = \frac{1}{3}\left(R_{i+1}^3 - R_i^3\right)\left\{\cos\left[(\theta_j+\theta_{j+1})/2\right] - \cos\left(\theta_{j+1}\right)\right\}\Delta\varphi \quad (3.24)$$

$$V^{(\theta)}(i+1,j-1) = \frac{1}{3}\left[(R_{i+1}+\Delta R)^3 - R_{i+1}^3\right] \left\{\cos\left(\theta_{j-1}\right) - \cos\left[(\theta_{j-1}+\theta_j)/2\right]\right\}\Delta\varphi \quad (3.25)$$

$$V^{(\theta)}(i+1,j) = \frac{1}{3}\left[(R_{i+1}+\Delta R)^3 - R_{i+1}^3\right] \left\{\cos\left[(\theta_{j-1}+\theta_j)/2\right] - \cos\left[(\theta_j+\theta_{j+1})/2\right]\right\}\Delta\varphi \quad (3.26)$$

$$V^{(\theta)}(i+1,j+1) = \frac{1}{3}\left[(R_{i+1}+\Delta R)^3 - R_{i+1}^3\right] \left\{\cos\left[(\theta_j+\theta_{j+1})/2\right] - \cos\left(\theta_{j+1}\right)\right\}\Delta\varphi \quad (3.27)$$

In order to perform the interpolation of the azimuthal angular momentum u_φ^{C}, the following set of volume elements is required:

$$V^{(\varphi)}(i,j,k-1) = \frac{1}{3}\left(R_{i+1}^3 - R_i^3\right)\left[\cos\left(\theta_j\right) - \cos\left(\theta_{j+1}\right)\right]\Delta\varphi/2 \quad (3.28)$$

$$V^{(\varphi)}(i+1,j,k-1) = \frac{1}{3}\left[(R_{i+1}+\Delta R)^3 - R_{i+1}^3\right] \left[\cos\left(\theta_j\right) - \cos\left(\theta_{j+1}\right)\right]\Delta\varphi/2 \quad (3.29)$$

$$V^{(\varphi)}(i,j+1,k-1) = \frac{1}{3}\left(R_{i+1}^3 - R_i^3\right) \left[\cos\left(\theta_{j+1}\right) - \cos\left(\theta_{j+1}+\Delta\theta\right)\right]\Delta\varphi/2 \quad (3.30)$$

$$V^{(\varphi)}(i+1,j+1,k-1) = \frac{1}{3}\left[(R_{i+1}+\Delta R)^3 - R_{i+1}^3\right] \left[\cos\left(\theta_{j+1}\right) - \cos\left(\theta_{j+1}+\Delta\theta\right)\right]\Delta\varphi/2 \quad (3.31)$$

$$V^{(\varphi)}(i,j,k) = 2\,V^{(\varphi)}(i,j,k-1) \quad (3.32)$$

$$V^{(\varphi)}(i,j+1,k) = 2\,V^{(\varphi)}(i,j+1,k-1) \quad (3.33)$$

$$V^{(\varphi)}(i+1,j,k) = 2\,V^{(\varphi)}(i+1,j,k-1) \quad (3.34)$$

$$V^{(\varphi)}(i+1,j+1,k) = 2\,V^{(\varphi)}(i+1,j+1,k-1) \quad (3.35)$$

$$V^{(\varphi)}(i,j,k+1) = V^{(\varphi)}(i,j,k-1) \quad (3.36)$$

$$V^{(\varphi)}(i,j+1,k+1) = V^{(\varphi)}(i,j+1,k-1) \quad (3.37)$$

$$V^{(\varphi)}(i+1,j,k+1) = V^{(\varphi)}(i+1,j,k-1) \quad (3.38)$$

$$V^{(\varphi)}(i+1,j+1,k+1) = V^{(\varphi)}(i+1,j+1,k-1). \quad (3.39)$$

Equations 3.28 through 3.39 imply that the denominator of equation (3.10) is also equivalent to $2\sum_{ij} V^{(\varphi)}(i,j,k)$.

3.5.2 Flux Corrections

We now explain the procedure through which mass fluxes at grid interfaces are corrected. To do so, we will restrict to the two-dimensional case. In spherical polar coordinates flux vector components are three, but radial and azimuthal fluxes are treated in the same manner as they are treated in 2D, provided that the correct metric factors are introduced in the formulas.

In order to guarantee global mass and momentum conservation for the whole hierarchy, we have to make sure that the normalized momentum flux components

$$\boldsymbol{\mathcal{F}}_{\rm 2D} = \left[\frac{\Sigma\, u_r}{r\,\Delta\varphi\,\Delta t}, \frac{\Sigma\, r^2\,\omega}{\Delta r\,\Delta t}\right], \tag{3.40}$$

across the border between a subgrid and its host grid (indicated in Fig. 3.4), are equal in both level solutions whenever the grid has evolved for the same time as the subgrid. However, each grid evolves independently and for a time interval different from that of the lower one. Thus, even after the solution updating process described above, the amount of momentum flowed across the borders might not coincide in the respective solutions. To remove this possible discrepancy, at the coarse-fine grid border, these quantities are taken from the fine grid integration.

In Figure 3.7 the situation for the azimuthal momentum flux is depicted. Two fine cells participate in this process. Referring to the integration cycle traced in § 3.4, $f_k^j(l)$ represents the value of the quantity $\Sigma\, r^2\,\omega/(\Delta r\,\Delta t)$, at the grid-grid interface location, as computed during the k-th cycle step on level l. An additional index ($j = 1, 2$) is needed to identify the radial position of the two fine cells involved (for example, on level 3), but it does not concern the coarse grid quantity to be replaced (on level 2).

Suppose we are at the end of the third cycle, when the first interaction, between levels 2 and 3, occurs (first straight arrow in Fig. 3.3). Because of the refinement ratio established by equation (3.3), quantity $f_3(2)$ will be reset as:

$$f_3(2) = \frac{1}{2}\,\frac{\Delta t_1(3)\,\sum_j f_1^j(3) + \Delta t_2(3)\,\sum_j f_2^j(3)}{\Delta t_3(2)} \tag{3.41}$$

This correction is accounted for directly while performing the advection of radial and angular momenta.

In three-dimensions, the normalized flux components, with which the above correction is accomplished, are

$$\boldsymbol{\mathcal{F}}_{\rm 3D} = \left[\frac{\rho\, u_r}{R^2\,\sin\theta\,\Delta\theta\,\Delta\varphi\,\Delta t}, \frac{\rho\, R\, u_\theta}{R\,\sin\theta\,\Delta\varphi\,\Delta R\,\Delta t}, \frac{\rho\, R\,\sin\theta\, u_\varphi}{R\,\Delta\theta\,\Delta R\,\Delta t}\right]. \tag{3.42}$$

3.6 Upward Information Transfer

The boundary conditions on the main grid are usually imposed depending on the physics and geometry of the problem: symmetry, periodicity, etc. In the case of a subgrid, boundary values must be attached, in some way, to the values of the underlying grid. This

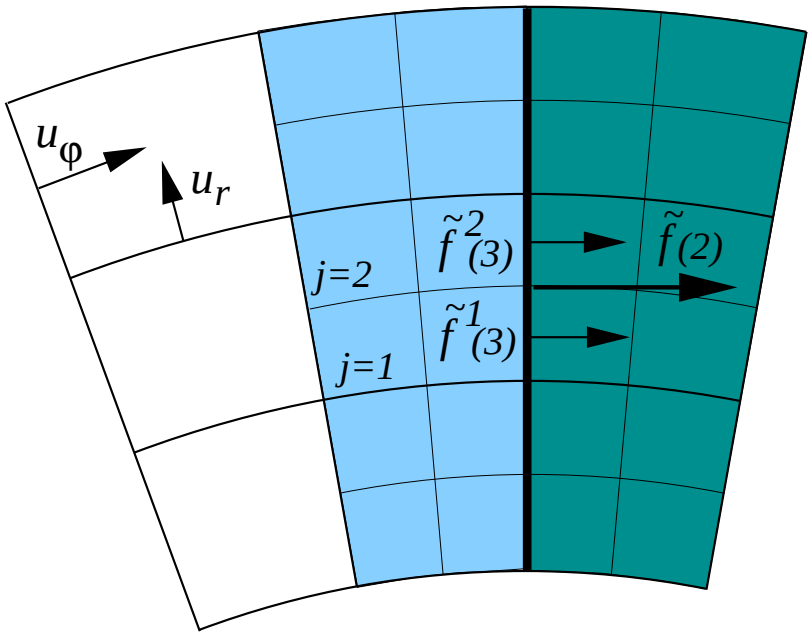

Figure 3.7: Momentum flux correction scheme in 2D. Momentum flux components are centered as velocity field components, whose locations are shown in the upper left corner. $\tilde{f}(2)\,\Delta r(2) = f_3(2)\,\Delta t_3(2)\,\Delta r(2)$ represents the amount of angular momentum, flowed across the coarse cell border, during the third cycle step (see Section 3.4). $\tilde{f}^1(3)\,\Delta r(3) = f_1^1(3)\,\Delta t_1(3)\,\Delta r(3) + f_2^1(3)\,\Delta t_2(3)\,\Delta r(3)$ represents the same quantity transported, during the first two cycle steps, across the $j = 1$ fine cell border. The coarse quantity is replaced by $\left[\tilde{f}^1(3) + \tilde{f}^2(3)\right]\,\Delta r(3)$.

point turned out to be extremely delicate for our calculations. In NIRVANA, the boundary values of a certain level l were just set by means of a linear interpolation of the quantities on the lower level $l - 1$. Because of the strong variations in density and velocity, due to the formation of shock fronts in our simulations, this method fails and produces numerical inconsistencies.

Therefore, we raised the order of the interpolation. However, this introduces another potential trap. In fact, a high-order interpolation (higher than the first order) is not monotonic and can produce a new minimum. This is not acceptable since, for example, the density is a non-negative quantity. Then the interpolating function should be monotonised. In order to handle this problem we have used the same approach as described in Ruffert (1992), that is by employing the *monotonised harmonic mean* (van Leer 1977).

Then, if we have a function sampled at $x - \Delta x$, x and $x + \Delta x$, with values g_L, g and g_R, respectively (as shown in Fig. 3.8), the averaged value at $x + \varepsilon$ is

$$g(\varepsilon) = g + \frac{2\,\varepsilon}{\Delta x}\,\max\left[\frac{(g - g_\mathrm{L})\,(g_\mathrm{R} - g)}{g_\mathrm{R} - g_\mathrm{L}}, 0\right], \tag{3.43}$$

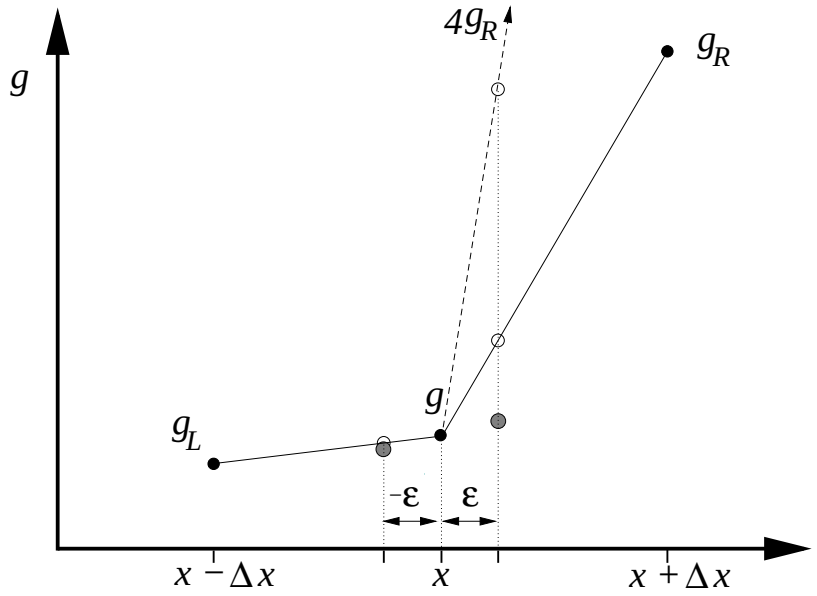

Figure 3.8: Behavior of a harmonic mean against a geometric mean. Grey filled circles indicate the *harmonic* values assumed by g_ε. Open circles indicate the corresponding values when the geometric mean is applied. The plot intends to simulate a shock front. If we keep the left value $g_{\rm L}$ unchanged and make the right one $g_{\rm R}$ four times as large, the geometric mean value will increase proportionally. In turn, the harmonic mean will change so slightly that its variation is not visible on this plot.

provided that $-\Delta x/2 \le \varepsilon \le \Delta x/2$.

If we adopt this kind of average on a 2D-mesh, each interpolation generally involves 3×3 coarse quantities. On a 3D-mesh it takes $3 \times 3 \times 3$ coarse volume elements, thus the procedure may consume a fair fraction of the whole simulation time if total number of grid levels $ng \ge 4$. It proceeds by averaging the selected coarse values along a certain direction, three at a time. This results in three new quantities. A further harmonic average of these, along the other direction, generates the subgrid boundary value at the correct position. Figure 3.9 shows how the procedure works in the case of the surface density. In three dimensions, the first step produces nine quantities. A second step reduces them to three and a third one yields the final result. The step order is expected to have only little influence on the final outcome.

As density is cell-centered, ε_r and ε_φ are always one fourth of the coarse grid linear size. Since the averaging process is performed for each direction separately and the grid is always logically cubic, it is not affected by the metric of the mesh, i.e. it is performed as if a Cartesian grid were used.

For the velocity components we have to distinguish two different cases (see Fig. 3.10 for a two-dimensional representation): whether the boundary value lies on a coarse cell border or whether it does not. In the first case, either ε_r or ε_φ is zero. Then only three coarse values participate in the average (nine in three dimensions), along either the azimuthal or

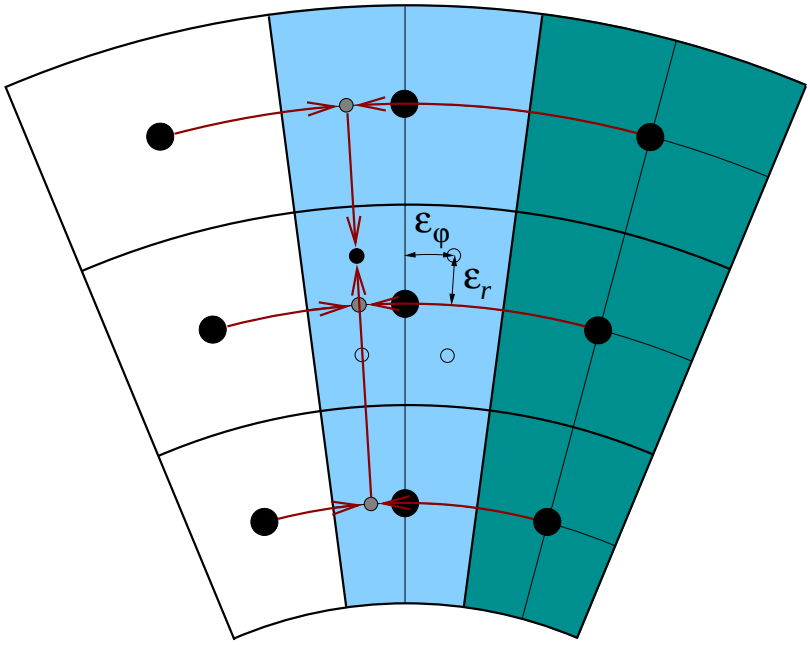

Figure 3.9: Harmonic average: surface density boundary values. The light-colored zone indicates subgrid ghost cells. Darker region belongs to the active subgrid zone. Nine coarse values (big black circles) are engaged in the average. The value to be interpolated is shown as a small black circle. During a first step, equation (3.43) is applied three times along the φ-direction. Three new values are generated (gray small circles), having the correct, final azimuthal coordinate. These are averaged to obtain the final value at the correct radial location. Small open circles refer to the other boundary quantities whose value depends on the same coarse quantities.

the radial direction. In the second case the interpolation proceeds exactly as explained for the surface density.

In case that the set of unknowns were enriched with other variables (such as the gravitational potential Φ, the thermal energy E, the magnetic field $\boldsymbol{B}$, etc.) all the boundary conditions for scalar quantities would be fixed as done for the mass density, whereas vectors would be treated as the velocity.

3.7 Final Remarks

In this section we will discuss the computational abilities of the nested grid technique, when applied to disk-planet interaction calculations.

The particular properties of such an astrophysical system make it optimal for the application of this kind of static mesh refinement method. In fact, it allows a detailed description of the flow feature nearby the protoplanet, while accounting for the whole protostellar disk, which is physically very important. This will be proved in the next chapters, where

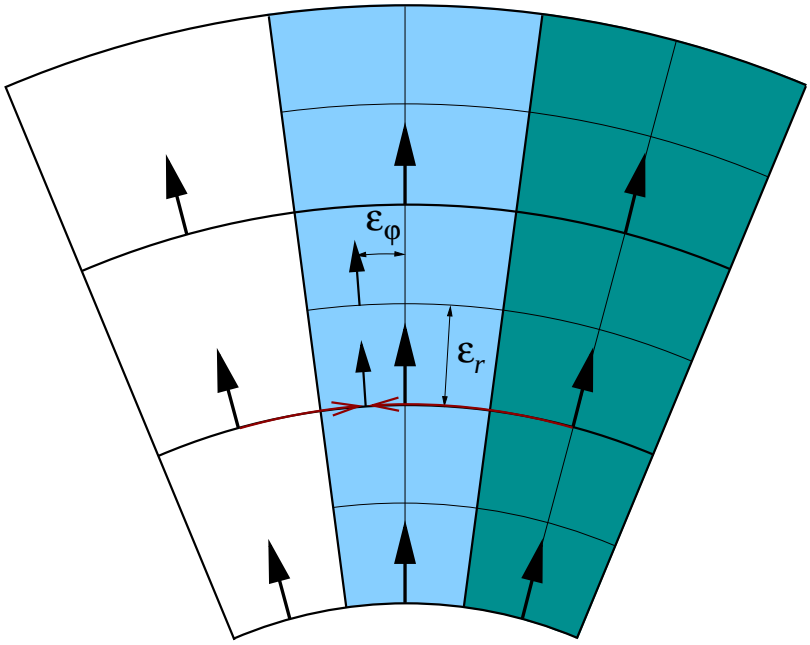

Figure 3.10: Harmonic average of radial velocity component in two dimensions. Two cases are shown. In one case the position of the velocity component lies on a coarse grid border (thick lines), requiring only three coarse quantities (one single average). In the other case nine coarse quantities are needed as for the density interpolation. The only difference is that ε_r is one half of the radial coarse size.

two- and three-dimensional models are presented.

The applicability of the method relies, however, on the assumption that the orbital eccentricity is zero. One could object that, because of gravitational interactions, the planet's orbit cannot be *a priori* considered circular. Yet, there are theoretical arguments suggesting that eccentricity growth is very unlikely in the situations we deal with. Furthermore, the rate of variation of the semi-major axis of the orbit, due to migration, is very small and no change could be appreciated over the simulated evolutionary time. Anyway, this static refinement method could be modified and brought to a more sophisticated level with not much effort. First of all, the grid hierarchy could be allowed to move in order to follow the planet orbital migration and / or eccentricity variation. Secondly, subgrids levels could be added and destroyed during the system evolution whenever and wherever necessary. This would make it a semi-adaptive method.

Because of the small array size of the subgrids, a finite difference algorithm based on nested grids is not appropriate to be run on vector processors. In contrast, the method would suit to be adapted and run on multi-processors computers. Yet, this issue has not been considered during this work, but planned for the future.

Thereupon, the following considerations are based on single-processor computations. Up to a certain nesting degree, computational time is determined by the size of the main

grid or level $l = 1$. This can be easily proved. Let $\mathfrak{M}_1 \times \mathfrak{M}_2 \times \mathfrak{M}_3$ be the size of the main grid and $\mathfrak{S}_1 \times \mathfrak{S}_2 \times \mathfrak{S}_3$ be that of any nested subgrid. Let's name $\mathfrak{T}_\mathfrak{M}$ the amount of time needed to integrate the set of equations over the basic grid. Then, if $\mathfrak{R}_k = \mathfrak{M}_k/\mathfrak{S}_k$, the time taken to perform the integration over a single subgrid patch is:

$$\mathfrak{T}_\mathfrak{S} = \frac{\mathfrak{T}_\mathfrak{M}}{\mathfrak{R}}, \tag{3.44}$$

where $\mathfrak{R} = \mathfrak{R}_1 \times \mathfrak{R}_2 \times \mathfrak{R}_3$. In two dimensions, for convention, $\mathfrak{R}_2$ is always equal to one. Now, according to what explained in § 3.4, each level $l + 1$ is integrated twice for a single integration of the level l. Thereby, the overall time required for moving across a hierarchy with ng levels is:

$$\mathfrak{T} = \mathfrak{T}_\mathfrak{M} + \mathfrak{T}_\mathfrak{S} \sum_{l=2}^{ng} 2^{l-1}, \tag{3.45}$$

which, recalling equation (3.44), can be otherwise written as

$$\mathfrak{T} = \mathfrak{T}_\mathfrak{M} + \frac{\mathfrak{T}_\mathfrak{M}}{2\,\mathfrak{R}} \sum_{l=2}^{ng} 2^{l}. \tag{3.46}$$

It can be easily demonstrated that the summation in equation (3.44) is equal to $\left(2^{ng+1} - 4\right)$, thus the computing time is

$$\mathfrak{T} = \mathfrak{T}_\mathfrak{M} + \frac{\mathfrak{T}_\mathfrak{M}}{\mathfrak{R}} \left(2^{ng} - 2\right). \tag{3.47}$$

Equation (3.47) implies that a large gain in local resolution can be achieved without a great cost, compared to a single grid simulation. In fact, to simply double the linear resolution in a single-grid mode, the number of grid points in one direction has to be doubled, which roughly makes the computation two times as long. When the resolution is the double in all the directions, the time is enlarged by a factor 2^D, where D is the dimension of the problem. In contrast, according to equation (3.47), $\mathfrak{T}$ doubles only when $(2^{ng} - 2) \approx \mathfrak{R}$. In the highest resolution simulations that we have performed so far, in two-dimensional as well as in three-dimensional geometry, $\mathfrak{R} \simeq 15$. Hence $\mathfrak{T} \simeq 2\,\mathfrak{T}_\mathfrak{M}$ only when $ng = 4$, which implies a local increase in resolution equal to $8 \times 8 \times 8$. When $l > 5$, most of the computing time is spent on the integration of the equations over the subgrids. At this point every time a subgrid level is added the simulation takes two times as long.

In CHAPTER 4 will be presented two-dimensional simulations in which up to seven grid levels are employed, obtaining a resolution that would require a 4267×4258 single-grid computation to be attained. In CHAPTER 5 we will discuss three-dimensional simulations in which up to five grid levels are used, reaching a resolution equivalent to a single-grid size of $1067 \times 825 \times 1064$ cells.

It's lovely to live on a raft. We had the sky, up there, all speckled with stars, and we used to lay on our backs and look up at them, and discuss about whether they was made, or only just happened – Jim he allowed they was made, but I allowed they happened; I judged it would have took too long to make so many. Jim said the moon could a laid them; well, that looked kind of reasonable, so I didn't say nothing against it, because I've seen a frog lay most as many, so of course it could be done. We used to watch the stars that fell, too, and see them streak down. Jim allowed they'd got spoiled and was hove out of the nest.

MARK TWAIN,
THE ADVENTURES OF HUCKLEBERRY FINN,
1885

CHAPTER 4

TWO-DIMENSIONAL COMPUTATIONS WITH NESTED GRIDS

In this chapter we will present the first application of the nested-grid technique to the problem of disk-planet interaction. Though these simulations are restricted to the flat geometry, they will show how powerful this scheme is since it allows to reach a resolution, and hence an accuracy, around the protoplanet by far finer than all the previous computations.

4.1 Introduction

Almost all of the computations, performed so far, have used a single grid which resolves the Roche lobe of a Jupiter-mass planet only with very few grid cells. As an example, in the highest resolutions presented in CHAPTER 2 at most 9 grid cells lie across the Roche lobe of a planet. Recently, Ciecieląg et al. (2000b,a) used an Adaptive Mesh Refinement method to resolve the immediate surroundings of the planet, but they did not give any estimate of the mass accretion rate onto the planet and magnitude of the gravitational torques acting on it. This might be a hint that, though very powerful, that technique is not easily applicable to planets in disks.

In order to achieve better resolutions some authors (see § 1.5.1) have relied on local simulations, i.e., only an azimuthal portion around the planet is taken into account. However, since density waves induced by embedded planet-like objects can travel a long distance (on the order of many AU) into a protostellar nebula, local simulations remain a rather disputable issue.

For this reason we aim at the structure and dynamics of the gas flow in the close vicinity of the planet, while performing global disk simulations. In order to obtain the necessary high spatial and temporal resolution, we use a nested-grid formalism which allows an accurate computation of fluid dynamics around protoplanets and, along with it, a precise evaluations the mass flow onto the planet and the acting torques.

In the next section we layout the equation which govern the system evolution and which are solved by means of the strategy outlined in CHAPTER 3. We describe the setup of the various numerical models in § 4.3. The main results are presented in § 4.4 and our conclusions are given in § 4.5.

4.2 Physical Model

For the purpose of this study, we assume that the opening angle of the protostellar accretion disk is very small. We describe the disk structure by means of a two-dimensional, infinitesimal thin, model using vertically averaged quantities, such as the surface mass density

$$\Sigma = \int_{-\infty}^{+\infty} \rho \, \mathrm{d}z,$$

where ρ is the regular, three-dimensional mass density. We work in a cylindrical coordinate system (r, φ, z) whose origin is fixed at the center of mass of the star and the planet, and where the plane of the disk coincides with the $z = 0$-plane.

The gas in the disk is non-self-gravitating and is orbiting a protostar having a mass $M_\star = 1\ M_\odot$. The total mass of the disk M_D, within the simulated region, which extends from 2.08 to 13 AU, is $3.5 \times 10^{-3}\ M_\odot$. Embedded in this disk there is a massive protoplanet with a mass M_p, which ranges from one Earth-mass ($M_\oplus$) to one Jupiter-mass ($M_\jupiter$), depending on the considered model. The planet is assumed to be on a fixed circular orbit throughout the evolution. We employ a rotating coordinate system, corotating with the planet, whose azimuthal position is kept constant at $\varphi_\mathrm{p} = \pi$. The angular velocity Ω of the rotating frame is then given by

$$\Omega = \Omega_p = \sqrt{\frac{G\,(M_\star + M_\mathrm{p})}{a^3}}, \tag{4.1}$$

where G is the gravitational constant and a is the distance of the planet from the star.

The evolution of the disk is given by the two-dimensional (r, φ) continuity equation for Σ and the Navier-Stokes equations for each of the two components of the velocity field $\boldsymbol{u} \equiv (u_r, u_\varphi)$. Thus, the set of equations reads

$$\frac{\partial \Sigma}{\partial t} + \nabla \cdot (\Sigma\, \boldsymbol{u}) = 0, \tag{4.2}$$

$$\frac{\partial (\Sigma\, u_r)}{\partial t} + \nabla \cdot (\Sigma\, u_r\, \boldsymbol{u}) = \Sigma\, r\, (\omega + \Omega)^2 - \frac{\partial P}{\partial r} - \Sigma\, \frac{\partial \Phi}{\partial r} + f_r, \tag{4.3}$$

$$\frac{\partial [\Sigma\, r^2\, (\omega + \Omega)]}{\partial t} + \nabla \cdot [\Sigma\, r^2\, (\omega + \Omega)\, \boldsymbol{u}] = -\frac{\partial P}{\partial \varphi} - \Sigma\, \frac{\partial \Phi}{\partial \varphi} + f_\varphi. \tag{4.4}$$

Here $\omega = u_\varphi / r$ is the angular velocity and P is the vertically integrated (two-dimensional) pressure. The gravitational potential Φ, generated by the protostar and the planet, is given by

$$\Phi = \Phi_\star + \Phi_\mathrm{p} = -\frac{G\, M_\star}{|\boldsymbol{r} - \boldsymbol{r}_\star|} - \frac{G\, M_\mathrm{p}}{|\boldsymbol{r} - \boldsymbol{r}_\mathrm{p}|}, \tag{4.5}$$

where $\boldsymbol{r}_\star$ and $\boldsymbol{r}_\mathrm{p}$ are the radius vectors to the star and the planet, respectively. The effects of viscosity are contained in the terms f_r and f_φ which give the viscous force per unit area acting in the radial and azimuthal (f_φ / r) direction:

$$f_r = \frac{1}{r}\, \frac{\partial (r\, S_{rr})}{\partial r} + \frac{1}{r}\, \frac{\partial S_{r\varphi}}{\partial \varphi} - \frac{S_{\varphi\varphi}}{r},$$

$$f_\varphi = \frac{1}{r}\frac{\partial (r^2\, S_{r\varphi})}{\partial r} + \frac{\partial S_{\varphi\varphi}}{\partial \varphi}.$$

Since we assume a zero bulk viscosity ζ, a constant kinematic viscosity ν and we do not include any artificial viscosity in our numerical models, the relevant non-zero components of the three-dimensional viscous stress tensor $\mathbf{S}$ are

$$S_{rr} = 2\,\nu\,\Sigma\,\left(\frac{\partial u_r}{\partial r} - \frac{1}{3}\,\nabla\cdot\boldsymbol{u}\right), \tag{4.6}$$

$$S_{\varphi\varphi} = 2\,\nu\,\Sigma\,\left(\frac{\partial \omega}{\partial \varphi} + \frac{u_r}{r} - \frac{1}{3}\,\nabla\cdot\boldsymbol{u}\right), \tag{4.7}$$

$$S_{r\varphi} = \nu\,\Sigma\,\left(\frac{1}{r}\frac{\partial u_r}{\partial \varphi} + r\,\frac{\partial \omega}{\partial r}\right), \tag{4.8}$$

where the divergence of the velocity field can be written as

$$\nabla\cdot\boldsymbol{u} = \frac{1}{r}\frac{\partial (r\,u_r)}{\partial r} + \frac{\partial \omega}{\partial \varphi}. \tag{4.9}$$

A more general form of the relations (4.6), (4.7) and (4.8), within the two-dimensional cylindrical approximation, is given for example in Kley (1999).

In the set of equations above we have omitted the energy equation because in this study we will be concerned only with a relatively simple equation of state which does not require the solution of an energy equation. We shall use an isothermal equation of state where the surface pressure P is related to the density Σ through

$$P = c_{\rm s}^2\,\Sigma. \tag{4.10}$$

The local isothermal sound speed $c_{\rm s}$ is given here by

$$c_{\rm s} = \frac{H}{r}\,v_{\rm K}, \tag{4.11}$$

where $v_{\rm K} = \sqrt{G\,M_\star/r}$ denotes the Keplerian orbital velocity of the unperturbed disk. Equation (4.11) follows from vertical hydrostatic equilibrium. The ratio h of the vertical height H to the radial distance r is taken as a fixed input parameter. With this choice, the temperature T is proportional to $1/r$, as written in CHAPTER 2. Here we use a standard value

$$h = \frac{H}{r} = 0.05,$$

which is typical for protostellar accretion disks having a mass inflow rate of $\dot{M} \approx 10^{-7}$ $M_\odot\,{\rm yr}^{-1}$. With this value of h, our kinematic viscosity coefficient is equivalent to $\alpha = 4\times 10^{-3}$ at the radial position of the planet ($\nu = \alpha\,c_s\,H$).

Since the mass of the planet is very small in comparison to the mass of the star, because we always use here a ratio $q = M_{\rm p}/\,M_\star$ smaller than 10^{-3}, the center of mass is located very close to the position of the star. In the following we will often identify the radial distance from the origin of the coordinate system with the distance from the central star.

The set of equations written above is solved numerically, on a set of stacked grids, by NIRVANA, as explained in CHAPTER 3.

4.3 General Model Design

The main goal of this study is the investigation of the characteristic features of the hydrodynamic flow within the Roche lobe of the planet. This means that we must be able to resolve a characteristic length, the Hill radius:

$$R_{\rm H} = a \left(\frac{M_{\rm p}}{3\, M_{\bigstar}} \right)^{\frac{1}{3}}. \tag{4.12}$$

Moreover, we intend to do that for a variety of planet-to-star mass ratios. In order to reach such resolutions, we build a series of grid systems having the planet located approximately in the middle, at each level of the hierarchy. Smaller planets require higher degrees of nesting.

From now on, we refer to non-dimensional units. All the lengths are expressed in units of the distance a. This is constant because the planet moves on a fixed circular orbit, with radius

$$r_{\rm p} = \frac{a}{(1+q)}. \tag{4.13}$$

Masses are in units of the central stellar mass and time is given in units of the planet's orbital period. However, in order to convert them into conventional physical units, we assume that $a = 5.2$ AU and, as already mentioned, $M_{\bigstar} = 1\ M_{\odot}$. This implies that one planet orbit takes 11.8 years.

The whole azimuthal range of the disk is taken into account by considering a computational domain represented by $2\,\pi \times [r_{\rm in}, r_{\rm out}]$, where $r_{\rm in} = 0.4$ and $r_{\rm out} = 2.5$. This is covered by a 142×422 mesh (main grid), allowing a resolution such that $\Delta r(1) = \Delta\varphi(1) = 0.015$ and constraining the resolution on each other grid level, according to equation (3.3). The size of any higher grid level is 64×64.

4.3.1 Smoothing of the Potential

The perturbing action of the planet is exerted via its gravitational potential $\Phi_{\rm p}$. From a numerical point of view, it is usually smoothed in order to prevent numerical problems near the planet. Thus, we write the denominator of $\Phi_{\rm p}$ in equation (4.5) as $\sqrt{|\boldsymbol{r} - \boldsymbol{r}_{\rm p}|^2 + \delta^2}$. However, the smoothing length δ cannot be the same all over the grid system because of the different grid size involved at each level. Then we use the following grid-dependent length:

$$\delta(l) = \min\left[\frac{R_{\rm H}}{5}, \lambda(l) \right], \tag{4.14}$$

where

$$\lambda(l) = \sqrt{\Delta r^2(l) + r_p^2\, \Delta\varphi^2(l)} \simeq \sqrt{2}\, \Delta r(l). \tag{4.15}$$

The value of constant part, in equation (4.14), has become a kind of standard in single grid simulations (Kley 1999; Lubow et al. 1999; Kley 2000). This is always used on the main grid whereas the grid dependent part always prevails on the highest grid level. This choice results in a very deep potential in the immediate vicinity of the planet.

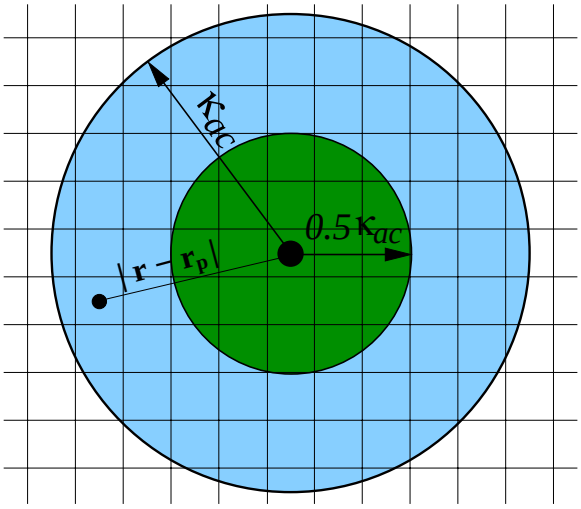

Figure 4.1: Planet mass accretion scheme. Wherever a cell center lies in the dark-colored zone, after each integration its density is lowered by an amount $\Delta\Sigma$ such that $\Delta\Sigma/\Sigma = 2\pi\kappa_{\rm ev}\Delta t$, where Δt is the integration time step interval. If the cell center falls into the light-colored zone $\Delta\Sigma$ is only one third of that value. For a typical main grid time interval and $\kappa_{\rm ev} = 5$, we would get $\Delta\Sigma/\Sigma \approx 1.2 \times 10^{-2}$. Anyway, this evacuation process is performed only on the highest grid level for better accuracy.

4.3.2 Mass Accretion Procedure

The presence of the planet affects the nearby disk density also because it can accrete matter. Planet accretion is accounted for by removing some mass from the region defined by $|\boldsymbol{r}-\boldsymbol{r}_{\rm p}| \leq \kappa_{\rm ac}$. Using this notation, we refer not only to the radial extent of the accretion region but also to the fact that the region is centered at $\boldsymbol{r}_{\rm p}$.

Since mass is removed from the system after each integration step, the evacuation rate depends on an input parameter $\kappa_{\rm ev}$ as well as on the integration time step. The details of the accretion process are given in Figure 4.1. This removal is accomplished only on the highest (finest) hierarchy level and the removed mass is not added to the dynamical mass of the planet, but just monitored. A standard value $\kappa_{\rm ev} = 5$ is used, while we set $\kappa_{\rm ac}$ between 8.0×10^{-2} and 9.4×10^{-2} $R_{\rm H}$. These values are such that only few grid cells, on each side of the planet, are involved in the gas accretion, making it a locally confined process. For the Jupiter-mass planet, $\sim 12 \times 12$ cells participate. The lowest number of employed cells is $\sim 8 \times 8$, which is used for the smallest planet ($M_{\rm p} = 1\ M_{\jupiter}$). The largest is $\sim 18 \times 18$ and is adopted for a planet with $M_{\rm p} = 0.5\ M_{\saturn}$ ($166\ M_{\jupiter}$). This circumstance is due to the high numerical resolution of the model (see Table 4.1).

Note that the sphere of influence of the accretion process consists of a region with a typical radius of $0.1\ R_{\rm H}$, quite smaller than the protoplanetary radius, whereas the planet is usually assumed to fill its Roche lobe during the growth phase (Bodenheimer and Pollack 1986; Tajima and Nakagawa 1997). As the present study does not take the energy equation into account, it precludes a detailed treatment of the internal structure of the protoplanet (see Wuchterl et al. 2000, and references therein; see also Fig. 4.9 below), hence the inferred accretion rates may still be unreliable.

4.3.3 Initial and Boundary Conditions

The initial density distribution is proportional to $r^{-1/2}$. However, we superimpose to this an axi-symmetric gap around the planet, obtained by an approximate balance of

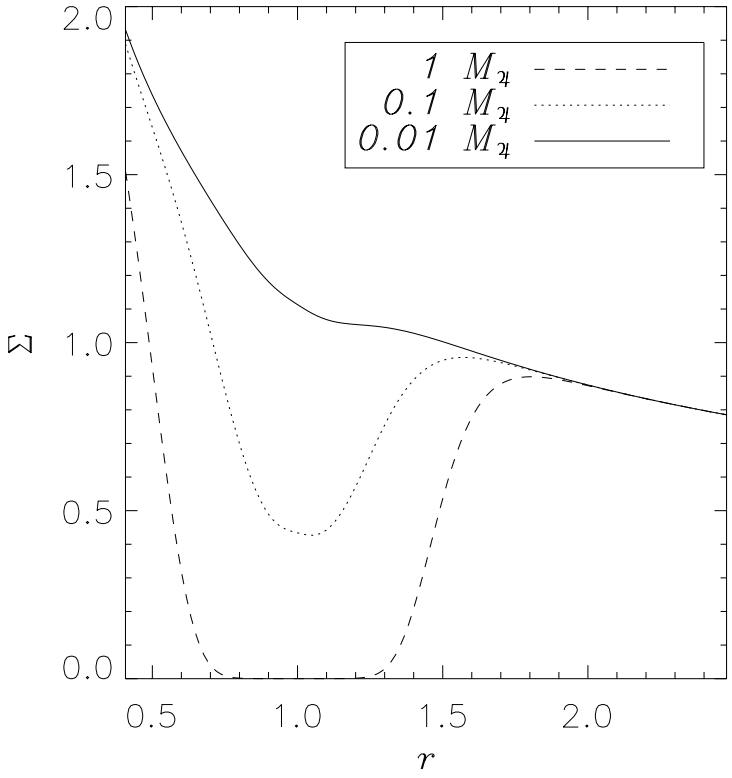

Figure 4.2: Initial surface density distribution for $q = 10^{-3}$, $q = 10^{-4}$, and $q = 10^{-5}$. $\Sigma(r, \varphi) = \Sigma(r)$ at $t = 0$. The gap greatly reduces when q gets small enough.

the viscous torque and the gravitational torque due to the planet (P. Artymowicz, private communication). Figure 4.2 shows the surface density, at $t = 0$, for some selected planet masses. The initial velocity field is that of a Keplerian disk.

As boundary conditions, periodicity is imposed at $\varphi = 0$ and $\varphi = 2\,\pi$. We allow matter to flow out of the computational domain at the inner radial border ($r_{\rm in}$) whereas we set reflective boundary conditions at the outer radial border ($r_{\rm out}$). The angular velocity is set equal to the unperturbed Keplerian value $\Omega_{\rm K} = \sqrt{G\,M_{\star}/\,r^3}$, both at $r_{\rm in}$ and $r_{\rm out}$.

For low-mass planets ($M_{\rm p} \lesssim 10\ M_{\oplus}$), boundary conditions should not affect much the system evolution because density waves damp before reaching $r = r_{\rm out}$ and are very weak when they reach $r = r_{\rm in}$. For more massive planets, some reflection is seen at the outer radial border. Further, the torque exerted by the planet pushes the inside-orbit material inwards. As a result, because of the open boundary at $r = r_{\rm in}$, the inner disk is partially cleared and consequently positive torques originating there reduce. The higher the planetary mass is the stronger these two effects appear.

4.3.4 Model Specifications

In this paper, we are mainly interested in investigating how disk-planet interactions change by varying q, the planet-to-star mass ratio. Table 4.1 summarizes the values of q used in different models along with the number of grid levels employed. For reference, a measure of the linear resolution ξ, in units of the Hill radius $R_{\rm H}$, is given for the highest level as well. Some models have different prescriptions than the ones outlined above, as specified in the Table 4.1.

Few models may deserve some comments. Model ELEN2 and WPRO1 aim at checking whether results from CIRO1 and CIRO2 (respectively) are resolution-dependent. This test is negative, as we show in the next sections. Since the planet position $(r_{\rm p}, \varphi_{\rm p})$ can fall anywhere within a grid cell according to the value of q in equation (4.13) and to the definition of the grid, some asymmetries could arise. These might have some effects on the finest levels, due to the small value of the smoothing factor δ. In order to achieve a complete symmetry, in the model GINO1 the planet is placed at the corner of a main grid cell (i.e., the intersecting point of four grid cells). This property is such that, on every other gird level, the planet always sits on the cross-point of four grid cells. CIRO3 and its counterpart, GINO1, give almost identical results. As we never noticed any significant difference in both torque and mass accretion rate calculations, when comparing "centered" and "non-centered" planet models, we decided not to center the planet for our convenience. Since in the Jupiter-mass case the inner-disk is greatly depleted, model ELEN1 was run to evaluate the influence of its presence on the gravitational torque. For this reason, in such model we prevent matter from draining out of the inner radial border by setting reflective boundary conditions.

4.4 Main Results

Hereafter we mainly discuss three models, namely CIRO1, CIRO2, and CIRO3. We concentrate on them because they cover a mass range from $1\ M_{♃}$ down to $3.3\ M_{♁}$. Nevertheless, whenever required by our discussion, we mention other particular models. Some results, concerning the whole set of models given in Table 4.1, are presented as well.

4.4.1 Overall Flow Structure

Large-scale interactions (whose effects extend over $2\,\pi$ in azimuth and cover a large radial extent) of a Jupiter-mass planet with the surrounding environment, have already been treated numerically in a number of papers (Artymowicz 1992; Kley 1999; Bryden et al. 1999; Kley et al. 2001). An example of large-scale features can be seen in Figure 4.3, where the comprehensive result of a nested-grid computation is displayed.

Planets with a lower value of q should perturb the disk less and have a weaker large-scale impact on it. For these reasons we discuss only the medium ($|\boldsymbol{r} - \boldsymbol{r}_{\rm p}| \sim R_{\rm H}$) and small ($|\boldsymbol{r} - \boldsymbol{r}_{\rm p}| \ll R_{\rm H}$) scale effects of such interactions.

Nonetheless, it's worthwhile to note that large-scale structures are clearly visible in our smallest mass models, as proved in Figure 4.4. In CIRO3 ($M_{\rm p} = 3.3\ M_{♁}$), a trailing density wave, emanating from the planet, spirals around the star for about $4\,\pi$, vanishing

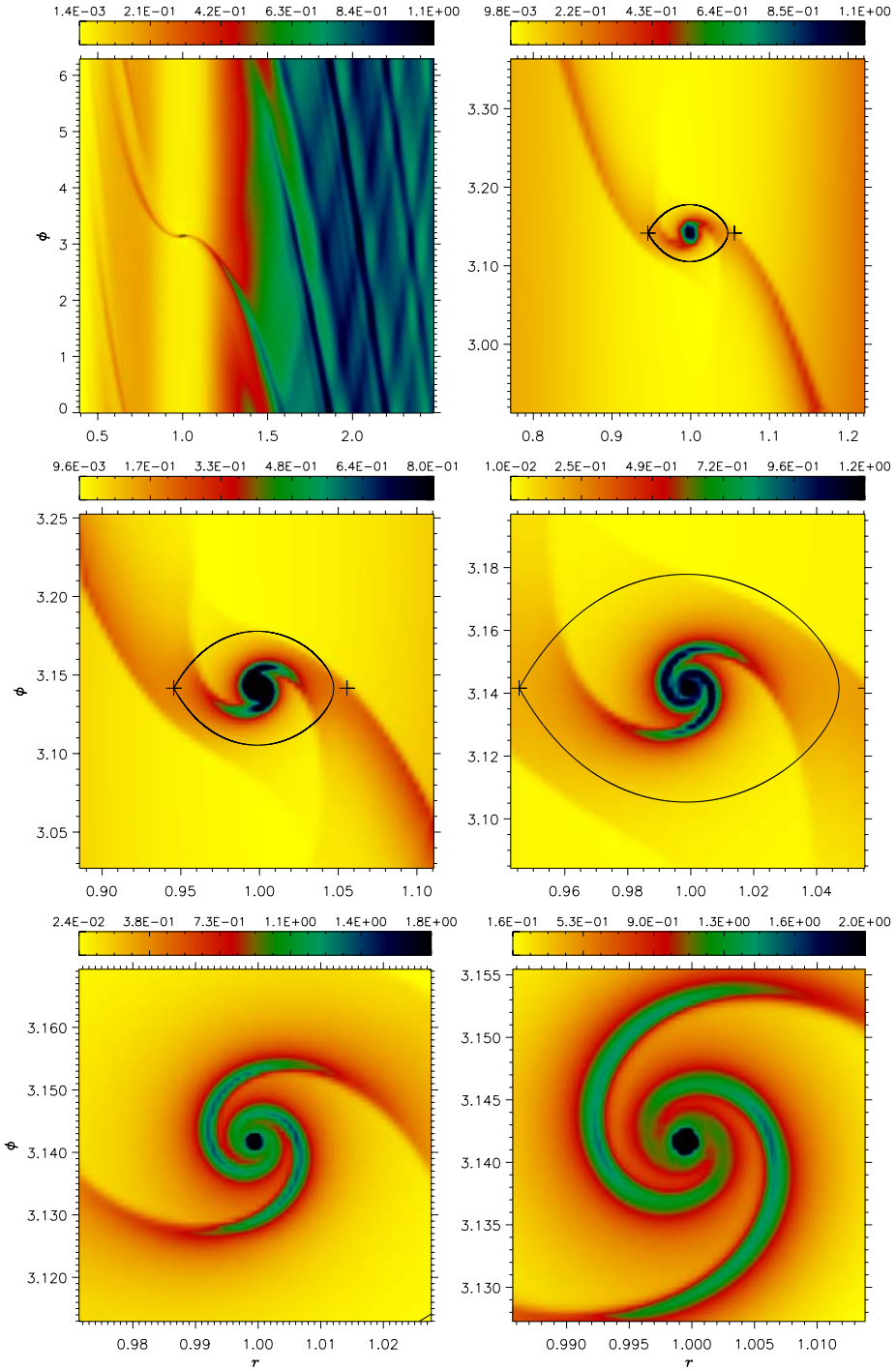

Figure 4.3: Overview of the surface density Σ on the six-grid system of model GINO3 ($M_{\rm p} = 0.5\ M_{\rm J}$), after 210 orbits. The top-left panel shows the main grid ($l = 1$) which encloses the whole simulated disk region. From left to right and top to bottom, the other panels zoom in onto the planet. The highest grid level lies over a surface, roughly $0.5 \times 0.5\ {R_{\rm H}}^2$, which comprises just four grid-cells on the main grid. The over-plotted curve represents the Roche lobe of the restricted three-body problem. Plus signs indicate the positions of L1 and L2 Lagrangian points, respectively on the left and the right of the planet.

Table 4.1: Model specific parameters: $q = M_{\rm p}/M_{\bigstar}$; ng is the number of grid levels; $\xi = \Delta r(ng)/R_{\rm H}$ is the normalized grid resolution on the finest level. Each model is let evolve, at least, till 200 orbits.

Model	q	ng	ξ	Notes
CIRO1	1.0×10^{-3}	5	1.3×10^{-2}	
CIRO2	1.0×10^{-4}	6	1.5×10^{-2}	
CIRO3	1.0×10^{-5}	7	1.6×10^{-2}	
PEPP1	3.0×10^{-6}	7	2.3×10^{-2}	
PEPP2	1.5×10^{-5}	7	1.4×10^{-2}	
PEPP3	3.0×10^{-5}	7	1.1×10^{-2}	
PEPP4	6.0×10^{-5}	7	8.6×10^{-3}	
WPRO1	1.0×10^{-4}	7	7.3×10^{-3}	
WPRO2	1.0×10^{-4}	6	1.5×10^{-2}	(a)
GINO1	1.0×10^{-5}	7	1.6×10^{-2}	(b)
GINO2	2.0×10^{-4}	6	1.2×10^{-2}	
GINO3	5.0×10^{-4}	6	8.5×10^{-3}	
ELEN1	1.0×10^{-3}	5	1.3×10^{-2}	(c)
ELEN2	1.0×10^{-3}	6	6.8×10^{-3}	
ELEN3	5.0×10^{-4}	6	8.5×10^{-3}	(d)

(a) Same as CIRO2, but $\kappa_{\rm ev} = 10$.
(b) Same as CIRO3, but the planet is symmetrically placed with respect to the grid cells.
(c) Same as CIRO1, but reflective boundary conditions are set at $r = r_{\rm in}$.
(d) Same as GINO3, but $\kappa_{\rm ac}$ is 40% smaller.

approximately at $r = 2$. In PEPP1 ($M_{\rm p} = 1\ M_{\jupiter}$), a similar feature spirals for almost $2\,\pi$, disappearing at $r = 1.5$. Although we did not investigate this issue any deeper, it may happen that results from local simulations could be influenced by not taking into account entirely such global features.

In Figure 4.5 the surface density is shown along with the velocity field for the three CIRO-models. As a reference, the Roche lobe (of the relative three-body problem) is over-plotted. From the upper row of this figure ($M_{\rm p} = 1\ M_{\saturn}$) we can see the patterns of the two main spirals (left panel). They reach the Roche lobe, but do not enter it. In fact, they are replaced by two streams of material which start from two points (located at $r = 0.94$, $\varphi = 3.12$ and $r = 1.07$, $\varphi = 3.07$, respectively), where the flow is nearly at rest with respect to the planet[1]. Each of them enters the Roche lobe, encircles the planet and hits the other one on the opposite side. As a result of the collision, the material is shocked and the flow is redirected towards the planet. Hence, these streams assume the form of two spirals, winding around the planet (right panel) for $2\,\pi$. That such smaller scale spirals

[1]They are designated as "X-points" by Lubow et al. (1999).

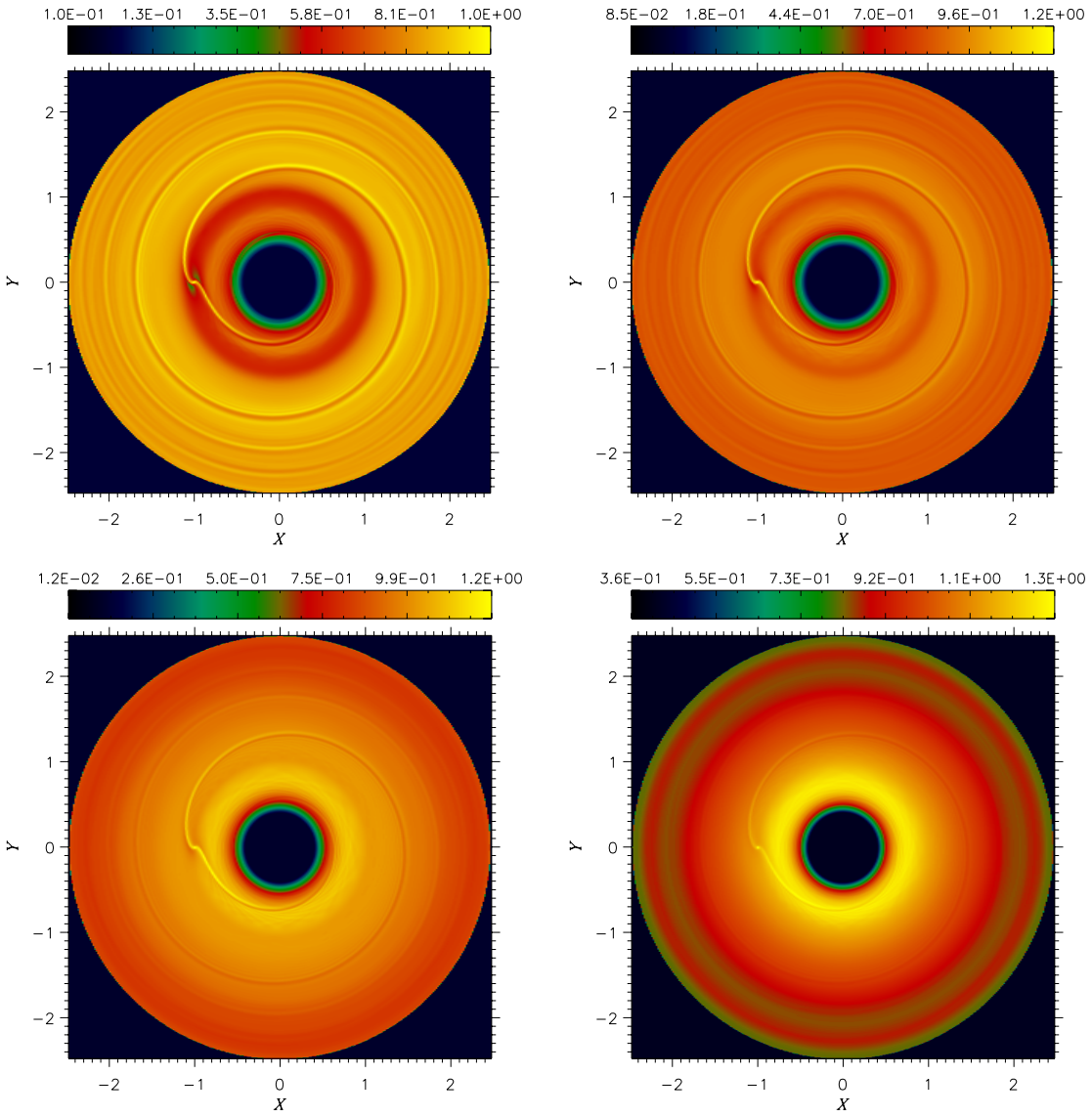

Figure 4.4: Global view of four simulated circumstellar disks in which intermediate-mass protoplanets are embedded: $M_{\rm p} = 20\ M_{\oplus}$ (**top left**), $M_{\rm p} = 10\ M_{\oplus}$ (**top right**), $M_{\rm p} = 3.3\ M_{\oplus}$ (**bottom left**), and $M_{\rm p} = 1\ M_{\oplus}$ (**bottom right**). These images show how the spiral perturbation fades as the perturbing mass of the planet is reduced. Although very weak, the spiral front winds for $2\,\pi$ even around a one Earth-mass planet.

are detached from the main ones can be inferred from the direction of the flow. Along the main spirals the material follows the disk rotation around the star, moving away from the planet. Along the small ones the gas orbits the planet. In fact, they represent the outstanding features of a *circumplanetary disk*. A more detailed description of the flow

regions around and inside the Roche lobe, concerning a Jupiter-mass planet, can be found in Lubow et al. (1999).

The case $M_{\rm p} = 33\ M_{\jupiter}$ (Fig. 4.5, middle row) has many analogies to the previous one. This planet is able to open a gap in the disk, as a permanent feature. However, it is neither so wide (the base width is 0.15 against 0.4) nor so deep (40% against 0.5% of the maximum surface density) as it is for a Jupiter-mass planet. The overall behavior of the matter entering the Roche lobe is very similar (left panel). The up-stream disk material, relative to the nearest X-point, reaches it, inverts partially the direction of its motion and flows into the Roche lobe. The gas stream penetrating from the left X-point turns about the planet, at $\varphi < \varphi_{\rm p}$, and collides with the stream incoming from the other X-point, generating the upper spiral arm (at $\varphi > \varphi_{\rm p}$). However, now the locations, from which these gas streams depart ($r = 0.97$, $\varphi = 3.14$ and $r = 1.03$, $\varphi = 3.135$, respectively), lie closer to the L1 and L2 points. The circumplanetary spirals are less twisted around the planet than before. They wrap around it for an angle π (right panel).

For the less massive planet, $M_{\rm p} = 3.3\ M_{\jupiter}$, the situation is somewhat different (bottom row of Fig. 4.5). In fact, within the Roche lobe, the signs of spiral fronts are very feeble, though some traces can still be seen. They assume the shape of a bar-like structure which extends, for $0.3\ R_{\rm H}$, from side to side of the planet at $\varphi \simeq \varphi_{\rm p}$. As indicated by the velocity field, the circumplanetary disk roughly occupies the entire Roche lobe (right panel).

Taking into account the other models as well, the following scenario can be proposed: the lower the value of q, the shorter and straighter the circumplanetary spirals become. For example, in model PEPP2, they track a tilde-like pattern, extending for a total length of $0.4\ R_{\rm H}$.

4.4.2 Density in the Planet's Environment

So far we have described qualitatively the main hydrodynamic structures which are present, near the planet, on the length scale of a Hill radius. We shall now discuss, more quantitatively, two aspects of the surface density, observable on shorter length scales ($\lesssim 0.5\ R_{\rm H}$). Both of them have repercussions on the torque exerted on the planet by the close-by matter, as explained later. First of all we should notice that $\Sigma(r,\varphi)$ is not perfectly symmetric with respect to the planet, in none of our reference models. Such property can be checked by means of an accurate examination of Figure 4.6. In this figure the contour lines of the surface density (i.e., lines on which Σ is constant) are plotted, for the finest grid levels $l = ng$. In case of CIRO1 (top-left panel, Fig. 4.6), one can see that the right-hand arm ($\varphi > \varphi_{\rm p}$) twists towards the planet more than the other one does. The curvature[2] ratio of the more external spiral parts (indicated by thick lines in the figure) is 0.9. Furthermore, the right-hand arm lies closer to the planet than the left-hand one, as can be evaluated from the positions of the arc centers (marked with plus signs). Contour line asymmetries are fainter in the case of CIRO2 (top-right panel, Fig. 4.6). However, a quantitative analysis shows that the external ridges of the spirals (thick lines) have slightly different curvatures. Moreover, their centers (plus signs) are not aligned with the planet position (represented by a big dot). In particular, if we consider the contours between 1.03 and 2.02 (arbitrary

[2]The curvature of a circle of radius R is $1/R$.

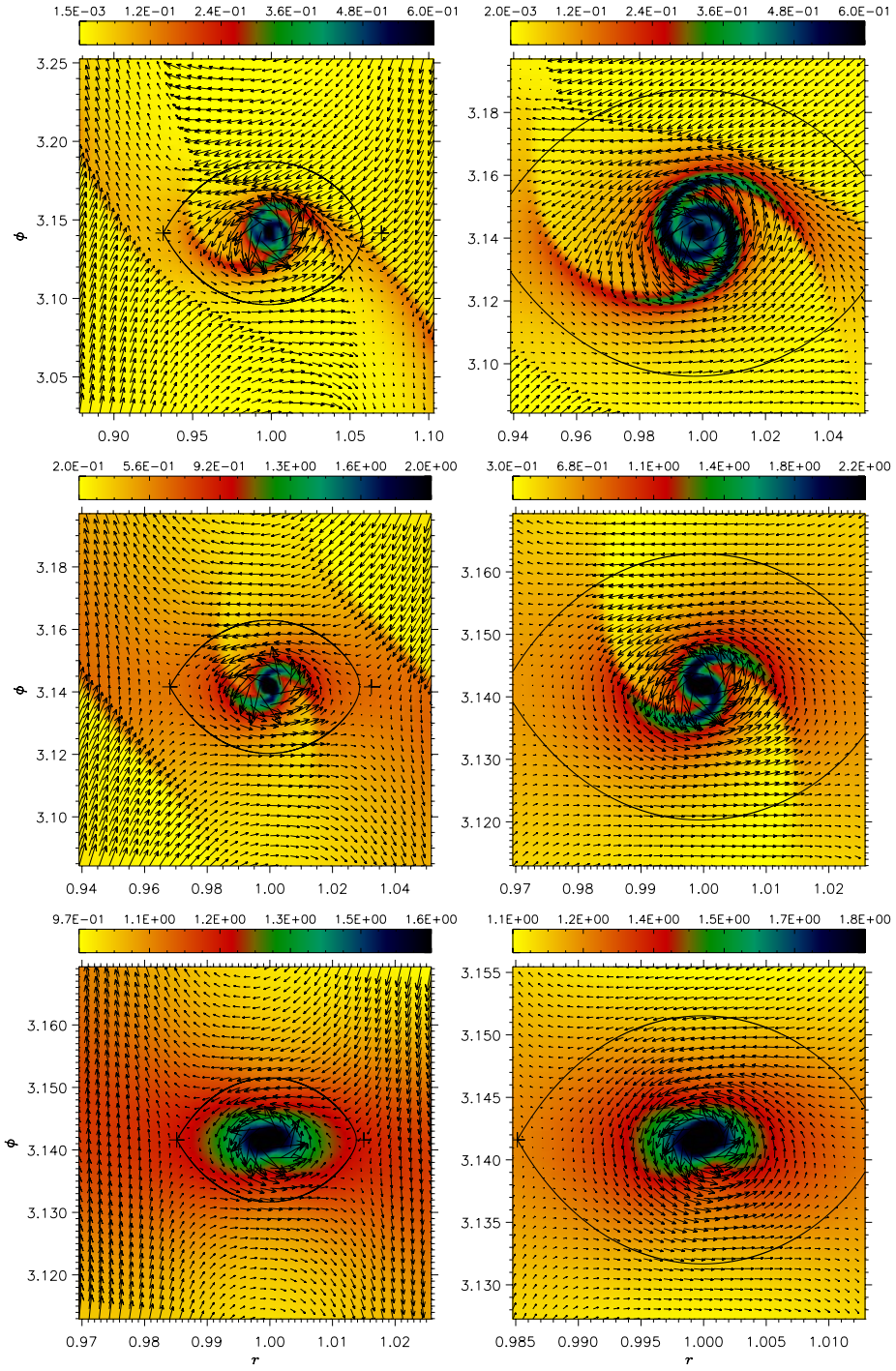

Figure 4.5: Surface density and velocity field for three selected models. **Top row**. CIRO1: grid level $l = 3$ (left panel) and $l = 4$ (right panel) at $t = 375$ orbits. **Middle row**. CIRO2: grid level $l = 4$ (left panel) and $l = 5$ (right panel) at $t = 325$ orbits. **Bottom row**. CIRO3: grid level $l = 5$ (left panel) and $l = 6$ (right panel) at $t = 225$ orbits. To avoid too much confusion, only 40% of the velocity field vectors are drawn. The over-plotted curve and plus signs have the same meaning as in Figure 4.3. Close to the planet, the velocity field is roughly Keplerian (see § 4.4.7).

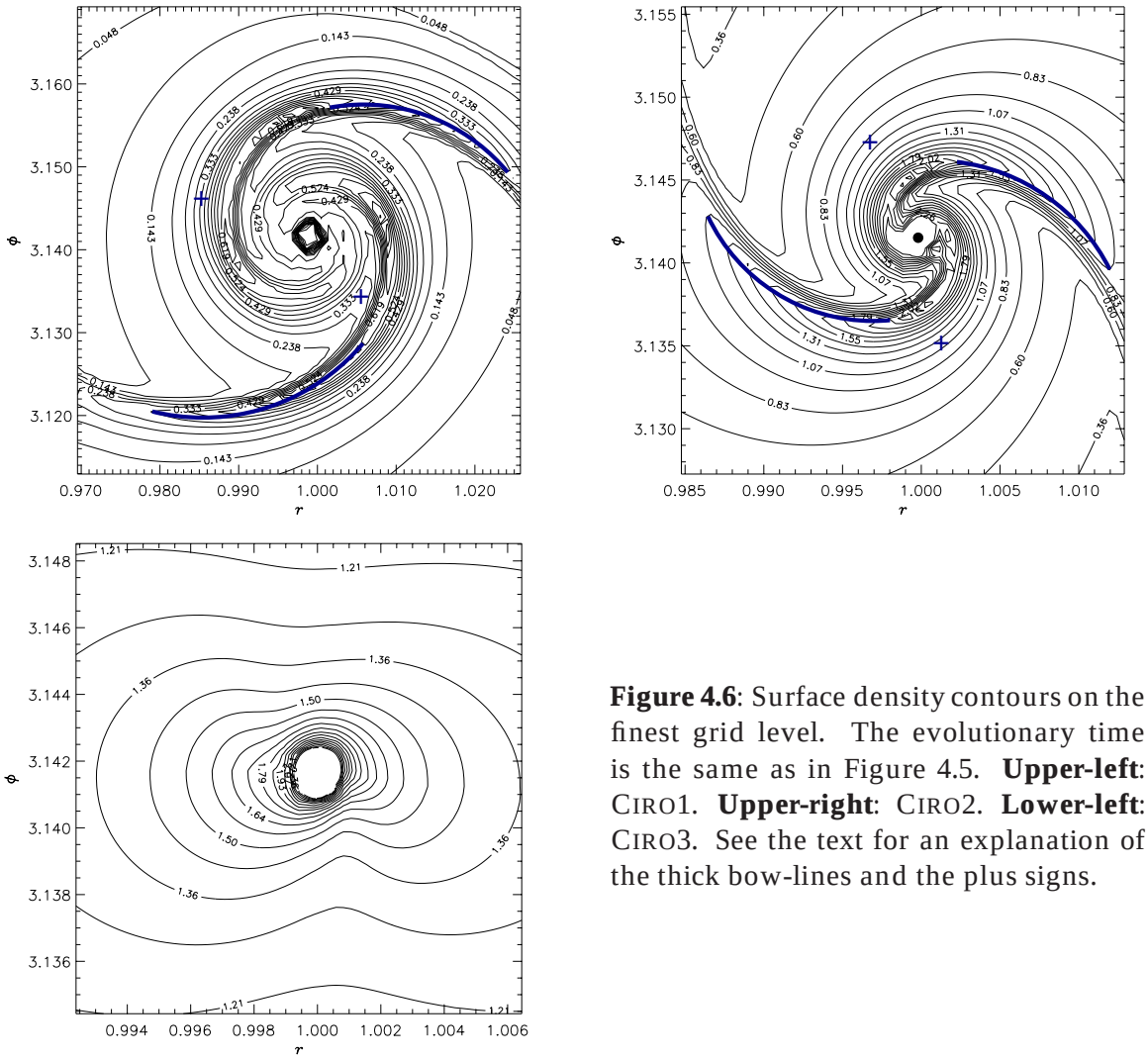

Figure 4.6: Surface density contours on the finest grid level. The evolutionary time is the same as in Figure 4.5. **Upper-left**: CIRO1. **Upper-right**: CIRO2. **Lower-left**: CIRO3. See the text for an explanation of the thick bow-lines and the plus signs.

units), the right-hand ridge is a little straighter than the left-hand one. In fact, the ratio between their curvatures is 0.93. Also in this case, the arc centers indicate that external parts of the right-hand arm are a little nearer to the planet than those of the left-hand arm. Indeed, surface density asymmetry is evident, in the case of CIRO3 (bottom-left panel, Figure 4.6). At $r \simeq 1.001$ and $\varphi < \varphi_{\rm p}$, the density is systematically lower than it is on the opposite side ($r \simeq 0.999$, $\varphi > \varphi_{\rm p}$). Following the shape of density contours, it is possible to track what remains of the spiral arms. The pre-shock material conveys the more convex form to these lines, at $r \simeq 0.999$ and $r \simeq 1.001$

4.4.3 Spiral Pattern

From the analytical point of view, a spiral arc is a polar function of the type $\Theta = \Theta(\varrho)$, where ϱ is the polar distance and Θ the polar angle. A spiral can be generally defined

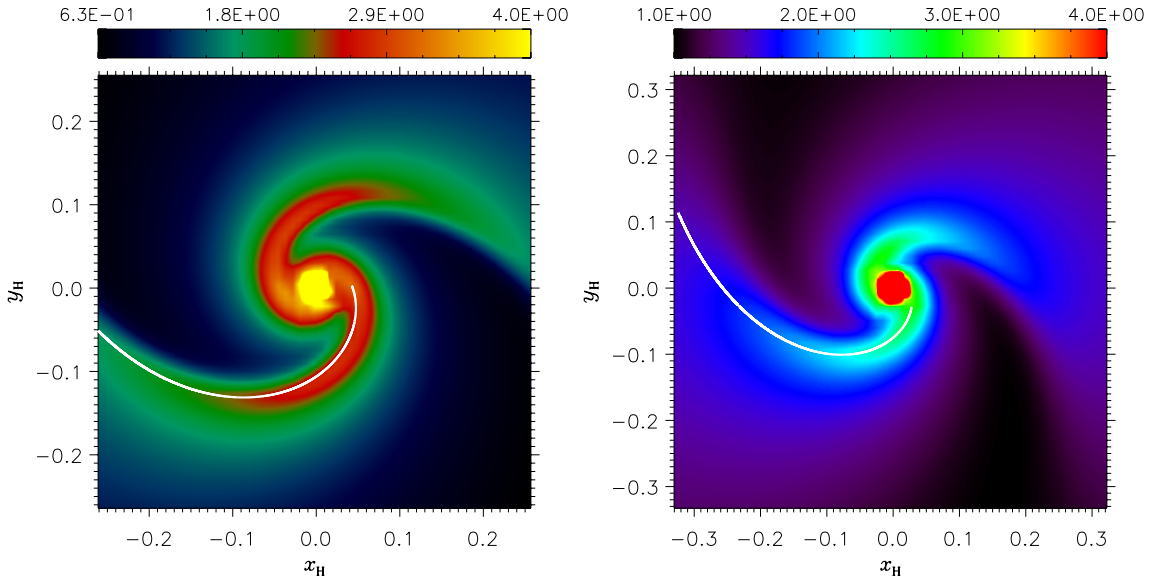

Figure 4.7: Analytical approximation of the spiral pattern observed in the circumplanetary disks. **Left panel**. Disk around a 20 $M_{\oplus}$ planet. **Right panel**. Disk around a 10 $M_{\oplus}$ planet. The white line is given by equation (4.17). The correction factor ς in both cases is very close to unity.

through its *opening angle* $\Upsilon(\varrho)$:

$$\frac{\mathrm{d}\Theta}{\mathrm{d}\varrho} = \tan\Upsilon(\varrho). \tag{4.16}$$

When displayed in a Cartesian x–y plane, the opening angle $\Upsilon(\varrho)$ represents the angle between the tangent to the curve and the polar distance ϱ.

Spiral shaped wave fronts are rather common in the astronomy context. Among the most striking examples of spiral features are the arms of a certain type of galaxies. On smaller scale, spiral waves are also induced within protostellar disks. The opening angle, as defined above, is approximately given by $\arctan\mathcal{M}$, where $\mathcal{M}$ is the local Mach number (Godon et al. 1998). Within a circumplanetary disk, very similar features are observed, as proved by Figure 4.5. Indeed, also the nature must be alike since, for a wide range of planetary masses,the ridges of the spirals are well reproduced by the following polar curve:

$$\Theta - \Theta_0 = 2\,k\left(\sqrt{\frac{r_\mathrm{p}}{\varrho_0}} - \sqrt{\frac{r_\mathrm{p}}{\varrho}}\right), \tag{4.17}$$

where $k = \varsigma\sqrt{M_p/M_*}/h$. The quantity $k\sqrt{r_\mathrm{p}/\varrho}$ represents the Mach number of the circumplanetary flow. The factor ς is a correction due to the fact that the flow regime around the protoplanet is slightly sub-Keplerian (see § 4.4.7). Figure 4.7 demonstrates how equation (4.17) fits to the spiral perturbation around intermediate-mass planets.

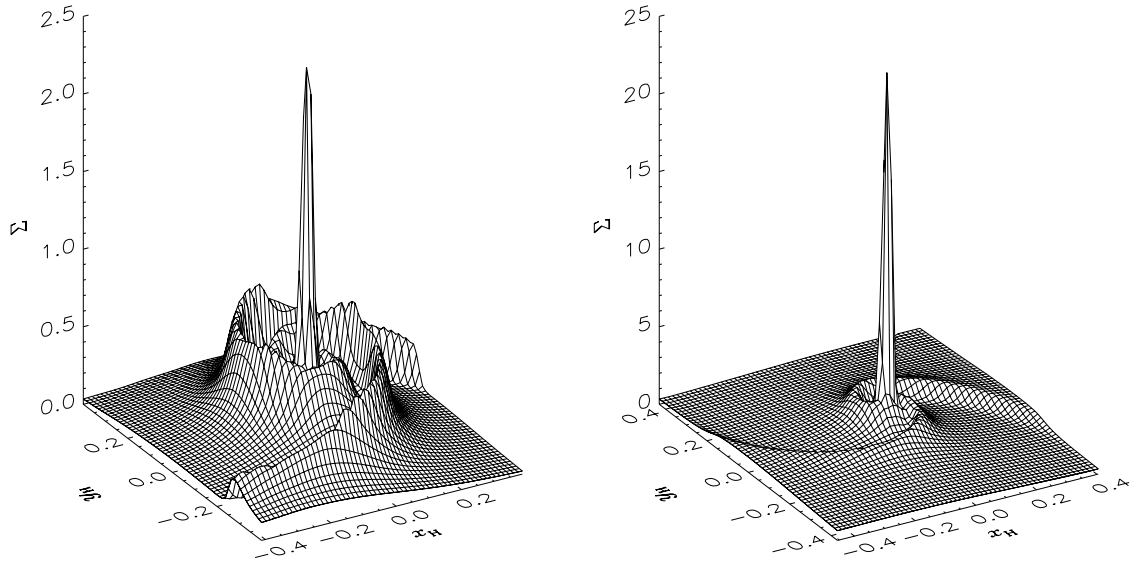

Figure 4.8: Surface density plot of the highest grid level. **Left**: CIRO1 at $t = 375$ orbits. **Right**: CIRO2 at $t = 325$ orbits. The Hill coordinates, $(x_{\rm H}, y_{\rm H})$, are so defined: $x_{\rm H} = [r_{\rm p}\,\cos(\varphi_{\rm p}) - r\,\cos(\varphi)]/R_{\rm H}$, $y_{\rm H} = [r_{\rm p}\,\sin(\varphi_{\rm p}) - r\,\sin(\varphi)]/R_{\rm H}$. The star is situated along the negative $x_{\rm H}$-axis. The azimuth φ increases with $y_{\rm H}$.

4.4.4 The Core

Finally, we would like to mention what happens, in our models, at very short distances from the planet. We described, in § 4.3.2, how material is removed from the neighborhood of the planet. This is usually a small fraction of the available matter, during each integration time step of the main grid. If $\Delta M^{\rm ev}$ is the evacuated amount of mass, then typically

$$\frac{\Delta M_{\rm ev}}{M} \approx \frac{\Delta\Sigma}{\Sigma} \approx 10^{-2}$$

(see the caption of Fig. 4.1). This choice accounts for the fact that a planet should not be able to accept, very rapidly, all the material the surrounding environment can offer (Wuchterl 1993).

Since not all of the matter is taken away, it should pile up at the location of the planet, eventually forming a very dense core. Indeed, this is what we find, as already visible in Figure 4.6, where density contour lines crowd around the planet at $(r_{\rm p}, \varphi_{\rm p})$. Figure 4.8 displays better how this feature looks like for models CIRO1 and CIRO2. In order to make a comparison of the linear extension of such cores with the Hill radius, we introduce the *Hill coordinates*. These are defined as a Cartesian reference frame with origin on the planet and coordinates normalized to $R_{\rm H}$ (see the caption of Fig. 4.8 for details). In these two cases, the core width, $2\,\eta$ (exactly defined below), can be estimated to be approximatively $0.1\ R_{\rm H}$.

One reason for the sharpness of these peaks is the very small length scale we adopt

to smooth the potential of the planet (§ 4.3.1). On the finest grid level the smoothing length δ is equal to $\lambda(ng) \simeq 1.4\,\Delta r(ng)$ (see eq. [4.15]). From Table 4.1 one can deduce that $\delta \sim 10^{-2}\ R_{\rm H}$ (though it changes a little for the different values of q). Despite that, the core width always equals at least $6\,\Delta r(ng)$. Other two hints suggest that such features are not just a numeric product. According to models CIRO2 and WPRO1 (which differ only in the number of grid levels), the core width is very similar. If we cut the peak at $\Sigma = 2$ on the finest level of each model, its extent, at $r = r_{\rm p}$, is 6 and 11 grid cells, respectively. Models CIRO1 and ELEN2 agree in a very similar way. Furthermore, the structure of these peaks does not depend on the exact placement of the planet within a grid cell, as models CIRO3 and GINO1 prove. Since the amount of core material may be related to the accretion process, the parameters $\kappa_{\rm ev}$ and $\kappa_{\rm ac}$ are likely to modify the local density. The core widths (as introduced before) of models CIRO2 and WPRO2 differ by about 20% while the difference is somewhat less in case of GINO3 and ELEN3.

However, in order to study the exact properties of such features a more detailed physical treatment is required in proximity of the planet. This may be part of future computations which include a more detailed treatment of the internal constitution of the protoplanet. Anyway, properties such as the local surface density profile and the velocity field indicate that the core structure could be approximated to that of a rotating and isothermal gas, in hydrostatic equilibrium. In model PEPP1 ($1\ M_{\odot}^{\pm}$), the rotation of the core is very slow. Hence, its density profile can be well reproduced by that of an isothermal and hydrostatic gas, as demonstrated in Figure 4.9, where we compare the numerical results (crosses) with an analytic solution for a hydrostatic isothermal core (solid line).

As pointed out, the material within the core region is strongly coupled to the planet, due to the small distances. In some way, it may be considered as part of the protoplanet itself, whose structure we may not resolve well enough in the present paper. Whatever its nature, it is very likely that the angular momentum transferred, by the core material to the planet, may influence the planet's spin angular momentum rather than its orbital one. As we are treating the planet as a point mass we cannot estimate its spin. Therefore we decided to exclude this region from the torque computation. To do that, we need a quantitative estimate of the core radius η, for every model in Table 4.1. We adopt the following procedure: the average density $\bar{\Sigma}$ is computed over the region $0.2\ R_{\rm H} \leq |\boldsymbol{r} - \boldsymbol{r}_{\rm p}| \leq 0.5\ R_{\rm H}$. Then we define the core width ($2\,\eta$) to be that where $\Sigma = 2\,\bar{\Sigma}$. In Figure 4.10 (left panel) the dependence of $2\,\eta$ versus q is displayed. The ratio $\eta/R_{\rm H}$ decreases for increasing values of q. However, between 3.3 and 33 $M_{\odot}^{\pm}$, it seems to vary very little. Our measure of the core sizes is performed at a particular time (for CIRO-models, they are indicated in Figure 4.5). Anyway, such estimates are not affected much by this choice because the cores reach a steady state, early during the system evolution. As an example, Figure 4.10 (right panel) shows how the core mass $M(\eta)$ assumes a static value very soon.

As already mentioned, the spiral features vanish for low values of q, and for Earth-mass planets the core becomes the most prominent feature within the Roche lobe.

4.4.5 Torque Exerted on the Planet

Any protoplanet embedded in a protostellar environment suffers gravitational torques, exerted by the surrounding disk material. If the density distribution were symmetric with

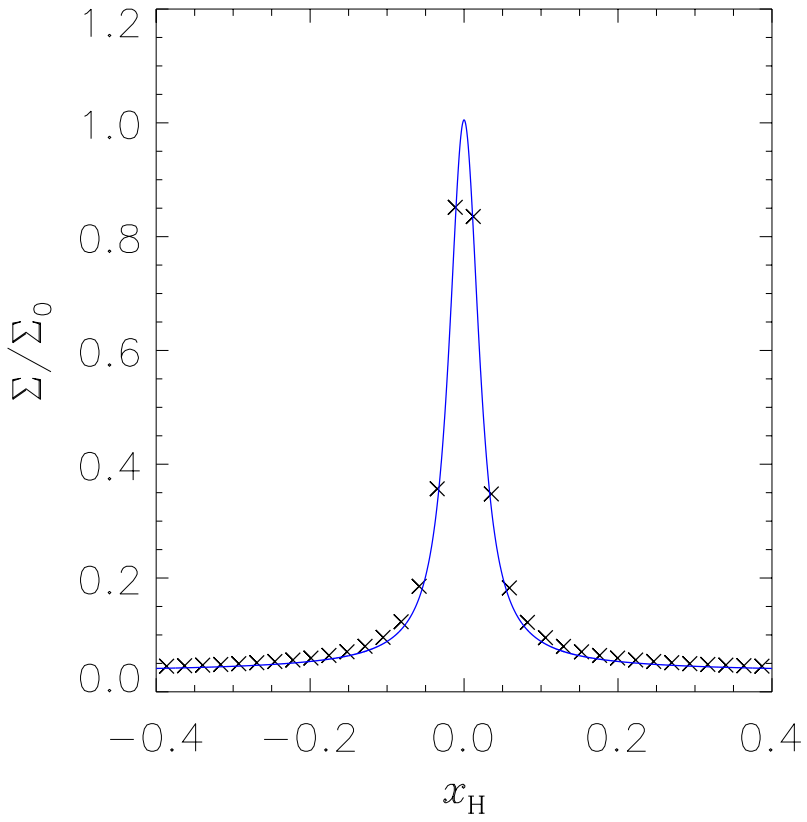

Figure 4.9: The core width is generally much larger than that proper for an isothermal, hydrostatic, configuration. In fact the centrifugal force, due to axial rotation of the gas around the planet, may play an important role in supporting the structure. This is not the case for the core around an Earth-mass planet (model PEPP1). Thus, the structure equation reads: $\mathrm{d}\,\Phi_{\rm p} = -c_{\rm s}^2\,\mathrm{d}\,\Sigma/\Sigma$, where $\Phi_{\rm p}$ is the smoothed potential of the planet. The constancy of the sound speed ($c_{\rm s} = h\,\sqrt{G\,M_\star/a}$) implies that the gas is isothermal. In the figure, the surface density of PEPP1, at $\varphi = \varphi_{\rm p}$ ($y_{\rm H} = 0$), is represented by "$\times$" signs. The over-plotted curve is the solution of the previous structure equation. Clearly, the peak density Σ_0 is somehow connected to the accretion procedure.

respect to the planet, or with respect to the line connecting the star with the planet, the resultant total torque would be zero. However, we have just seen that this is not the case, and even around a planet as small as $3.3\ M_{\oplus}$, the matter distribution is not axially symmetric. Thus, we expect a non-zero total torque from the disk, acting on the planet. In response to it, because of the conservation of the orbital angular momentum, the planet has to adjust its semi-major axis, which leads to a migration phenomenon.

In the present computations, we evaluate the torque exerted on the planet in a straightforward way. First the gravitational force acting on the planet $\boldsymbol{f_g}(i,j)$, due to each grid cell

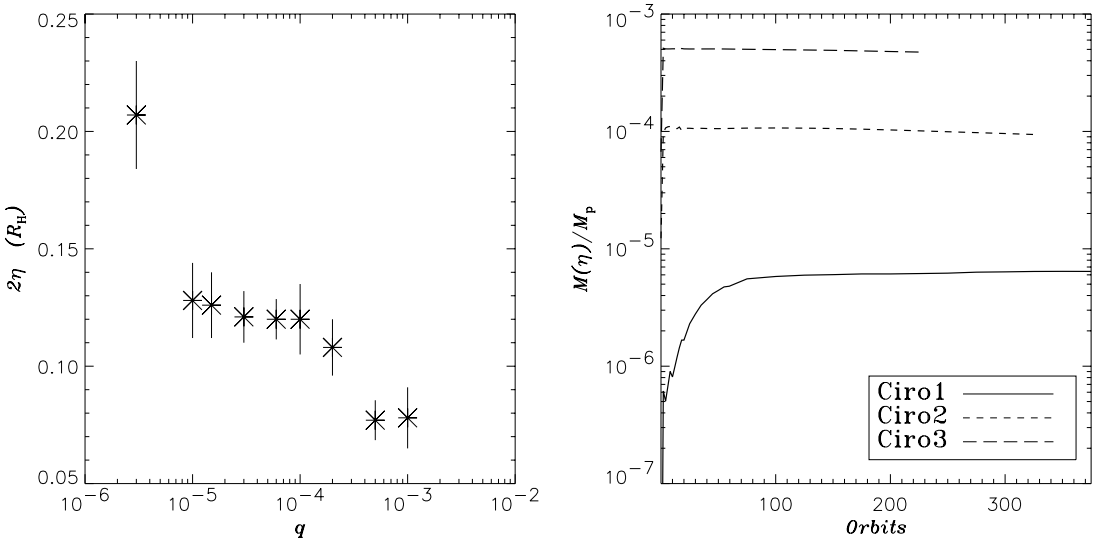

Figure 4.10: **Left panel**. Core width, $2\,\eta$, in units of the Hill radius as a function of the mass ratio q. CIRO and PEPP-models are considered along with GINO2 and GINO3. The measure errors are assumed to be equal to ξ (see Table 4.1). **Right panel**. Mass within a distance η from the planet versus time. The core mass $M(\eta)$ is normalized to the mass of the planet.

(i, j), is calculated. The torque, with respect to the star, is then

$$\boldsymbol{t}(i,j) = \boldsymbol{r}_{\rm p} \times \boldsymbol{f_g}(i,j). \tag{4.18}$$

Since we are interested in the z-component of this vector, we perform the scalar product $\hat{\boldsymbol{z}} \cdot \boldsymbol{t}(i,j) = t_z(i,j)$, where $\hat{\boldsymbol{z}}$ is the unit vector of the vertical direction. Finally, by summing over all i and j, we obtain the total disk torque $\mathcal{T}_{\rm D}$, whereas the simple contraction over the azimuthal index j gives the radial distribution of the torque.

The quantity $t_z(i,j)$ is computed on each grid level. Where the computational domain is covered by more than one level, the torque $t_z(i,j)$ on the finest grid is considered for the evaluation of $\mathcal{T}_{\rm D}$. We don't work with time averaged torques because they were checked not to vary considerably with time during the last 100 orbits of the computation. Thereupon we use their values at the end of the simulations.

In order to avoid the region dominated by the core, we exclude a certain area from the computation of $\mathcal{T}_{\rm D}$. Because of the way we defined the core radius η, some core material may still lie outside $|\boldsymbol{r} - \boldsymbol{r}_{\rm p}| = \eta$. Therefore, for safety reasons, we choose not to take into account the planet neighborhood defined by $|\boldsymbol{r} - \boldsymbol{r}_{\rm p}| \leq \beta = 2\,\eta$. The only level, upon which this operation is relevant, is the highest since it provides the gravitational torque form the regions closest to the planet. On coarser levels such operation is meaningless since inner torques are taken from elsewhere. But it can be useful to confer a more regular look to the radial torque profile. We generally adopt the value $\beta = 5\,\delta(l)$ for $l < ng$.

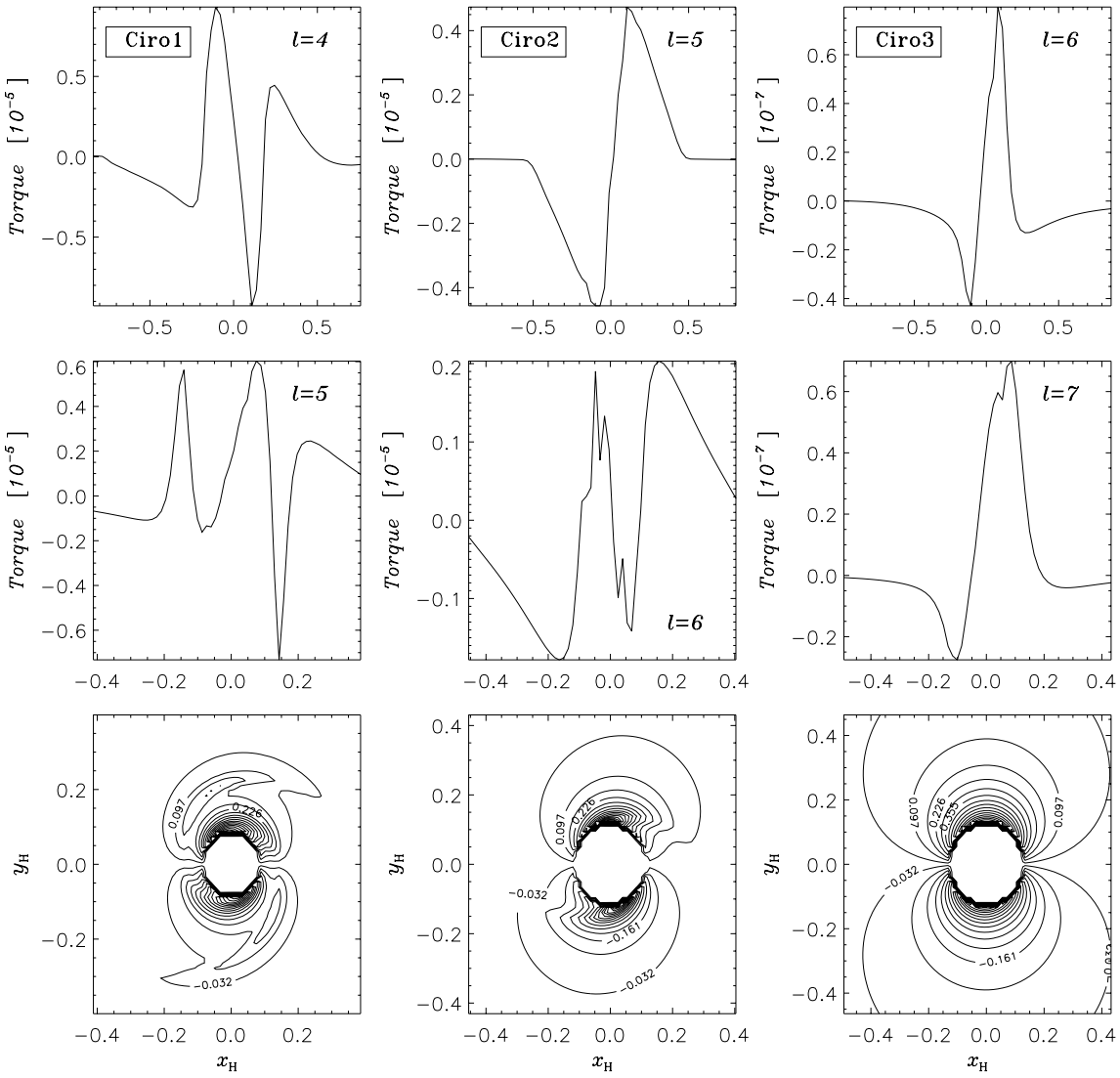

Figure 4.11: Radial distribution and two-dimensional contour map of the gravitational torque exerted by the disk on the planet. **Left panels**. CIRO1: levels $l = 4$ and $l = 5$. **Center panels**. CIRO2: levels $l = 5$ and $l = 6$. **Right panels**. CIRO3: levels $l = 6$ and $l = 7$. The two-dimensional torque distribution (bottom panels) is reported for the finest grid level and is normalized to its maximum, absolute, value.

However, as this might be somewhat arbitrary, we discuss in a separate section how the choice of β, on the finest level, affects the value of the total torque $\mathcal{T}_{\rm D}$.

Because of the global angular momentum transfer, the disk material (orbiting the star), at $r > r_{\rm p}$, exerts a negative torque on the planet whereas the inside-orbit gas tends to increase its angular momentum. This tendency changes, as material closer to the planet is

accounted for, and it may reverse eventually, once in the circumplanetary disk (for $M_{\rm p} = 1\,M_{\earth}$, such behavior was also found by Lubow et al. 1999). The radial torque distribution, from CIRO-models, is shown in Figure 4.11. The two sets of profiles belong to the grid levels $l = ng - 1$ (top row) and $l = ng$ (middle row). In the case of CIRO1 (top row, left panel), the sign reversal of the torque is not completed yet. However some negative torques are exerted from regions inside the planet orbit and some positive torques are exerted from the opposite side. On the domain covered by this grid (fourth level), the torque contribution coming from $x_{\rm H} < 0$ is positive while the one coming from $x_{\rm H} > 0$ is negative. The resulting net torque is positive, as the magnitude of the latter contribution is 2.4 times smaller than that of the former. The torque behavior gets more complex if we restrict to a region closer to the planet (middle row, left panel). Though not evident at a first glance, the signs are reversed if compared to the preceding grid level. The torque exerted by the region $x_{\rm H} > 0$ is definitely positive and, in magnitude, almost 30 times as large as that arising from the region $x_{\rm H} < 0$. Thus, this region exerts a strong, positive, net torque. Indeed, the phenomenon of the torque sign reversal is clear in the case of CIRO2 and CIRO3 (Fig. 4.11, center and right panels). For both grid levels, inside-orbit material lowers the angular momentum of the planet while outside-orbit material acts in the opposite direction. On the finest level of CIRO2, the ratio of the negative to the positive torque contribution is just 0.96 (in absolute value), whereas it is 0.3 for CIRO3.

In order to check which is the overwhelming contribution, between positive and negative torques, on the various grid levels, we can define the partial torque $\mathcal{T}(l)$. This represents the total torque computed over the entire domain but the part covered by the grid level $l + 1$ and such that $\mathcal{T}(ng) = \mathcal{T}_{\rm D}$. Figure 4.12 illustrates the sign of the partial torque and its relative strength, on each grid level, for CIRO-models. We can see that the total torque is negative in all of the three models. In CIRO1 and CIRO2 all levels, but the highest, contribute to lower the planet angular momentum. On the contrary, the matter inside the finest level raises the overall torque (of a fair amount in case of CIRO1). In CIRO3, a positive torque is exerted by the material outside a region, around the planet, with a linear extension $\sim 2\,h\,r_{\rm p}$. Instead, levels 3, 4, 5, and 6 provide negative torques, which are then weakened considerably by the positive torque coming from the finest level.

An overview of the torques exerted by different portions of the disk, for all the relevant models, is given in Table 4.2. First of all we notice that, within $0.5\,R_{\rm H}$, the phenomenon of the sign reversal is observed in all of the models, but PEPP1 and GINO2. Anyway, in the latter case, the torque inside this region is positive.

In CIRO-models and in model GINO3, the reversal of the sign is such to produce a positive torque over the domain $|\boldsymbol{r} - \boldsymbol{r}_{\rm p}| < 0.5\,R_{\rm H}$. This is because the surface density of the leading material is slightly higher than that of the trailing matter (§ 4.4.1 and Fig. 4.3). In contrast, the torque is negative in case of PEPP2, PEPP3, and PEPP4. We note, however, that the positive torques exerted by the outside-orbit material, within this region, strongly attenuate the magnitude of the negative net torque exerted by the rest of the disk.

Clearly, since neighboring material may tend to reduce the magnitude of negative torques acting on the planet, it could either slow down its inward migration or reverse the direction of its motion.

As anticipated, the sign reversal of the radial torque distribution is not observed in

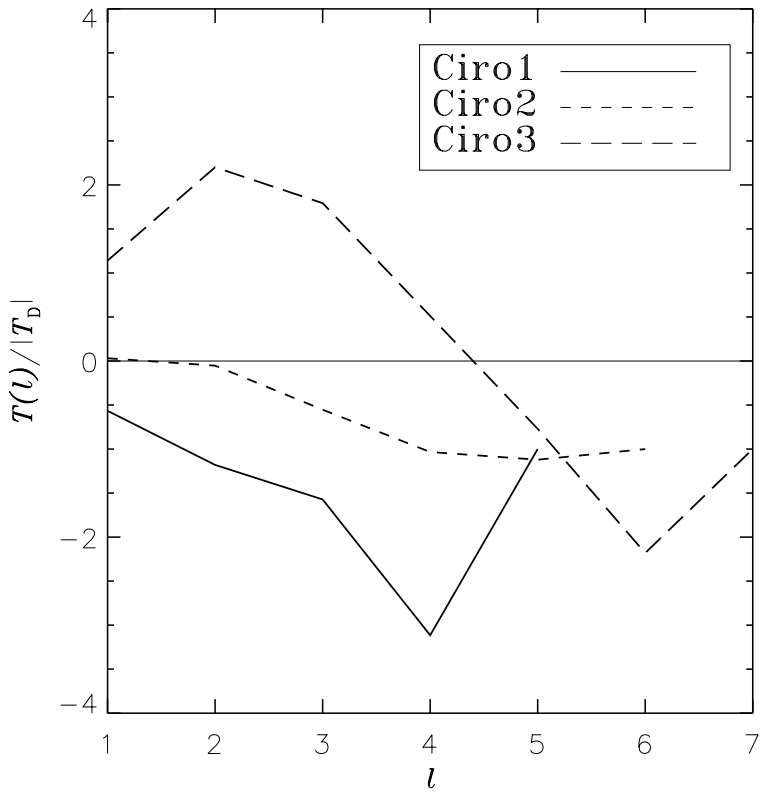

Figure 4.12: Partial torque $\mathcal{T}(l)$, normalized to $|\mathcal{T}_{\rm D}|$, plotted against the grid level l for: CIRO1, CIRO2, and CIRO3. $\mathcal{T}(ng)/|\mathcal{T}_{\rm D}| = -1$ because, by definition, $\mathcal{T}(ng) = \mathcal{T}_{\rm D}$ and $\mathcal{T}_{\rm D}$ is negative for these models.

model PEPP1 ($M_{\rm p} = 1\ M_{\oplus}$). Due to the very low mass of the perturber, the only structure present inside the Roche lobe is the density core. Whatever level is considered, the inside-orbit gas always provides positive torques while negative ones come from the outside (see also Table 4.2). Negative torques are somewhat stronger, on any grid level. Almost the 50% of the total torque is generated between $\sim 0.5\,h\,r_{\rm p}$ and $\sim h\,r_{\rm p}$, at the starting positions the disk spirals.

2D-Torque Distribution

The detailed balance of the torques, arising from very close material, depends on the medium and small-scale density structures around the planet, such as the shape of spirals. Therefore, referring to what was stated in the previous section, we can deduce that the radial torque asymmetry is a direct consequence of the asymmetric distribution of the gas with respect to the planet.

Table 4.2: Gravitational torque exerted on the planet arising from different disk regions, for the relevant models of Table 4.1. The entire domain is divided into three region: outside the Hill circle; inside the circle of radius $R_{\rm H}/2$ and the zone in between. Then they are divided further in order to distinguish between inside-orbit (*in*) and outside-orbit (*out*) contribution. The torque is computed over each of these regions, by employing $\beta = 2\,\eta$ and according to the value of the normalized distance from the planet $d = |\boldsymbol{r} - \boldsymbol{r}_{\rm p}|/R_{\rm H}$. Torques are normalized to $|\mathcal{T}_{\rm D}|$.

Model	$d \leq 0.5$		$0.5 < d < 1$		$d \geq 1$	
	in	*out*	*in*	*out*	*in*	*out*
CIRO1	-0.03	2.08	-1.18	-0.43	0.53	-1.97
CIRO2	-3.07	3.23	-1.06	0.94	2.04	-3.08
CIRO3	-1.93	3.13	-0.49	-0.97	7.26	-8.00
PEPP1	0.33	-0.40	0.33	-0.36	4.22	-5.12
PEPP2	-2.32	2.05	-0.18	-0.18	1.91	-2.28
PEPP3	-2.61	2.07	-0.16	-0.01	0.85	-1.14
PEPP4	-3.01	2.41	-0.29	0.25	0.84	-1.20
GINO2	2.47	-1.65	-1.44	1.02	2.56	-3.96
GINO3	-1.54	5.12	-2.06	-0.34	1.90	-4.08

Thus, a more comprehensive description of the torque behavior requires its full two-dimensional distribution. In the bottom panels of Figure 4.11, the contour lines of the two-dimensional torque, t_z, are shown for each reference model. The interesting point to notice here is that the largest magnitude torques arise from the corotation locations, i.e. where $r = r_{\rm p}$ ($x_{\rm H} \simeq 0$). Here in fact, $\boldsymbol{f_g}(i,j)$ is perpendicular to $\boldsymbol{r}_{\rm p}$ and the cross-product in equation (4.18) achieves its maximum (minimum). The material leading the planet (at $\varphi > \varphi_{\rm p}$ or $y_{\rm H} > 0$), pulls it ahead and makes it gain angular momentum. The trailing material brakes the planet making it lose angular momentum.

Let's consider two fluid elements at $(0, \pm\, y_{\rm H})$ and write their mass density as $\Sigma^{\pm}$. Then we can write $|t_z^{\pm}| \propto r_{\rm p}\,\Sigma^{\pm}/y_{\rm H}^2$, which yields:

$$|t_z^+| - |t_z^-| \propto r_{\rm p}\,\frac{\Delta\Sigma}{y_{\rm H}^2}, \tag{4.19}$$

where $\Delta\Sigma = \Sigma^+ - \Sigma^-$. Any mismatch of the surface density, $\Delta\Sigma$, causes a torque mismatch amplified by an amount equal to $y_{\rm H}^{-2}$. It's worth noticing that, on larger distances $|\boldsymbol{r} - \boldsymbol{r}_{\rm p}| \sim r_{\rm p}$, the torque mismatch is amplified less, in fact:

$$|t_z^+| - |t_z^-| \propto \frac{\Delta\Sigma}{r_{\rm p}}. \tag{4.20}$$

This is the reason why surface density asymmetries near the planet have a very strong impact on $\mathcal{T}_{\rm D}$, and they can easily prevail against the more distant ones.

The region responsible for the maxima and minima of the radial torque distributions in the middle row of Figure 4.11 can be identified by means of the 2D-torque maps. For

example, in the case of CIRO1, we see that the maximum at $x_{\rm H} = -0.15$ and the minimum at $x_{\rm H} \simeq 0.15$ are produced at $y_{\rm H} \simeq 0.1$ and $y_{\rm H} \simeq -0.1$, respectively. In the other two cases, radial distribution extremes rise from regions where the torque function t_z is steeper than it is on the opposite side of the planet.

4.4.6 Planet Migration

If we consider a planet moving on a circular orbit, we find that the rate of change of its orbital distance a, caused by an external torque $\mathcal{T}_{\rm D}$, is

$$\frac{{\rm d}a}{{\rm d}t} = \frac{2\,\mathcal{T}_{\rm D}}{M_{\rm p}\,a\,\Omega_{\rm p}}. \tag{4.21}$$

Analytical estimates of $\mathcal{T}_{\rm D}$ show that two limiting cases exist, depending on whether the planet is massive enough to generate a gap or not. In the first case of small planetary masses, we have the so-called *type I* migration. Ward (1997) derived the following expression:

$$\left(\frac{{\rm d}a}{{\rm d}t}\right)_{\rm I} \simeq -\frac{1}{2}\,q\;h^{-3}\,a\,\Omega_{\rm p}\left(\frac{\pi\,a^2\,\Sigma}{M_\star}\right). \tag{4.22}$$

The direction of the migration is inwards because of the dominating role of the outer Lindblad resonances[3] Ward (1986, 1997). In the second case the planet is more massive, opens up a gap, and the evolution is *locked* to that of the disk. As a general trend, the disk material drifts inwards on the viscous time scale, and so does the planet. It follows that

$$\left(\frac{{\rm d}a}{{\rm d}t}\right)_{\rm II} = -\frac{3\,\nu}{2\,a} = -\frac{3}{2}\,\alpha\,h^2\,a\;\Omega_{\rm p}, \tag{4.23}$$

which is known as *type II* migration. Comparing equation (4.22) with equation (4.23), it turns out that type I drift is faster than type II (i.e., faster than viscous diffusivity) whenever

$$q \gtrsim 3\,\alpha\,h^5\left(\frac{M_\star}{\pi\,a^2\,\Sigma}\right). \tag{4.24}$$

The parameter values employed here[4] yield a right-hand side equal to 2.8×10^{-6}, which is just a bit smaller than an Earth-mass ($0.93\;M_{\oplus}$). Fast type I migration should continue till the planet grows enough to impose a gap on the disk. By that time, however, it could have already impacted the parent star. Once entered this fast drifting regime, it seems that the planet may survive only if the growth time scale $\tau_{\rm G} \equiv M_{\rm p}/\dot{M}_{\rm p}$ is much smaller than the migration time scale $\tau_{\rm M} \equiv a/|\dot{a}|$.

In Figure 4.13 the migration time scale $\tau_{\rm M}$ is shown for the main models listed in Table 4.1. The drifting motion is directed inwards in all cases. The lowest migration velocity belongs to the Earth-mass planet (PEPP1). The second lowest drifting velocity is that

[3] This is true as long as the temperature gradient within the disk is negative (Ward 1986).

[4] If we take into account the dependence of the unperturbed surface density upon the radial distance r, the mass inside the planet's orbit is $\pi\,a^2\,\Sigma = 0.38\;M_{\rm D}$.

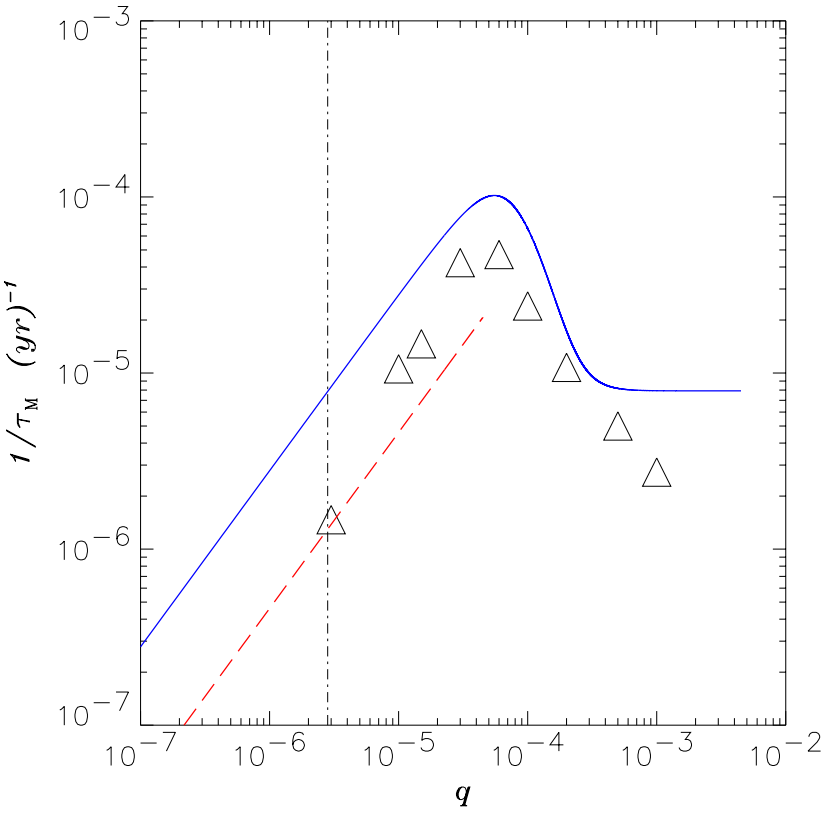

Figure 4.13: Migration time scale $\tau_{\rm M}$ versus the mass ratio q. Open triangles represent the results from models CIRO, PEPP, GINO2, and GINO3. The total disk torque $\mathcal{T}_{\rm D}$ is computed assuming $\beta = 2\,\eta$, for each model. This means that the region lying inside $|\boldsymbol{r} - \boldsymbol{r}_{\rm p}| = 2\,\eta$ is not taken into account. In order to express $\tau_{\rm M}$ into physical units, we suppose that the planet orbits at $a = 5.12$ AU in a disk with mass $M_{\rm D} = 3.5 \times 10^{-3}\ M_{\star}$. The solid curve over-plotted represents predictions of the analytical theory as formulated by Ward (1997), for the case of "strong" viscosity ($\alpha = 4 \times 10^{-3}$ in our case) and accounting *only* for Lindblad torques. It is derived assuming an unperturbed constant surface density and a disk temperature dropping as $1/r$. The behavior of this curve reduces to equation (4.22) and equation (4.23) letting $q \to 0$ and $q \to \infty$, respectively. The meaning of the dashed line is discussed in the text. The vertical line marks the value given by equation (4.24).

of the Jupiter-mass planet (CIRO1). The most rapidly migrating planet is the one having $M_{\rm p} = 20\ M_{\jupiter}$ (PEPP4).

In agreement with predictions of analytical theories, the drift velocity $|\dot{a}|$ increases for increasing planet mass, just as prescribed by type I migration (eq. [4.22]). The fast speed branch has a turning point around $q \simeq 6 \times 10^{-5}$, after which migration slows down considerably. Past this point, $|\dot{a}|$ drops as the planet mass increases. According to the linear

theory, this property announces the transition to type II migration (eq. [4.23]). As a comparison, the complete theoretical behavior of $\tau_{\rm M}$ (solid line) is also reported in Figure 4.13. It was derived by Ward (1997) for viscous disks with $\alpha \gtrsim 10^{-4}$. Equations. (4.22) and (4.23) represent the asymptotic branches of this curve for very light and very heavy planets, respectively. We also plot (long-dash line) the recent outcome by Tanaka et al. (2002). They derived a general formula which is comprehensive of both Lindblad and corotation torques, in 2D as well as in 3D. Their linear theory, which was developed for (vertically and radially) isothermal and inviscid disks, is applicable as long as the Hill radius of the planet is much smaller than the local disk scale height. Hence we can refer to it only in the Type I migration regime.

In all the models under examination, numerical simulations predict a slower drift than Ward's analytic theory does. Roughly, migration is two times as slow for models GINO2, GINO3, PEPP3, and PEPP4; three times as slow for CIRO1, CIRO2, CIRO3, and PEPP2; planets as massive as 3.3 and 67 Earth-masses migrate on the viscous time scale of the disk (eq. [4.23]). Such discrepancies are likely to arise also because the theoretical (solid) curve in Figure 4.13 *does not* include corotation torques. Yet, we have seen that just these torques slow down inward migration. This can be inferred also by comparing the two linear analyses presented in Figure 4.13.

It is generally assumed that the smaller the perturbations, the more suitable linear theories are in describing disk-planet interactions. Consequently, the migration time scale we compute for PEPP1 ($1\ M_{\oplus}$) should match as close as possible the theoretical prevision. Compared to Ward's prediction, $\tau_{\rm M}$ is six times as large, whereas the agreement with the formula by Tanaka et al. (2002) is complete. Between 3 and $10\ M_{\oplus}$, our simulations predict slightly faster migration velocities. This could be attributed to the inviscid approximation and to non-linearity effects. In this respect, Miyoshi et al. (1999) found that, at 5 AU, nonlinear effects appear whenever $M_{\rm p} \gtrsim 5\ M_{\oplus}$. The choice of β in the numerical experiments performed here may play some role as well.

It's worthy to note here that the relevance of co-orbital torques, to the orbital evolution of a protoplanet, was already pointed out by Ward (1993). A further increment of migration times is to be expected if a full three-dimensional treatment of the system is achieved, especially when low-mass planets are dealt with. Local simulations by Miyoshi et al. (1999), global simulations by Kley et al. (2001), and the linear wave theory by Tanaka et al. (2002) indicate that effects due to the disk thickness contribute to reduce the magnitude of the overall torque experienced by the planet. In a flat disk, gas is more efficient in generating torques because it constantly dwells in the planet's orbital plane. In a 3D geometry, material near the vertical of the planet exerts almost a vertical force which does not affect the z-component of the torque in equation (4.18).

β-dependence

In the above discussion, as explained in § 4.4.5, we do not account for the torque exerted by matter closer than $\beta = 2\eta$ to the planet. Now we would like to relax this assumption and consider how material, lying even closer, affects the overall torque $\mathcal{T}_{\rm D}$. Before, however, we inquire about the local effects of β. We mentioned already that the tendency of the nearby gas is to increase the angular momentum of the planet. As we

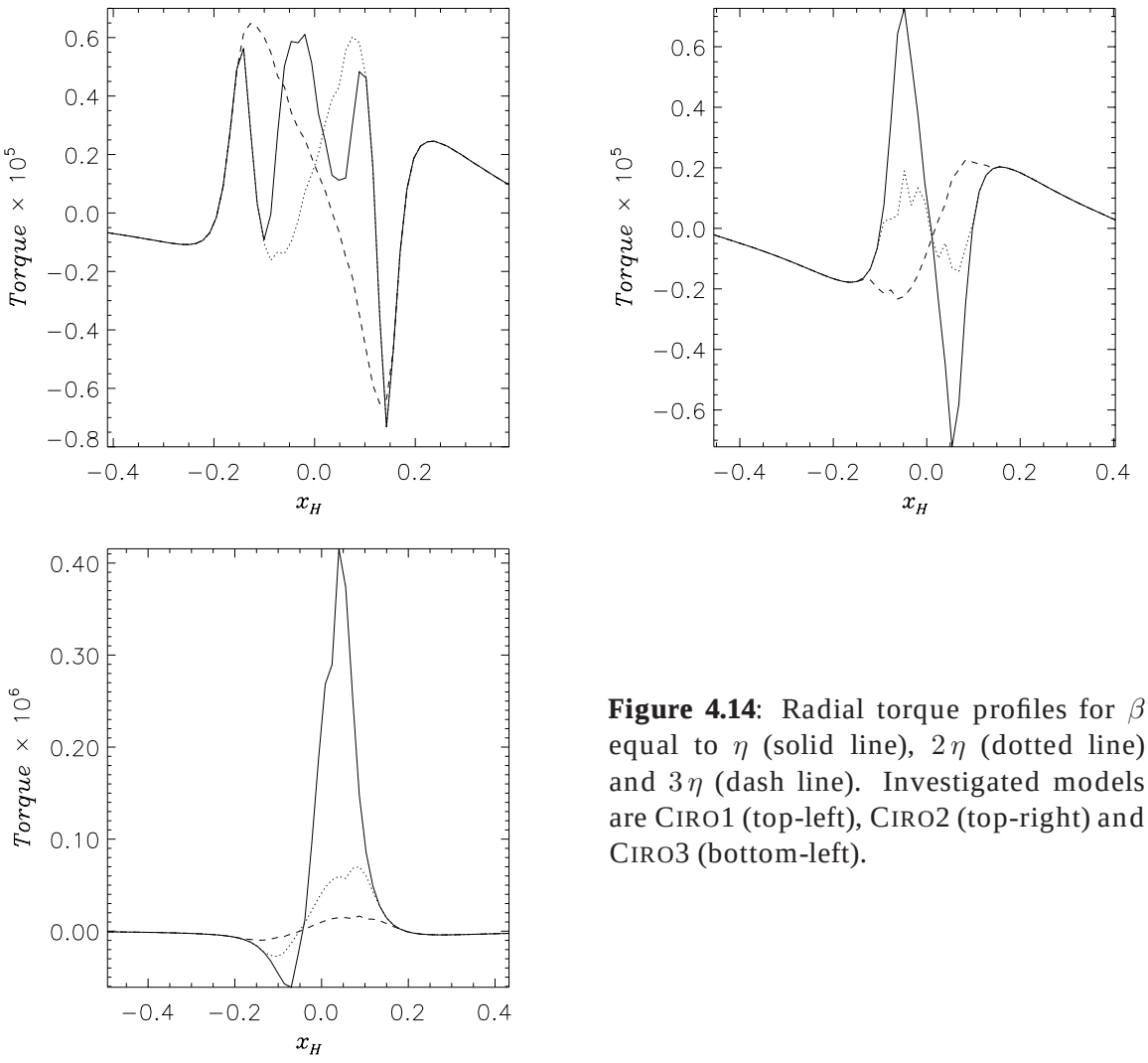

Figure 4.14: Radial torque profiles for β equal to η (solid line), $2\,\eta$ (dotted line) and $3\,\eta$ (dash line). Investigated models are CIRO1 (top-left), CIRO2 (top-right) and CIRO3 (bottom-left).

enter the core dominated zone, such tendency may grow stronger and stronger, reducing more and more the magnitude of the negative torque exerted by the rest of the disk. If we consider different values of β, we find out that the radial torque distribution changes drastically. In order to investigate that more quantitatively, we choose two other values: $\beta = \eta$ and $\beta = 3\,\eta$.

In Figure 4.14, for each of the reference models, the new torque profiles are compared to the previous one ($\beta = 2\,\eta$), on the relevant grid level ($l = ng$). For a Jupiter-mass planet (CIRO1), we obtain a gradually reinforcement of the positive torque exerted by the involved domain (top-left panel). In fact, with $\beta = 3\,\eta$, it results 20% smaller than it is by using $\beta = 2\,\eta$ and 45% larger if we adopt $\beta = \eta$. If we employed the value $\beta = \eta$, in place of $\beta = 2\,\eta$, the total torque would be still negative, but its magnitude would result 18 times as small and $\tau_{\rm M}$ would increase accordingly, as Equation (4.21) implies.

For $M_{\rm p} = 33\ M_{\oplus}^{\star}$ (CIRO2), the same trend is observed (Fig. 4.14, top-right panel). The

net torque contribution increases for decreasing values of β. It is negative for $\beta = 3\,\eta$ and positive for $\beta = \eta$ (and $\beta = 2\,\eta$, as mentioned above). Compared to the case $\beta = 2\,\eta$, the magnitude of the net torque, exerted by this level, is 6.5 and 8 times as large, for $\beta = 3\,\eta$ and $\beta = \eta$ respectively. Further, with $\beta = 3\,\eta$, $\mathcal{T}_{\rm D}$ gets 2 times as negative while, with $\beta = \eta$, it still keeps the negative sign but reduces of 6 times.

Finally we analyze the smallest reference planet $M_{\rm p} = 3.3\ M_{\jupiter}$ (CIRO3). As showed in Figure 4.11 (middle row, right panel) the radial torque profile is quite asymmetric and dominated by a huge maximum at $x_h \approx 0.05$. This is greatly enhanced by including in the torque computation matter closer to the planet (Fig. 4.14, top-left panel). In contrast, the net torque results negative, by using $\beta = 3\,\eta$, but so greatly attenuated that it almost vanishes. In fact its absolute value becomes 28 times as small as it is with $\beta = 2\,\eta$ and its contribution to $\mathcal{T}_{\rm D}$ is negligible ($\approx$ 2%). On the other hand, performing the torque computation by using $\beta = \eta$, a strong positive contribution is provided by the material on this level, such to compensate the negative torques arising from the rest of the disk and turning the overall torque sing to positive. The influence of close-by material, in this case, would reverse the direction of the planet migration.

An overview of the effects, due to nearby matter, on the migration time scale $\tau_{\rm M}$, is given in Figure 4.15. Actually, these plots show the dependence of $v/\tau_{\rm M} \propto \mathcal{T}_{\rm D}$ upon β, where $v = \dot{a}/|\dot{a}|$ indicates the direction of the planet's migration. The distance where $\beta = 2\,\eta$ is marked with a vertical, solid line. $\mathcal{T}_{\rm D}$ is directly proportional to the mass of the disk $M_{\rm D}$. Therefore, to remove this potential restriction, in these plots we let it as a free parameter and write $M_{\rm D}$ as $k \times 10^{-3}\ M_{\star}$, although we use $k = 3.5$ for our estimates. In Figure 4.15, $\mathcal{T}_{\rm D} = \mathcal{T}_{\rm D}(\beta)$ is presented for all of the three reference models.

In CIRO1 (upper-left panel), $\mathcal{T}_{\rm D}$ becomes larger as β gets smaller. The sign of the total torque changes around $\beta = \eta$, the threshold of the density core. As a comparison, the behavior of $\mathcal{T}_{\rm D}$, versus β, is reported also for the model ELEN1. In this case, because of the closed inner radial border, the amount of matter inside the orbit of the planet is five times as large as that of CIRO1. Outside the Hill circle, the torque exerted by the inner-disk, in case of ELEN1, is twice as large as that measured in CIRO1. Instead, torques arising from the outer-disk nearly coincide. Inside the Hill circle, in ELEN1, the contribution to $\mathcal{T}_{\rm D}$ is relatively small down to $\sim 0.1\ R_{\rm H}$ whereas, in CIRO1, it never appears to be negligible.

CIRO2 (upper-right panel) behaves somewhat differently from CIRO1. The total torque attains a minimum around $\beta = 0.15\ R_{\rm H}$, where $\tau_{\rm M} \simeq 3 \times 10^4$ years. Then the positive torques, exerted by close matter, increase the total torque, though it remains negative all the way down to $\beta = 0.03\ R_{\rm H}$. Below such value, $\mathcal{T}_{\rm D}$ diverges positively. Results from the higher resolution model, WPRO1, do not differ significantly (dashed line in Fig. 4.15).

$\mathcal{T}_{\rm D}$ varies smoothly, as a function of β, in case of CIRO3 (lower-left panel) . The torques arising from the region enclosed between $\beta \approx 0.2\ R_{\rm H}$ and $\beta \approx 0.4\ R_{\rm H}$ almost cancel out, so that the total torque appears nearly constant ($\tau_{\rm M} \approx 10^5$ years). At shorter distances, positive torques prevail over the negative ones and $\mathcal{T}_{\rm D}$ starts to increase. The sign of the total torque reverses at $\beta \simeq 0.12\ R_{\rm H}$. For example, at $\beta = \eta$, its value is quite positive, imposing an outward migration rate $\tau_{\rm M} \simeq 3 \times 10^4$ years.

Some comments should be devoted to how the smoothing length affects the total torque. We did not try to reduce further its value, however we ran some models, identical

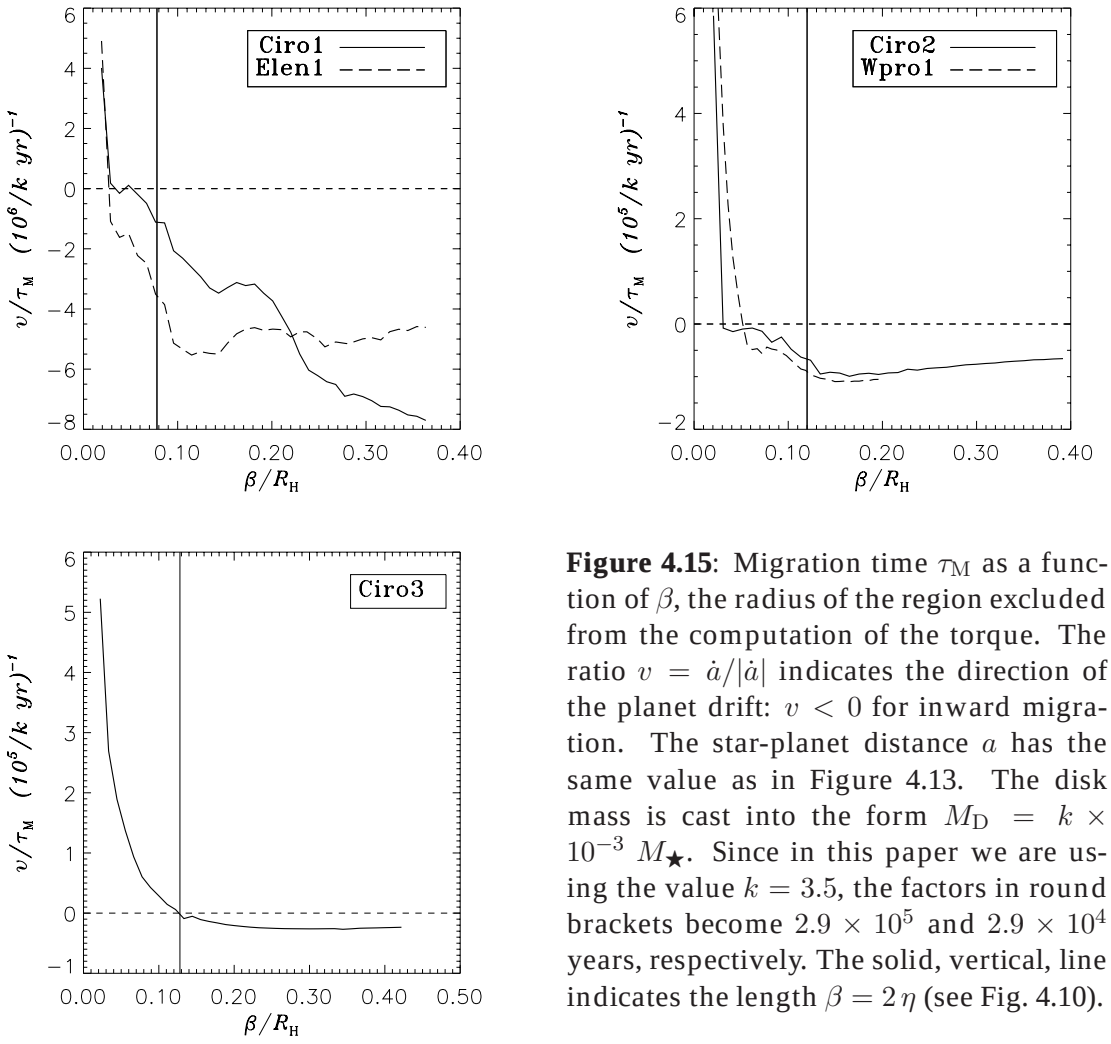

Figure 4.15: Migration time $\tau_{\rm M}$ as a function of β, the radius of the region excluded from the computation of the torque. The ratio $v = \dot{a}/|\dot{a}|$ indicates the direction of the planet drift: $v < 0$ for inward migration. The star-planet distance a has the same value as in Figure 4.13. The disk mass is cast into the form $M_{\rm D} = k \times 10^{-3}\ M_{\star}$. Since in this paper we are using the value $k = 3.5$, the factors in round brackets become 2.9×10^5 and 2.9×10^4 years, respectively. The solid, vertical, line indicates the length $\beta = 2\,\eta$ (see Fig. 4.10).

to CIRO1, but multiplying λ (see eq. [4.15]) by some integer number. A larger smoothing length tends to smear out more the surface density nearby the planet. Besides, it also causes the material to be distributed more symmetrically around it. Both tendencies contribute to reduce the magnitude of the net torque arising from a region with radius $\approx \lambda$.

4.4.7 Circumplanetary Disk: Gas Flow

In § 4.4.1 we described in detail how gas flows into the Roche lobe of a planet, for three particular values of its mass.

If a planet is massive enough, say $M_{\rm p} \gtrsim 10\ M_{\oplus}$, the streams of matter, entering the Roche lobe, produce strong shock waves which then rule the gas flow inside this region. Material passing through the shock fronts is deflected towards the planet, tightening its orbit on it. Less massive planets are not able to cause strong perturbations inside the

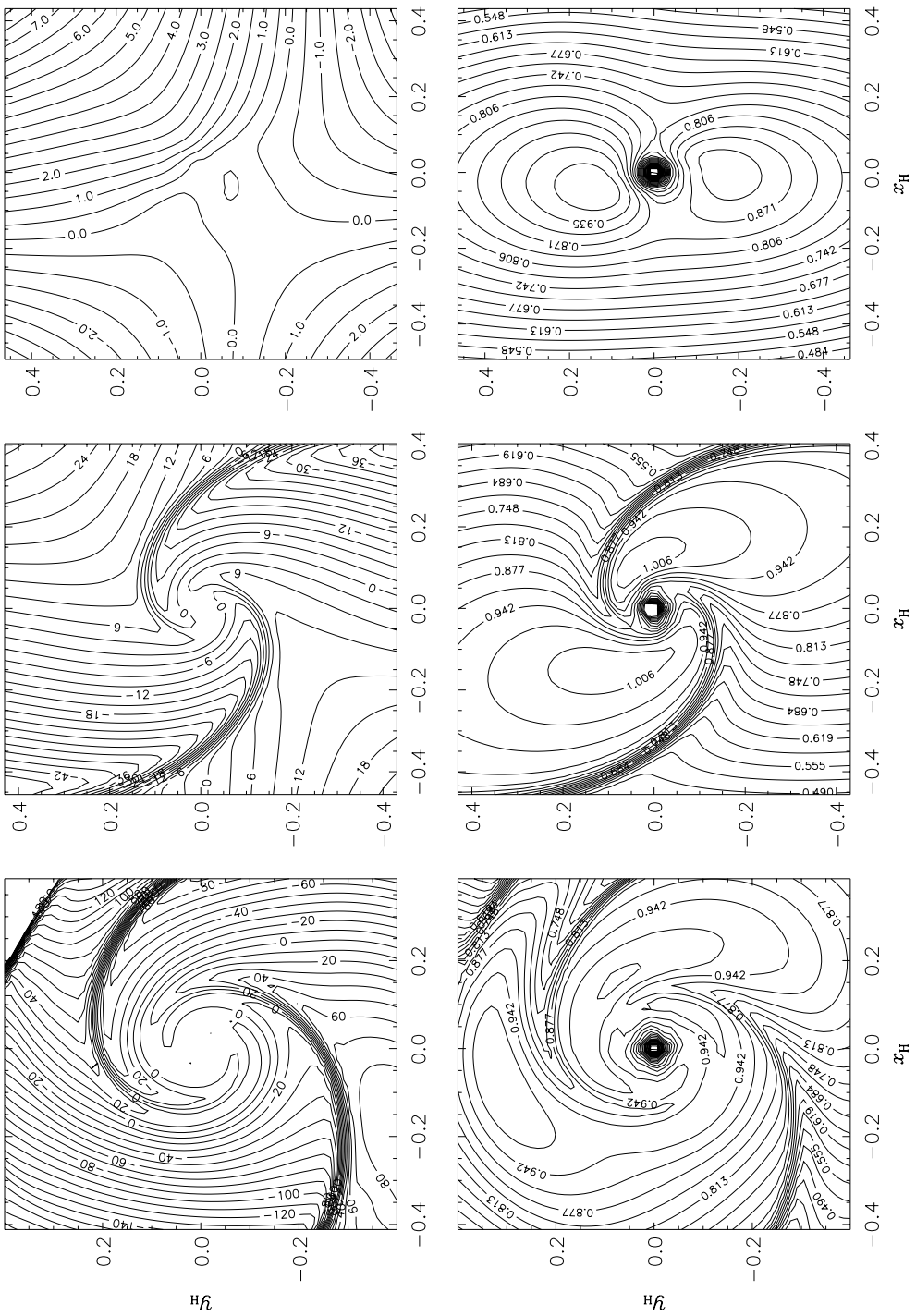

Figure 4.16: Contour lines of velocity ratios $w_{\rm in}/w_{\rm in}^{\rm D}$ and $w_{\rm rot}/w_{\rm rot}^{\rm K}$ **(top panels)** and $w_{\rm rot}/w_{\rm rot}^{\rm K}$ **(bottom panels)**. From left to right, we report the above quantities, as computed on the highest level, of models: CIRO1, CIRO2, and CIRO3. $w_{\rm in} > 0$ contours indicate places where the flow approaches the planet. At locations where the in-fall velocity is zero, the flow performs a pure rotation around the planet.

Roche lobe. As a consequence, the flow pattern appears more uniform around the planet.

Now we would like to investigate quantitatively the rotational regime of the gas inside the circumplanetary disks. In particular, we would like to estimate how much it resembles a Keplerian one. In order to address this issue we decompose the local velocity field $\boldsymbol{u}$, in two components, representing the in-fall velocity $w_{\rm in}$ and the rotational velocity $w_{\rm rot}$ of the fluid *relative to the planet*. The first component is defined as:

$$w_{\rm in} = -\boldsymbol{u} \cdot \frac{\boldsymbol{r} - \boldsymbol{r}_{\rm p}}{|\boldsymbol{r} - \boldsymbol{r}_{\rm p}|},$$

which is positive if a fluid element moves towards the planet. The quantity $w_{\rm rot}$ is the projection of $\boldsymbol{u}$ along the direction orthogonal to $\boldsymbol{r} - \boldsymbol{r}_{\rm p}$ and such that $(\boldsymbol{w}_{\rm rot} \times \boldsymbol{w}_{\rm in}) \cdot \hat{\boldsymbol{z}}$ is positive. With this choice $w_{\rm rot}$ is positive for a counter-clockwise rotation.

If circumplanetary disks were regular accretion disks, we should expect them to be in a "Keplerian" regime. This is characterized by the rotational velocity

$$w_{\rm rot}^{\rm K} = \sqrt{\frac{G\,M_{\rm p}}{|\boldsymbol{r} - \boldsymbol{r}_{\rm p}|}}, \tag{4.25}$$

and the inward viscous diffusion

$$w_{\rm in}^{\rm D} = \frac{3\,\nu}{2\,|\boldsymbol{r} - \boldsymbol{r}_{\rm p}|}. \tag{4.26}$$

Equations (4.25) and (4.26) don't include the smoothing length, δ, because its effects were checked to be unimportant. Comparing $w_{\rm rot}$ and $w_{\rm in}$ with equation (4.25) and equation (4.26), respectively, we can estimate how much the circumplanetary flow is close to be Keplerian, i.e. close that of an unperturbed viscous disk.

Figure 4.16 shows, for CIRO-models, the contour lines of $w_{\rm in}$ normalized to $w_{\rm in}^{\rm D}$ (top panels) and $w_{\rm rot}$ normalized to $w_{\rm rot}^{\rm K}$ (bottom panels).

As first remark we note that, if we compare Figure 4.16 to Figure 4.6, lines of equal surface density perturbation are also lines of equal velocity perturbation, as spiral wave theory predicts.

From the top panels of Figure 4.16, we can see that material approaches the planet along well defined patterns. Contours $w_{\rm in} = 0$ mark locations where the flow rotates around the planet without altering its distance from it. They also separate regions in which material proceeds towards the planet from those where it moves away. One of these contours runs along the spiral ridges. Across it, the in-fall velocity changes abruptly its sign.

The ratio $w_{\rm in}/w_{\rm in}^{\rm D}$ becomes smaller as the gas comes closer to the planet. Since the viscous diffusion $w_{\rm in}^{\rm D}$ is not related to $M_{\rm p}$, it's possible to compare the magnitude of $w_{\rm in}$ for the different cases. Contour level values indicate that it gradually reduces as $M_{\rm p}$ gets smaller.

As regards the rotational component of the velocity field $w_{\rm rot}$ (Fig. 4.16, bottom panels), we can see that it is generally slightly below $w_{\rm rot}^{\rm K}$. For the Jupiter-mass case, this can be seen also in Figure 4.17. Centrifugal over-balance regions are not present around the smallest planet ($M_{\rm p} = 3.3\ M_{\jupiter}$). Instead, they are observed in CIRO1, at $(x_{\rm H}, y_{\rm H}) \approx (-0.1, 0.3)$

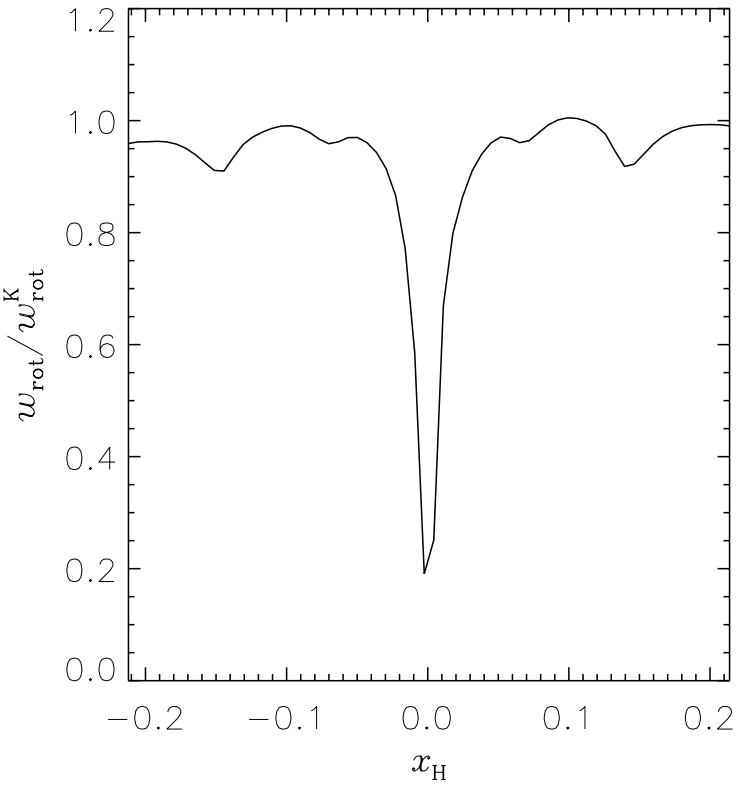

Figure 4.17: The plot shows the ratio $w_{\rm rot}/w^{\rm K}_{\rm rot}$ at $\varphi = \varphi_{\rm p}$ ($y_{\rm H} = 0$), as computed on the grid level $l = 6$ of the model ELEN2 ($M_{\rm p} = 1\ M_{\rm J}$). The core area, in the Jupiter-mass case, extends for $[0.08 \times 0.08]\ {R_{\rm H}}^2$ (see Figure 4.10, left panel). The resolution, in ELEN2, is such that this is covered by $\sim 12 \times 12$ grid cells.

and $(0.15, 0.1)$, and in CIRO2, where they are labeled. In both cases, anyway, the ratio $w_{\rm rot}/w^{\rm K}_{\rm rot}$ is very close to unity. Centrifugal under-balance is mainly established along spiral ridges. This is in agreement with the idea that spiral arms are zones of compression, hence pressure plays a more active role in supporting the gas.

In all of the three cases shown in Figure 4.16, $w_{\rm rot}$ reveals somewhat a circular symmetry only within a distance $\sim \eta$ from the planet. Yet, we have to notice that this coincides nearly with the region from which matter is removed to simulate the gas accretion. Figure 4.17 also indicates that the core material (§ 4.4.4) rotates slower, when it approaches its center.

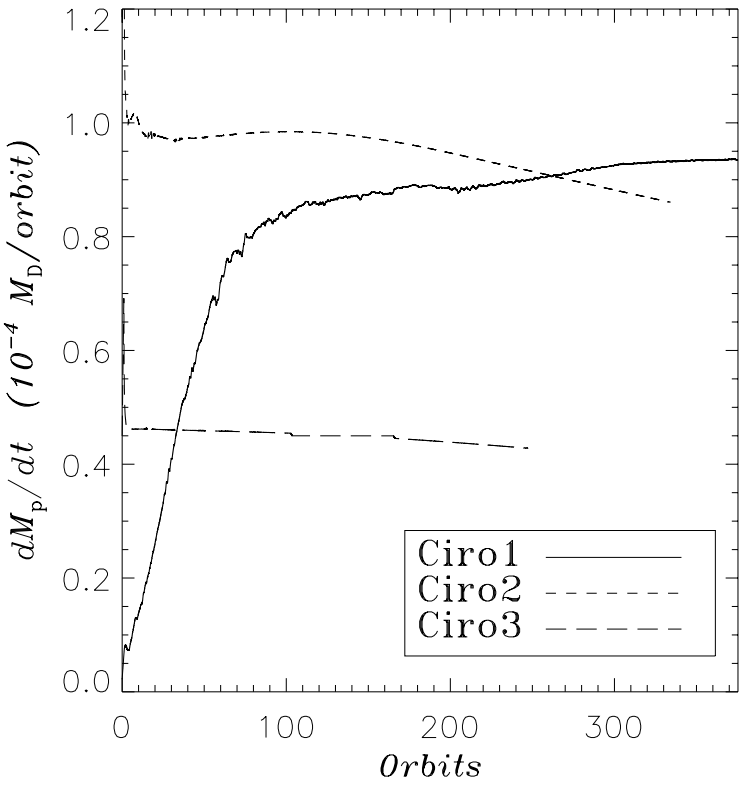

Figure 4.18: Mass accretion rate onto the planet versus time, in units of 10^{-4} disk masses per orbital period of the planet. For $M_{\rm D} = 3.5 \times 10^{-3}\ M_{\star}$ and $a = 5.2$ AU, one dimensionless unit corresponds to $2.95 \times 10^{-5}\ M_{\earth}\ {\rm yr}^{-1}$. The initial accretion rate is very small for model CIRO1 because of the imposed initial gap.

4.4.8 Accretion onto the Planet

Gas matter closely orbiting the planet is eligible to be accreted once its distance, $|\boldsymbol{r} - \boldsymbol{r}_{\rm p}|$, is less than $\kappa_{\rm ac} \approx 9 \times 10^{-2}\ R_{\rm H}$. The details of this process are described in § 4.3.2 (see also Fig. 4.1). In general, the mass accretion rate of a planet, $\dot{M}_{\rm p}$, becomes relatively constant after the gap (if any) has evolved to a quasi-stationary state.

For a Jupiter-mass planet (CIRO1) this happens around 100 orbital periods, as indicated by the solid line in Figure 4.18. The theoretical gap imposed at the beginning of the evolution (see Fig. 4.2) is deeper and wider, at $\varphi = \varphi_{\rm p}$, than it is later on. For this reason $\dot{M}_{\rm p}$ is negligibly small at early evolutionary times. The partial replenishment is related to the formation of the circumplanetary disk which supplies matter for the accretion process.

Smaller planets dig narrower and shallower gaps so this quasi-steady regime is reached even earlier. For both CIRO2 (Fig. 4.18, short-dash line) and CIRO3 (long-dash line), $\dot{M}_{\rm p}$

reduces a little as the evolution proceeds. This is likely due to the depletion of the inside-orbit disk. In case of CIRO1, most of the inner-orbit material is cleared out during the transitional phase (75% after 100 orbits). Therefore, it does not contribute much during the quasi-steady phase.

In Figure 4.19, the accretion rate is plotted against the mass ratio (left panel), in dimensionless units as in Figure 4.18. $\dot{M}_{\rm p}$ increases as the planet mass increases and reaches a maximum around $0.5\ M_{♃}$ (model GINO3). Beyond this point the curve starts to drop. In fact, the accretion rate of CIRO1 lies between those of CIRO2 ($M_{\rm p} = 33\ M_{♃}$) and GINO2 ($M_{\rm p} = 67\ M_{♃}$). The accretion rates for planets with masses above about $10^{-4}\ M_{★}$ ($33\ M_{♃}$) are consistent with those obtained by recent models studying the evolution of giant protoplanets (Tajima and Nakagawa 1997). For smaller masses our accretion rates are substantially higher. Two-dimensional approximation may be partially responsible for this since all the gas is confined to the disk midplane. Actually, Kley et al. (2001) showed that accretion rates in disks with thickness are smaller than those in infinitesimally thin disks as soon as the scale height of the disk becomes comparable with the Hill radius of the planet. However, all the more detailed studies of protoplanetary evolution are spherically symmetric (see the review by Wuchterl et al. 2000), and accretion via a planetary accretion disk may allow, anyway, for higher rates.

We did not perform computations involving planets heavier than one Jupiter-mass so we cannot follow the trend of the curve for larger values of q. However, Lubow et al. (1999) found that $\dot{M}_{\rm p}$ decreases in the mass range from 1 to 6 $M_{♃}$.

In the right panel of Figure 4.19 the growth time scale $\tau_{\rm G} \equiv M_{\rm p}/\dot{M}_{\rm p}$ is plotted versus q. Logarithmic scaling of the axes shows that the curve decreases almost linearly with respect to the mass of the planet. If we perform a linear least-square fit of the values for which $q \geq 2 \times 10^{-4}$, corresponding to $M_{\rm p} = 67\ M_{♃}$, we get:

$$\frac{\mathrm{d}\log(1/\tau_{\rm G})}{\mathrm{d}\log(q)} = -0.66.$$

This equation yields:

$$\tau_{\rm G} \propto q^{0.66} \simeq q^{2/3}. \tag{4.27}$$

At higher values of q, the curve steepens, decreasing more rapidly. Taking into account the growth time scales relative to the two most massive planets, one finds

$$\tau_{\rm G} \propto q^{1.34} \simeq q^{4/3}. \tag{4.28}$$

Therefore, as a planet becomes more massive, the growth time scale grows with an increasing power of its mass. Thus, we can argue that very high mass planets should be extremely rare.

Influence of Numerics

Finally, we comment on the influence of some numerical parameters upon the mass accretion rate. Table 4.3 lists some results, after the same number of orbits, for various models which can be useful to the goal. The value of $\dot{M}_{\rm p}$ may depend on the mass evacuation rate $\kappa_{\rm ev}$ as well as on the radius $\kappa_{\rm ac}$ of the accretion region. By comparing models

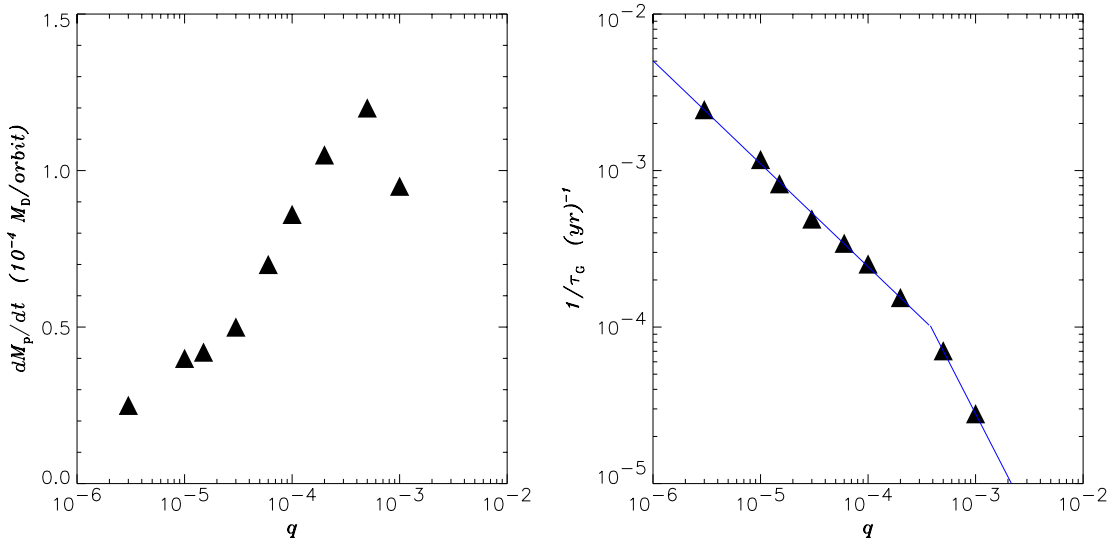

Figure 4.19: **Left panel**. Mass accretion rate $\dot{M}_{\rm p}$ as function of the mass ratio q. Quantities are normalized to the disk mass $M_{\rm D}$. **Right panel**. Dependence of the growth time scale $\tau_{\rm G} \equiv M_{\rm p}/\dot{M}_{\rm p}$ on the planet mass (filled triangles). $M_{\rm D} = 3.5 \times 10^{-3}\ M_{\star}$ is employed to express $\tau_{\rm G}$ into years. The two-branch solid line represents the first-order polynomial fitting the data (see equations 4.27 and 4.28).

CIRO2 and WPRO2, it turns out that doubling $\kappa_{\rm ev}$, the accretion rate is only 11% higher. In order to estimate how relevant the extension of the accretion region may be, we ran the model ELEN3 for which we adopted a length $\kappa_{\rm ac}$ equal to 0.6 times that used for GINO3 (the rest of the model set-up being identical). We obtain an accretion rate 8% smaller.

Further, $\dot{M}_{\rm p}$ could depend on the numerical resolution as well. Indeed, this dependency turns out to be very weak, as indicated by two sets of models. ELEN2 and WPRO1 have, in the accretion region, a resolution two times as high as that of CIRO1 and CIRO2, respectively (see Table 4.1). Despite this fact, in the first case, the accretion rates differ by just 2%, whereas the difference amounts to 4% in the second.

As mentioned in § 4.3.4, the planet in not symmetrically centered within a grid cell. Model GINO1 was designed to accomplish a fully symmetric configuration (as already explained in § 4.3.4). However, the planet accretion rate is not affected by this position shift, as can be seen by comparing the values in Table 4.3, belonging to CIRO3 and GINO1.

The accretion procedure we use in the present work is the same as in Kley et al. (2001). Their evaluations of $\dot{M}_{\rm p}$, for two-dimensional models with $M_{\rm p} = 0.5$ and $1\ M_{\rm J}$, are roughly twice as high as the estimates given in the left panel of Figure 4.19. Yet, in that paper, though $\kappa_{\rm ev}$ was set to 5, $\kappa_{\rm ac}$ is equal to $0.5\ R_{\rm H}$, thus the accretion region exceeds by 40 times that used in this paper for models GINO3 and CIRO1.

Table 4.3: Mass accretion rate onto the planet for different numerical parameters. This quantity is reported at the same evolutionary time for similar models. $\dot{M}_{\rm p}$ is given in units of disk masses per orbit.

Model	q	$\dot{M}_{\rm p}$	Orbits
CIRO1	1.0×10^{-3}	8.7×10^{-5}	200
ELEN2	1.0×10^{-3}	8.9×10^{-5}	200
GINO3	5.0×10^{-4}	1.2×10^{-4}	200
ELEN3	5.0×10^{-4}	1.1×10^{-4}	200
CIRO2	1.0×10^{-4}	9.0×10^{-5}	280
WPRO1	1.0×10^{-4}	8.6×10^{-5}	280
WPRO2	1.0×10^{-4}	1.0×10^{-4}	280
CIRO3	1.0×10^{-5}	4.5×10^{-5}	120
GINO1	1.0×10^{-5}	4.5×10^{-5}	120

4.5 Conclusions

A number of numerical simulations concerning disk-planet interactions have been performed to get new insights into the scenario of the joint evolution of protoplanets and their environment. They have confirmed analytical theories for gap formation and planet migration.

However, many open questions still remain. The most important unsolved issue is the influence of the ambient gas on the dynamical evolution of a planet. Another one is the way disk-planet interaction changes when small planets, in the mass range of Neptune and Earth, are considered.

We began to investigate in both directions by means of a nested-grid technique, which is particularly suitable for treating these problems. The main asset of this numerical scheme is the possibility of achieving, locally, a very high spatial and temporal resolution. With such a method we are able to resolve very accurately both the inner parts of the Hill sphere of the planet *and* the global structure of the disk; consequently we can treat the whole azimuthal extent of the disk.

As regards the issues mentioned above, with the present chapter we tackled some outstanding problems concerning the growth and migration of protoplanets, covering a range from one Jupiter-mass down to one Earth-mass. Thus, even though we do not include the detailed energetic balance of the planetary structure, which is still beyond present day computer facilities, this study represents a definite improvement in the determination of the torque balance on protoplanets.

Our main achievements can be summarized as follows.

Inside the Hill sphere of the planet a circumplanetary disk forms. Within it strong spiral density waves develop, if the planet mass is larger than $\sim 5\ M_{\oplus}$. These waves assume the shape of a two-arm pattern. The two spiral arms are slightly asymmetric with respect to the planet. For decreasing planet masses, they stretch and shorten. Matter is observed to pile up at the location of the planet, generating a very high density zone (we

named as density "core"), which might represent its primordial gaseous envelope.

Nearby material exerts positive torques on the planet, slowing down, considerably in some cases, its inward migration. Most of these torques arise from corotation regions, i.e. from gas lying on the planet's orbit. Not all analytical models about migration include them. This can be one of the reasons why our estimates of the migration time scales give somewhat higher values than those predicted by Ward's 1997-theory. On the other hand, Tanaka et al. (2002) account also for corotation torques, but non-linearity and viscosity may play some role in the little discrepancies between their formula and our results.

Within a distance of $\sim 0.1\ R_{\rm H}$ from the planet, the point-mass approximation becomes too restrictive and maybe not appropriate. Therefore, the structure of the planet should be also taken into account over such a length scale. This is absolutely necessary if one wants to evaluate how much of the angular momentum, transferred by closely orbiting matter, is conveyed to the spin of the planet rather than to its orbital angular momentum.

The Keplerian rotational regime of circumplanetary disks is affected by spiral perturbations. Just as for the mass density, the more massive the planet is, the stronger such perturbations are. Gas material, passing through the spiral fronts, is deflected towards the planet. Instead, in the inter-arm regions it moves away from it. This is in analogy with the spiral wave theory in galaxies. Around Earth-mass planets, the rotation of the gas is very slow if compared to the Keplerian rotation. In fact, in this particular case, the density core has nearly a hydrostatic structure.

The mass accretion rate, as a function of the mass of the planet, has a maximum around $M_{\rm p} = 0.5\ M_{\earth}$. As long as $M_{\rm p} \lesssim 0.2\ M_{\earth}$, the growth time scale of a planet increases, approximatively, as ${M_{\rm p}}^{2/3}$. For more massive planets, it increases roughly as ${M_{\rm p}}^{4/3}$. Such a dependence may contribute to limit the size of a massive planet.

Since we just started to explore these new grounds, each of the items above may deserve a more specific and dedicated study.

Next efforts should be devoted to refine the physical model, especially in the vicinity of the planet, and to approach high resolution three-dimensional computations. Thereupon, some of the future developments will be:

- improving the equation of state by using an alternative form which accounts for the planet's structure;
- evaluating possible effects due to the two-dimensional approximation of the disk, via nested-grid three-dimensional simulations;
- including an energy equation, by implementing an approximate treatment of radiative transfer and viscous dissipation.

The people come with nets to fish for potatoes in the river, and the guards hold them back; they come in rattling cars to get the dumped oranges, but the kerosene is sprayed. And they stand still and watch the potatoes float by, listen to the screaming pigs being killed in a ditch and covered with quicklime, watch the mountains of oranges slop down to a putrefying ooze; and in the eyes of people there is the failure; and in the eyes of the hungry there is a growing wrath. In the souls of the people the grapes of wrath are filling and growing heavy, growing heavy for the vintage.

JOHN STEINBECK,
THE GRAPES OF WRATH,
1939

CHAPTER 5

THREE-DIMENSIONAL COMPUTATIONS WITH NESTED GRIDS

This chapter is dedicated to the application of the nested grid technique to global calculations in three dimensions. Furthermore, the assumption of handling the protoplanet as a point-mass is overcome by means of analytical models for planetary envelopes. The necessity of describing the physics of disk-planet interactions by accounting for all the three spatial dimensions arises from the intrinsic nature of the problem. In fact, though the slimness hypothesis is safely applicable to circumstellar disks, it is not guaranteed that such hypothesis works as well in circumplanetary disks, i.e., in the vicinity of forming planets.

5.1 Introduction

In the majority of the previous studies, the disk is modeled as a two-dimensional (r–φ) system, by using vertically-averaged quantities. Two main arguments lie behind this choice. First, on a physical basis, the validity of a two-dimensional description is consistent because the Hill radius of a massive object is larger or comparable to the disk semi-thickness. In fact, this basically means that the sphere of gravitational influence of the embedded body, i.e., the Hill sphere, contains the whole vertical extent of the disk. But this usually implies that the planet must have a mass on the order of one Jupiter-mass. Second, a less massive planet has a weaker impact on the disk, requiring a higher resolution to compute properly and highlight its effects. Such requirement typically rules out a full three-dimensional treatment. Although there is still a lot of information to be gained by performing 2D simulations (e.g., to study radiative effects or multi-planet systems) in particular in the case of large and medium mass planets, provided that the local resolution around the planet is accurate enough, three-dimensional effects become more and more important as the mass of the simulated planet is reduced.

Yet, in many instances, the use of the two-dimensional approximation is merely dictated by the computational costs of 3D calculations which are generally not affordable.

Depending on the resolution one is interested in, 3D runs still take more than an order of magnitude of CPU time with respect to 2D runs. As a proof of the severe limitations posed by fully three-dimensional calculations, only very few papers have been published on this issue (see § 1.5.1).

In CHAPTER 1 it was pointed out that to obtain reliable results in three dimensions, the flow within the Roche lobe needs to be accurately resolved. Calculations presented in CHAPTER 4 have proved that the *nested-grid* technique comfortably adapts to simulate planets in disks because global-, small-, and very small-scale features of the flow can be captured simultaneously with a high degree of accuracy.

In this chapter we intend to combine the fully three-dimensional and global treatment of disk-planet interactions with a nested-grid refinement technique in order to carry out an extensive study on migration, accretion, and flow features around large- and small-size protoplanets. Thus, the work presented here comes as an extension to that reported in CHAPTER 2 and 4. In addition, here we abandon the standard approach of treating the planet as a point-mass but rather assume it has an extended structure.

The outline of the chapter is as follows. Section 5.2 deals with those aspects of the physical description that we adopt and which were not already specified in CHAPTER 2. We explain how we approximate the protoplanet's structure by using different solutions for the gravitational potential. Section 5.3 presents a brief overview about the numerical procedures employed in this work and describes the technical details of the models. As for the implementation of the nested grids in three dimensions, for brevity we mainly refer to the two-dimensional strategy traced in CHAPTER 4. The various results of our simulations are addressed in § 5.4. Fluid circulation, gravitational torques, orbital migration, mass accretion rates, and how all of them depend on the perturber mass are examined. A comparison between 2D and 3D models and an analysis of some numerical effects are also carried out. In § 5.5 two issues related to 2D and 3D geometry effects are discussed in more detail; we finally present our conclusions in § 5.6.

5.2 Physical Description

The nature of most astrophysical objects is such that their behavior can be approximated to that of *fluids*. This is indeed the case for circumstellar disks, hence we can rely on the hydrodynamic formalism to describe them. The equations of motion that govern the evolution of a disk in a spherical polar coordinate system $\{O; R, \theta, \varphi\}$ are presented in CHAPTER 2 and therefore, for the sake of brevity, we refer the interested reader to it. We assume the disk to be a viscous medium and include the viscosity terms explicitly by employing a complete stress tensor for Newtonian fluids (see e.g., Mihalas and Weibel Mihalas 1999,Chapter 3).

The set of equations for the hydrodynamic variables $(\rho, u_R, u_\theta, u_\varphi)$ is written with respect to a reference frame rotating at a constant rate Ω, around the polar axis $\theta = 0$, and whose origin O resides in the center of mass of the star–planet system. The planet is maintained on a fixed circular orbit, lying in the midplane of the disk ($\theta = \pi/2$). If we let Ω coincide with the angular velocity of the planet $\Omega_{\rm p}$, the planet does not move within the reference frame. The assumption that a single protoplanet, not heavier than Jupiter, moves

on a circular orbit is reasonable because the global effect of the resonances, arising from disk–planet interactions, in most of the cases favors an eccentricity damping (Papaloizou et al. 2001; Agnor and Ward 2002).

Disk material evolves under the combined gravitational action of a star and a massive body. As long as the inner parts of low-mass protostellar disks are concerned, self-gravity can be neglected. Indicating with $\boldsymbol{R}_\star$ the radius vector pointing to the position of the star, the gravitational potential Φ of the whole system is represented by

$$\Phi = -\frac{G\,M_\star}{|\boldsymbol{R}-\boldsymbol{R}_\star|} + \Phi_\mathrm{p}, \tag{5.1}$$

where $M_\star$ is the stellar mass. In equation (5.1), the function Φ_p identifies the perturbing potential of the planet, which we leave unspecified for the moment.

Since the energy equation is not considered in the present work, we join an established trend (e.g., Kley 1999; Lubow et al. 1999; Miyoshi et al. 1999; Nelson et al. 2000; Papaloizou et al. 2001; Tanaka et al. 2002; Masset 2002; Tanigawa and Watanabe 2002) and use a locally isothermal equation of state as closure of the hydrodynamic equations

$$p = c_\mathrm{s}^2\,\rho, \tag{5.2}$$

where the sound speed c_s equals the Keplerian velocity v_K times the disk aspect ratio $h = H/(R\sin\theta)$ (H is the pressure scale-height of the disk). As the ratio h is assumed to be constant, the disk is azimuthally and vertically isothermal, whereas radially $T \propto h^2 M_\star/(R\sin\theta)$. This simplified approach permits to circumvent the difficulties posed by the solution of a complete energy equation which nobody has tackled yet. In fact this kind of computations would require a length of time which is presently not affordable. As reference, even without including energetic aspects, the CPU-time consumed by our three-dimensional global simulations is already between ten and twenty times as long as that spent by two-dimensional ones. An investigation into the effects that may arise in two-dimensional disks when an energy equation is also taken into account, will be presented in CHAPTER 6.

However, an important issue to improve the physical description of the system in the vicinity of the protoplanet is to adopt an appropriate equation of state which can account for the protoplanetary envelope. Yet, in our case this would imply that either p or ρ should be specified in some volume around the planet. In order to avoid this, we choose to constrain the local structure by means of suitable analytic expressions for Φ_p. We assume that the protoplanet has a measurable size, i.e., it can be resolved by the employed computational mesh. Within the planetary volume, we approximately take into account the effects due to self-gravity by imposing a certain gravitational field. Since we aim at covering various possible scenarios, we utilize four different forms of planet gravitational potential, each representing a protoplanet with different characteristics. It is worthwhile to point out that with this choice none of the hydrodynamic variables $(\rho, u_R, u_\theta, u_\varphi)$ is prescribed in any case. They simply evolve in a particular gravitational field. Therefore, planetary material is allowed to interact with the surrounding environment so that their mutual evolutions are still connected.

5.2.1 Planet Gravitational Potential

With no exception, both numerical and analytical work that have so far investigated the interactions between massive bodies and protostellar disks have made the *point-mass* assumption, i.e., the protoplanet has a finite mass $M_{\rm p}$ but no physical size, as is done in CHAPTER 2 and 4. This property is expressed through the gravitational potential

$$\Phi_{\rm p}^{\rm PM} = -\frac{G\,M_{\rm p}}{|\boldsymbol{R}-\boldsymbol{R}_{\rm p}|}, \tag{5.3}$$

where $\boldsymbol{R}_{\rm p}$ is the radius vector indicating the position of the planet.

Because of the singularity at $\boldsymbol{R}=\boldsymbol{R}_{\rm p}$, a parameter ε is introduced in order to smooth the function over a certain region. If we denote $\boldsymbol{S}=\boldsymbol{R}-\boldsymbol{R}_{\rm p}$ the position vector relative to the planet, the smoothed point-mass potential can be written in the following form

$$\Phi_{\rm p}^{\rm PM} = -\frac{G\,M_{\rm p}}{\varepsilon}\left[1+\left(\frac{S}{\varepsilon}\right)^2\right]^{-\frac{1}{2}}. \tag{5.4}$$

A physical meaning of the smoothing length can be deduced from equation (5.4). The potential $\Phi_{\rm p}$ enters the Navier-Stokes equations through its derivatives, which can be reduced to $\partial\Phi_{\rm p}/\partial S$ because of the spherical symmetry of the gravitational field. Restricting to distances $S<\varepsilon$, a binomial expansion of that derivative yields

$$\frac{\partial\Phi_{\rm p}^{\rm PM}}{\partial S} \simeq \frac{G\,M_{\rm p}}{\varepsilon^2}\left(\frac{S}{\varepsilon}\right)\left[1-\frac{3}{2}\left(\frac{S}{\varepsilon}\right)^2\right] \approx \frac{G\,M_{\rm p}}{\varepsilon^2}\left(\frac{S}{\varepsilon}\right). \tag{5.5}$$

As we will see in § 5.2.1, equation (5.5) can be interpreted as the sign-reversed gravitational force, per unit mass, exerted by a spherically homogeneous medium of radius ε. Thus, the smoothing may act as an indicator of the size of the planet.

Equation (5.4) may be appropriate to describe the solid core of a protoplanet which does not possess any significant envelope. Indicating with q the planet-to-star mass ratio $M_{\rm p}/M_{\bigstar}$, in these computations we apply the potential $\Phi_{\rm p}^{\rm PM}$ in models with $q>6\times10^{-5}$, i.e., twenty times the Earth mass ($M_{\oplus}$) when $M_{\bigstar}=1\ M_{\odot}$. In all cases the smoothing parameter ε is set to 10% of the Hill radius $R_{\rm H}$ [1]. Along with equation (5.4), we introduce three alternative expressions for $\Phi_{\rm p}$, namely the potential of a homogeneous sphere ($\Phi_{\rm p}^{\rm HS}$); that describing a fully radiative and static envelope ($\Phi_{\rm p}^{\rm ST}$); and finally that proper for a fully convective and static envelope ($\Phi_{\rm p}^{\rm KW}$). A comparative example of their behavior is reported in Figure 5.1.

Among the last three solutions, only the gravitational potential generated by a homogeneous sphere has a completely different behavior from that given in equation (5.4), while $\Phi_{\rm p}^{\rm ST}$ as well as $\Phi_{\rm p}^{\rm KW}$ compare better to a smoothed point-mass potential. This is clearly seen in Figure 5.1 and formally shown in § 5.2.1 and § 5.2.1. Thereupon, one should expect that computation results should depend only marginally on the adopted gravitational potential, except when $\Phi_{\rm p}=\Phi_{\rm p}^{\rm HS}$.

[1] The Hill sphere is a measure of the volume of the Roche lobe. In a purely restricted three-body problem, parcels of matter inside the Roche lobe are gravitationally bound to the secondary. Hence, they are confined to that volume of space.

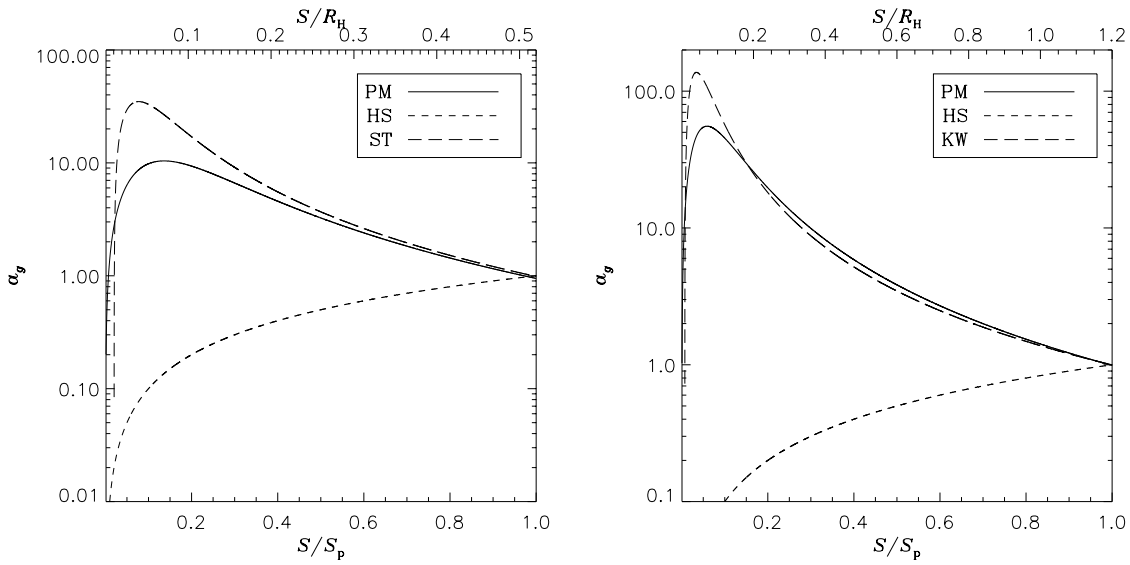

Figure 5.1: **Left panel.** Gravitational acceleration ($-\partial\Phi_{\rm p}/\partial S$) inside a $20\,M_{\oplus}$ planet as generated by the three potential functions $\Phi_{\rm p}^{\rm PM}$, $\Phi_{\rm p}^{\rm HS}$, and $\Phi_{\rm p}^{\rm ST}$ (eqs. [5.4], [5.6], and [5.7] respectively). Accelerations are normalized to $-G\,M_{\rm p}/S_{\rm p}^2$, where $S_{\rm p}$ is the envelope radius. The core mass (see § 5.2.1) is $15\,M_{\oplus}$ while $S_{\rm p} = 0.52\,R_{\rm H}$. The core is supposed to have a density of $5.5\ {\rm g\,cm^{-3}}$. The point-mass potential is smoothed over a length $\varepsilon = 0.1\,R_{\rm H}$ whereas in the Stevenson's potential $\delta = 5 \times 10^{-2}\,R_{\rm H}$. **Right panel.** The same quantity is displayed inside a $90\,M_{\oplus}$ planet but this time involving the potential solution $\Phi_{\rm p}^{\rm KW}$ (eq. [5.9]). The adiabatic exponent is $\Gamma = 1.43$ while the core mass is $60\,M_{\oplus}$. In all circumstances, the gravitational potential outside the envelope radius is of the type given in equation (5.4).

Homogeneous Sphere Solution

The gravitational potential generated by a homogeneous spherical distribution of matter can be calculated in a straightforward way by a direct integration of the gravitational force. Thereby one finds

$$\Phi_{\rm p}^{\rm HS} = \begin{cases} -\frac{G\,M_{\rm p}}{2\,S_{\rm p}}\left[3 - \left(\frac{S}{S_{\rm p}}\right)^2\right] & \text{if} \quad S \leq S_{\rm p} \\ \\ -\frac{G\,M_{\rm p}}{S} & \text{if} \quad S > S_{\rm p} \end{cases}, \tag{5.6}$$

where $S_{\rm p}$ is the radius of the sphere, i.e., the planet's radius. No smoothing is needed in this case since the force converges linearly to zero as the distance S approaches zero. Thus, there is no risk of numerical instabilities.

Strictly speaking, equation (5.6) is valid inside very extended and nearly homogeneous envelopes without considerable cores. Then, one may think of the functions $\Phi_{\rm p}^{\rm PM}$ and $\Phi_{\rm p}^{\rm HS}$ as rendering two opposite extreme situations. Though $\Phi_{\rm p}^{\rm HS}$ does not represent a

very realistic scenario of planet formation, for the sake of comparison and completeness, we will apply this potential to high- as well as low-mass bodies.

Stevenson's Solution

Stevenson (1982) proposed a simplified analytical model of protoplanets having envelopes with constant opacity and surrounding an accreting solid core. He developed a *radiative zero solution* for hydrostatic and fully radiative spherical envelopes, which implies that both hydrostatic and thermal equilibrium are assumed inside the planet's atmosphere. Under these hypotheses, the core can grow up to a *critical mass* whose value is that beyond which at least one of the two equilibria ceases to exist (see discussion in Wuchterl 1991) and the structure cannot be strictly static any longer. The critical core mass also sets an upper limit to the envelope and total mass of the planet. It can be proved that, at this critical point, $M_{\rm c}/M_{\rm p} = 3/4$, where the mass of the core $M_{\rm c}$ is influenced by neither the nebula density nor its temperature.

The potential of the gravitational field established by a fully radiative envelope can be obtained from the density profile (see Stevenson 1982) by applying the Poisson equation. Since the solid core size is by far below the resolution limit of these computations, the form of the Stevenson's potential can be cast in the form

$$\Phi_{\rm p}^{\rm ST} = \begin{cases} -\frac{G\,M_{\rm c}}{\sqrt{S^2+\delta^2}} - \frac{G\,M_{\rm e}^{\dagger}}{\sqrt{S^2+\delta^2}}\left[1 - \left(\frac{S}{S_{\rm p}}\right) + \ln\left(\frac{S}{S_{\rm c}}\right)\right] & \text{if} \quad S \le S_{\rm p} \\ -\frac{G\,M_{\rm p}}{\sqrt{S^2+\delta^2}} & \text{if} \quad S > S_{\rm p} \end{cases} . \tag{5.7}$$

In equation (5.7) we have indicated with $S_{\rm c}$ the core radius. The quantity $M_{\rm e}^{\dagger}$ is equal to the planet's envelope mass $M_{\rm e} = M_{\rm p} - M_{\rm c}$ divided by $\ln(S_{\rm p}/S_{\rm c})$. The presence of the parameter δ, also in the solution valid outside the envelope, is necessary for continuity reasons at $S = S_{\rm p}$. In these simulations we set $\delta = 0.05\,R_{\rm H}$.

If the core has a density $\rho_{\rm c} = 5.5\ {\rm g\,cm^{-3}}$ and accretes at the rate of $5 \times 10^{-7}\ M_{\oplus}\,{\rm yr^{-1}}$, assuming an envelope opacity equal to $1\ {\rm cm^2\,g^{-1}}$ and a mean molecular weight of 2.2, the critical total mass is $36\ M_{\oplus}$. Hence we will use equation (5.7) only for protoplanets whose total mass $M_{\rm p}$ is less than that value. Furthermore, we will suppose that the ratio of the total planetary mass to the core mass is the critical one. Therefore the core mass is always known once the mass $M_{\rm p}$ is assigned a value. Then, supplying $\rho_{\rm c}$, the radius $S_{\rm c}$ can be fixed.

The effects caused by equation (5.7) are actually similar to those caused by equation (5.4), as seen in Figure 5.1. In a more formal way, inside of the sphere $S = S_{\rm p}$, the normalized difference $\mathcal{R}^{\rm ST}$ between the two gravitational fields can be quantified by the ratio of $\left|\partial\Phi_{\rm p}^{\rm ST}/\partial S - \partial\Phi_{\rm p}^{\rm PM}/\partial S\right|$ to $\partial\Phi_{\rm p}^{\rm PM}/\partial S$, that is

$$\mathcal{R}^{\rm ST} = \frac{1}{4\,\ln(S_{\rm p}/S_{\rm c})}\left[\left(\frac{\delta}{S}\right)^2 - \left(\frac{\delta}{S_{\rm p}}\right)\left(\frac{\delta}{S}\right) + \ln\left(\frac{S_{\rm p}}{S}\right)\right]. \tag{5.8}$$

In the above relation, the equality $\epsilon = \delta$ was imposed. $\mathcal{R}^{\rm ST}$ is a decreasing function of S. Referring to the models addressed in the left panel of Figure 5.1, $\mathcal{R}^{\rm ST} \simeq 5\%$ at $S/S_{\rm p} = 1/3$.

This result is only slightly affected by the mass of the planet because $S_{\rm p}$ is a slowly varying function of $M_{\rm p}$.

Wuchterl's Solution

Along with the fully radiative envelope, other static solutions were found. Following the track of Stevenson's arguments, Wuchterl (1993) developed an analytical model for protoplanets with spherically symmetric and fully convective envelopes. In this case the hydrostatic structure is determined by the constant entropy requirement that is appropriate when convection is very efficient. Supposing that the adiabatic exponent $\Gamma = {\rm d}\ln p/{\rm d}\ln\rho$ is constant throughout the envelope, integrating the envelope density one finds that a solution for the planet gravitational potential is

$$\Phi_{\rm p}^{\rm KW} = \begin{cases} -\frac{G\,M_{\rm c}}{\sqrt{S^2+\delta^2}} - \frac{G\,M_{\rm e}^{\ddagger}}{\sqrt{S^2+\delta^2}} \left[\left(\frac{\zeta}{\zeta-1}\right)\left(\frac{S}{S_{\rm p}^{\Gamma}}\right) - \left(\frac{1}{\zeta-1}\right)\left(\frac{S}{S_{\rm p}^{\Gamma}}\right)^{\zeta} - \Pi \right] & \text{if} \quad S \le S_{\rm p}^{\Gamma} \\ -\frac{G\,M_{\rm p}}{\sqrt{S^2+\delta^2}} & \text{if} \quad S > S_{\rm p}^{\Gamma} \end{cases}, \tag{5.9}$$

where we set $\zeta = (3\,\Gamma - 4)/(\Gamma - 1)$ and $\Pi = (S_{\rm c}/S_{\rm p}^{\Gamma})^{\zeta}$. Moreover, the envelope mass is written as $M_{\rm e} = (1-\Pi)\,M_{\rm e}^{\ddagger}$. The condition for stability of gas spheres ($\Gamma > 4/3$) implies that ζ is positive. This particular form of $\Phi_{\rm p}^{\rm KW}$ is obtained by choosing an envelope radius equal to $S_{\rm p}^{\Gamma} = (\Gamma - 1)\,R_{\rm ac}$, with $R_{\rm ac} = G\,M_{\rm p}/c_{\rm s}^2$ the accretion radius. Outside $R_{\rm ac}$ the thermal energy of the gas is higher than the gravitational energy binding it to the planet.

As in Stevenson's solution, critical mass values exist for the envelope structure to be static. However, unlike the fully radiative envelope case, now the critical core mass depends on both the temperature and the density of ambient material. Furthermore, the critical mass ratio is $M_{\rm c}/M_{\rm p} = 2/3$ (for details see Wuchterl 1993). Setting Γ to 1.43 and the mean molecular weight to 2.2, if nebula conditions are $T_{\rm Neb} = 100$ K and $\rho_{\rm Neb} = 10^{-10}\ {\rm g\,cm^{-3}}$, the critical total mass is $M_{\rm p} = 274\ M_{\oplus}$.

Wuchterl's solution well applies to massive protoplanets since they are likely to bear convective envelopes.

Concerning the differences between equation (5.9) and equation (5.4), the situation is alike to that met in § 5.2.1 (see right panel of Fig. 5.1). In this circumstance, for $S \le S_{\rm p}$, the normalized difference can be written as

$$\mathcal{R}^{\rm KW} = \left(\frac{1}{3}\right)\,\frac{1}{1-\Pi}\left\{1 + \left(\frac{\zeta}{\zeta-1}\right)\left(\frac{\delta}{S_{\rm p}}\right)\left(\frac{\delta}{S}\right)\left[1 - \left(\frac{S}{S_{\rm p}}\right)^{\zeta-1}\right] - \left(\frac{S}{S_{\rm p}}\right)^{\zeta}\right\}. \tag{5.10}$$

As before, the equality $\epsilon = \delta$ is assumed and $\mathcal{R}^{\rm KW}$ decreases with S. Using the parameters adopted for the models illustrated in the right panel of Figure 5.1, $\mathcal{R}^{\rm KW} \simeq 18\%$ at $S/S_{\rm p} = 1/3$. In the considered range of masses, this number is nearly constant. In fact, equation (5.10) can be approximated to

$$\mathcal{R}^{\rm KW} \approx \left(\frac{1}{3}\right)\left[1 - \left(\frac{S}{S_{\rm p}}\right)^{\zeta}\right]. \tag{5.11}$$

5.2.2 Physical Parameters

We consider a protostellar disk orbiting a one solar mass star. The simulated region extends for $2\,\pi$ around the polar axis and, radially, from 2.08 to 13 AU. The aspect ratio is fixed to $h = 0.05$ throughout these computations. As in CHAPTER 2, the disk is assumed to be symmetric with respect to its midplane. This allows us to reduce the latitude range to the northern hemisphere only, where θ varies between 80° and 90°. The co-latitude interval includes 3.5 disk scale heights and therefore it assures a vertical density drop of more than six orders of magnitude (see § 5.3.3). The mass enclosed within this domain is $M_\mathrm{D} = 3.5 \times 10^{-3}\ M_\odot$, which implies, in our case, that a mass equal to $0.01\ M_\odot$ is confined inside 26 AU. Disk material is supposed to have a constant kinematic viscosity $\nu = 10^{15}\ \mathrm{cm^2\,s^{-1}}$, corresponding to $\alpha = 4 \times 10^{-3}$ at the planet location.

The orbital radius of the planet is $R_\mathrm{p} = 5.2$ AU and its azimuthal position is fixed to $\varphi = \varphi_\mathrm{p} = \pi$. We concentrate on a mass range stretching from $1.5\ M_\oplus$ to one Jupiter mass ($M_\jupiter$), implying that the mass ratio $q = M_\mathrm{p}/M_\star \in [4.5 \times 10^{-6}, 10^{-3}]$ if $M_\star = 1 M_\odot$. A detailed list of the examined planetary masses, along with the adopted potential form is given in Table 5.1.

The choice of few of the above parameters represents one typical example during the early phase of plant formation. Additionally these simulations offer the good advantage that in fact the system of equations is cast in a non-dimensional form, thus all of the outcomes are "scale-free" with respect to $M_\star$, M_D, and R_p.

According to studies of the early evolution of protoplanets, the Roche lobe is usually filled during the growth phase. In such calculations the envelope is allowed to extend to either the Hill radius R_H or the accretion radius R_ac (Bodenheimer and Pollack 1986; Wuchterl 1991; Tajima and Nakagawa 1997). Except for Wuchterl's solution, where we set $S_\mathrm{p} = S_\mathrm{p}^\Gamma = (\Gamma - 1)\, R_\mathrm{ac}$, the estimates of planet radii used in the simulations were provided by P. Bodenheimer (2001, private communication). They originate from a combination of R_H and R_ac at an ambient temperature of $T = 100$ K (see Fig. 5.2). The values of S_p, employed in each model, are also reported in Table 5.1.

It is worthwhile to stress that the planetary (or more properly, the envelope) radius S_p does not represent any real physical boundary but only the distance beyond which the planet's potential reduces to one of the type given in equation (5.4).

5.3 Numerical Issues

The set of hydrodynamic equations that characterize the temporal evolution of a disk-planet system is solved numerically by means of a finite difference scheme provided by an early FORTRAN-coded version of NIRVANA (Ziegler and Yorke 1997; Ziegler 1998). The code has been modified and adapted to our purposes as described in CHAPTER 2, CHAPTER 3, and references therein. In order to investigate thoroughly the flow dynamics in the neighborhood of the planet, a sufficient numerical resolution is required. We accomplish that by employing a nested-grid strategy. This can be pictured as either a set of grids, each hosting an inner one, or a pyramid of levels: the main grid (level one) includes the whole computational domain, while inner grids (higher levels) enclose smaller volumes around

Table 5.1: List of all the simulated planet masses: $q = M_{\rm p}/M_\star$ is the non-dimensional quantity that enters the simulation. Note that $M_{\rm p} = 333\ M_{\jupiter} = 1.05\ M_{\saturn}$. The ratio $R_{\rm H}/a$ is equal to $(q/3)^{1/3}$ (see § 5.2.1). Unless stated otherwise, envelope radii $S_{\rm p}$ are expressed through a combination of the Hill ($R_{\rm H}$) and the accretion ($R_{\rm ac}$) radius of the planet, as plotted in Figure 5.2 (courtesy of P. Bodenheimer). When required, we set $M_{\rm c} = (2/3)\,M_{\rm p}$ for a fully convective envelope and $M_{\rm c} = (3/4)\,M_{\rm p}$ for a fully radiative one. The core radius is computed assuming a constant density $\rho_{\rm c} = 5.5\ {\rm g\,cm^{-3}}$ in both cases.

$M_{\rm p}{}^{(a)}\ /M_{\jupiter}$	q	$S_{\rm p}/R_{\rm H}$	$R_{\rm H}/a$	Potential
333	1.00×10^{-3}	0.87	6.9×10^{-2}	PM, HS
253	7.60×10^{-4}	$2.30^{(b)}$	6.3×10^{-2}	KW
166	5.00×10^{-4}	$0.78, 1.70^{(b)}$	5.5×10^{-2}	PM, KW, HS
93	2.80×10^{-4}	$1.20^{(b)}$	4.5×10^{-2}	KW
67	2.00×10^{-4}	$0.70, 0.96^{(b)}$	4.0×10^{-2}	PM, KW
33	1.00×10^{-4}	0.60	3.2×10^{-2}	PM, HS
29	8.80×10^{-5}	0.58	3.1×10^{-2}	ST
20	6.00×10^{-5}	0.52	2.7×10^{-2}	HS, ST
15	4.50×10^{-5}	0.46	2.5×10^{-2}	ST
12.5	3.75×10^{-5}	0.44	2.3×10^{-2}	ST
10	3.00×10^{-5}	0.38	2.1×10^{-2}	PM, HS, ST
7	2.10×10^{-5}	0.34	1.9×10^{-2}	ST
5	1.50×10^{-5}	0.29	1.7×10^{-2}	HS, ST
3	1.00×10^{-5}	0.23	1.5×10^{-2}	ST
1.5	4.50×10^{-6}	0.16	1.1×10^{-2}	ST

$^{(a)}$ Values are rounded to the nearest integer numbers.
$^{(b)}$ Planetary radius used in the Wuchterl's solution: $S_{\rm p} = S_{\rm p}^{\Gamma} = (\Gamma - 1)\,R_{\rm ac}$ (see § 5.9).

the planet, with increasing resolution. Levels greater than one are also called subgrids since they are usually smaller in size. The linear resolution, in each direction, doubles when passing from a grid to the inner one.

The basic principles upon which the nested-grid technique relies and how it is applied to disk-planet simulations in two dimensions is explained in detail in CHAPTER 3 and references therein. The extension to the three-dimensional geometry, though requiring some more complexity in the exchange of information from one grid level to the neighboring ones, is nearly straightforward (see CHAPTER 3 for details).

5.3.1 General Setup

For the study of the variety of planetary masses indicated in Table 5.1, meeting both the requirements of high resolution and affordable computing times, we realized a series of five grid hierarchies, whose characteristics are given in Table 5.2. With mass ratios q larger than 2×10^{-4} ($67\ M_{\jupiter}$) only grids G0 and G1 are utilized whereas smaller bodies are investigated with the other grid hierarchies. Thereupon, the finest resolution we obtain

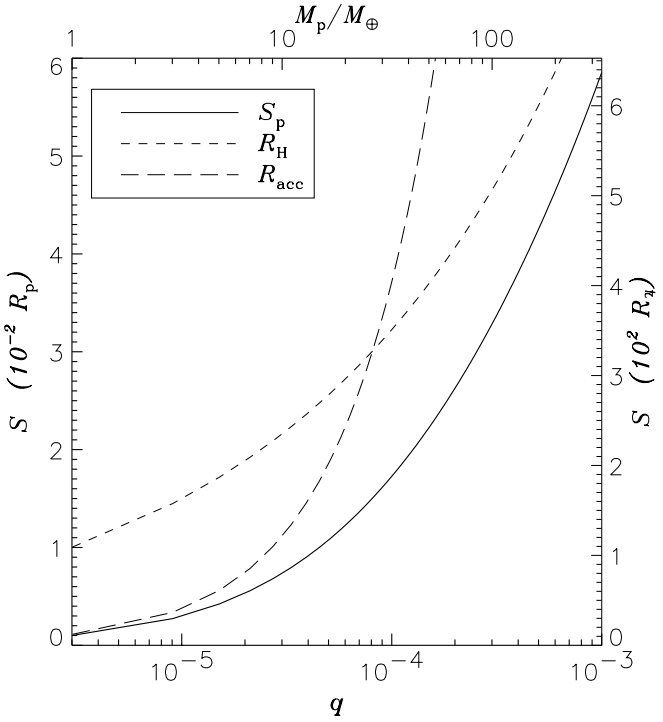

Figure 5.2: Envelope radius S_p, as provided by P. Bodenheimer (2001, private communication), compared to the Hill radius R_H and the accretion radius R_acc. In a locally isothermal disk with aspect ratio h, R_H is larger than R_ac when $q < h^3/\sqrt{3}$. While the scale of the left vertical axis is referred to orbital radius $R_\mathrm{p} = 5.2$ AU, the scale on the right one is compared to the radius of Jupiter $R_\downarrow = 7.1 \times 10^4$ km.

in the whole set of simulations varies form 0.03 to $0.06\,R_\mathrm{H}$. In all of the models presented here, the planet is centered at the corner of a main grid cell, which property is retained on any higher hosted subgrid. As the planet radial distance is $R_\mathrm{p} = a/(1+q)$, we adjust it by tuning the value of the star-planet distance a. Adjustments never exceed 0.7% over the nominal value of R_p given in § 5.2.2. Every model is evolved at least till 200 orbits. The evolution of massive planets ($M_\mathrm{p} \geq 67\ M_\downarrow$) is followed for 300 to 400 orbital periods because they take longer to settle on a quasi-stationary state.

Gas accretion is estimated following the procedure sketched in CHAPTER 4. For better accuracy, mass is removed only from the finest grid level according to an accretion sphere radius κ_ac and an evacuation parameter κ_ev. The former defines the spherical volume which contributes to the accretion process whereas the latter can be regarded as a measure of the removal time scale in such volume. Two-dimensional simulations showed that the procedure is fairly stable against these two parameters. We constrain the amount of removed mass per unit volume not to exceed 1% of that available, as was done in CHAPTER 4. Regarding the extension of the sphere of accretion κ_ac, we performed simulations using different values, as stated in Table 5.3. Since the planet actually works as a sink, our procedure only furnishes upper limits to realistic planetary accretion rates (see discussion in Tanigawa and Watanabe 2002).

However, we also inquire how mass removal can possibly affect gravitational torques and, more generally, the dynamics of the flow in the planet neighborhood by means of models in which accretion is prohibited.

Table 5.2: Grid sizes are reported as the number of grid points per direction: $N_R \times N_\theta \times N_\varphi$. The third column ($ng$) indicates the number of levels within the hierarchy. In order to achieve sufficient resolution within the Roche lobe of the planet, grids G0 and G1 have been used only for planetary masses in the range $[67\ M_{\jupiter}, 1\ M_{\earth}]$. Grids are ordered according to their computing time requirements, which grow from top to bottom. The hierarchy G5 has been employed to execute the model with $M_{\rm p} = 12.5\ M_{\jupiter}$ (see discussion at the end of § 5.4.2).

Grid	Main Grid Size	ng	Subgrid Size	No. of models
G0	$121 \times 13 \times 319$	4	$54 \times 12 \times 48$	10
G1	$143 \times 13 \times 423$	4	$64 \times 12 \times 64$	5
G2	$121 \times 13 \times 319$	5	$54 \times 12 \times 48$	19
G3	$143 \times 13 \times 423$	5	$64 \times 12 \times 64$	12
G4	$121 \times 23 \times 319$	5	$54 \times 22 \times 48$	4
G5	$133 \times 13 \times 395$	5	$84 \times 16 \times 84$	1

5.3.2 Boundary Conditions

In order to mimic the accretion of the flow towards the central star, an outflow boundary condition is applied at the inner radial border of the computational domain. The outer radial border is closed, i.e., no material can flow in or out of it. The same condition exists at the highest latitude $\theta = 80°$. Since the disk is symmetric with respect to its midplane as mentioned in § 5.2.2, symmetry conditions are set at $\theta = 90°$. On subgrids, except for the midplane where symmetry conditions are applied, boundary values are interpolated from hosting grids, by means of a monotonised second-order algorithm (see CHAPTER 3 for details).

The open inner radial boundary causes the disk to slowly deplete during its evolution. For all the models under study, we observe a depletion rate $\dot{M}_{\rm D} = -\dot{M}_{\star}$ measuring $\approx 10^{-8}\ M_{\odot}\,{\rm yr}^{-1}$, in agreement with the expectations of stationary Keplerian disks: $\dot{M}_{\star} = 3\,\pi\,\nu\,\Sigma$ (Lynden-Bell and Pringle 1974).

In cases of gap formation, material residing inside the planet's orbit tends to drain out of the computational domain. Since this material transfers angular momentum to the planet, the lack of it may contribute to reduce both the migration time scale and the planet's accretion rate. To evaluate these effects, a Jupiter mass model was run with a closed (i.e., reflective) inner radial border.

5.3.3 Initial Conditions

The initial density distribution is a power-law of the distance from the rotational axis $r = R\,\sin\theta$ times a Gaussian in the vertical direction

$$\rho(t=0) = \rho_0(r)\,\exp\left[-\left(\frac{\cot\theta}{h}\right)^2\right], \tag{5.12}$$

Table 5.3: The parameter $\kappa_{\rm ac}$ represents the radius of the accreting region. Within this sphere the mass density is reduced by roughly 1% after every time step. The length $\kappa_{\rm ac} = 0.1\,R_{\rm H}$ should be small enough to make the accretion procedure almost independent of the evacuation parameter $\kappa_{\rm ev}$ (Tanigawa and Watanabe 2002). At $q = 3 \times 10^{-5}$ ($M_{\rm p} = 10\ M_{\jupiter}^{\pm}$) a non-accreting simulation was performed with $\Phi_{\rm p} = \Phi_{\rm p}^{\rm HS}$ (eq. [5.6]) as well as with $\Phi_{\rm p} = \Phi_{\rm p}^{\rm ST}$ (eq. [5.7]). In the case of lowest mass model ($M_{\rm p} = 1.5\ M_{\jupiter}^{\pm}$), we allowed the ratio $\kappa_{\rm ac}/S_{\rm p}$ to be less than 0.5, as in all of the other models. For a better evaluation of $\dot{M}_{\rm p}$, we used a modified version of the grid system G3 which contains a sixth level, comprising (approximately) the planet's Hill sphere.

$M_{\rm p}/M_{\jupiter}^{\pm}$	q	$\kappa_{\rm ac}/R_{\rm H}$	Accreting Only[a]
333	1.0×10^{-3}	0.20, 0.15, 0.10	No
253	7.6×10^{-4}	0.10	Yes
166	5.0×10^{-4}	0.10	Yes
93	2.8×10^{-4}	0.10	Yes
67	2.0×10^{-4}	0.20, 0.10	No
33	1.0×10^{-4}	0.20, 0.10	No
29	8.8×10^{-5}	0.20, 0.10	No
20	6.0×10^{-5}	0.15, 0.10	No
15	4.5×10^{-5}	0.10	Yes
12.5	3.75×10^{-5}	0.10	Yes
10	3.0×10^{-5}	0.10	No
7	2.1×10^{-5}	0.10	Yes
5	1.5×10^{-5}	0.10	No
3	1.0×10^{-5}	0.10	Yes
1.5	4.50×10^{-6}	0.07	Yes

[a] " No" entry stands for the existence of a non-accreting model.

which is appropriate for a thin disk in thermal and hydrostatic vertical equilibrium. The dependency of the midplane value $\rho_0(r)$ with respect to r is such that the initial surface density profile Σ decays as $1/\sqrt{r}$, as required by the constant kinematic viscosity. However, we also ran a few models where the form of $\rho_0(r)$ is such to account for an axi-symmetric gap, as often done to speed up the computations at early evolutionary times.

The initial velocity field of the fluid is a purely, counter-clockwise, Keplerian one corrected by the grid rotation: $\boldsymbol{u}(t=0) \equiv (0, 0, v_{\rm K} - \Omega_{\rm p}\, r)$. Thus, the partial support due to the radial pressure gradient is neglected in the beginning.

5.4 Simulation Results

5.4.1 Flow Dynamics near Protoplanets

Two-dimensional computations have shown that a circumplanetary disk forms around Jupiter-type planets, extending over the size of its Roche lobe (Kley 1999; Lubow et al.

1999; Tanigawa and Watanabe 2002). The numerical experiments conducted in CHAPTER 4 proved this characteristic to belong not only to massive bodies but also to protoplanets as small as $3\ M_{\sun}$. It was demonstrated that the flow of such disks is approximately Keplerian down to distances $\sim 0.1\,R_{\rm H}$ from the planet. One of the main features of these disks is a two-arm spiral shock wave whose opening angle (that between the wave front and the direction toward the planet) is an increasing function of the mass ratio q and, below $M_{\rm p} = 67\ M_{\sun}$, it is roughly given by $\arctan(\mathcal{M})$, in which $\mathcal{M} = |\boldsymbol{u}|/c_{\rm s}$ is the Mach number of the circumplanetary flow. The spiral patterns shorten and straighten as the perturber mass decreases (see § 4.4.3). Eventually, for even smaller masses they disappear and are not observable anymore when one Earth mass is reached.

Three-dimensional simulations shed new light on these circumplanetary disks, demonstrating that they can behave somehow differently from what depicted by two-dimensional descriptions. Differences become more marked as the mass of the embedded protoplanet is lowered. A major point is that spiral waves are not so predominant as they are in the 2D geometry. This is clearly seen in the left columns of Figure 5.3 and 5.4, where the midplane ($\theta = \pi/2$) density is displayed for four different planetary masses. The double pattern of the spiral is still visible around a $67\ M_{\sun}$ protoplanet (Fig. 5.3, bottom left panel). However, when considering a planet half of that size, spiral traces are too feeble to be seen on the image (Fig. 5.4, top left panel). Such an occurrence was to be expected since the energy of the flow is not only converted into the equatorial motion but can be also transferred to the vertical motion of the fluid. It was already known from wave theories for circumstellar disks (Lubow 1981; Lubow and Pringle 1993; Ogilvie and Lubow 1999) and related numerical calculations (Makita et al. 2000) that the three-dimensional propagation of spiral perturbations may be significantly different from that obtained in two dimensions because of the existence of vertical resonances. Furthermore, Miyoshi et al. (1999) already noted in their shearing sheet models the weakening effect of the finite disk thickness upon the formation of spiral waves around embedded protoplanets. Hence we may argue that the averaging of the pressure and the gravitational potential, which is accomplished in an infinitesimally thin disk, enhances spiral features in disks.

The remainder of this section is devoted to a general description of the vertical circulation of the material in the vicinity of the planet. We start inspecting what happens in the slice $\varphi = \varphi_{\rm p}$, i.e., in the R–θ surface containing the planet (see middle panels in Fig. 5.3 and 5.4). The first thing to note is that the material above the equatorial plane moves toward the planet with a negligible meridional component, in fact $|u_\theta| \ll u$ (where $u = |\boldsymbol{u}|$). Therefore matter is nearly confined to θ-constant surfaces. This circumstance favors the use of 2D outcomes as predictions of 3D expectations (Masset 2002). However this turns out to be true only far away from the planet. In fact, as the fluid enters a certain region around the Hill sphere, its dynamics changes drastically. The beginning of this zone is marked by two shock fronts, which actually develop well outside the Roche lobe of the restricted three body problem. The distance of the shock fronts from the perturber, if compared to $R_{\rm H}$, shrinks from 2.61 to 1.16 as $M_{\rm p}$ is increased from $10\ M_{\sun}$ to $1\ M_{\jupiter}$. Generally, shocks are not placed symmetrically with respect to the planet. Past these shocks, material is deflected upward and recirculates downward, while approaching the radial position of the planet (see middle panels in Fig. 5.3 and 5.4).

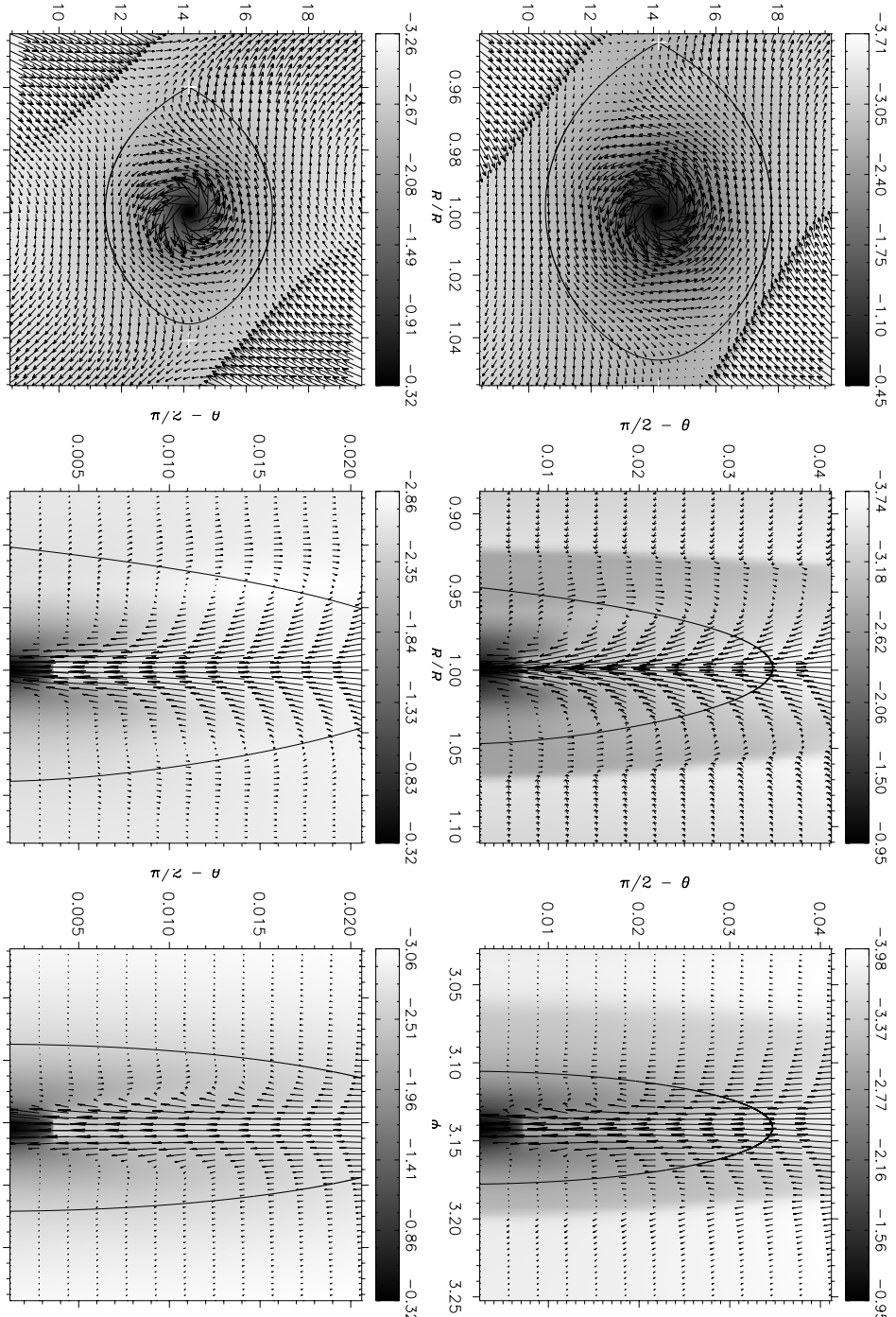

Figure 5.3: Density slices with an overplotted two-component velocity field. In order to comprise the whole density range, the color scale represents the logarithm of the density ($\log \rho$). The evolutionary time is 200 orbital periods. Slices are cut at the planet location: $\theta = \pi/2$ **(left)**, $\varphi = \varphi_\mathrm{p}$ **(middle)**, and $R = R_\mathrm{p}$ **(right)**. Both models are accreting and executed with Wuchterl's potential. In physical units, $\rho = 10^{-2}$ is equivalent to $4.22 \times 10^{-11}\ \mathrm{g\,cm^{-3}}$. **Top panels**. Planet with a total mass $M_\mathrm{p} = 166\ M_\oplus$ and a core mass equal to $2/3\, M_\mathrm{p}$ (critical core mass). **Bottom panels**. Planet with $M_\mathrm{p} = 67\ M_\oplus$ and a critical core mass. The curve drawn in each panel indicates the trace of the Roche lobe. In the left and right top panels, the flow reaches velocities equal to ~ 3 and $\sim 2\ \mathrm{km\,s^{-1}}$, respectively. In the other panels, maximum velocities are on the order of $\sim 4\ \mathrm{km\,s^{-1}}$.

At $R \approx R_{\rm p}$, matter suffers an unbalanced gravitational attraction by the planet and accelerates downward towards it. Velocities are supersonic, reaching a Mach number $\mathcal{M} \simeq 8$, when 67 $M_{\earth} \lesssim M_{\rm p} \leq 1\ M_{\jupiter}$, and $\mathcal{M} \simeq 2$ if $M_{\rm p} = 20\ M_{\earth}$. They become subsonic for planetary masses between 10 and 1.5 $M_{\earth}$, ranging from 30 to 5% of the local sound speed. Because of the sinking material, at $\theta = \pi/2$ the flow field is slightly horizontally divergent from the planet location.

As one can judge from Figure 5.4 (middle panels), the flow gets less and less symmetric, with respect to $R_{\rm p}$, as the planet mass is reduced. Recirculation persists before the planet ($R < R_{\rm p}$) but vanishes behind it ($R > R_{\rm p}$). Any symmetry disappears starting from $M_{\rm p} = 5\ M_{\earth}$ downwards.

Along the azimuthal direction (slice $R = R_{\rm p}$, i.e., in the surface φ–θ containing the planet), the right panels of Figure 5.3 and 5.4 show an even more complex situation. Below 166 $M_{\earth}$, the region of influence of the planet appears to be more comparable in size with the Roche lobe. However, apart from that, the general behavior of the flow differs from case to case, having in common a rapid descending motion when the material lies above the planet. Around Jupiter-sized planets some kind of weak, non-closed, recirculation may be seen. This flow feature is still present at both sides of a 29 $M_{\earth}$ planet (top right panel, Fig. 5.4), whereas it tends to vanish in models with lower q-ratios.

Non-accreting Protoplanets

Here we should dedicate some attention to the differences existing between accreting and non-accreting protoplanets. Since the gas is locally isothermal, pressure is proportional to the density according to equation (5.2). Because of the mass removal, density nearby the planet is lower in accreting models than it is in non-accreting ones. In Table 5.4 the mass $\widehat{M}_{\rm e}$ enclosed within the envelope radius $S_{\rm p}$ is quoted for the two sets of models, along with the mean density $\widehat{\rho}_{\rm e}$. These values demonstrate that the amount of material contained in the volumes of non-accreting planets can be considerably larger than in the other case (even 6 times as much). Since the pressure must converge in the two cases, when the distance from the planet $S \gg S_{\rm p}$, a higher mean pressure in the envelope intuitively implies a larger magnitude of the pressure gradient inside this region.

As an example, we illustrate in Figure 5.5 the velocity field in two perpendicular slices $\theta = \pi/2$ (i.e., the equatorial plane) and $\varphi = \varphi_{\rm p}$ (i.e., the surface R–θ passing through the planet), in order to show how the enhanced density values affect the local circulation. The targeted body has $M_{\rm p} = 20\ M_{\earth}$ because, among the eight available models for which accretion is not considered (see Table 5.3), this is the one that suffers an orbital migration substantially different from accreting counterpart models. From the isodensity lines displayed in Figure 5.5, one can infer that matter is spherically distributed around the non-accreting protoplanet (upper panels). For this reason the net torque arising within a region of radius $\approx R_{\rm H}$ is nearly zero. This does not happen in the other case because the symmetry is not so strict.

The lower left panel clearly indicates the existence of a rough balance between gravitational and centrifugal force, with the pressure gradient playing a marginal role in opposing the planet potential gradient. On the other hand, from the circulation in the upper-left

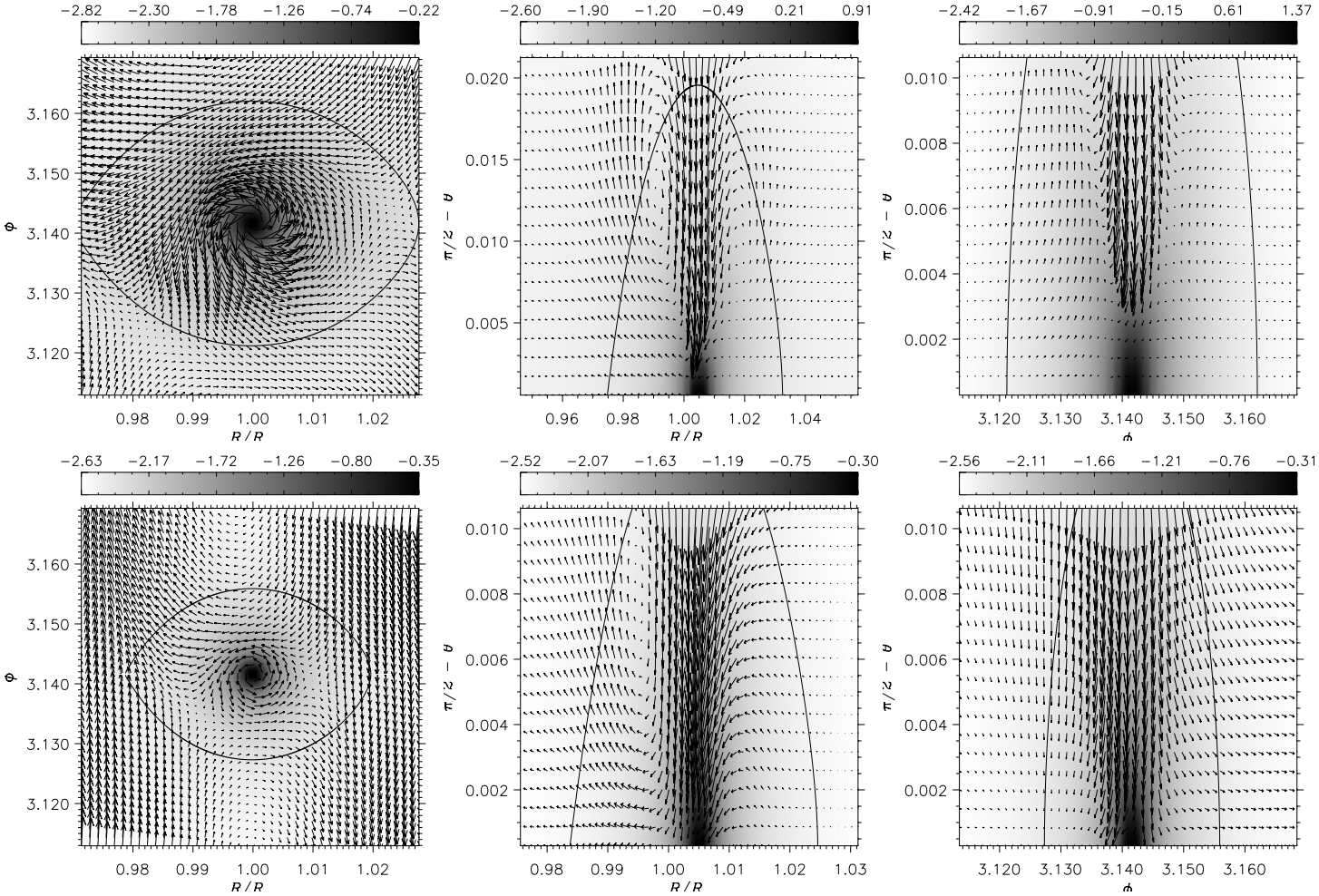

Figure 5.4: Density slices of the same type as in Figure 5.3, illustrating low-mass accreting planets after 200 orbits. In these simulations, Stevenson's potential is employed. In physical units, the density scale is as in Figure 5.3. The density value $\rho = 10^{-2}$ corresponds to $4.22 \times 10^{-11}\ \mathrm{g\,cm^{-3}}$. **Top panels**. Planet with $M_\mathrm{p} = 29\ M_{\oplus}$ and a critical core mass $M_\mathrm{c} = 21.7\ M_{\oplus}$. Maximum flow speeds are around $1\ \mathrm{km\,s^{-1}}$ in each of the three panels. **Bottom panels**. Planet with $M_\mathrm{p} = 10\ M_{\oplus}$ and a core mass and $M_\mathrm{c} = 7.5\ M_{\oplus}$. Inside of the Hill sphere, maximum velocities are on the order of $0.2\ \mathrm{km\,s^{-1}}$.

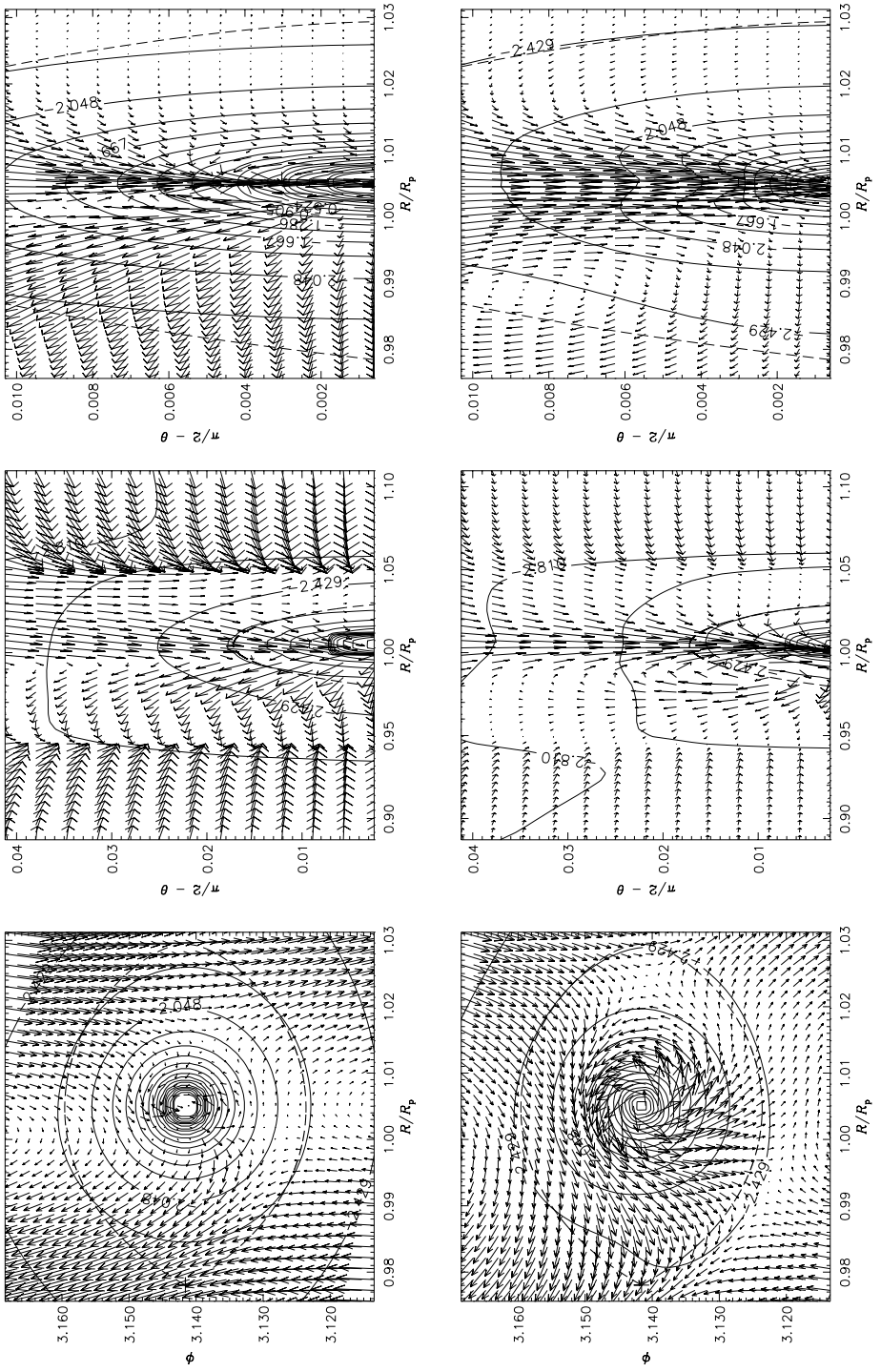

Figure 5.5: Two-component velocity field on the equatorial plane (first column) and on the slice $\varphi = \varphi_{\rm p}$ (second and third columns) for a non-accreting, 20 $M_\oplus$ planet (**top panels**), and an accreting planet of the same mass (**bottom panels**) with an accreting sphere radius $\kappa_{\rm ac} = 0.15\,R_{\rm H}$. Lines of equal $\log\rho$ are also drawn. The dashed line represents the Roche lobe of the restricted three-body problem. In the accreting model, the equatorial flow ($\theta = \pi/2$) in the planet's envelope has a Mach number $\mathcal{M} \lesssim 1.2$ whereas, for the meridional flow, $\mathcal{M} \lesssim 2$. In the non-accreting computation the fluid travels subsonically in both the midplane and the meridional slice ($\mathcal{M} \lesssim 0.2$).

Table 5.4: All masses are relative to the Earth mass. The mean density $\widehat{\rho}_{\rm e}$ within the planet's radius is expressed in cgs units. We consider only simulations which were run with the Stevenson's potential. The mass $\widehat{M}_{\rm e}$ is evaluated assuming a disk mass $M_{\rm D} = 3.5 \times 10^{-3}\, M_{\odot}$. Hence, the values in the Table do not account for the disk depletion rate $\dot{M}_{\rm D}$, which is on the order of $3 \times 10^{-3}\, M_{\oplus}\, {\rm yr}^{-1}$.

	No Accretion		Accretion		
$M_{\rm p}$	$\widehat{M}_{\rm e}$	$\widehat{\rho}_{\rm e}$	$\widehat{M}_{\rm e}{}^{a}$	$\widehat{M}_{\rm e}{}^{b}$	$\widehat{M}_{\rm e}{}^{c}$
67	7.07×10^{-1}	9.37×10^{-11}	1.07×10^{-1}	...	7.67×10^{-2}
29	2.74×10^{-1}	1.45×10^{-10}	6.49×10^{-2}	...	...
20	2.26×10^{-1}	2.43×10^{-10}	3.68×10^{-2}	3.18×10^{-2}	...
10	1.29×10^{-2}	7.12×10^{-11}	9.76×10^{-3}	...	...
5	2.24×10^{-3}	5.56×10^{-11}	2.17×10^{-3}	...	...

$^{(a)}$ From models with $\kappa_{\rm ac} = 0.10\, R_{\rm H}$.
$^{(b)}$ From models with $\kappa_{\rm ac} = 0.15\, R_{\rm H}$.
$^{(c)}$ From models with $\kappa_{\rm ac} = 0.20\, R_{\rm H}$.

panel of Figure 5.5 one can deduce that the pressure gradient is no longer negligible compared to the potential gradient and can therefore counterbalance its effects.

Moreover, the flow above the disk midplane (upper center and upper right panels) suggests that gas is ejected at $R < R_{\rm p}$. Such phenomenon must be ascribed to the pressure gradient as well, since the fluid opposes any further compression. These qualitative arguments will be quantitatively corroborated in § 5.5, where we will show that the increased amount of matter causes the envelope to be pressure supported.

We mention in the caption of Figure 5.5 that the flow may travel supersonically within the atmospheric region, though both Stevenson's and Wuchterl's gravitational potential rely on the hypothesis of quasi-hydrostatic equilibrium. Such discrepancy can be attributed to the rate of mass removal from the innermost parts of the planet's envelope, which is not considered in the derivation of those analytic solutions. In fact, while supersonic speeds have been measured in some accreting models, the flow is always subsonic the envelope of non-accreting planets. This can be also understood with simple arguments. We said before in this section that mass accretion is responsible for the Keplerian-like circulation around protoplanets, in the disk midplane. Hence, the local (equatorial) Mach number should be on the order of $\sqrt{q\, R_{\rm p}/S}/h$. If evaluated at $S \approx S_{\rm p}$, this quantity yields $\mathcal{M} \approx 1.3$ for a $20\, M_{\oplus}$ body, which is comparable to the value reported in the caption of Figure 5.5. Along the vertical direction, if the velocity is approximated to that of a spherically accreting flow then $u_\theta \approx \dot{M}_{\rm p}/(4\,\pi\, S^2\, \rho)$. At $S = \kappa_{\rm ac} = 0.1\, R_{\rm H}$, that relation gives a (meridional) Mach number $\mathcal{M} \approx 1.8$ when applied to the accreting model shown in Figure 5.5. Also this number is similar to the measured value.

5.4.2 Gravitational Torques

Gravitational torques are believed to be responsible for the migration of protoplanets from their initial formation sites. In this work torques are directly estimated from the gravitational force exerted by each fluid element of the circumstellar disk on the planet. When computing the gravitational force, we consider the density solution on the finest available grid level. This procedure permits to obtain higher accuracy because of the increasing resolution of hierarchy levels.

Since the planet is an extended object, torques acting on each of its portions should be calculated and then added up to give the total torque vector, whose most general expression is

$$\boldsymbol{\mathcal{T}_{\mathbf{D}}} = \int_{M_{\rm D}} \int_{M_{\rm p}} (\boldsymbol{R}_{\rm p} + \boldsymbol{S}) \times \frac{G\, dM_{\rm D}(\boldsymbol{R})\, dM_{\rm p}(\boldsymbol{S})}{|\boldsymbol{R} - \boldsymbol{R}_{\rm p} - \boldsymbol{S}|^3}\, \boldsymbol{R}, \tag{5.13}$$

in which all of the gravitational contributions due to star, the planet, and disk self-gravity, etc. are implicitly enclosed in the differentials $dM_{\rm D}(\boldsymbol{R})$ and $dM_{\rm p}(\boldsymbol{S})$. Equation (5.13) explicitly states that circumstellar material can alter both the orbital and rotational spins of a protoplanet. However, here we shall confine our study to variations of the planet's orbital angular momentum because the evaluation of the rotational spin requires a rigorous treatment of the envelope self-gravity. This is not done here, as stated in § 5.2 (see eq. [5.1]). Thereby, we can proceed as if the whole planetary mass were concentrated in its geometrical center $\boldsymbol{R} = \boldsymbol{R}_{\rm p}$ and integrate the force over the whole disk domain, excluding the volume $\mathcal{V}_{\rm p}$ occupied by the planetary envelope. Yet, outside of such volume the gravitational potential is always that of a point-mass object (see the behavior of eqs. [5.4], [5.6], [5.7], and [5.9], for $S > S_{\rm p}$), therefore equation (5.13) simplifies and becomes

$$\boldsymbol{\mathcal{T}_{\mathbf{D}}} = \boldsymbol{R}_{\rm p} \times \int_{\boldsymbol{R} \notin \mathcal{V}_{\rm p}} \nabla \Phi_{\rm p}^{\rm PM}\, \rho(\boldsymbol{R})\, dV(\boldsymbol{R}). \tag{5.14}$$

The orbital angular momentum of a protoplanet can be affected only by the z-component (that parallel to the polar axis) of the torque vector $\boldsymbol{\mathcal{T}_{\mathbf{D}}}$. To avoid useless distinctions, we indicate this component as $\mathcal{T}_{\rm D}$. The sign of $\mathcal{T}_{\rm D}$ determines the gain (positive torques) or loss (negative torques) of orbital spin. Larger spins correspond to more distant orbits. Since torques generally change on time scales on the order of ~ 50 revolutions, we work with their final magnitudes. We usually observe a slow decay of $|\mathcal{T}_{\rm D}|$ with time (see end of § 5.4.4).

Two-dimensional computations reveal that torques exerted by circumplanetary material may amount to a fair fraction of the total torque, unless a suitable smoothing length (usually of the size of the Hill radius) is used in the planet gravitational potential $\Phi_{\rm p}$. This is caused by the high surface densities reached around the planet and the lack of a vertical torque decay which naturally occurs in three dimensions (see § 5.5). In fact, in 3D, we observe that torques arising from locations close to the planet do not play such an important role as they do in 2D.

Analyzing the relative strength of torques exercised by different disk portions, it turns out that in the mass range $q \in [2 \times 10^{-4}, 1 \times 10^{-3}]$, dominating negative torques arise from distances $S \gtrsim 1.2\, h\, R_{\rm p}$, where h is the disk aspect ratio. Below 33 $M_{\dot{\oplus}}$, the most effective

contributions are generated by material lying between $S \simeq 0.6\,h\,R_{\rm p}$ and $S \simeq 2.2\,h\,R_{\rm p}$. Therefore we can conclude that predominant torques are exerted at distances from the planet comparable with the Hill radius. Not more than 10% of $\mathcal{T}_{\rm D}$ is built up by matter located within $S \approx 0.6\,h\,R_{\rm p}$.

Apart from the $20\ M_{\oplus}$ protoplanet, the total torque evaluated in non-accreting models does not deviate considerably from that estimated in accreting ones, independently of the used potential. In fact, simulations based on the potentials $\Phi_{\rm p}^{\rm PM}$, $\Phi_{\rm p}^{\rm HS}$, and $\Phi_{\rm p}^{\rm ST}$ (eqs. 5.4, 5.6, and 5.7 respectively) supply values of $\mathcal{T}_{\rm D}$ which differ by less than 40%. This circumstance may signify that, whether or not a protoplanet is still accreting matter from its surroundings, this is not generally crucial to the gravitational torques by the circumstellar disk. Thereby, being an exception, the case $M_{\rm p} = 20\ M_{\oplus}$ deserves some comments. For such mass, the torque integrated over the first two grid levels ($S \gtrsim 2.2\,h\,R_{\rm p}$) yields a positive value for both accreting and non-accreting planets. When adding the contributions from the third and forth level ($0.6\,h\,R_{\rm p} \lesssim S \lesssim 2.2\,h\,R_{\rm p}$), the torque experienced by the planet lowers but, while it becomes negative in the accreting case, it still remains positive in the non-accreting counterpart. It is especially matter residing between 1 and $2\,R_{\rm H}$ from the planet that builds up the difference. As material in the uppermost grid level ($S \lesssim 0.6\,h\,R_{\rm p}$) of the non-accreting simulation does not exert any significant torques (some little negative contribution is indeed measured in the accreting model), $\mathcal{T}_{\rm D}$ keeps the positive sign although, in magnitude, it is eleven times as small as that evaluated in the accreting case. This phenomenon of torque reversal for non-accreting planets with masses of about $20\ M_{\oplus}$ may be related to the very long migration time scales obtained for fully accreting models having masses $M_{\rm p} \approx 10\,M_{\oplus}$ (see below, and Fig. 5.6).

5.4.3 Orbital Migration

Conservation of orbital angular momentum implies that a protoplanet has to adjust its orbital distance from the central star because of external torques exerted by the disk. If the orbit remains circular, the time scale over which this radial drift motion happens is inversely proportional to $\mathcal{T}_{\rm D}$, according to the formula:

$$\tau_{\rm M} = \frac{a}{|\dot{a}|} = \frac{M_{\rm p}\,a^2\,\Omega_{\rm p}}{2\,|\mathcal{T}_{\rm D}|}. \tag{5.15}$$

In equation (5.15) we indicated with $\Omega_{\rm p}$ and a the planet's angular velocity and its distance from the star, respectively. Linear, analytical theories (e.g., Ward 1997) provide two separate regimes governing the migration of low- (*type I*) and high-mass (*type II*) protoplanets. Both migration types predict that the planet moves toward the star. More recent studies by Masset (2001) and Tanaka et al. (2002) have reconsidered the role of co-orbital corotation torques and proved that they can be very effective in opposing Lindblad torques. Hence, they can significantly slow down inward migration. Two-dimensional results presented in CHAPTER 4 well fit to these predictions. A further reduction of the migration speed is expected from a full 3D treatment of torques, as also derived numerically by Miyoshi et al. (1999) and theoretically predicted by Tanaka et al. (2002).

Figure 5.6 shows our estimates for the migration time scale $\tau_{\rm M}$ as computed for models having different masses and in which the potential solutions $\Phi_{\rm p}^{\rm PM}$, $\Phi_{\rm p}^{\rm KW}$, and $\Phi_{\rm p}^{\rm ST}$ were

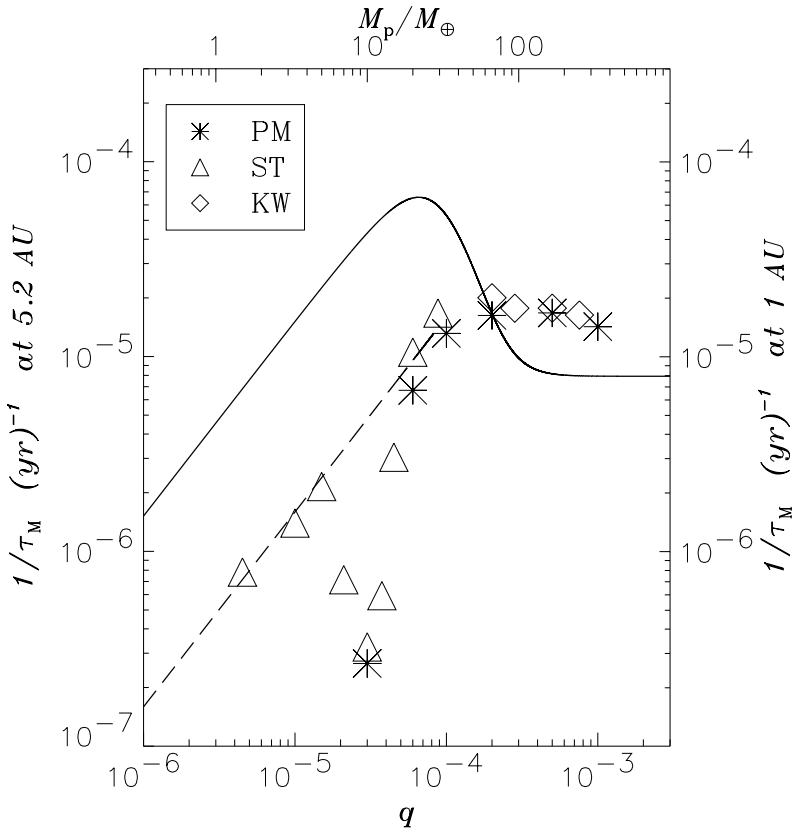

Figure 5.6: Migration time scale versus the mass ratio $q = M_{\rm p}/M_{\bigstar}$. Outcomes from simulations carried out with the various forms of gravitational potential are marked with different symbols. At $q = 10^{-4}$ and 6×10^{-5}, calculations carried out with the point-mass potential were initiated with a density gap (see § 5.3.3). To avoid confusion, migration rates obtained from models with $\Phi_{\rm p} = \Phi_{\rm p}^{\rm HS}$ (eq. [5.6]) are quoted in Table 5.5. The solid line represents the theoretical prediction by Ward (1997), which It does not include corotation torques and 3D effects. Both are indeed accounted for in the analytical model by Tanaka et al. (2002) (dashed line). The scale on the right vertical axis gives the migration rates of a protoplanet orbiting at 1 AU from the primary.

adopted. We compare these values with the two analytical theories developed by Ward (1997) (solid line) and Tanaka et al. (2002) (dashed line). The first of them comprises both migration regimes, though accounting only for Lindblad torques. The second theory is limited to type I migration, albeit it treats both Lindblad and corotation torques. Moreover, the first is explicitly two-dimensional whereas the second is applicable in two as well as three dimensions.

As one can see from Figure 5.6, numerical results are very similar for $M_{\rm p} \geq 67\ M_{\oplus}$, yielding $\tau_{\rm M} \approx 5 \times 10^4$ years, whatever of the four gravitational potential is used (see also

Table 5.5: Migration rates from accreting and non-accreting models in which $\Phi_{\rm p} = \Phi_{\rm p}^{\rm HS}$ (eq. [5.6]). Time scales are different from those indicated in Figure 5.6 only at $M_{\rm p} = 33$, 20, and 10 $M_{\oplus}$.

		$\tau_{\rm M}$ [years]	
$M_{\rm p}/M_{\oplus}$	q	Accretion	No Accretion
333	1.0×10^{-3}	5.04×10^{4}	4.80×10^{4}
166	5.0×10^{-4}	4.76×10^{4}	...
33	1.0×10^{-4}	2.10×10^{5}	2.54×10^{5}
20	6.0×10^{-5}	5.74×10^{5}	...
10	3.0×10^{-5}	5.26×10^{5}	4.78×10^{5}
5	1.5×10^{-5}	6.19×10^{5}	...

Table 5.5). While this time scale is consistent with Ward's 1997 description if $M_{\rm p} = 67\ M_{\oplus}$, for more massive planets it is nearly two times as short as the theoretical prediction. The depletion of the disk inside the planet's orbit is probably responsible for part of the discrepancy (see § 5.4.6), because Ward's theory assumes a disk with a constant unperturbed surface density. In the type I regime, our numerical experiments with $\Phi_{\rm p} = \Phi_{\rm p}^{\rm ST}$ (eq. [5.7]) well reproduce the behavior of the analytical curve when $M_{\rm p} = 30$, 20, 5, 3.3, and 1.5 $M_{\oplus}$.

Computations executed with $\Phi_{\rm p} = \Phi_{\rm p}^{\rm HS}$ (eq. [5.6]) probably underestimate the magnitude of differential torques because of the much weaker gravitational field. Nevertheless, for Jupiter-mass and Earth-mass protoplanets, migration times yielded by these models well compare to those displayed in Figure 5.6, as proved by the values reported in Table 5.5.

Significant deviations from the linear estimate of Tanaka et al. (2002) are observed in the mass interval $[7, 15]\ M_{\oplus}$, where the migration time is longest at 10 $M_{\oplus}$. For this planet $\tau_{\rm M}$, estimated with Stevenson's as well as the point-mass potential, is thirty times as long as the theoretical description by Tanaka et al. (2002) predicts. This depends on the strong positive torques arising at $S > 2\,h\,R_{\rm p}$ which are not efficiently contrasted by negative ones generated inside $S \simeq h\,R_{\rm p}$. However, for this particular planetary mass, we obtain discrepant estimates from computations performed with different resolutions. In fact, the simulation carried out with the grid G2 yields a positive total torque acting on the planet, i.e., it predicts an outward migration, whereas models based on the higher resolution hierarchies G3 and G4 provide a negative total torque. Yet, the absolute value of $\mathcal{T}_{\rm D}$ evaluated with grid G4 is a seventh of that achieved with grid G3.

Since we believe that gravitational torques are accounted for in a more accurate fashion by hierarchy G3 than by grid G4 because of the arguments in § 5.4.6, we may rely more on the outcome of the hierarchy G3 (shown Fig. 5.6) rather than on the other two. We note that such migration time ($\tau_{\rm M} = 3.3 \times 10^{6}$ years) is roughly the double of that supplied by the 10 $M_{\oplus}$ non-accreting model.

We have further inquired into the matter by running a simulation with $M_{\rm p} = 12.5\ M_{\oplus}$ and $\Phi_{\rm p} = \Phi_{\rm p}^{\rm ST}$ (see Table 5.1). Based on the experience acquired with models executed with

grids G3 and G4, we set up the high-resolution hierarchy G5 (see Table 5.2). This grid is designed to better resolve those regions responsible for the strongest torque contributions in the mass interval $[7, 15]\ M_{\sun}$. As seen in Figure 5.6, the resulting migration rate follows the trend established by the other assessments in this range of masses.

The interesting property that computed migration time scales are very long for ten Earth-mass planets may be caused by non-linearity effects. We note, in fact, that in numerical simulations the first traces of a trough in the density structure is observed around the same value of $M_{\rm p}$ and gap formation starts when disk-planet interactions become non-linear. However, this issue needs to be addressed more thoroughly with future computations.

5.4.4 Mass Accretion

Three-dimensional computations of one Jupiter-mass bodies provide estimates of the mass accretion rate $\dot{M}_{\rm p}$ on the same order of magnitude as those obtained by two-dimensional ones (see CHAPTER 2). Two-dimensional calculations performed by the authors reveal a maximum of the accretion rate, as function of the mass, around $0.5\ M_{\earth}$ (see CHAPTER 4). Yet, those estimates appear surprisingly high in the very low-mass limit. Part of the reasons may lie in the assumed flat geometry which cannot account for the vertical density stratification. The present simulations overcome this restriction, hence they permit to evaluate also the effects due to the disk thickness.

The values of $\dot{M}_{\rm p}$ is plotted against the planetary mass in Figure 5.7. As comparison, estimates relative to models with different gravitational potential solutions are shown. The overall behavior of the data points resembles that reported in CHAPTER 4, with a peak around $0.3\ M_{\earth}$. For $M_{\rm p} = 1\ M_{\earth}$ the agreement between two and three-dimensional models is very good and not much discrepancy is seen down to $M_{\rm p} = 20\ M_{\sun}$, since values are comparable within a factor 3 (see § 5.4.5). Below this mass, however, the accretion rate rapidly declines, which drop is not observed in 2D outcomes. In fact, one can infer from Figure 5.7 that the dynamical range of $\dot{M}_{\rm p}$ stretches for more than two orders of magnitude. By using model results obtained applying the point-mass, Stevenson's, and Wuchterl's potential (eqs. [5.4], [5.7], and [5.9] respectively) the following approximate relation can be found:

$$\log\left[\frac{\dot{M}_{\rm p}}{M_{\sun}/yr}\right] \simeq b_0 + b_1\ \log q\ + b_2\ (\log q)^2\,, \tag{5.16}$$

whose coefficients are $b_0 = -18.47 \pm 0.76$, $b_1 = -9.25 \pm 0.38$, and $b_2 = -1.266 \pm 0.046$. Equation (5.16) holds as long as the mass ratio $q \in [4.5 \times 10^{-6}, 10^{-3}]$ or, for a one solar-mass star, when $1.5\ M_{\sun} \leq M_{\rm p} \leq 1\ M_{\earth}$. Such an equation can be applied to scenarios studying the global long-term evolution of young planets.

Calculations in which the homogeneous sphere potential $\Phi_{\rm p}^{\rm HS}$ (eq. [5.6]) is adopted yield accretion rates substantially lower (from 3 to 15 times) than those achieved when the other potential forms are employed. This is due to the weak gravitational attraction this potential exerts within the planet's envelope. As proved by Figure 5.1, the gravitational field can be 100 times as small as that established by the other three potential functions for

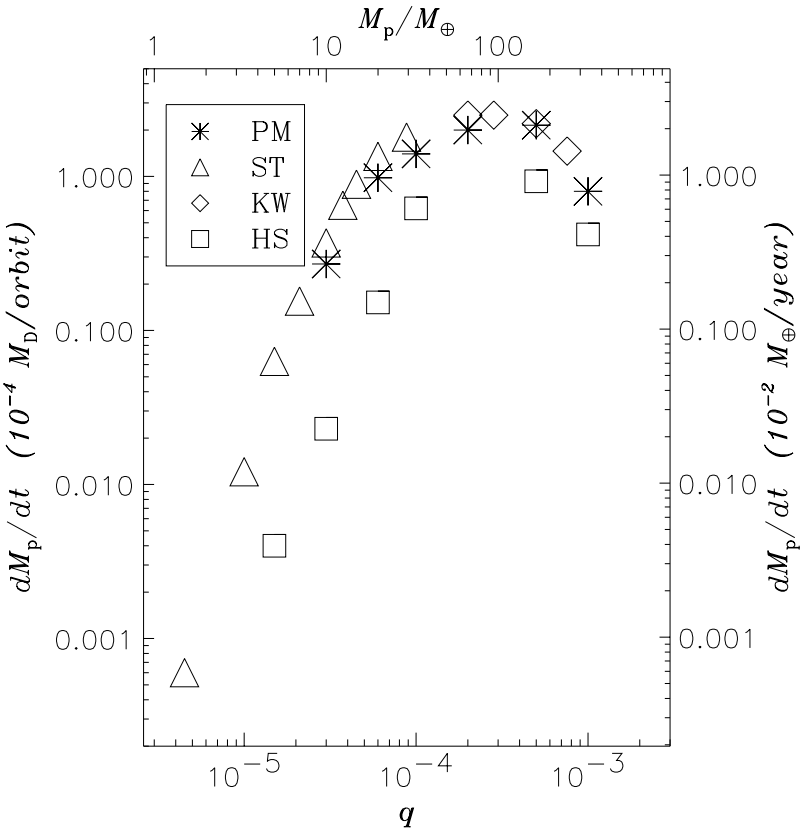

Figure 5.7: Planet's accretion rate as function of the normalized planet mass q. Different symbols stand for the different forms of gravitational potential $\Phi_{\rm p}$ adopted in the computations. Apart from those models run with the homogeneous sphere potential $\Phi_{\rm p}^{\rm HS}$ (see eq. [5.6]), mass is removed from a volume, centered on the planet, with radius $\kappa_{\rm ac} = 0.1\,R_{\rm H}$ (see Table 5.3 for some details concerning the simulation with $M_{\rm p} = 1.5\ M_{\oplus}$). Models for which $\Phi_{\rm p} = \Phi_{\rm p}^{\rm HS}$ have $\kappa_{\rm ac}$ equal to $0.2\,R_{\rm H}$ if $M_{\rm p} > 20\ M_{\oplus}$ and to $0.15\,R_{\rm H}$ if $M_{\rm p} = 20\ M_{\oplus}$; otherwise $\kappa_{\rm ac}$ is set to $0.1\,R_{\rm H}$.

$S \leq S_{\rm p}$. Also in this circumstance, a relation similar to equation (5.16) exists for which the coefficients are $b_0 = -19.42 \pm 2.68$, $b_1 = -9.96 \pm 1.41$, and $b_2 = -1.42 \pm 0.18$.

While the accretion rate is fairly stable with time for masses below $30\ M_{\oplus}$, it keeps reducing for higher masses. Between $67\ M_{\oplus}$ and $0.8\ M_{\jupiter}$, $\dot{M}_{\rm p}$ drops by 10 to 20% during the last 50 orbits of the simulations. This is an indication of a deepening gap and a depleting disk. As for the dependency upon the accretion volume, from our numerical experiments it is found that doubling the radius $\kappa_{\rm ac}$, the accretion rate grows at most by 30%. The smaller the planet mass, the less sensitive $\dot{M}_{\rm p}$ is to the parameter $\kappa_{\rm ac}$.

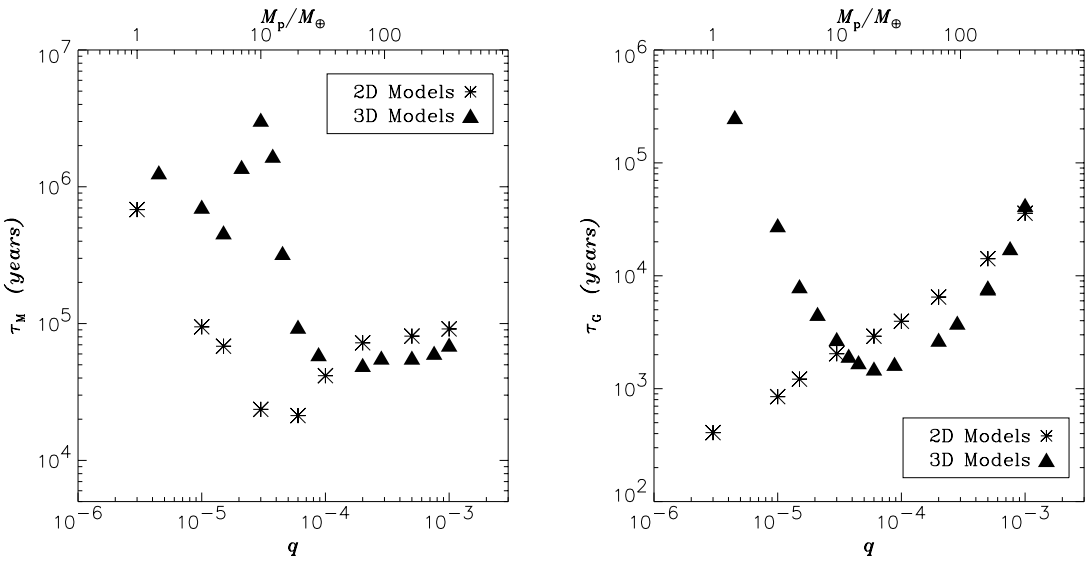

Figure 5.8: **Left panel**. Migration rates as evaluated in two-dimensional (CHAPTER 4) and three-dimensional models (this paper). **Right panel**. Using the same sources as in the left panel, a comparison of the growth time scales $\tau_{\rm G} \equiv M_{\rm p}/\dot{M}_{\rm p}$, between 2D and 3D outcomes, is shown. Filled triangles, in both panels, indicate results obtained from three-dimensional models in which the planetary gravitational potential is $\Phi_{\rm p}^{\rm PM}$, $\Phi_{\rm p}^{\rm ST}$, or $\Phi_{\rm p}^{\rm KW}$.

5.4.5 Comparison with 2D Models

In this Section we aim at comparing the migration time scale as well as the planet's accretion rate obtained in these simulations with those presented in CHAPTER 4. However, while two-dimensional estimates of $\dot{M}_{\rm p}$ (Fig. 4.19 in CHAPTER 4) are directly comparable to those plotted here in Figure 5.7, the time scales $\tau_{\rm M}$ shown in Figure 4.13 of CHAPTER 4 are not completely consistent with those in Figure 5.6. Therefore they need to be corrected.

This is because in the present study torques are integrated all over the disk domain excluding the planet envelope, i.e., the sphere of radius $S = S_{\rm p}$. Instead, in CHAPTER 4 the excluded region has a radius $\approx 0.1\,R_{\rm H}$ (for details see CHAPTER 4, § 5.4). From Table 5.1 one can see that, above $33\ M_{\jupiter}$, the envelope radius $S_{\rm p}$ can be much larger than a tenth of the Hill radius.

Figure 5.8 illustrates the migration rate $\tau_{\rm M}$ (left panel) and the growth time scale $\tau_{\rm G} \equiv M_{\rm p}/\dot{M}_{\rm p}$ (right panel) as computed in the two geometries. Orbital migration estimated by means of 3D simulations is slower than that evaluated in 2D calculations only below $33\ M_{\jupiter}$ ($q = 10^{-4}$). As for planet's accretion, the most important difference is the rapid drop, for $M_{\rm p} < 10\ M_{\jupiter}$, observed in disks with thickness. The larger values of three-dimensional estimates, measured in the range $10\ M_{\jupiter} \lesssim M_{\rm p} \lesssim 1\ M_{\saturn}$, are due to the gap which is not so deep as it is in two-dimensional models, hence the average density around the planet is higher. This fact can be partly attributed to gravitational potential effects that, as we

mentioned in § 5.4.1, are intensified by the flat geometry approximation.

5.4.6 Numerical Effects

In CHAPTER 4 it was found that, upon increasing the smoothing parameter, there is a reduction of the torques' mismatch, over a region around the planet whose linear size is comparable with the double of the smoothing length. A 33 $M_{\oplus}$ model was run with a point-mass potential without any kind of softening. This is possible because none of the hydrodynamical variables is placed at a cell corner, where the planet lives. A similar simulation was performed applying a grid dependent smoothing of the type described in CHAPTER 4. Resulting migration time scale and mass accretion are not significantly affected by the smoothing choice.

As for the consequences of the circumstellar disk depletion, inside the planet's orbit, we ran a Jupiter mass model with both inner and outer radial borders closed. Since more material is available in the disk portion $R < R_{\rm p}$ (roughly twelve times as much), one should expect larger values for both $\dot{M}_{\rm p}$ and $\tau_{\rm M}$. Indeed, accretion is two times as much as that calculated in the model with open inner border. Positive torques arising from the inner disk are also stronger and $\mathcal{T}_{\rm D}$ is reduced by 50%, i.e., the migration time scale is two times as long.

When simulating a Jupiter-size body embedded in a disk with no initial gap, a density indentation is gradually carved in. In order to skip the gap formation phase, an approximate analytical gap is sometimes imposed in the initial density distribution (see Kley 1999). We performed three computations adopting this choice. In these cases a partial shrinking and refilling of the analytical gap is observed. Besides, material drains out of the inner radial border faster than it does in our standard models (no initial gap). Hence, the inner disk depletion is intensified. With respect to standard models, we measure smaller accretion rates and longer migration time scales. Discrepancies in both quantities stay below 20%, after 200 orbits. However, since the model outcomes indicate a tendency to converge as the evolution proceeds, a more appropriate comparison should be made after a long-term evolution.

Grid Resolution

Hardly any hydrodynamic calculation is strictly resolution independent. Thus, for completeness we analyze in this section how our estimates on migration and accretion vary because of different hierarchy resolutions. Two tests are presented for each of the quantities $\dot{M}_{\rm p}$ and $\mathcal{T}_{\rm D}$. They are computed with the aid of grid systems G3 and G4 and then results are tested against those calculated with the less resolved hierarchy G2 (see Table 5.2). In this way we aim at checking finite resolution effects in the radial and azimuthal directions and, separately, those in the meridional direction. In fact, G3 and G2 have the same number of grid points in the vertical direction but $\Delta R[\mathrm{G3}] = 0.82\,\Delta R[\mathrm{G2}]$ and $\Delta\varphi[\mathrm{G3}] = 0.75\,\Delta\varphi[\mathrm{G2}]$. In the other test case (G4 against G2), R and φ gridding is unchanged while the number of latitude grid points is nearly doubled.

With regard to the mass accretion rate (Fig. 5.9, left panel) differences are below 20%. Though the number of grid cells in the accretion sphere is enlarged by a factor either 1.7 or

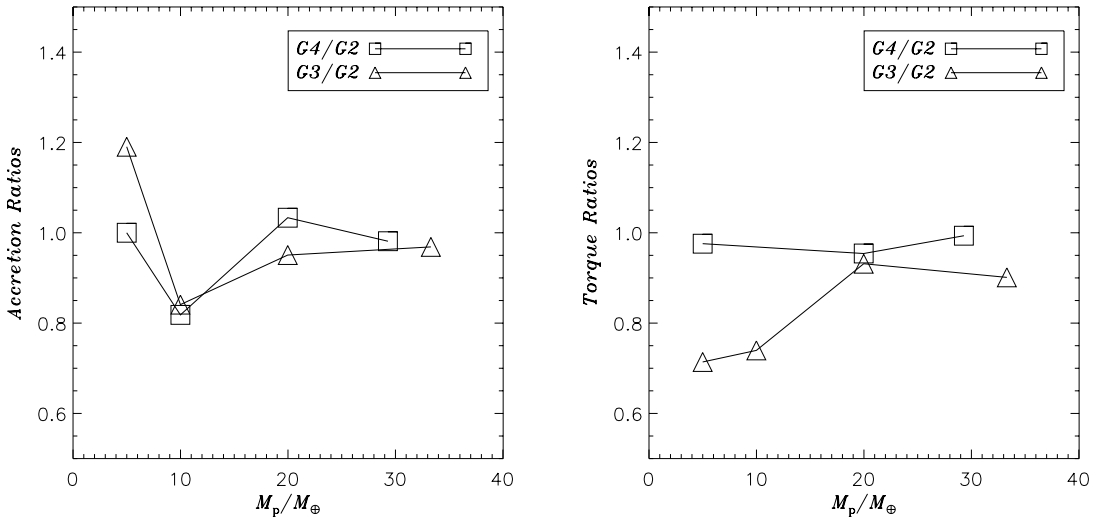

Figure 5.9: **Left panel**. Comparison of the accretion rate $\dot{M}_{\rm p}$ as computed on grid systems with different resolutions. Squares indicate that the ratios $\dot{M}_{\rm p}[{\rm G4}]/\dot{M}_{\rm p}[{\rm G2}]$ are drawn, whereas triangles refer to the ratios $\dot{M}_{\rm p}[{\rm G3}]/\dot{M}_{\rm p}[{\rm G2}]$ (see text). **Right panel**. The same type of comparison for the total torque $\mathcal{T}_{\rm D}$ experienced by the protoplanet. Squares and triangles have the same meaning as before. At $M_{\rm p} = 10\ M_{\jupiter}$, we compare results from models with the homogeneous sphere potential given in equation (5.6), when available (for this particular mass value, see the comments in § 5.4.2).

2, no systematic tendency seems to arise from this test. Something different happens to the total torque (right panel). In fact, while the increased resolution in the latitude direction θ does not play any considerable role, the larger number of grid points in R and φ causes a reduction of the total torque magnitude between 20 and 30%. This is not at all unexpected. On one hand circumstellar disk spirals are better captured by a finer gridding in the radial and azimuthal dimension. Thus Lindblad torques are accounted for in a more accurate fashion. The Figure proves this to be especially true when the ratio q is small, because of the diminishing wave amplitudes. On the other hand, due to the vertical exponential drop of the density and the lack of temperature stratification, disk layers above the midplane don't contribute very much to $\mathcal{T}_{\rm D}$. A finer resolution along the vertical dimension cannot sensitively modify the total torque outcome.

5.5 Discussion

Here we devote some further comments to the differences between accreting and non-accreting protoplanets and then to the effects of the vertical density structure on the gravitational torques acting on embedded objects.

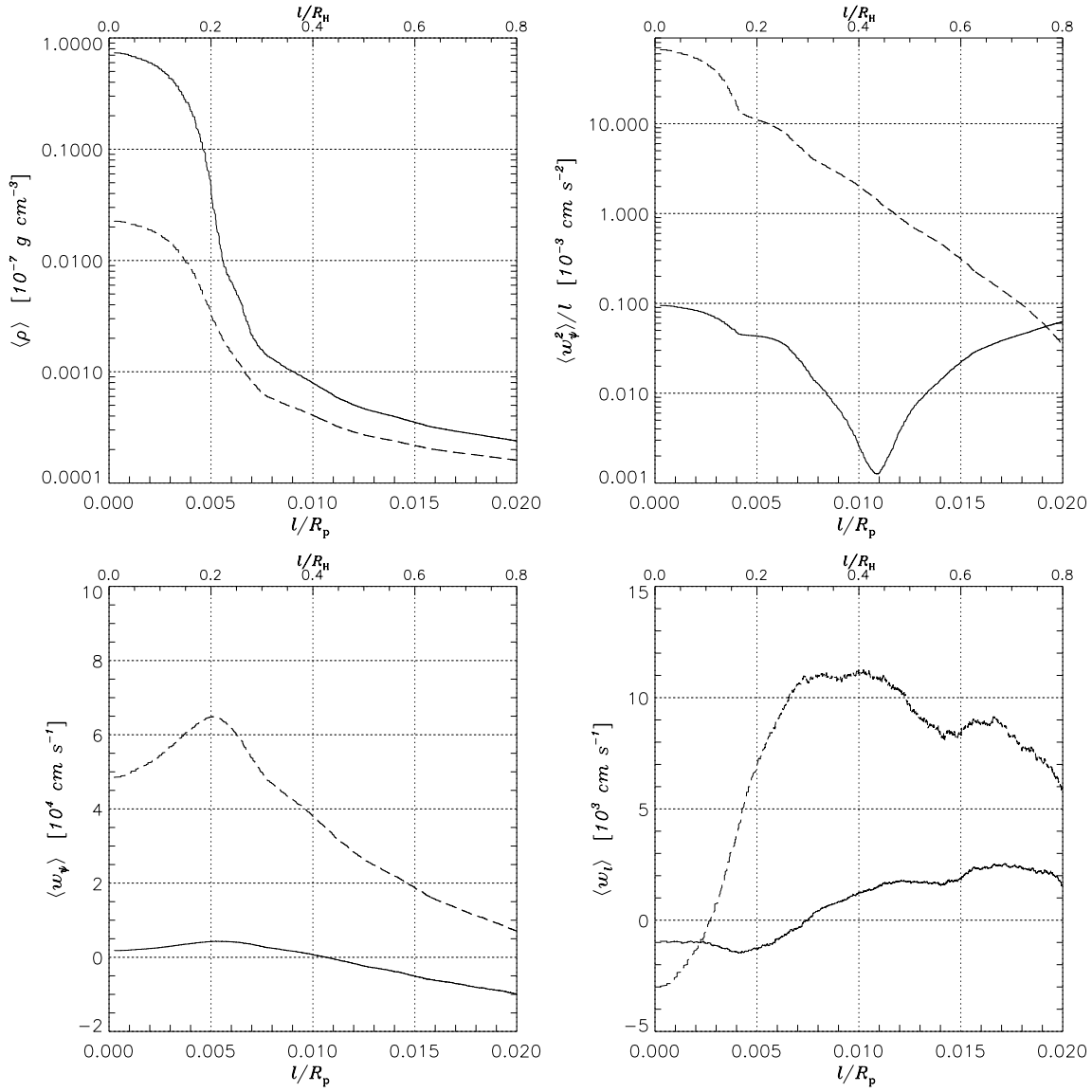

Figure 5.10: Midplane quantities ($z = 0$ or $\theta = \pi/2$) azimuthally averaged around the protoplanet for two simulations in which $\Phi_{\rm p} = \Phi_{\rm p}^{\rm ST}$ and $M_{\rm p} = 20\ M_{\dot{\odot}}$. The solid line belongs to the a non-accreting model, the dashed line to an accreting one. **Left-Top**: mass density. **Right-Top**: centrifugal acceleration. **Left-Bottom**: rotational velocity. **Right-Bottom**: velocity component along the radial distance l (see § 5.5). All of the four quantities indicate that the envelope is mostly pressure supported in the non-accreting case whereas it is mainly centrifugally supported in the other.

5.5.1 Pressure Effects in Protoplanetary Envelopes

For the purpose of carrying out a local analysis in the vicinity of accreting and non-accreting protoplanets, we introduce a cylindrical coordinate reference system $\{O'; l, \psi, z\}$

with its origin O' coinciding with the planet position and the z-axis perpendicular to the disk midplane. Hence, we will have that $S^2 = l^2 + z^2$. The longitude angle ψ is counter-clockwise increasing, and $\psi = \pi$ points toward the star. Supposing that the flow nearby the planet is stationary, neglecting fluid advection and viscosity, the Navier-Stokes equation for the radial momentum reads:

$$\frac{w_\psi^2}{l} = \frac{\partial \Phi_\mathrm{p}}{\partial l} + \frac{1}{\rho}\frac{\partial p}{\partial l}, \tag{5.17}$$

where w_ψ is the azimuthal velocity component around the planet. Excluding the particular situation represented by a homogeneous sphere (eq. [5.6]), the first term on the right hand side of equation (5.17) is positive (see Fig. 5.1). Recalling equation (5.2), we see that the second term is proportional to the density gradient, which is negative, and therefore it reduces the centrifugal acceleration w_ψ^2/l. In Figure 5.10 we show some quantities, at $z = 0$, averaged over the angle ψ, regarding the same simulations addressed in § 5.4.1 ($M_\mathrm{p} = 20\ M_{\stackrel{\star}{\odot}}$ with $\Phi_\mathrm{p} = \Phi_\mathrm{p}^\mathrm{ST}$). From the top left panel one can realize that the mean density is indeed higher in the non-accreting case (solid line) than it is in the accreting case (dashed line), as it was argued in § 5.4.1 from the values in Table 5.4. In order to evaluate how much the pressure gradient affects the left hand side of equation (5.17) in both cases, we plot the average of such quantity ($\langle w_\psi^2 \rangle / l$) in the top right panel of Figure 5.10. The centrifugal acceleration is much smaller in the envelope of the non-accreting model (solid line) than it is in that of the accreting one. Such circumstance is a clear indication that the envelope is pressure supported in the first case. The behavior of the averaged velocities $\langle w_\psi \rangle$ and $\langle w_l \rangle$ is shown in the two bottom panels. As expected in a pressure dominated flow, the magnitude of both velocity components is smaller in the non-accreting model (dashed lines).

5.5.2 Torque Overestimation in 2D Geometry

Gravitational torques exerted by a three-dimensional disk onto a medium- or low-mass protoplanet are weaker than those generated by a two-dimensional disk. Miyoshi et al. (1999) state that the total torque $\mathcal{T}_\mathrm{D}$ in 3D is 0.43 times as small as that in 2D. Something similar was found by Tanaka et al. (2002). Our fully non-linear calculations predict that low-mass protoplanets have a migration rate an order of magnitude less in disks with thickness than they have in infinitesimally thin disks. One of the main reasons for that relies upon the vertical decay of the density, as one can demonstrate easily with a simplified approach.

Let t_z be the z-component of the gravitational torque exerted by a column of mass $\Sigma\, l\, \mathrm{d}l\, \mathrm{d}\psi$, located at distance l from the planet (see § 5.5.1). The surface density is defined as $\Sigma = \int \rho\, \mathrm{d}z$. If f_g is the force exerted by such mass distribution, projected on the equatorial plane, then we can write

$$t_z = R_\mathrm{p}\, f_\mathrm{g}\, \sin\psi. \tag{5.18}$$

The ratio of $t_z[\mathrm{3D}]$ to $t_z[\mathrm{2D}]$ is therefore equal to

$$\chi = \frac{f_g[\mathrm{3D}]}{f_g[\mathrm{2D}]} = \frac{l^3}{\Sigma}\int_{-\infty}^{+\infty} \frac{\rho}{(l^2+z^2)^{3/2}}\, \mathrm{d}z. \tag{5.19}$$

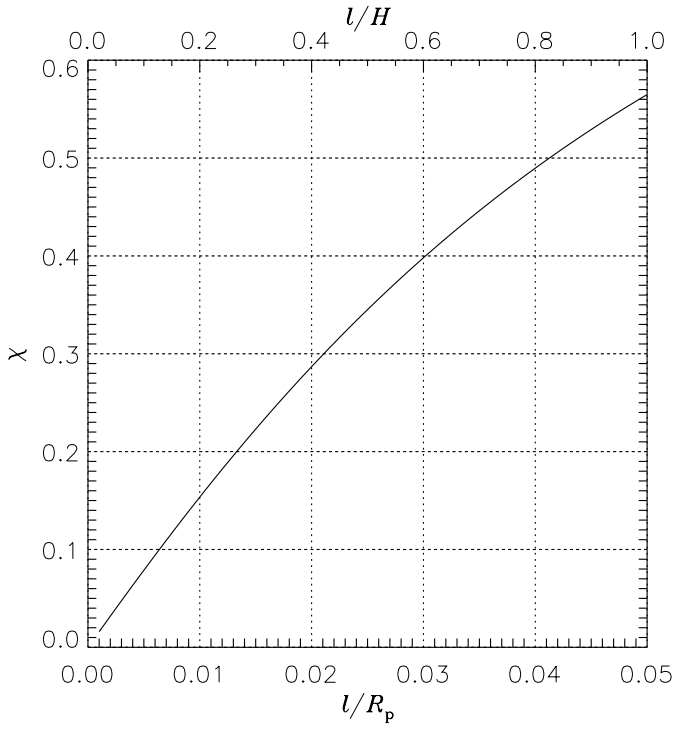

Figure 5.11: Ratio of the tree-dimensional to the two-dimensional torque exerted by a column of material lying at a mid-plane distance l from the protoplanet (see § 5.5). The upper x-axis is in units of the disk semi-thickness at the planet location: $H = h\,R_{\rm p}$.

Since $f_g[3\mathrm{D}]$ and $f_g[2\mathrm{D}]$ are coherent in sign, χ is also equal to the ratio of $|t_z[3\mathrm{D}]|$ to $|t_z[2\mathrm{D}]|$. In order to quantify this quantity, we can assume a Gaussian mass density profile with a scale height H, which is appropriate as long as no deep gap has formed. Thus

$$\chi = \frac{l^3}{\sqrt{2\pi}\,H} \int_{-\infty}^{+\infty} \frac{\exp\left(-\frac{z^2}{2\,H^2}\right)}{(l^2+z^2)^{3/2}}\,\mathrm{d}z. \tag{5.20}$$

The ratio χ as function of l is plotted in Figure 5.11 and it evidences how a two-dimensional geometry overestimates the magnitude of gravitational torques acting on the protoplanet. In the limit $l^2 \gg z^2$, χ converges to 1, which proves that only torques arising from locations near to the planet ($l \lesssim H$) are magnified.

Though larger torque magnitudes do not necessarily imply faster migration speeds, they can favor a larger mismatch between negative and positive torques and therefore shorter $\tau_{\rm M}$.

5.6 Conclusions

On the background of the numerical computations of disk-planet interaction presented in CHAPTER 2 and IV, we have combined the full 3D geometry of a circumstellar disk with a nested-grid technique in order to investigate in detail flow dynamics, orbital decay, and mass accretion of protoplanets in the mass range $[1.5\ M_{\oplus}, 1\ M_{\mathcal{4}}]$. Besides, we

overcome the point-mass assumption by employing analytic expressions of the gravitational potential derived from simple theoretical models of protoplanetary envelopes. Each of them applies to distinct physical situations: when the envelope mass is negligible with respect to the core mass; when the envelope is homogeneous and much more massive than the core; when the envelope is fully radiative, and finally when it is fully convective.

Through a series of 48 simulations, we inspect the evolution and differences of protoplanets represented by the aforementioned gravitational potentials. We analyze the behavior of both accreting and non-accreting objects. Furthermore, we evaluate physical and numerical effects due to our standard set-up of the models. The computations clearly show that to accurately determine the early physical evolution of planets three-dimensional effects have to be taken into account.

The main results of our studies can be summarized as follows.

Above the disk midplane the flow is nearly laminar only far away from the planet. The region of influence of the planet extends well outside the Hill sphere and its boundaries are marked by vertical shock fronts. Past the shock, matter is deflected upward and then downward. In some cases, a closed recirculation is also observed. In the disk midplane, spiral waves around the planet are not as strong and tight as they appear in two dimensions because of wave deflection in the vertical direction.

In the mass range of their applicability, Stevenson's and Wuchterl's gravitational potentials produce flow structures, close to the planet, similar to those determined by a smoothed point-mass potential. Migration times and accretion rates are alike. In contrast models with the (unrealistic) potential of a homogeneous sphere yield different dynamics though, as for $\tau_{\rm M}$ and $\dot{M}_{\rm p}$, not much difference is observed for Jupiter and Earth-size bodies.

Since the numerical accretion procedure might be considered somewhat arbitrary, we ran several models in which the protoplanet does not accrete at all. Non-accreting models behave differently from accreting ones in a volume whose size is roughly comparable with the Hill sphere. Within this region matter is pressure supported and thus a spherical envelope builds up. Except for the case $M_{\rm p} = 20\ M_{\oplus}$, the total torque $\mathcal{T}_{\rm D}$ exerted by the disk is on the same order of magnitude as that measured in accreting models.

According to Ward's theory (Ward 1997), the migration speed settles to a constant value when the planet-to-star mass ratio $q \gtrsim 4 \times 10^{-4}$. Our numerical results give a similar trend at a slightly different magnitude though. Most of these simulations predict an inward migration except the one where a $20\ M_{\oplus}$, non-accreting, protoplanet is involved. In the mass range $[7\ M_{\oplus}, 15\ M_{\oplus}]$ migration speeds can be 30 times as slow as those predicted by Tanaka et al. (2002) although, outside of this range, the agreement between our computational data and the type I migration by the same authors is remarkably good. We suspect that this surprising outcome may be caused by the onset of non-linear effects appearing around ten Earth's masses, which conspire to give such long migration time scales. If correct, this much slower inward motion may help to solve the problem of the too rapid drift of planets toward their host stars.

In agreement with studies on planet formation (Bodenheimer and Pollack 1986; Tajima and Nakagawa 1997), the growth time scale shortens as the protoplanet's mass increases. The minimum is found at $M_{\rm p} = 20\ M_{\oplus}$. Albeit the feeding process slows down as soon as

angular momentum transferred by the planet to the surrounding material is large enough to dig a density gap. Then, at $M_{\rm p} \approx 1\ M_{\earth}$, the accretion rate greatly reduces and the growth time scale becomes consistently very long. We present an analytical formula for the growth rate which may be useful for global studies in planet formation.

As long as migration and mass accretion are concerned, two-dimensional computations still yields reliable results when the mass ratio $q \gtrsim 10^{-4}$ ($M_{\rm p} \gtrsim 30\ M_{\jupiter}$ if $M_{\star} = 1\ M_{\odot}$). In practice, 2D geometry is applicable whenever the Hill radius $R_{\rm H}$ exceeds the 60% of the local pressure scale height of the disk H. But for smaller masses three-dimensional calculations have to be considered.

The three-dimensional calculations presented here achieve a new level of accuracy by using a sophisticated nested-grid technique. This numerical feature allows a global and local resolution not obtained hitherto. However, similar to all of the previous calculations, the models presented here have one principal limitation: the lack of an *appropriate* energy equation. Because of this we could not couple the thermal and the hydrodynamical evolution of the system. If one wishes to do that in three dimensions, the energy equation has to include radiation and convective transfer. Yet, only with massive parallel computations one can hope to pursue this goal.

I have seen wicked men and fools, a great many of both; and I believe that both get paid in the end; but fools first.

ROBERT LOUIS STEVENSON,
KIDNAPPED,
1886

CHAPTER 6

BEYOND LOCAL ISOTHERMAL DISK MODELS

In this final chapter we return to modeling disk-planet interactions by means of models in two dimensions. However, in contrast to the computations presented in the preceding chapters and all those available in the literature, the system will not be considered locally isothermal. In other terms, also the thermal evolution of the protostellar disk will be simulated. Nested grids are applied in order to investigate the global behavior of the circumstellar disk along with the local thermal effects in the protoplanet environment. Although only a simplified form of energy equation is solved, these simulations represent another step forward in the field of planet formation and evolution.

6.1 Introduction

The history of numerical simulations in astrophysics has always been tied to the availability of computing resources and associated numerical algorithms. Computations of planets in disks have had a similar fate.

Since the very first attempt of modeling a protoplanet interacting with its primitive nebula by Miki (1982), two decades have passed. Seventeen years had to go by for tackling this problem with the strength of new and more powerful tools (Kley 1999; Bryden et al. 1999; Lubow et al. 1999). Revitalized by the mounting interest in extrasolar planets, boosted by seven years of uninterrupted new detections, the scientific community has devoted an extraordinary effort to disk-planet interaction calculations that has grown stronger and stronger in the last three years. A glance at the "Extra-solar Planets Bibliography" (`http://www.obspm.fr/encycl/bibli.html`) is instructive.

Although the directions of investigation are diverse, according to the personal belief of the "fundamental" processes ruling formation and evolution of planets, limitations and restrictions represent an issue to deal with. As a matter of fact, numerical calculations still lag behind our present knowledge of the possible physical effects occurring in those systems. Thereupon, simplifying assumptions and prescriptions are always demanded. Nonetheless, steps forward have been made to reduce their number.

The track of all this work has adapted to this philosophy. We have performed the first three-dimensional global computations of planets in disks; we have conducted the first planet mass-dependent study, with extremely high resolution calculations, both in two and three dimensions. We conclude this work by relaxing another approximation: that of treating a disk as a locally isothermal system.

The literature is full of studies on accretion disk modeling, with various degree of sophistication. And the most sophisticated ones usually adopt the 2D or 1+1D schemes[1]. The reason for this resides in the difficulty of dealing with all the necessary ingredients in a full 3D scheme. Numerical simulations usually involve a parameter study, because laboratory experiments and / or observations do not provide the required information. Thereby, wasting thousands of hours of CPU time, with extremely detailed models based on poorly known parameters, would be just insane. That's why, until very recently, radiation (e.g., Dullemond et al. 2002), convection (e.g., Agol et al. 2001), magnetic fields (e.g., Matt et al. 2002) , mixture of gas and dust (e.g., Suttner and Yorke 2001), and chemical evolution (e.g., Markwick et al. 2002) have been approached via vertical r–z models. In this manner, at least one can acquire a spectrum of possible approximate and restricted solutions.

In order to overcome the local-isothermal hypothesis, we introduce an energy transport in 2D, (r–φ) models. We include all the (supposedly) major causes responsible for generation, transfer, and loss of energy in low-temperature circumstellar disk environments. We take advantage of the small aspect ratio of the disk, and assume that all the radiation transport is effective only in the vertical direction. Such restriction has been proved to work reasonably well in accretion disks, away from the boundary layer (see, e.g., Pringle 1981). It heavily relies on the disk slimness assumption, thus it might still be inappropriate in the local environment around a protoplanet. However, around there, the disk becomes even thinner when the planet gravitational action is accounted for. Hence, the amount of energy transported by radiation in the vertical direction still may be larger than that transported horizontally. This might not be the best kind of thermal description, nonetheless it allows to investigate processes which have never been considered so far, i.e., the joint thermo-hydrodynamics evolution of disk-planet interactions.

The outline of this chapter is the following. In the next section we introduce the physical formulation of the problem. Since the equations of hydrodynamics in cylindrical coordinates have already been written down in CHAPTER 4, here we focus on the equation for the thermal energy density and all the constitutive equations which are necessary to solve it. Thus, the choice of the opacity table is discussed along with the issue of how the disk scale height is consistently computed. Then, the artificial viscosity topic is addressed. Section 6.3 concerns the numerical method utilized to solve the energy equation. Besides this, a series of tests is presented, with the aim at checking the validity of the numerical solutions provided by the method. In § 6.4 we specify the models' parametrization and other details. Section 6.5 describes some global properties of "Hot", "Warm", and "Cold" models with different masses. Section 6.6 deals with the discussion of the local flow around protoplanets. In § 6.7 we report the results for mass accretion and gravitational migration. Our conclusions are presented in § 6.8.

[1] Although some 3D simulations of MHD effects in accretion disks have also been performed.

6.2 Physical Formalism

As mentioned in the previous section, we are going to tackle the problem of energy transfer in accretion disks. Since solving the full set of equation in three dimensions (i.e., continuity, momentum, and an appropriate energy equation) is computationally difficult at the moment (see § 6.1), as first approximation we go back to infinitesimally thin disk models.

The reason for this choice is two-folded. On one hand, it allows affordable computational times; on the other, it permits to adopt a strategic assumption in writing the energy equation, i.e., that the horizontal energy transport can be neglected compared to the vertical one. In other words, in a 2D disk one can assume that radiation transport is only effective along the direction perpendicular to the equatorial plane of the disk[2].

Hence, let us describe the disk material via the same Navier-Stokes equation introduced in § 4.2, where the working coordinate frame is a cylindrical one $\{O; r, \varphi\}$. Throughout this chapter the notations are the same as those used in CHAPTER 4. The origin is located at the center of mass of the star and the planet. From equations 4.2, 4.3, and 4.4, it turns out that the unknowns of the problem are[3] $(\Sigma, u_r, u_\varphi, \Phi, P)$.

As in the computations discussed before, we avoid dealing with the Poisson equation and rather assume that the gravitational field is only determined by the star and the planet, neglecting the self-gravity of the disk material itself. Thereby, we rely on a smoothed point-mass gravitational potential of the type described in CHAPTER 4 and 5:

$$\Phi = -\frac{G\,M_\star}{|\boldsymbol{r} - \boldsymbol{r}_\star|} - \frac{G\,M_\mathrm{p}}{\sqrt{|\boldsymbol{r} - \boldsymbol{r}_\mathrm{p}|^2 + \delta^2}}, \tag{6.1}$$

where $\boldsymbol{r}_\star$ and $\boldsymbol{r}_\mathrm{p}$ are the radius vectors indicating the positions of the star and the planet, respectively. However, instead of imposing a smoothing length different on each grid level, as done in CHAPTER 4, we set the parameter δ as a constant length, as already experimented in CHAPTER 5 (see § 6.4 for quantitative details).

So far the set of equations has been closed by adding an equation of state which connects the local gas (two-dimensional) pressure to the surface density via a local isothermal sound speed c_s^iso:

$$c_s^\mathrm{iso} = h\sqrt{\frac{G\,M_\star}{r}}. \tag{6.2}$$

Thus, the Mach number of the flow is considered constant throughout the system, constrained solely by the disk aspect ratio $h = H/r$ (e.g., Kley 1999; Lubow et al. 1999; Miyoshi et al. 1999; Nelson et al. 2000; Papaloizou et al. 2001; Tanaka et al. 2002; Masset 2002; Tanigawa and Watanabe 2002).

Only Kley (1999) and Tanigawa and Watanabe (2002) ran some simulations using a polytropic equation of state of the type $P = K\,\Sigma^\gamma$. However, never an energy equation of any kind has been taken into account.

[2] In principle, such an assumption can also be made in three-dimensional thin disks.

[3] More generally, the set of unknown quantities comprises mass density, velocity components, gravitational potential, temperature, and radiation energy.

In the present calculations we use an ideal equation of state which directly ties the gas pressure P to the thermal energy density (energy per unit area) E:

$$P = (\gamma - 1)\, E, \tag{6.3}$$

where the adiabatic index γ is a constant.

If we suppose that disk material behaves as a perfect gas, then the temperature can be retrieved from the ratio of the density to the pressure:

$$T = \left(\frac{\mu\, m_{\rm H}}{k}\right) \frac{P}{\Sigma}, \tag{6.4}$$

where μ is the mean molecular weight, $m_{\rm H}$ is the hydrogen mass, and k the Boltzmann constant. The adiabatic sound speed is given by

$$c_s = \sqrt{\gamma \left(\frac{k\, T}{\mu\, m_{\rm H}}\right)}. \tag{6.5}$$

In writing equation (6.3) we have implicitly assumed that radiation pressure $P_{\rm rad}$ is small compared to gas pressure, thus it can be neglected. Such hypothesis is connected to the low temperatures we deal with (in fact $P_{\rm rad} \propto T^4$) and can be checked afterward.

6.2.1 Energy Equation

Because of the employed equation of state (eq. [6.3]), now we have five unknowns and four equations. Thus, an equation for E is necessary in order to close the system.

Equations for energy transport differ according to the processes that have to be included for a correct description of the energy budget of fluid elements. In our case, we suppose that a parcel of disk fluid can gain or lose thermal energy only because of flow advection (due to the fact that the parcel itself is in motion), compressional work, viscous dissipation (i.e., the work made by viscous shear forces that goes into heat), and dissipative effects due to radiation transport. In this sense, rather than strictly treating the transfer of radiation in the disk, we will account only for the cooling effects that radiation causes. Then, the energy equation takes the following form

$$\frac{\partial E}{\partial t} + \nabla \cdot (E\, \boldsymbol{u}) = -P\, \nabla \cdot \boldsymbol{u} + \Upsilon - \Lambda. \tag{6.6}$$

In equation (6.6) we indicated with Υ the dissipation function and with Λ the radiated energy. In two dimensions, either of these quantities is an energy flux. We will soon see that both functions are always positive, thereby the former acts as a heating source, whereas the latter as a cooling term. In this study we do not consider irradiation from the central star which is presumably an effective heating mechanism only in the outer parts of circumstellar disks (see, e.g., D'Alessio et al. 1998), whose effects however are reduced by small disk scale heights.

For our numerical purposes, the function Υ can be directly computed from the components of the viscous stress tensor (Mihalas and Weibel Mihalas 1999) S_{rr}, $S_{\varphi\varphi}$, and $S_{r\varphi}$, whose expression is given in CHAPTER 4 (eqs. 4.6 through 4.8):

$$\Upsilon = \frac{1}{2\,\nu\,\Sigma}\left(S_{rr}^2 + S_{\varphi\varphi}^2 + S_{r\varphi}^2\right) + \frac{2\,\nu\,\Sigma}{9}\,(\nabla\cdot\boldsymbol{u})^2, \tag{6.7}$$

where $\nabla\cdot\boldsymbol{u}$ is given in equation (4.9). With some algebraic computations it can be proved that equation (6.7) is equivalent to equation (12) of Collins et al. (1998). The divergence term in the equation arises because a three-dimensional definition of stress tensor $\mathbf{S}$ is adopted. Since S_{rr}, $S_{\varphi\varphi}$, and $S_{r\varphi}$ must be computed for the integration of the momentum equations, equation (6.7) is the most straightforward way to calculate the dissipation function.

In a full three-dimensional disk, the last term on the right-hand side of equation (6.6) is equal to $\nabla\cdot\boldsymbol{F}$, where $\boldsymbol{F}$ is the frequency-integrated radiation flux:

$$\boldsymbol{F} = -\frac{16\,\sigma_{\rm R}}{3\,\kappa\,\rho}\,T^3\,\nabla T. \tag{6.8}$$

In the above equation $\sigma_{\rm R}$ is the Stefan-Boltzmann constant, κ is the opacity coefficient[4], ρ is the mass density, and T the gas temperature. As mentioned before, we will suppose that the amount of energy transported by radiation in the vertical direction is much larger than that transported horizontally, i.e., $|F_r|, |F_\varphi| \ll |F_z|$. The validity of this statement holds as long as the vertical extent of the disk remains very small compared to the disk extent in the other directions. Thus, in a two-dimensional cylindrical disk we will have

$$\Lambda = \int_{-\infty}^{+\infty} \nabla\cdot\boldsymbol{F}\,{\rm d}z \simeq \int_{-\infty}^{+\infty} \frac{\partial F_z}{\partial z}\,{\rm d}z. \tag{6.9}$$

Since the vertical disk structure is not meant to be accounted for, it is possible to equate the pressure scale height to the photospheric scale height and assume that all the radiation is liberated at $z = \pm H$. Thereupon, equation (6.9) becomes

$$\Lambda = \int_{-H}^{+H} \frac{\partial F_z}{\partial z}\,{\rm d}z = F(H) - F(-H) = 2\,F(H). \tag{6.10}$$

In 2D disks it is useful to measure the emitted flux by means of an *effective temperature*: $F(H) = \sigma_{\rm R}\,T_{\rm eff}^4$, therefore

$$\Lambda = 2\,\sigma_{\rm R}\,T_{\rm eff}^4. \tag{6.11}$$

The factor 2 indicates that in a disk radiation escapes from both of its sides.

A simple relation between the midplane temperature and the emergent radiation flux, i.e., a relation $T_{\rm eff} = T_{\rm eff}(T)$, can be found by writing equation (6.10) in the following form

$$\Lambda = 2\int_0^H \frac{\partial F_z}{\partial z}\,{\rm d}z = 2\,\left[F(H) - F(0)\right], \tag{6.12}$$

[4]The opacity coefficient is a frequency-dependent quantity. However, when dealing with a frequency-independent radiative transfer, opacity is integrated over the frequency range, by using weighing functions. This process generates mean opacity coefficients such as, for example, Planck's and Rosseland's (see, e.g., Mihalas and Weibel Mihalas 1999).

and then applying equation (6.8):

$$[F(H) - F(0)] = -\frac{4}{3}\frac{\sigma_{\rm R}}{\kappa\,\rho}\left[\frac{\partial T^4}{\partial z}\right]_0^H \approx \frac{4}{3}\frac{\sigma_{\rm R}}{\kappa\,\rho\,H}\left[T^4(0) - T^4(H)\right]. \tag{6.13}$$

In the inner parts of a circumstellar disk the inequality $T^4(0) \gg T^4(H)$ generally holds (e.g., Bell et al. 1997; D'Alessio et al. 1998), hence equation (6.13) yields

$$\Lambda \approx \frac{2\,\sigma_{\rm R}\,T^4}{(3/4)\,\tau}, \tag{6.14}$$

in which we introduced the optical thickness $\tau = \kappa\,\rho\,H = \frac{1}{2}\,\kappa\,\Sigma$ (we generally adopt a Rosseland mean opacity). We notice that with the previous definition the total disk optical thickness is $2\,\tau$. From now on, the quantity T refers to the disk midplane temperature.

Equation (6.14) represents a fairly good approximation when the medium is optically very thick, i.e., $\tau \gg 1$. This is indeed the case in those regions of unperturbed accretion disks which we simulate, because Σ is large enough. Yet, because of the action of massive bodies, in our case deep density gaps form where material is very diluted and the disk may become very thin. In addition there are zones, where the disk spirals interact with the circumplanetary disk spirals, which can have very low densities. Such conditions make equation (6.14) not applicable. Hubeny (1990) found a more rigorous relation between the effective and midplane accretion disk temperature, which represents a generalization of the *gray model* of the classical stellar atmospheres in local thermodynamic equilibrium. According to Hubeny's theory, in a circumstellar disk the following equality holds:

$$\Lambda = 2\,\sigma_{\rm R}\,T^4\left[\frac{3\,\tau}{8} + \frac{\sqrt{3}}{4} + \frac{\varepsilon_{\rm H}}{4\,\tau}\right]^{-1}. \tag{6.15}$$

According to equation (6.15), the emitted flux is inversely proportional to τ in optically thick disk portions, whereas it becomes proportional to τ in the opposite limit. The quantity $\varepsilon_{\rm H}$ is equal to the ratio between the Rosseland and the Planck mean opacities. This quantity can be also roughly interpreted as the ratio of *total extinction* (i.e., absorption plus scattering coefficient) to the pure absorption coefficient: $\kappa_{\rm ext} = \kappa_{\rm abs} + \kappa_{\rm sc}$. As for it concerns the computations we have carried out, we set $\varepsilon_{\rm H} = 1$ because we neglect radiation scattering (see § 6.3.1). Thus no distinction is made between the extinction and the absorption coefficients.

Equation (6.15) mimics the radiative losses of both optically thick and optically thin media, and therefore is very suitable to our purposes. In fact, it has been successfully applied to many studies on accretion disks (Popham et al. 1993; Godon 1996; Collins et al. 1998; Huré et al. 2001).

6.2.2 Opacity Table

In order to calculate the disk optical semi-thickness τ, we adopt the opacity formulas derived by Bell and Lin (1994) (see Fig. 6.1), as an improvement of those by Lin and Papaloizou (1985). Eight temperature regimes are identified according to the dominant processes active in each of them. Transitions between two confining regimes are smoothed,

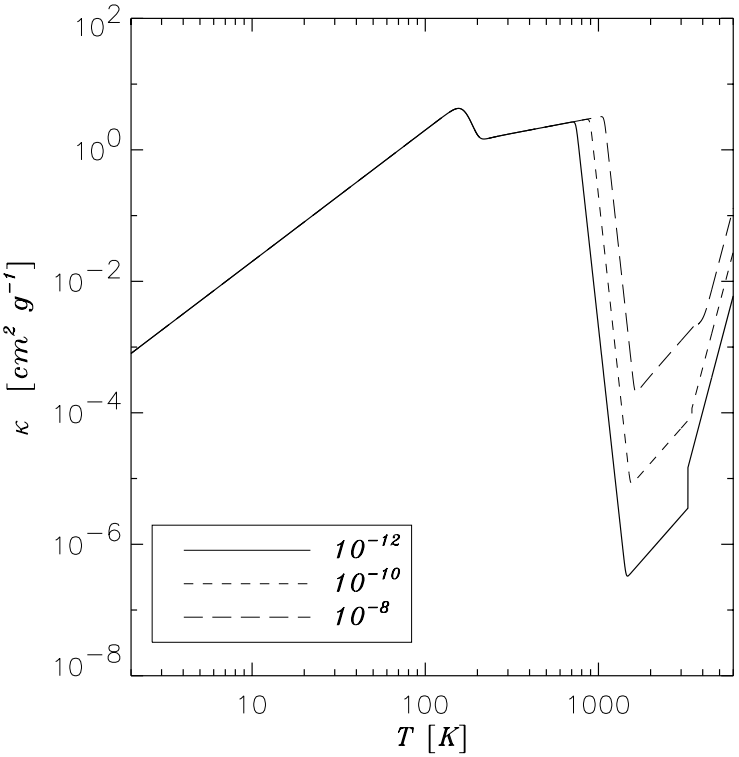

Figure 6.1: Rosseland opacity coefficient κ as function of the temperature for three different values of the mass density ρ (from Bell and Lin 1994). The legend quotes the density magnitude in $\mathrm{g\,cm^{-3}}$. One can realize, from the figure, that opacity is nearly independent of the ρ up to 800 K. Afterward, κ becomes sensitive to ρ.

following the procedure described in Lin and Papaloizou (1985). Contributions from dust grains, molecules, atoms, and ions are accounted for. Since we simulate a distance range where disk material is generally relatively cold (below a few hundred Kelvin degrees), dust opacity is crucial for an accurate estimation of radiative losses (Lin 1981). Because of this, Bell's opacity includes grain absorption as tabulated by Alexander et al. (1989).

However, for the sake of comparison we ran some test cases (see § 6.3.1) with a new opacity coefficient developed by Dimitry Semenov and collaborators (2001, private communication) and based on the improved grain opacity tables by Henning and Stognienko (1996). They aimed at coupling gas and dust opacities, focusing on the temperature range proper to protostellar disk environments.

In either case, the midplane temperature T and mass density ρ have to be provided in cgs units. In turn $\kappa = \kappa(T, \rho)$, has units of square centimeters per gram. We have explained in CHAPTER 4 that in the infinitesimally thin disk approximation, dynamics variables are vertically integrated. Thus, the mass density ρ is not directly available. It must be retrieved

from the surface density and the disk semi-thickness H. For this purpose, we assume that

$$\rho = \frac{\Sigma}{2\,H}. \tag{6.16}$$

In the next section we explain how the disk scale height H is calculated in a fashion such to account also for the gravitational influence of the planet. This guarantees a more refined and consistent modeling of the system.

6.2.3 Disk Scale Height

Inside a circumstellar disk it is natural to assume that material is in hydrostatic equilibrium along the vertical direction (Pringle 1981; Frank et al. 1992). Let g_z be the gravitational acceleration in the z-direction within the disk, then the hydrostatic equilibrium reads:

$$\frac{P}{\Sigma} = 2\int_0^H g_z\,\mathrm{d}z. \tag{6.17}$$

The factor 2 is necessary because the midplane pressure sustains both sides of the disk.

In the preceding chapters we have used equation (6.17) to obtain the disk pressure from the density and the pressure scale height, assuming that $g_z = G\,M_\star/(r^2+z^2)$ and omitting the planet gravitational attraction.

In the present study, we compute the pressure directly from the thermodynamics processes occurring in the gas, thus we can use equation (6.17) to estimate the disk scale height H in a consistent fashion. This quantity, in fact, is needed to obtain the mass density from the surface density (see § 6.2.2). Since the left-hand side of equation (6.17) is equal to c_s^2/γ, and thus an independent quantity, we can integrate the right-hand side in order to get an implicit function of H. Furthermore, the effects due to the gravitational field of the protoplanet can be included in this evaluation. If we set $q = M_\star/M_\mathrm{p}$ and $s = |\boldsymbol{r} - \boldsymbol{r}_\mathrm{p}|$, equation (6.17) generates the implicit function

$$\frac{H^2}{2\,r^2} - \frac{q}{\sqrt{(s/r)^2+(H/r)^2}} = \frac{r}{2\,\gamma}\left(\frac{c_s^2}{G\,M_\star}\right) - q\,\left(\frac{r}{s}\right). \tag{6.18}$$

Although there are no constraints on the ratio s/r, because with nested grid computations that ratio can be very small, the aspect disk ratio H/r is smaller than one, by working hypothesis, otherwise the 2D geometry would not be consistent. Therefore, the second term on the left-hand side can be expanded in a binomial series in H/r (up to the its second power), obtaining H as an explicit function:

$$H^2 = \frac{r}{\gamma}\left(\frac{c_s^2}{G\,M_\star}\right)\left[\frac{1}{r^2} + q\left(\frac{r}{s^3}\right)\right]^{-1}. \tag{6.19}$$

We note that, in the limit $q \to 0$ or $s \gg r$, equation (6.19) yields $\sqrt{\gamma}\,H = c_s/\Omega_\mathrm{K}$, as in regular accretion disks. Close by the planet, i.e., in the circumplanetary disk where $s \ll r$, the above relation reduces to $\sqrt{\gamma}\,H = c_s/\sqrt{G\,M_\mathrm{p}/s^3}$, which resembles the previous

limit because the circumstellar orbital frequency is replaced by the circumplanetary one. Rearranging the terms in equation (6.19), a more compact expression can be written:

$$H^2 = \frac{1}{\gamma}\left(\frac{c_s}{\Omega_{\rm K}}\right)^2 \left[1 + q\left(\frac{r}{s}\right)^3\right]^{-1}. \tag{6.20}$$

Equation (6.20) has a singularity at $s = 0$. This arises from the corresponding singularity in the gravitational potential Φ, which is overcome by introducing the smoothing length (eq. [6.1]). In our computations, for consistency reasons, the distance $\sqrt{s^2 + \delta^2}$ substitutes s in equation (6.19).

6.2.4 Artificial Viscosity

Non-linear effects in wave propagation inevitably lead to shock formation. This is indeed the case in our simulations as shown in the previous chapters. In ideal fluids shocks are mathematical discontinuities. Therefore, in finite-differencing schemes, they must extend only over one or two grid points. In order to provide the correct jump conditions, ahead and behind a shock front, dissipative terms have to be present in the equations. This is usually done by introducing a non-linear viscous pressure otherwise known as *artificial viscosity*. In contrast to the calculations presented in the other chapters, now it is possible that stronger shocks develop, since the pressure is no longer proportional to the density. Therefore, the physical viscosity might not be sufficient to provide the correct conditions across shock fronts.

The classical way of dealing with artificial viscosity is that introduced by von Neumann and Richtmyer back in 1950. This approach is based on the analysis of planar shocks in one dimension. The extension to multidimensional problems has been proved to be adequate enough as long as space geometry is Cartesian. Yet, the most rigorous treatment of shocks in a multidimensional space, with a generic metric tensor, requires the definition of an isotropic viscous stress tensor $\mathbf{Q}$ (Winkler and Norman 1986), whose components are (Mihalas and Weibel Mihalas 1999):

$$Q_{ij} = \mu_{\rm Q}\left[(\nabla \boldsymbol{u})_{ij} - \frac{1}{3}\nabla\cdot\boldsymbol{u}\right]\delta_{ij}. \tag{6.21}$$

Because of the Kronecker symbol δ_{ij}, only the diagonal elements survive. We chose to discard the off-diagonal tensor components because they may lead to artificial angular momentum transport. The coefficient of artificial is so defined:

$$\mu_{\rm Q} = -\mathcal{L}^2\,\Sigma\,\min\left(\nabla\cdot\boldsymbol{u}, 0\right), \tag{6.22}$$

where $\mathcal{L}$ represents the length over which the shock is smeared. This is usually fixed to the maximum grid spacing. The coefficient $\mu_{\rm Q}$ is positive only for compression and zero for expansion, so the artificial viscosity is large in shocks and negligibly small elsewhere.

Since the artificial viscous tensor acts as a pseudo-pressure, it affects both momentum and energy equations through the terms $\nabla\cdot\mathbf{Q}$ and $\mathbf{Q}\cdot\nabla\boldsymbol{u}$ (meant as a tensor product), respectively. Both equations are updated, by using the corrects components Q_{ij}, as explained in Stone and Norman (1992a). One side-effect is that $\mathbf{Q}$ can reduce the viscous time step by a factor which is proportional to $\left[\mathcal{L}^2\,\nabla\cdot\boldsymbol{u}\right]^{-1}$.

6.3 Energy Equation Solver

The general numerical method employed to solve the hydrodynamical equations on a hierarchy of nested grids, applied to simulations of disk-planet interactions, has been explained in CHAPTER 3. In contrast to previous calculations, thermal energy density E now appears as an independent variable. Here we outline how the source terms (right-hand side of eq. [6.6]) are dealt with. In the framework of the nested-grid scheme, whenever required, E is interpolated from a finer to a coarser grid and *vice versa*, according to the procedures depicted in § 3.5 and § 3.6, respectively.

The energy equation (eq. [6.6]) is solved by means of a multi-step operator splitting method. The first step takes care of the energy advection and this is done in the same fashion as the advection of the other dynamical quantities, i.e., through the van Leer's algorithm. Viscous dissipation and radiative cooling are treated by means of a predictor-corrector scheme, which is second-order accurate in time. This proceeds as follows:

$$\begin{aligned} \frac{E^{\rm pred} - E_n}{\Delta t_n} &= \Upsilon_n - \Lambda_n, \\ \Lambda^{\rm pred} &= \Lambda[E^{\rm pred}], \\ \frac{E_{n+1} - E_n}{\Delta t_n} &= \Upsilon_n - \frac{1}{2}\left(\Lambda_n + \Lambda^{\rm pred}\right). \end{aligned} \tag{6.23}$$

In the above equation we have indicated with the subscript n the quantity values from the preceding sub-step and with Δt_n the computing time interval. The heating and cooling terms are considered simultaneously because they have definite and opposite signs, and in a stationary disk without planets, they determine the local energy budget (i.e., $\Upsilon \simeq \Lambda$).

During the course of the first experiments, it was discovered that, due to very high pressures and large values of the flow divergence (in the wake of the circumplanetary spirals), the compressional work could lower the thermal energy by a large amount. Consequently, the predictor-corrector procedure applied to this equation term occasionally resulted unstable, producing negative energy values. Therefore we decided to take advantage of equation (6.3) and use an analytic solution for updating the energy.

In the framework of the operator-splitting approach, in order to correct the energy because of the gas compression / dilation, we have to solve numerically the equation

$$\frac{\partial E}{\partial t} = -P\,\nabla\cdot\boldsymbol{u}, \tag{6.24}$$

which becomes, with the aid of the state equation

$$\frac{\partial E}{\partial t} = -(\gamma-1)\,E\,\nabla\cdot\boldsymbol{u}. \tag{6.25}$$

Equation (6.25) has an analytic solution, given by $E = E_0\,\exp\left[-(\gamma-1)\,\Delta t\,\nabla\cdot\boldsymbol{u}\right]$, where Δt is a time interval over which the divergence $\nabla\cdot\boldsymbol{u}$ has not changed. Hence, thermal energy density can be updated as follows:

$$E_{n+1} = E_n\,\exp\left[-(\gamma-1)\,\Delta t_n\,\nabla\cdot\boldsymbol{u}_n\right]. \tag{6.26}$$

We notice that, expanding the exponential of equation (6.26) in a Taylor series and keeping all the terms up to the second order in Δt_n, one gets

$$\frac{E_{n+1} - E_n}{\Delta t_n} = -P_n \nabla \cdot \boldsymbol{u}_n + \frac{1}{2} (\gamma - 1) P_n \Delta t_n (\nabla \cdot \boldsymbol{u}_n)^2, \tag{6.27}$$

where $P_n = (\gamma - 1) E_n$. It easy to prove that equation (6.27) is equivalent to a predictor-corrector scheme. The above equation also shows that the second-order correction always increase the thermal energy.

Although the procedure in equation (6.26) is not so general as the predictor-corrector algorithm, it is more accurate and unconditionally stable. Furthermore, contrary to what may seem at first glace, from the computational viewpoint it is faster than the other because it requires less mathematical operations.

6.3.1 Some Tests

We have tested the equation energy solver from both the numerical and the physical point of view. Here we will present some of these tests.

The first test is intended to check whether the equation of energy furnishes physically consistent results by comparing the computed temperature to that derived from some analytical, significant solution of equation (6.6). If we deal with a stationary Keplerian disk then the energy budget simplifies enormously. In fact, in a pure Keplerian flow both energy advection and compressional work are negligibly small. Therefore equation (6.6) reduces to (e.g., see Pringle 1981)

$$\Upsilon - \Lambda = 0. \tag{6.28}$$

From the same hypotheses, it follows that the dissipation function can be written in a simple form

$$\Upsilon = \Sigma \nu \left(r \frac{\mathrm{d}\Omega_\mathrm{K}}{\mathrm{d}r} \right)^2 = \frac{9}{4} \Sigma \nu \Omega_\mathrm{K}^2. \tag{6.29}$$

In fact, in a Keplerian flow, $(\partial u_r / \partial r)^2$ and $(u_r / r)^2$ are both much less than $(r \, \partial \Omega_\mathrm{K} / \partial r)^2$. If we additionally assume that the disk is optically thick then the emitted flux can be approximated to

$$\Lambda = 2 \sigma_\mathrm{R} T_\mathrm{eff}^4 \simeq \frac{2 \sigma_\mathrm{R} T^4}{(3/8) \tau}, \tag{6.30}$$

as implied by equation (6.15), when $\tau \gg 1$. Recalling that $\tau = \frac{1}{2} \kappa \Sigma$, then, equating equation (6.29) and equation (6.30) yields

$$T^4 = \frac{27}{128} \frac{\kappa \nu}{\sigma_\mathrm{R}} \Sigma^2 \Omega_\mathrm{K}^2. \tag{6.31}$$

Now we assume that disk material has an opacity which we can be cast in the form

$$\kappa = \kappa_0 T^2 \ \mathrm{cm}^2 \, \mathrm{g}^{-1}. \tag{6.32}$$

Morfill et al. (1985) relied on this Kramer-type law with $\kappa_0 = 2 \times 10^{-6}$ to investigate the global properties of viscous accretion disks, extending over a wide range of astronomical

units, and the consequences for the protoplanetary environment. Placing equation (6.32) in equation (6.31), one finds

$$T = \sqrt{\frac{27}{128}\,\frac{\kappa_0\,\nu}{\sigma_{\rm R}}}\,\Sigma\,\Omega_{\rm K}. \tag{6.33}$$

Such expression allows a direct comparison with the temperature distribution obtained from simulations, whose setup involves equation (6.29), equation (6.30), and the opacity law 6.32.

In order to carry out a comparison of this kind, we simulated an unperturbed disk (i.e., without any embedded body), with borders at 1 and 20 AU, surrounding a Solar-mass star. The disk mass is $M_{\rm D} = 0.03\ M_{\bigstar}$ and the kinematic viscosity is $\nu = 5 \times 10^{16}\ {\rm cm^2\,s^{-1}}$. Both the initial surface density and temperature are constant: $\Sigma(t=0) = 197\ {\rm g\,cm^{-2}}$ and $T(t=0) = 352$ K. Once the system has reached a stationary state, the surface density is expected to decay as $1/\sqrt{r}$, because ν is constant. (Lynden-Bell and Pringle 1974). Indeed, this is what one can observe in Figure 6.2 (left panel), where the azimuthally averaged, computed surface density $\langle\Sigma\rangle$ (crosses) is fitted by the power-law

$$\Sigma = 300\,\sqrt{\frac{5\ {\rm AU}}{r}}\ {\rm g\,cm^{-2}}. \tag{6.34}$$

On the other hand, equation (6.33) states that $T \sim \Sigma\,\Omega_{\rm K} \sim 1/r^2$, or more precisely, $T = 104\,(5\,{\rm AU}/r)^2$ K. Figure 6.2 (right panel) shows how the calculated averaged temperature $\langle T\rangle$ (crosses) fits to this analytic estimation.

For the sake of completeness, we repeated the same type of test in which, instead of the above relation (eq. [6.32]), we chose the Kramer's law $\kappa = 6.6 \times 10^{22}\,\rho\,T^{-3.5}\ {\rm cm^2\,g^{-1}}$, as in Frank et al. (1992). From the physical viewpoint, it must be noted that the validity of this formula is restricted to the inner parts of accretion disks and thus it does not suit to the simulated radial extent as well as equation (6.32) does. Anyway, even in this circumstance, we got a very good agreement between analytical and numerical results.

With the second type of test we intend to make sure that the algorithm is numerically stable in the sense that it always converges to the same solution whatever the initial conditions are. To do that we set up two simulations in which the full form of equation (6.6) is solved. This means that the dissipation function is given by equation (6.7), the irradiated flux is that in equation (6.15), and the Bell's opacity coefficient (§ 6.2.2) is employed. The disk radial domain is the same as before, but now the disk mass is smaller ($M_{\rm D} = 0.01\ M_{\bigstar}$) and so is the viscosity ($\nu = 10^{16}\ {\rm cm^2\,s^{-1}}$). The initial Σ is imposed to be constant and equal to $66\ {\rm g\,cm^{-2}}$ for both models. As initial temperature, in one model $T(t=0) = 14.5$ K, while in the other $T(t=0) = 580$ K. The "cold" as well as the "hot" model soon evolve toward a stationary state. Figure 6.3 contains initial and stationary profiles of $\langle\Sigma\rangle$ (left panel) and $\langle T\rangle$ (right panel) of the two simulations. Clearly, in each of the cases, the solutions match. This indicates that initial values play no role in the equilibrium solution achieved after the system has relaxed. The relaxation time somehow depends on $\Sigma(t=0)$, whereas scarcely any dependency on $T(t=0)$ is measured.

Finally, we examine some implications related to the opacity tables. A simulation was performed with the same parametrization as the "hot" model discussed before (see blue line in Fig. 6.3). But instead of choosing Bell's opacity, this model is based on the new

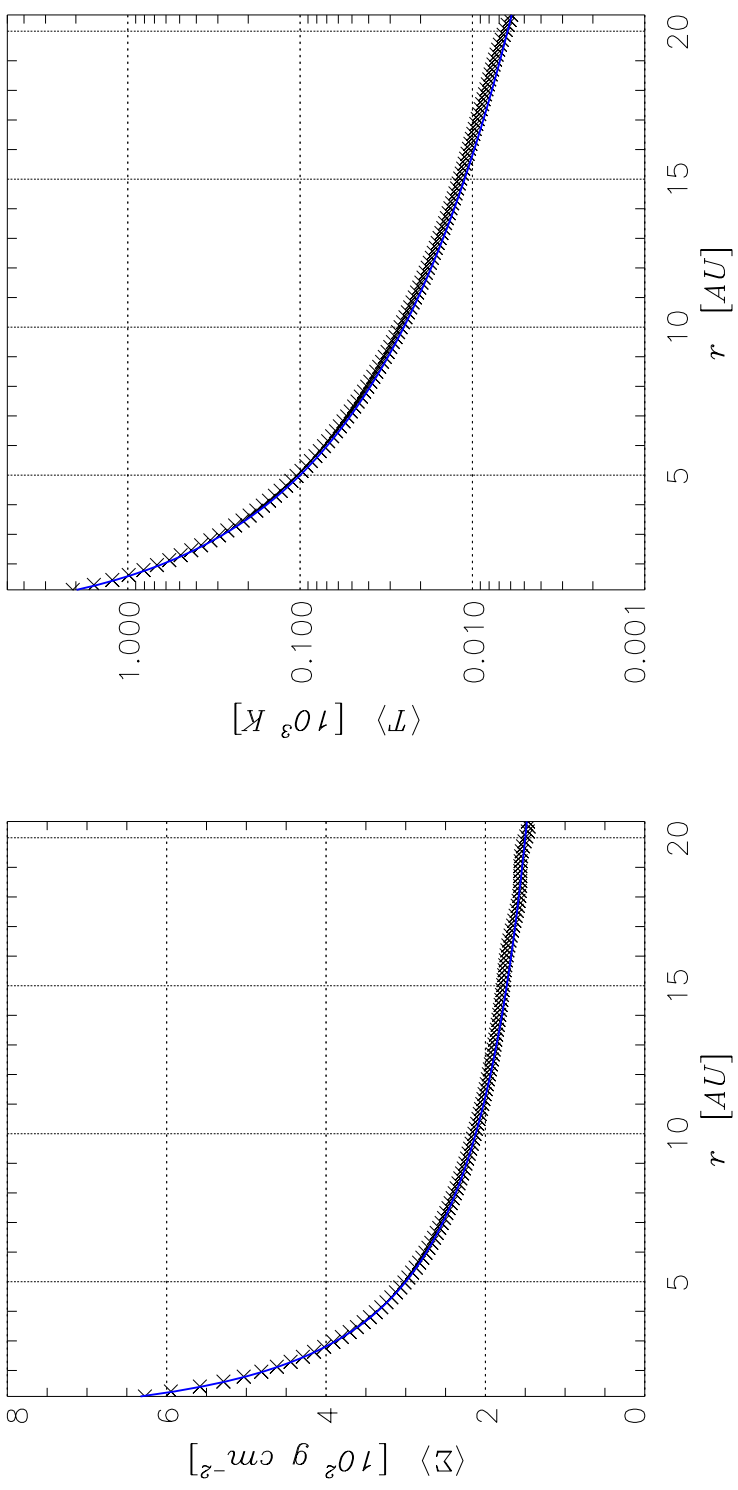

Figure 6.2: Test simulation of an unperturbed disk in which the relations 6.29, 6.30, and 6.32 are implemented. **Left Panel**. Crosses represent the computed Σ, averaged along the azimuth. The blue solid line indicates the power-law $\Sigma = \Sigma_0/\sqrt{r}$ (see text). **Right Panel**. The analytical formula for the midplane temperature (eq. [6.33]) is indicated in the plot by a blue solid line. Crosses represent the computed average temperature

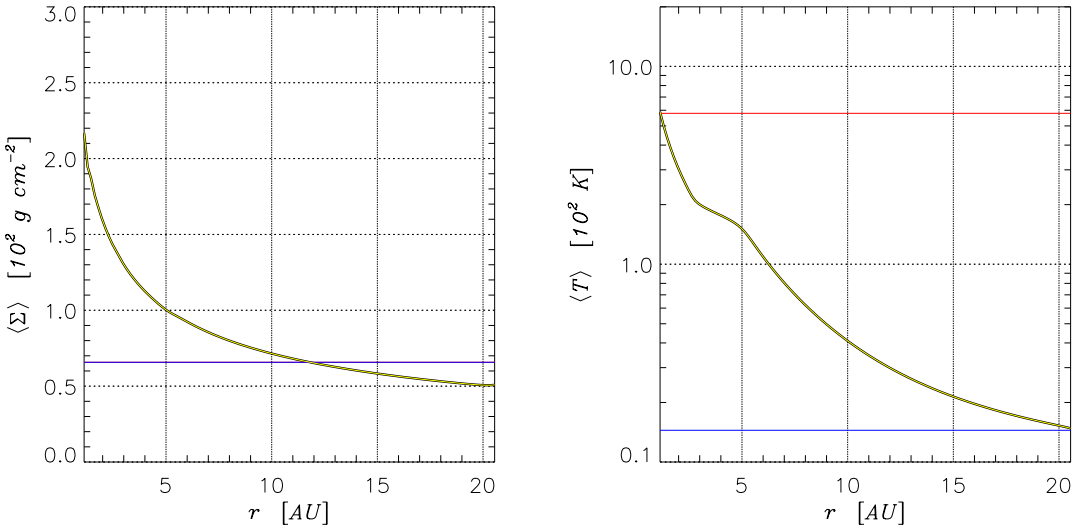

Figure 6.3: Simulations intended to check whether stationary solutions are connected to the initial temperature and density. In this case the full energy equation is solved (eq. [6.6]) along with equation (6.7) and equation (6.15). The opacity table is that by Bell and Lin (1994). Some additional model details are reported in the text. Averaged surface density is displayed in the left panel and the averaged temperature in the right panel. The solid blue and red lines represent the initial "cold" and "hot" distributions, respectively (they coincide in the left panel). The two overlapping curves (thick black and thin yellow lines) indicate the stationary solution for the two models.

tables by Semenov and collaborators (2001, private communication). The resulting surface density distribution, at equilibrium, is hardly distinguishable from that in the left panel of Figure 6.3. Indeed, not much difference is observed between the stationary averaged temperature profiles, as demonstrated in Figure 6.4. The result is not surprising, since already Liu and Meyer-Hofmeister (1997) tested the influence of different opacity tables on the vertical structure of accretion disks and found that the change in disk structure, due to an improved opacity coefficient, is hardly perceivable when compared to the uncertainties connected with the general disk parameterization.

Hence, throughout these simulations we use the opacity coefficient by Bell and Lin (1994), without any further inquiry on its reliability and / or applicability to the protostellar environment conditions that we simulate. Yet, it is worthy to note that this opacity table is well tested and has been extensively adopted in accretion disk studies (see, e.g., Godon 1996; Bell et al. 1997; Klahr et al. 1999; Armitage et al. 1999; Papaloizou and Terquem 1999; Nomura 2002).

Equation (6.15) contains the quantity $\varepsilon_{\rm H}$ which can be interpreted as the ratio of extinction to the absorption coefficient. Yet, the physical conditions of the protostellar environment are such that it is allowed to neglect radiation scattering and write $\kappa_{\rm ext} \simeq \kappa_{\rm abs}$, and

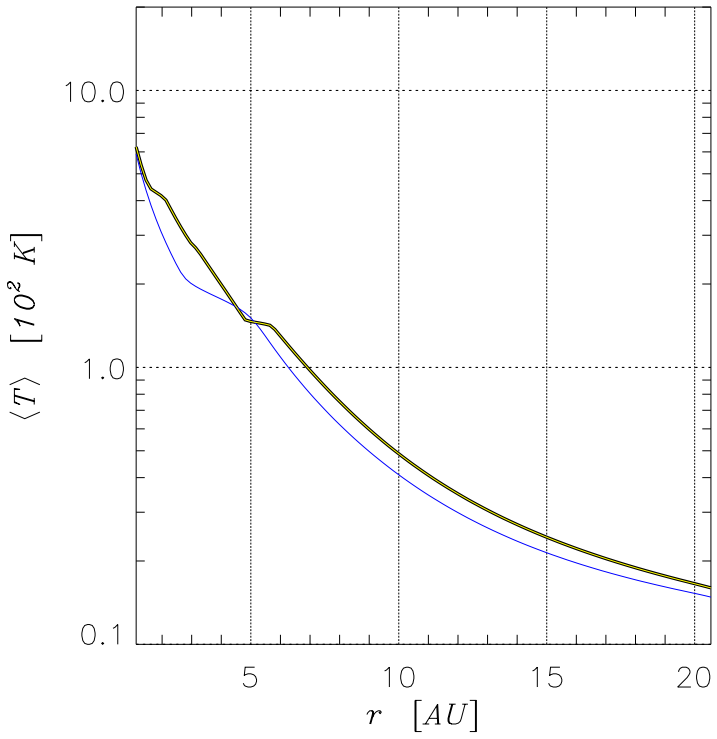

Figure 6.4: Comparison between two protostellar disk models which differ only on the choice of the opacity tables. The solid blue line is produced by the model run with Bell's opacity formulas (Bell and Lin 1994), whereas the thick black line comes from the model executed with the new opacity tables by Semenov and collaborators (2001, private communication). The temperature is slightly larger in this second case with respect to the first one. Discrepancies generally stay within 20%. In all of the simulations we will present hereafter, the quantity $\varepsilon_{\rm H}$ (see eq. [6.15]) is set to one. The reason for this is shown in this plot. The thin yellow line belongs to a simulation in which opacity by Semenov et al. was employed and $\varepsilon_{\rm H}$ computed as $\kappa_{\rm ext}/\kappa_{\rm abs}$. No differences exist with the model where the postulate $\varepsilon_{\rm H} = 1$ is made.

hence $\varepsilon_{\rm H} \simeq 1$. As proof of this, one calculation was executed by including $\varepsilon_{\rm H} = \kappa_{\rm ext}/\kappa_{\rm abs}$, in equation (6.15). The resulting temperature is shown in Figure 6.4 as a thin yellow line. Obviously, the hypothesis $\varepsilon_{\rm H} = 1$ is quite correct in our applications.

6.4 Model Parameters

Model parametrization deserves more attention in these computations than it did in the simulations presented so far. The reason for this resides in the nature of the opacity

coefficient (see § 6.2.2). In fact, κ is always in cgs units, because it is mostly derived by means of experimental measures. Hence, lengths and masses are to be fixed in physical units and consequently outcomes will not be scale-free, as they were before.

As in previous simulations, we model a circumstellar disk, orbiting a one-solar-mass star ($M_\star = 1\ M_\odot$), whose radial borders are $r_{\rm min} = 2$ AU and $r_{\rm max} = 13$ AU. The initial mass enclosed in this domain is $M_{\rm D} = 4.8 \times 10^{-3}\ M_\star$, i.e., $0.01\ M_\star$ within 20 AU (D'Alessio et al. 1998). That is 1.37 times as much as the value assumed in the other chapters. Since in stationary Keplerian disks, the energy budget is regulated by the balance between viscous dissipation and radiative losses (eq. [6.28]), the magnitude of viscosity may play an important role. Hence, we will cover three viscosity regimes: $\nu = 1.0 \times 10^{15}$, 5.0×10^{15}, and $1.0 \times 10^{16}\ {\rm cm^2\,s^{-1}}$ (Bell et al. 1997). Besides physical viscosity, we consider an artificial viscosity, which is active only in compression regions, according the tensor formulation explained in § 6.2.4. The length $\mathcal{L}$ is chosen to be equal to the maximum grid spacing, on each grid level (Stone and Norman 1992a; Ziegler 1998). The mean molecular weight is $\mu = 2.39$ (Morfill et al. 1985) and the adiabatic index $\gamma = 1.4$.

Figure 6.5 shows some averaged quantities of non-perturbed, stationary disks with the aforementioned characteristics. To distinguish among the different viscosity (and temperature) disk regimes, models will be generally referred to as "Hot" (H), "Warm" (W), and "Cold" (C).

An embedded planet is placed at $r_{\rm p} = 5.2$ AU ($\varphi_{\rm p} = \pi$). We make the same choice as in CHAPTER 5, and force the planet position to coincide with a main-grid cell corner, by fixing an adequate value of the planet-to-star distance a. In order to obtain reliable outcomes in the two-dimensional geometry, we consider a planetary mass range extending from $M_{\rm p} = 33\ M_{\earth}$ to $M_{\rm p} = 1\ M_{\jupiter}$ or, in terms of mass ratios $q = M_{\rm p}/M_\star$, we have models with $q = 1 \times 10^{-4}, 2 \times 10^{-4}, 5 \times 10^{-4}$, and $q = 1 \times 10^{-3}$. It was demonstrated in CHAPTER 5 that, concerning gravitational torques and mass accretion, 3D models agree quite well with 2D ones in that mass range.

However, since the disk thickness may be sufficiently small, even for low protoplanetary masses (see eq. [6.20]), we go as far as to simulate an additional C-model with $M_{\rm p} = 20\ M_{\earth}$. Figure 6.6 shows the disk semi-thickness in the planet's neighborhood, proving that the condition $H \lesssim R_{\rm H}$ locally holds.

The smoothing length δ is set to $2 \times 10^{-2}\, R_{\rm H}$ (see eq. [6.1]). All of the models are executed in an accreting and a non-accreting mode. When accretion onto the planet is allowed, the procedure outlined in § 4.3.2 is utilized. The evacuation parameter $\kappa_{\rm ev}$ is equal to 5, as in CHAPTER 4, whereas $\kappa_{\rm ac} = 0.1\, R_{\rm H}$. The latter length should be short enough to let the whole accretion procedure to be almost independent of $\kappa_{\rm ev}$, as proved by Tanigawa and Watanabe (2002).

Figure 6.7 illustrates the influence of the domain radial extent (both inner and outer one) for Jupiter C-models. Models provide quite consistent outcomes over the matching domain. Differences exist only close to the inner border, due to inflow boundary conditions. A smaller inner radius implies larger (Keplerian) fluid velocities to take care of. Thus, because of the Courant condition, smaller time steps are used in the calculations if one does not wish to lose resolution. For the example presented in Figure 6.7, since the two computations have the same numerical resolution, the larger domain model is computed

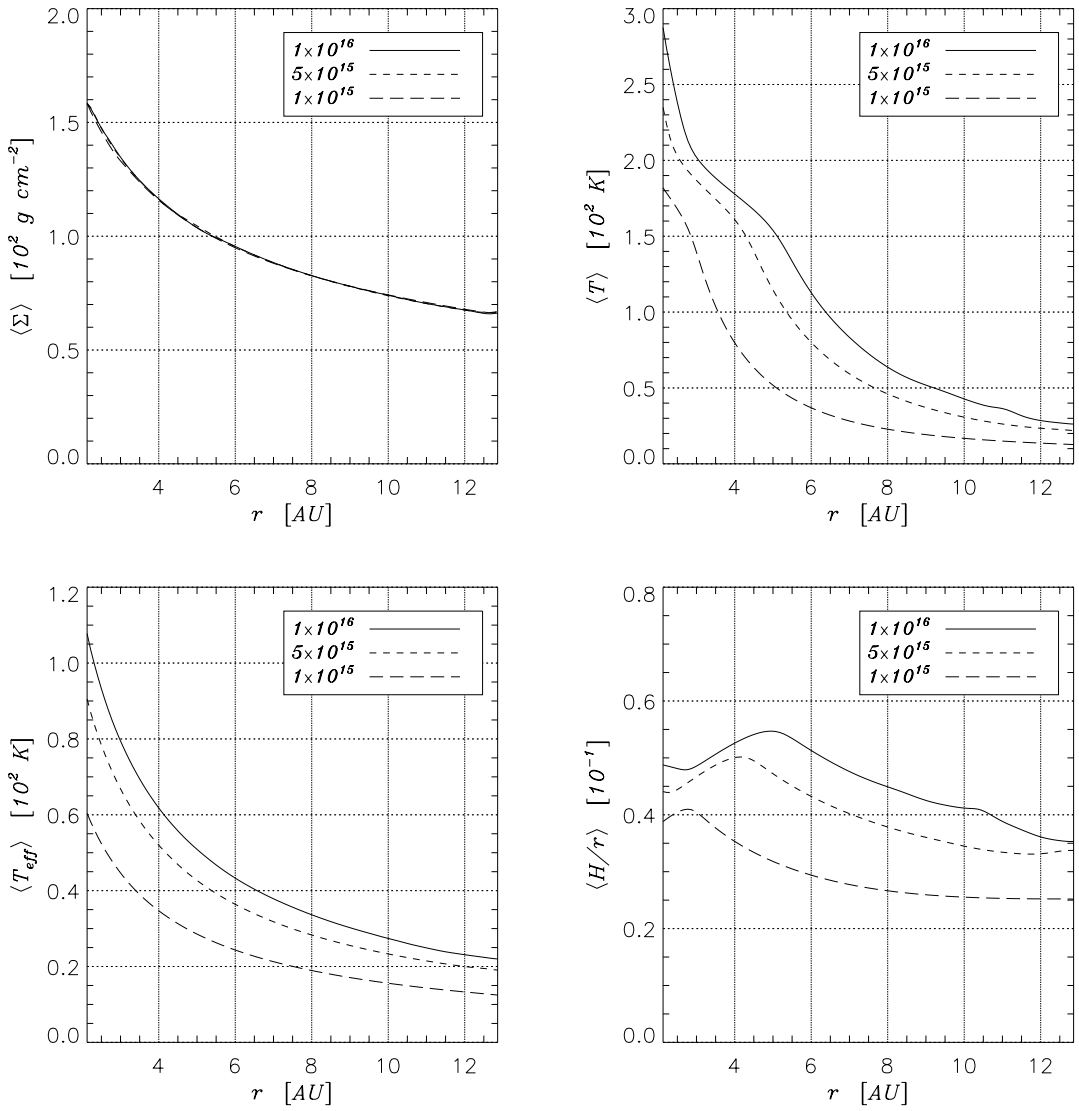

Figure 6.5: Some characteristics of radiative, unperturbed and stationary disks, as function of the kinematic viscosity. Radial boundaries are closed in order to achieve a strict stationarity by preventing mass losses. The surface density drops as $1/\sqrt{r}$. As long as the total disk mass is independent of ν, Σ does not depend on it either (**top-left panel**). At $r = r_{\rm p} = 5.2$ AU, the midplane temperature (**top-right panel**) varies form 50 to 150 K, when ν is increased from 10^{15} to 10^{16} $\rm cm^2\,s^{-1}$. Differences between the highest and lowest values, at radial boundaries, are even smaller. Disk effective temperatures (i.e., irradiated energy to the $1/4$ power) change only by a factor of roughly $1/2$ (**bottom-left panel**). The disk aspect ratio $h = H/r$ is not strictly constant (**bottom-right panel**), slightly declining as the radial distance increases. Variations are confined within 20, 30%.

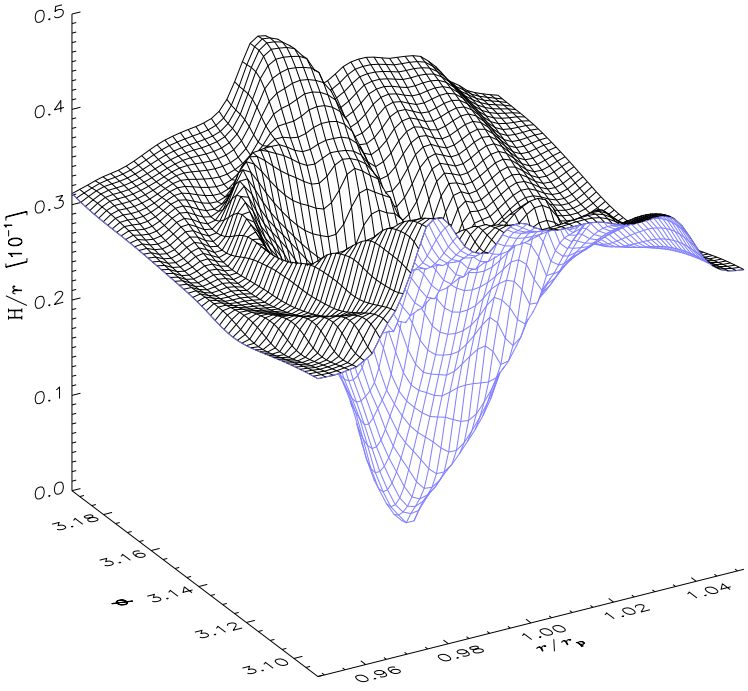

Figure 6.6: Because of the gravitational field of the embedded planet, the disk scale height may reduce considerably in its proximity, as prescribed by equation (6.20). This effect is shown here in case of a 20 $M_{\oplus}$ object within a C disk model. For comparison, $R_{\rm H}/r_{\rm p} = 0.027$.

with a time step which is generally a half of that used in the other model.

6.4.1 Initial and Boundary Conditions

Initial conditions require the assignment of the three functions $\Sigma(t=0)$, $E(t=0)$, and $\boldsymbol{u}(t=0)$ that we suppose to be axi-symmetric because we start from a stationary disk. However, instead of choosing the initial energy density, we prefer to fix the initial temperature and retrieve E via equations (6.3) and (6.4).

The theoretical surface density profile of a stationary accretion disk, with constant ν, is a power-law of the radial distance r (Lynden-Bell and Pringle 1974), which was also numerically demonstrated in § 6.3.1. Thus, as starting density distribution for our simulations, we set

$$\Sigma(t=0) = \Sigma_0 \sqrt{\frac{r_{\rm p}}{r}}. \tag{6.35}$$

where Σ_0 is determined by the disk mass value $M_{\rm D}$. Calculations are carried out for three different viscosity magnitudes, which imply three temperature regimes (see Fig. 6.5) in the protostellar environment. According to them, the initial temperature distribution is fixed. The behavior of the profiles in top-left panel of Figure 6.5 can be roughly reproduced by the power-law

$$T(t=0) = T_0(\nu) \left(\frac{r_{\rm p}}{r}\right)^{1.8}. \tag{6.36}$$

The initial temperature at $r = r_{\rm p}$ is given in Table 6.1 for the three values of ν. Finally, the initial circumstellar flow $\boldsymbol{u}(t=0)$ is a Keplerian one, corrected for the grid rotation.

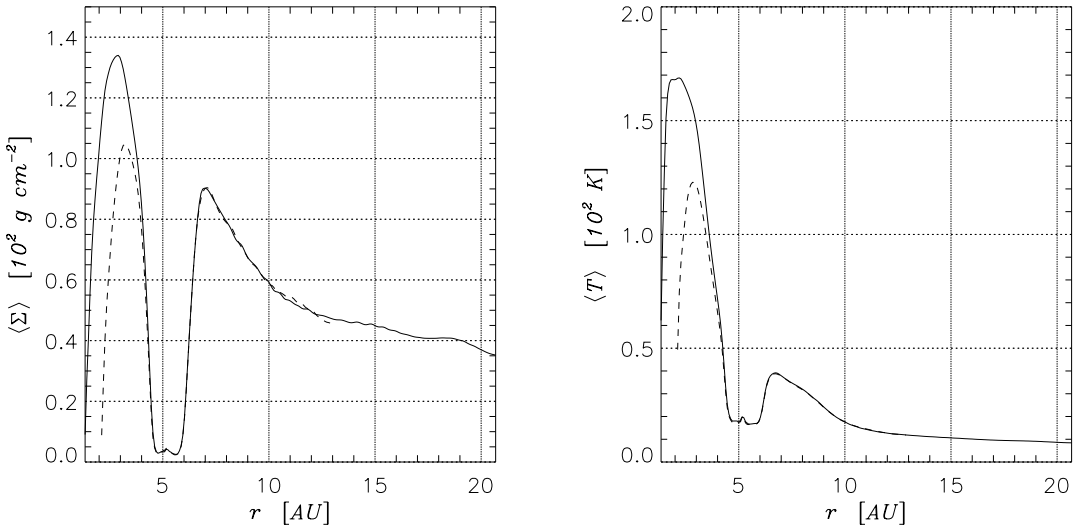

Figure 6.7: Average surface density (**left panel**) and temperature (**right panel**) profiles belonging to two Jupiter-mass test models which differ only by the extension of the radial domain. The solid line refers to a model for which $r_{\rm min} = 1.3$ AU and $r_{\rm max} = 20.8$ AU ($M_{\rm D} = 7.5 \times 10^{-3}\ M_{\bigstar}$), whereas the dashed line represents a standard radial domain model ($[2, 13]$ AU with $M_{\rm D} = 3.5 \times 10^{-3}\ M_{\bigstar}$). The kinematic viscosity corresponds to those employed in C-models.

As for the boundary conditions, all models are run with a partially open inner radial border and a reflective outer one. Thus, matter is free to flow out of the computational domain, at $r = r_{\rm min}$, but the opposite is not allowed. This is the same expedient invoked in CHAPTERS 4 and 5 to artificially mimic the mass accretion toward the central star and avoid spurious wave reflection at the inner domain edge, which is the closer to the planet. The flow field is Keplerian both at $r_{\rm min}$ and $r_{\rm max}$: $\boldsymbol{u} = [0, r\,(\Omega_{\rm K} - \Omega_{\rm p})]$.

6.4.2 Numerical Specifications

Numerical issues have been presented in detail elsewhere, in the present chapter and in preceding ones. Here we intend to give only some further specifications. As in CHAPTER 4, the basic computational mesh is made of $N_r \times N_\varphi = 143 \times 423$ (ghost cells included). Subgrids are all 64×64. All of the computations are based on a five-grid hierarchy. Thus, the finest resolution ranges from 1.3×10^{-2} (if $M_{\rm p} = 1\ M_{\earth}$) to $3.4 \times 10^{-2}\ R_{\rm H}$ (if $M_{\rm p} = 20\ M_{\earth}$), where $R_{\rm H} = a\ (q/3)^{1/3}$ is the planet's Hill radius.

Although we have not implemented a very sophisticated energy transport treatment, these simulations take between 35 and 40% longer than those discussed in CHAPTER 4 for equal-size grid hierarchies.

Table 6.1: Values of the initial temperature as function the three values of the kinematic viscosity. Temperatures are sampled at $r = r_{\rm p} = 5.2$ AU (T_0), $r = r_{\rm max} = 2.1$ AU ($T_{\rm max}$), and $r = r_{\rm min} = 13$ AU ($T_{\rm min}$).

ν [cm^2 s^{-1}]	T_0 [K]	$T_{\rm max}$ [K]	$T_{\rm min}$ [K]
1.0×10^{15}	50	180	13
5.0×10^{15}	110	235	22
1.0×10^{16}	150	295	26

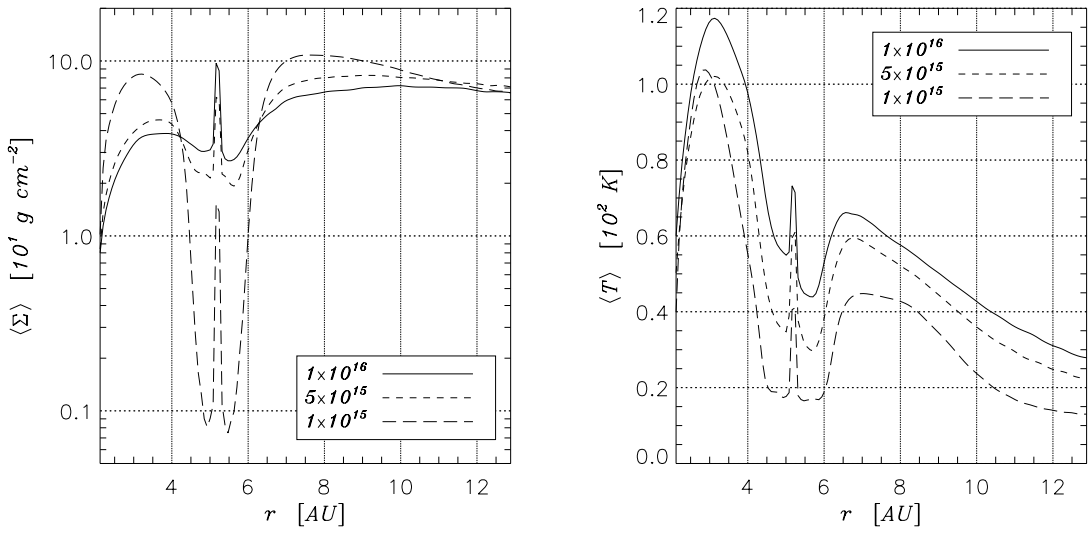

Figure 6.8: Average surface density (**left panel**) and temperature (**right panel**) in Jupiter-mass models after 240 orbital periods. By this evolutionary time, models have settled on a quasi-equilibrium state. The different profiles refer to different values of ν, as indicated in the legends. The density gap, in the C-model ($\nu = 10^{15}$ cm^2 s^{-1}), is more than an order of magnitude deeper (long-dash line) than it is in the other models. The temperature gap follows the same trend, though differences are somewhat less pronounced.

6.5 Global Model Properties

First of all we examine the behavior of global quantities for some selected models. Figure 6.8 shows both the averaged surface density and temperature in Jupiter-mass computations with different kinematic viscosity. We note that matter (left panel) is more uniformly distributed in the H- (solid line, $\nu = 1.0 \times 10^{16}$ cm^2 s^{-1}) and W-model (short-dash line, $\nu = 5.0 \times 10^{15}$ cm^2 s^{-1}), with respect to the C-model (long-dash line, $\nu = 1.0 \times 10^{15}$ cm^2 s^{-1}). The density gap is not very deep and actually looks like a depression, because of the larger viscosity coefficient and the depletion of the inner disk. Actually, these two effects have

a common cause. On one hand, in fact, a large viscosity prevents the formation of wide and deep gaps, as will be soon clarified. On the other hand, a large viscosity facilitates the inner-disk depletion, since $\dot{M}_{\rm D} = -3\,\pi\,\nu\,\Sigma$ (Lynden-Bell and Pringle 1974).

In contrast, in the Jupiter-mass C-model a well-defined and deep gap is carved in, where the density is more than an order of magnitude lower than it is in the other two models. Since material removed from gap regions is disposed at short distances, due to the small damping length of the waves launched by the secondary, gap shoulders have very high densities. Some authors have argued that these density enhancements might trigger planet formation. If so, low viscosity disks should be more efficient in doing that. The density peak in the middle of the gap is the signature of the circumplanetary disk. The accumulation of material around the protoplanet in these models is highly enhanced by the fact that no accretion is permitted onto the planet. When accretion is also accounted for, the local density value at the planet location can become up to two orders of magnitude smaller than that attained in non-accreting models (see § 6.6).

As it was to expect, a temperature gap accompanies the density gap (right panel, Fig. 6.8). Also in this case the most extreme situation is represented by the C-model, where temperatures drop below 20 K. Anyway, the general trend of temperature distributions is such to allow 30, 40 K difference between temperatures in H- and C-models.

Global views of both density and temperature 2D-distributions are displayed in Figure 6.9. The top row illustrates the surface density, while the bottom one shows the temperatures. From the density maps one can see that disk spirals get closer to each other toward the outer border of the domain. In fact, circumstellar spirals propagate at a velocity equal to the sound speed, which is proportional to $\sqrt{T}$ (see eq. [6.5]). Thus, the propagation velocity reduces as r increases and faster waves overtake slower ones. Past the gap region, temperature decays more rapidly in the C-model (Fig. 6.8, right panel), hence this phenomenon is more evident.

Shifting toward smaller masses, one realizes that the gap is gradually refilled. This is visible in Figure 6.10, where non-accreting C-models of different mass are compared. At $M_{\rm p} = 0.1\ M_{\jmath}$, the gap is completely filled and does not exist any longer. The striking thing to notice is that at $M_{\rm p} = 0.2\ M_{\jmath}$ however, a density trough is not only still present but it is also fairly deep. Henceforth, we can conclude that the non-linear terms in the disk-planet interaction, responsible for the gap formation, cease to exercise their role between $M_{\rm p} = 0.1\ M_{\jmath}$ and $M_{\rm p} = 0.2\ M_{\jmath}$. The standard criterion to open a gap in a disk require two conditions (Lin and Papaloizou 1985, 1993). The first is a shock formation condition given by:

$$\left(\frac{M_{\rm p}}{M_{\star}}\right) > 3\,\left(\frac{H}{r}\right)^3 = 3\,h^3, \tag{6.37}$$

i.e., the Roche lobe must be larger than the disk scale height. Because of planet's gravity (see eq. [6.20]) and the low temperatures established in gap regions, this condition is always fulfilled when $M_{\rm p} \gtrsim 0.2\ M_{\jmath}$. However, equation (6.37) is not satisfied by H-models with $M_{\rm p} \lesssim 0.1\ M_{\jmath}$. The second condition concerns the requirement that tidal torques exceed viscous torques and reads

$$\left(\frac{M_{\rm p}}{M_{\star}}\right) > \left(\frac{40}{\mathcal{R}}\right), \tag{6.38}$$

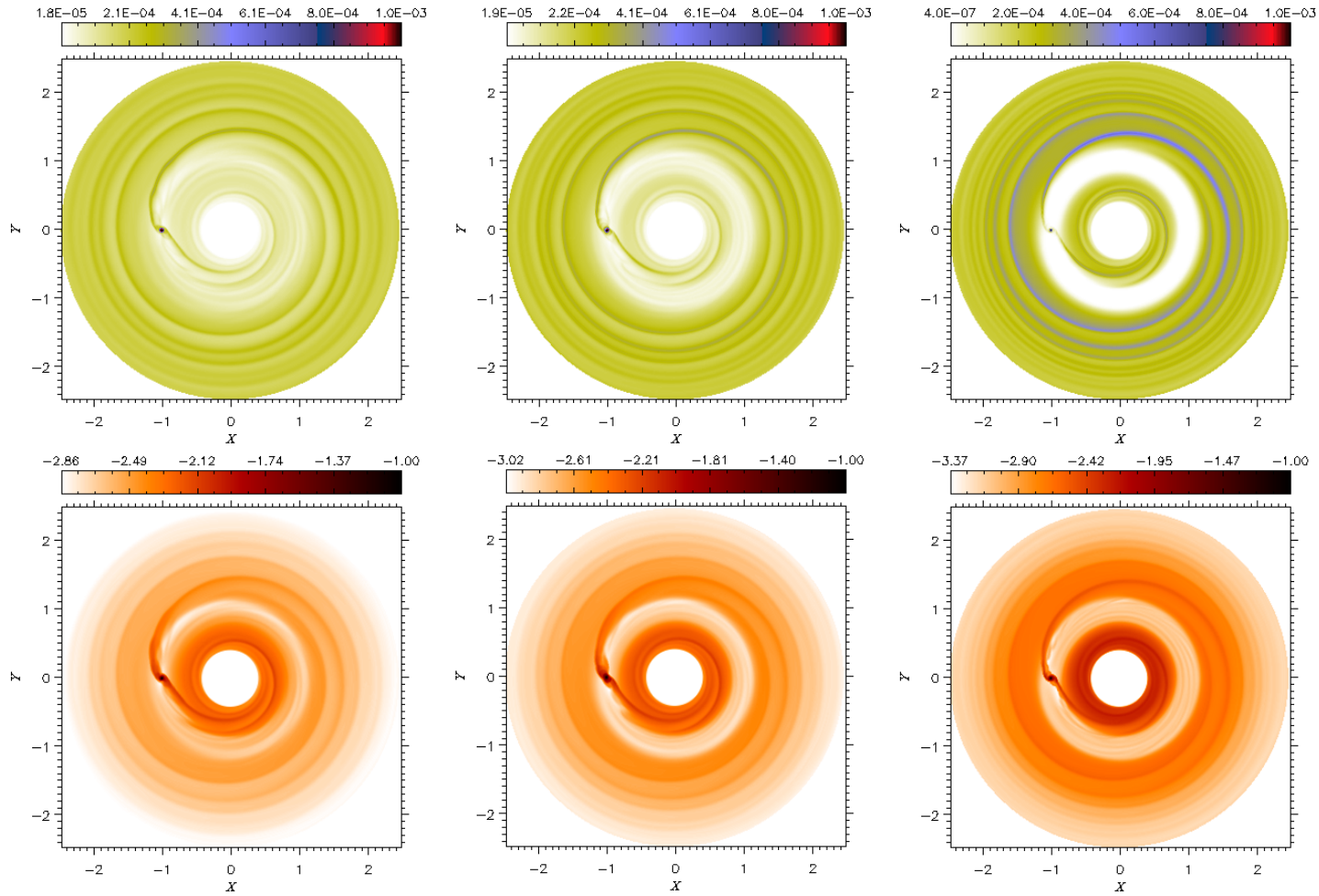

Figure 6.9: Two-dimensional surface density (**top panels**) and temperature (**bottom panels**) distributions for Jupiter-mass models. In the top panels the color scale is linear; in the bottom ones the colors scale logarithmically. In this plot, $\Sigma = 10^{-3}$ corresponds to $328.7\ \mathrm{g\,cm^{-2}}$, whereas $T = 0.1$ equals 1977 K. From left to right H-, W-, and C-model are considered. Density distributions show clear evidences that the a well-defined gap needs a cold (i.e., low viscosity) environment to be established. The same is true for the temperature distribution.

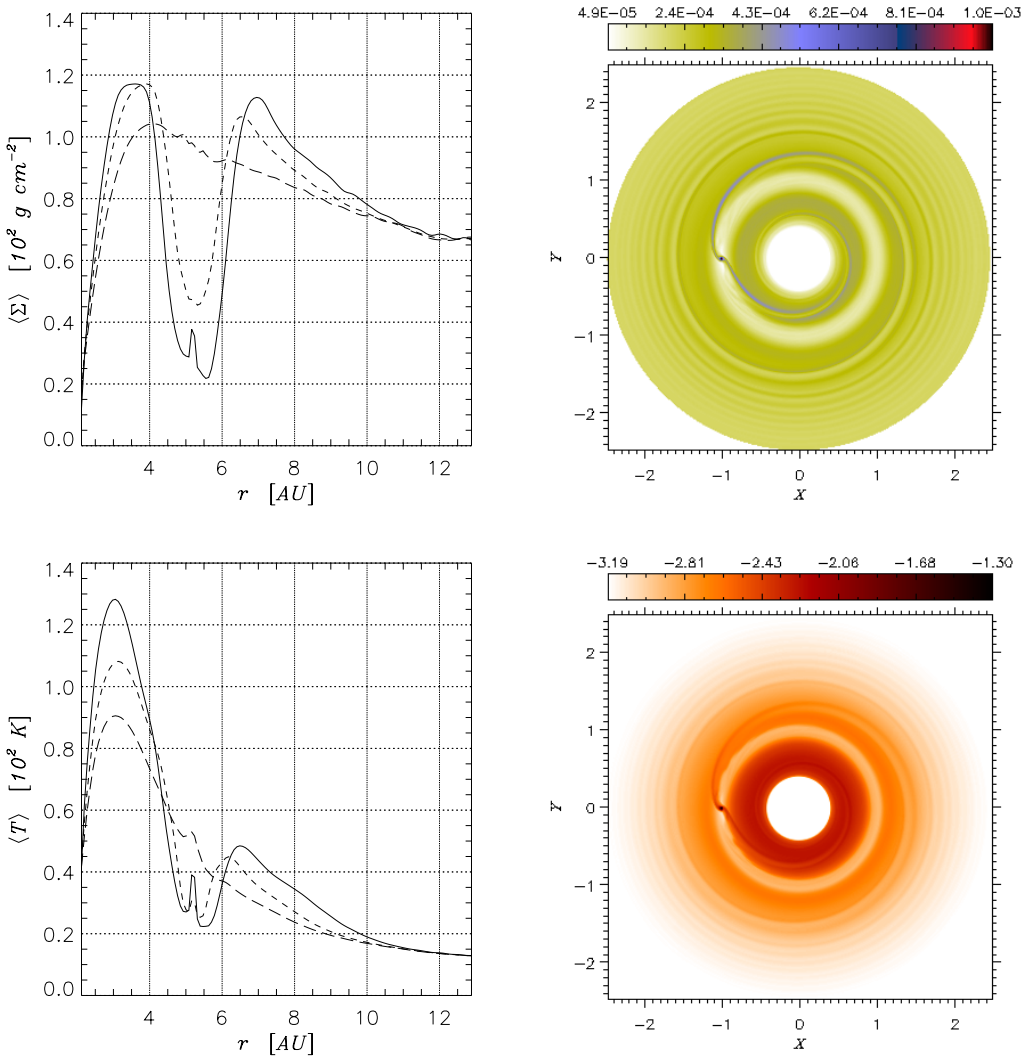

Figure 6.10: **Left Panels**. Averaged surface density and temperature in C-models ($\nu = 10^{15}\ \mathrm{cm^2\,s^{-1}}$) with different masses: $M_\mathrm{p} = 0.5\ M_{\mathfrak{Y}}$ (solid line), $M_\mathrm{p} = 0.2\ M_{\mathfrak{Y}}$ (short-dash line), and $M_\mathrm{p} = 0.1\ M_{\mathfrak{Y}}$ (long-dash line). **Right Panels**. 2D-distribution of the surface density (top) and temperature (bottom) of a C-model with $M_\mathrm{p} = 0.2\ M_{\mathfrak{Y}}$. The density is scaled linearly, while temperature is scaled logarithmically. Conversion factors are the same as in Figure 6.9.

where $\mathcal{R} = r^2\,\Omega_\mathrm{K}/\nu$ is the Reynolds number. The right hand side of equation (6.38) is proportional to ν and in our case goes from $\approx 4 \times 10^{-3}$ (H-models) to $\approx 4 \times 10^{-4}$ (C-models). Thereby, we should not obtain gaps in any of the H-models. Figure 6.8 (solid line) decently agrees with this prediction, since only a trough is dug in H- and W-models. However, condition 6.38 is partly violated in the low-viscosity regime (Fig. 6.10), because

Table 6.2: Ratio of the minimum density in the gap to the density at the gap's taller shoulder (rounded to the first significant digit). Values are recovered from the azimuthal average of Σ around the star. The letters "NG" stand for "No Gap". The symbol "✓" appear whenever at least one of criterion 6.37 and 6.38 is not fulfilled (N.F.).

$M_{\rm p}/M_{\star}$	C-MODELS			H-MODELS		
	ACC.	NON-ACC.	N.F.	ACC.	NON-ACC.	N.F.
1.0	< 0.01	< 0.01		0.6	0.8	✓
0.5	0.06	0.2		0.9	NG	✓
0.2	0.3	0.4	✓	NG	NG	✓
0.1	0.6	NG	✓	NG	NG	✓
0.06	0.8	NG	✓			✓

a clear gap is visible for the $M_{\rm p} = 0.2\ M_{\star}$ case. One reason why the mentioned criterion could not perfectly apply to our calculations resides in the fact that it was derived for simple polytropic disks, while we simulate also the thermal evolution of the system. In Table 6.2 we report the gap occurrence and depth for all of the models.

As regards the circumstellar disk spirals, only feeble traces are left. Temperature distributions behave similarly, though large-scale signatures due to the planet are even weaker. As explained further in this section, the absence of global disk features produced by an embedded body invalidates direct imaging observations as a detection tool in the intermediate-mass range, i.e., around a few times of Uranus' mass.

From the thermal point of view, we can notice that the optical thickness of the models is generally larger than one, throughout the computational domain (Fig. 6.11, left panel). The averaged τ stays above 1 also at the outer disk (computational) edge. This is in agreement with what was found for accretion disks around T *Tauri* stars (D'Alessio et al. 1998). The density and temperature gap reflects in a similar feature in the distribution of τ (as shown in Fig. 6.11). Nonetheless, even within the gap region, material is generally optically thick ($\tau \gtrsim 1$). The exception is represented by the C-model. In this case, the central parts of the gap have an optical thickness around 0.01 (see Fig. 6.11, right panel). The most diluted portions of the gap, situated where the circumplanetary disk merges into the gap, have values of τ on the order of 10^{-2}, 10^{-3}.

Finally, we give a look at the emitted flux Λ, computed according to equation (6.15) (see Fig. 6.12). From the observational point of view, disk gaps could represent a probe for protoplanet detection. In fact, this is by far the most extensive imprint that a planet leaves on a circumstellar disks. Prospective studies on observability of gaps due to Jupiter-mass protoplanets, have already been presented by Wolf et al. (2002), and speculations on a developing gap around the *T Tauri* star[5] *TW Hya* have already been reported by Calvet et al. (2002). Here we do not intend to address the issue of whether gaps (or disk inhomogeneities in general) are really observable or to what extent they are. However, we have to notice that a necessary but not sufficient condition is that they must be wide and deep

[5] Actually, claims have been made (Brittain and Rettig 2002) that there exists a density gap also in the disk surrounding Herbig AeBe star HD141569.

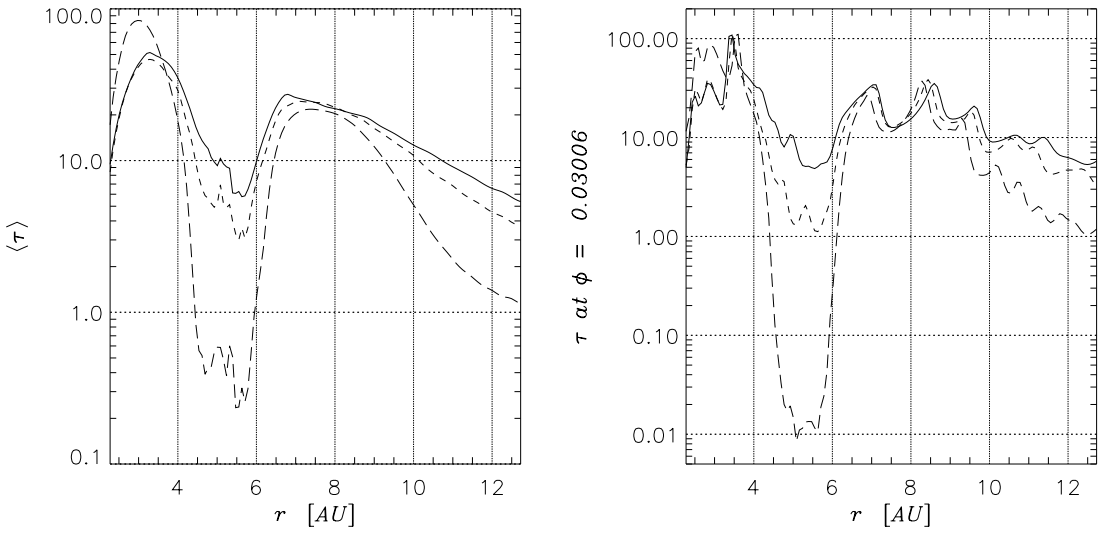

Figure 6.11: Circumstellar disks are usually very optically thick. This plot shows that this is generally the case even when a disk contains a Jupiter-mass bodies. The line sequence is the same as in Figure 6.8 (data refer to the same models). **Left panel**. Optical thickness averaged around the star. Only in the C-model, $\langle\tau\rangle$ drops below 1. **Right panel**. Profiles at $\varphi \simeq 0$, i.e., 180° away from the planet location. As before, only in the gap region of the C-model τ drops below 1.

in order for the flux emitted from this region to have the strongest contrast with respect to the surrounding environment. From the lower panels of Figure 6.12 it appears clear that low kinematic viscosities would favor this kind of investigation. Disk spirals are probably too elusive to be captured by present-day ground-based instruments, despite the track exhibited by the $M_{\rm p} = 1\ M_{\mathfrak{P}}$ H-model (top-left panel.) As mentioned earlier, we also argue that it would seem rather unlikely to detect planetary masses smaller than Jupiter's, by means of these measurements. Center and right panels of Figure 6.12 display the emitted flux in case of a $M_{\rm p} = 0.2\ M_{\mathfrak{P}}$ and $M_{\rm p} = 0.1\ M_{\mathfrak{P}}$ models. In both cases, the quantity Λ furnished by H-models (top) looks quite smooth. Instead, some more inhomogeneities appear in C-models (bottom).

6.6 Protoplanet Structure and Environment

Before the discussion of the smaller-scale flow features, i.e., those computed on higher hierarchy levels, we shall return briefly to an hypothesis which now can be verified.

Equation (6.3) implicitly assumes that the radiation pressure is much smaller than the gas pressure. Since there is little doubt about the validity of such assumption in an unperturbed accretion disk, away from the boundary layer, we shall verify it in a region

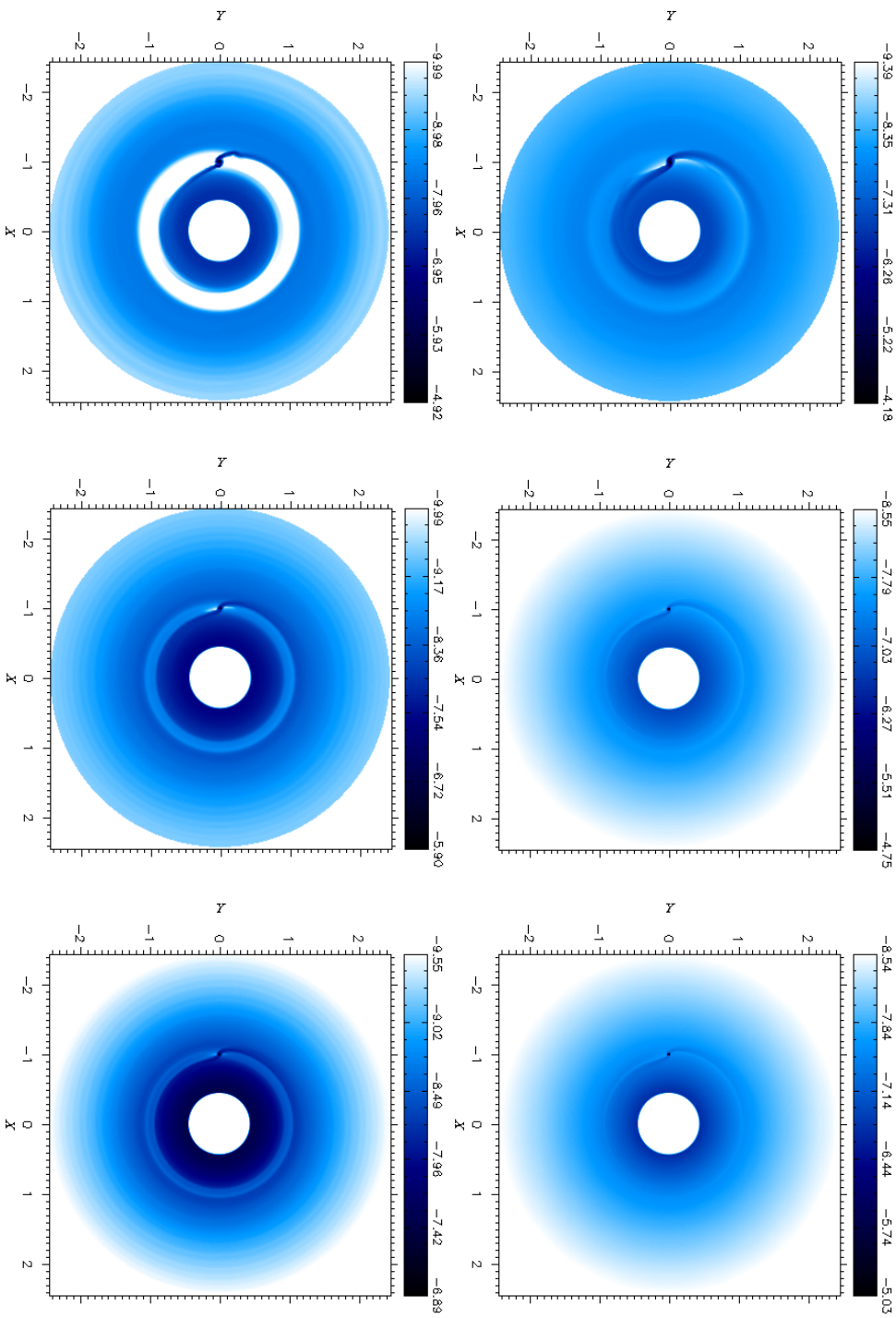

Figure 6.12: Flux radiated (i.e., Λ, see § 6.2.1 for details) by H-models **(top panels)** and C-models **(bottom panels)**. Left panels regard simulations of Jupiter-mass objects. Center panels refer to calculations with $M_{\rm p} = 0.2\ M_{\rm J}$, whereas right panels describe models $M_{\rm p} = 0.1\ M_{\rm J}$ ($M_{\rm p} = 33\ M_{\oplus}$). The color scale in both panels is logarithmic. In plot units, 10^{-5} means an energy flux of 4.7×10^4 erg cm^{-2} s^{-1}. For comparison, the surface flux of the Sun is 6.3×10^{10} erg cm^{-2} s^{-1}.

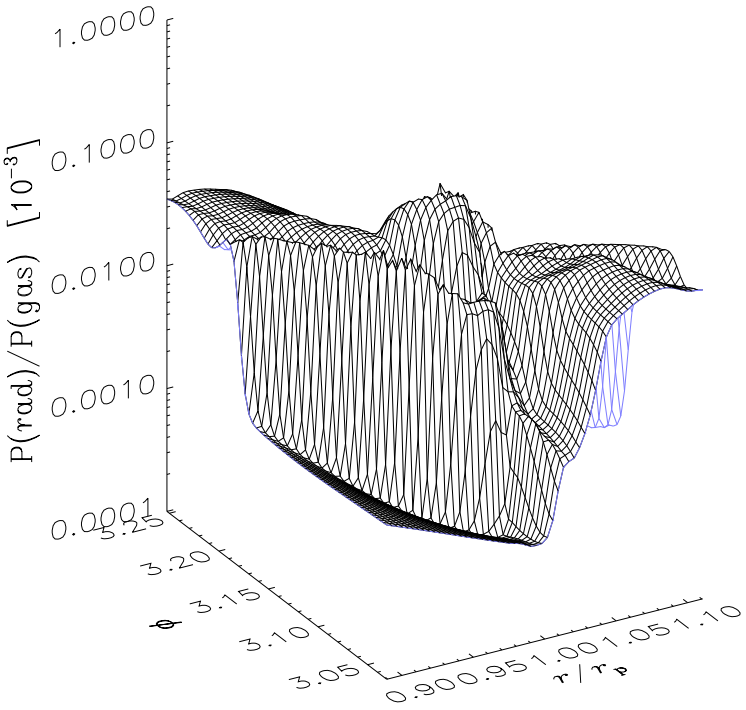

Figure 6.13: Ratio between the radiation and the gas pressure, around the protoplanet, for the Jupiter H-model. The two-dimensional map clearly shows that physical conditions, namely high densities and not sufficiently high temperatures, allow to consider the gas pressure as the only effective one.

around a massive protoplanet and within the gap. This is done in Figure 6.13. Radiation pressure usually dominates over gas pressure in regions of high temperatures and low densities ($P_{\rm rad} = a_{\rm R}\, T^4$, where $a_{\rm R}$ is the radiation density constant). We have seen that inside the gap density may be very low, when Jupiter-mass planet are involved and the viscosity is small enough. Yet, we have also showed that temperatures are extremely low in those cases. In contrast, close to a Jupiter-mass body ($s \lesssim R_{\rm H}$), T can even be some thousands of Kelvin degree, which may definitely boost radiation pressure. However, the highest temperatures are campaigned (and actually caused) by the highest densities, therefore the ratio between the radiation and gas pressure still lies much below one. A two-dimensional plot of $P_{\rm rad}/P_{\rm gas}$ is illustrated in Figure 6.13 for a $M_{\rm p} = 1\ M_{\oplus}$ H-model. The same dynamical range results from (both accreting and non-accreting) W- and C-models.

6.6.1 Accreting Models

In this section we will restrict to the discussion of accreting H- and C-models, while non-accreting counterparts will be examined in § 6.6.2.

Figure 6.14 indicates that, inside of the Roche lobe, the general aspect of the flow circulation around $1\ M_{\oplus}$ and $0.1\ M_{\oplus}$ protoplanets resembles that obtained with local isothermal models in two dimensions (CHAPTER 4). However, specific characteristics of the flow do differ. A circumplanetary disk, extending approximately over the entire Roche lobe, can be unambiguously distinguished for both masses and viscosity regimes. The mass of such sub-disks around one Jupiter-mass protoplanets, within the 80% of the Hill

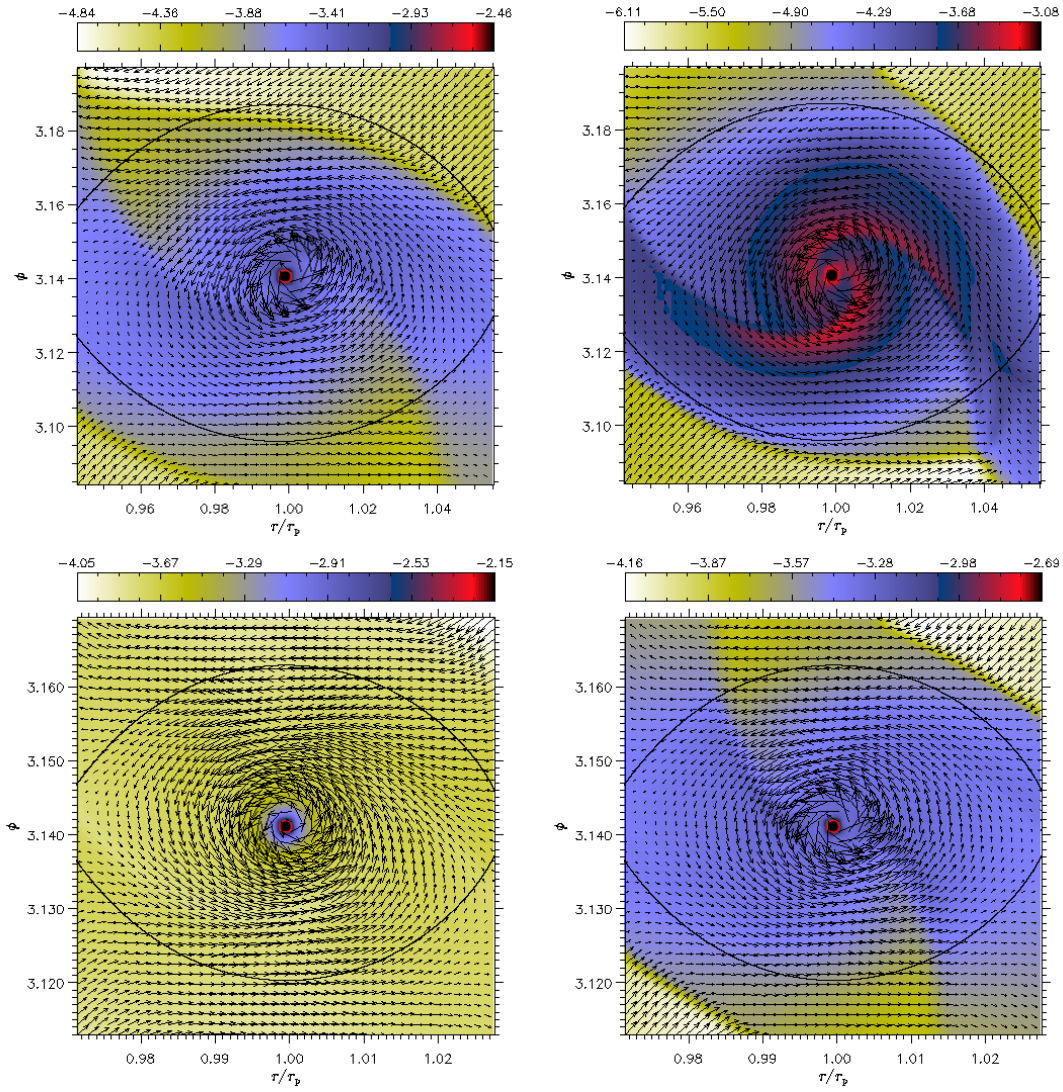

Figure 6.14: Density distribution and velocity field around $M_{\rm p} = 1\ M_{\rm J}$ (**upper panels**) and $M_{\rm p} = 0.1\ M_{\rm J}$ (**lower panels**) models. Right panels refer to H-models ($\nu = 10^{16}\ {\rm cm^2\,s^{-1}}$) whereas left ones refer to C-models ($\nu = 10^{15}\ {\rm cm^2\,s^{-1}}$). In each panel, color scales are logarithmic. In the units used in the color bar, -3 corresponds to $\Sigma = 328.7\ {\rm g\,cm^{-2}}$.

radius, is $1.03 \times 10^{-5}\ M_{\rm J}$ in the H-model and $5.36 \times 10^{-6}\ M_{\rm J}$ in the C-model. As regards calculations with $M_{\rm p} = 0.1\ M_{\rm J}$ planets, the mass measured in the sub-disk of the C-model is $4.03 \times 10^{-6}\ M_{\rm J}$, while the amount is nearly two times less in the H-model. It is worthy to note that, considering the whole set of accreting models, the ratio of the sub-disk to the planetary mass is always between $\approx 5 \times 10^{-6}$ and $\approx 5 \times 10^{-5}$.

The azimuthal average of the surface density distribution around the planet, inside

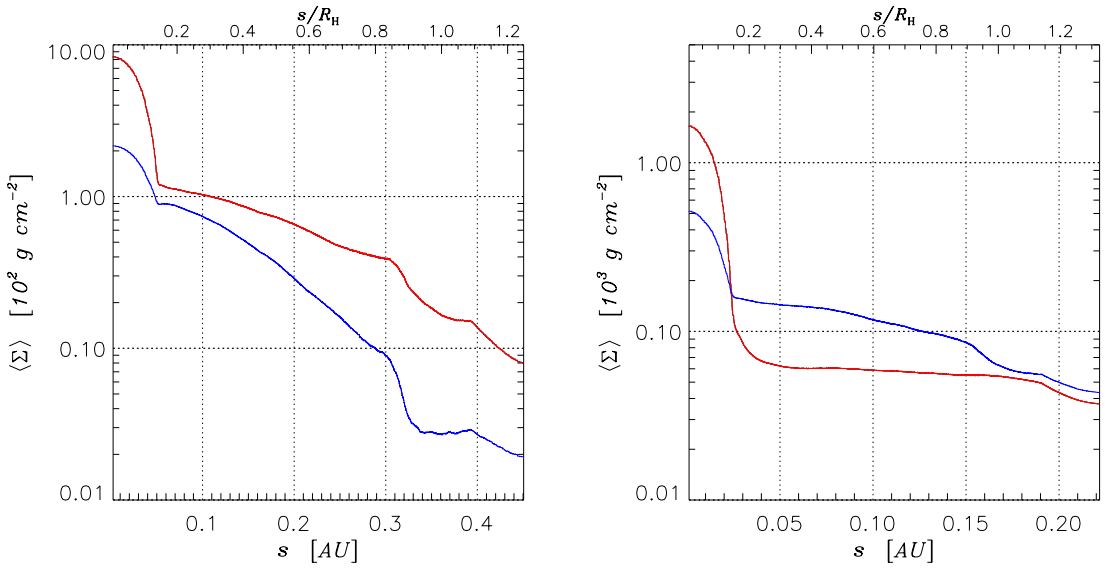

Figure 6.15: Average surface density performed around a $M_\mathrm{p} = 1\ M_{\mathrm{Earth}}$ (**left panel**) and $M_\mathrm{p} = 0.1\ M_{\mathrm{Earth}}$ (**right panel**) protoplanets. Red and blue profiles refer to the H- and C-models, respectively.

Table 6.3: Parameters that enter equation (6.39). This curve is a linear best-fit of the averaged density $\langle\Sigma\rangle$ computed inside of the Hill sphere.

$M_\mathrm{p}/M_{\mathrm{Earth}}$	C-MODELS			H-MODELS		
	$\langle\Sigma\rangle_0$ [g cm^{-2}]	a_1	RANGE	$\langle\Sigma\rangle_0$ [g cm^{-2}]	a_1	RANGE
1.0	2.92×10^2	-4.4	$[0.2, 1.0]\ R_\mathrm{H}$	2.14×10^2	-2.3	$[0.2, 1.0]\ R_\mathrm{H}$
0.5	1.59×10^2	-2.0	$[0.2, 1.0]\ R_\mathrm{H}$	1.35×10^2	-1.3	$[0.2, 1.0]\ R_\mathrm{H}$
0.2	2.32×10^2	-1.5	$[0.1, 1.0]\ R_\mathrm{H}$	8.57×10^1	-0.5	$[0.1, 1.0]\ R_\mathrm{H}$
0.1	1.99×10^2	-0.9	$[0.1, 1.0]\ R_\mathrm{H}$	6.75×10^1	-0.2	$[0.2, 1.0]\ R_\mathrm{H}$
0.06	1.47×10^2	-0.4	$[0.2, 1.0]\ R_\mathrm{H}$			

the Roche lobe, can be fitted by a relation of the type:

$$\langle\Sigma\rangle \simeq \langle\Sigma\rangle_0\, e^{a_1 (s/R_\mathrm{H})}, \tag{6.39}$$

where $s/R_\mathrm{H} \leq 1$ and larger than a threshold length (either 0.1 or $0.2\ R_\mathrm{H}$). The value of $\langle\Sigma\rangle_0$ is reported in Table 6.3, along with the other fit parameter a_1. One can see from this Table that the exponential decay of the averaged density increases as M_p grows. For the reference models, $\langle\Sigma\rangle$ is shown in Figure 6.15.

The presence of spiral features in the density distribution is a clear indication that the circumplanetary flow is Keplerian-like. Indeed, decomposing the velocity field $\boldsymbol{u}$ into the in-fall velocity (toward the planet) w_in and the rotational velocity (around the planet) w_rot

(see § 4.4.7 for details), it turns out that the former is more than an order of magnitude less than the latter. In Jupiter-mass models, the rotational velocity drops nearly as $1/s$ because of the action of the pressure gradient. As a consequence, the ratio of $w_{\rm rot}$ to the local Keplerian velocity decreases from 0.9, at $s = 0.1\,R_{\rm H}$, to ≈ 0.5, at $s = 0.8\,R_{\rm H}$. For $0.1\ M_{♃}$ models, this ratio declines at a similar rate. Moreover, in either case, the rotational regime is nearly independent of the viscosity magnitude, in the range investigated by these computations. Also the small magnitude of $w_{\rm in}$ implies some contribution from the pressure gradient in supporting the orbiting material.

Comparing the right panels (C-models) of Figure 6.14 to Figure 4.5, one can clearly see that spiral perturbations are less intense and more open. This is related to the lower values of the Mach number in the circumplanetary flow, which governs the inclination of the spiral wave with respect to the direction of the rotational motion. In fact, in local isothermal models $\mathcal{M}_{\rm iso} \simeq \sqrt{q\,(r_{\rm p}/s)}/h$. If $M_{\rm p} = 1\ M_{♃}$, the Mach number drops from ≈ 8, at $s = 0.1\,R_{\rm H}$, to 2, at $s = 1\,R_{\rm H}$. As comparison, in the circumplanetary disk displayed in the upper-left panel of Figure 6.14, $\mathcal{M}$ lies between 2.4 and 1.4, whereas the low viscosity Jupiter-model (upper-right panel) provides values between 3 and 1.5. The reason for this mainly resides in the larger value of the sound speed (which is proportional to the square root of the temperature: see eq. [6.5]). Hence, perturbations can travel faster and are less distorted by the background motion of the flow. Besides this, the negative temperature gradient within the sub-disk (see right panels of Fig. 6.16) prevents the Mach number from diminishing too rapidly toward the outer regions of the circumplanetary disk. In the Jupiter-mass models, illustrated in Figure 6.14, the azimuthally averaged $\mathcal{M}$ is approximately proportional to either $s^{-0.1}$ (H-model) or $s^{-0.2}$ (C-model). In the limit of a nearly constant Mach number, wave perturbations assume the form of Archimedes' spirals (see § 4.4.3).

Figure 6.16 shows the two-dimensional temperature distribution (left panels) around $M_{\rm p} = 1\ M_{♃}$ (top) and $M_{\rm p} = 0.1\ M_{♃}$ (bottom) C-models. The surface plots indicate that these distributions are rather symmetric with respect to the planet's position, though they are marked by weak spiral perturbations. In the Jupiter-mass case, maximum temperatures range from roughly 1500 to 1000 K, whereas T reaches the value of the ambient medium ($\lesssim 50$ K) at the border to the Hill sphere. From the upper-right panel of Figure 6.16 one can realize that the average temperature in the inner part of the Roche lobe differ by less than a factor two for the two viscosity regimes. In the low-mass case ($M_{\rm p} = 0.1\ M_{♃}$), the peak temperature is around one thousand kelvins and $T \approx 50$ K at $s = R_{\rm H}$, for both H- and C-model. Indeed, the average temperature profiles are very similar in such models (see the lower-right panel).

Over the entire sub-disk domain, $\langle T \rangle$ can be well fitted by the curve:

$$\langle T \rangle \simeq \langle T \rangle_{\bar{s}} \left(\frac{\bar{s}}{s} \right)^{\xi}, \tag{6.40}$$

in which the length $\bar{s}$ is set to $0.1\,R_{\rm H}$, for convenience. Fitting parameters are reported in Table 6.4, together with the validity range of the fitting function. From entries in the Table, it turns out that the temperature generally falls off as $1/s$.

Accreted matter would also contribute to raise the temperature of the circumplanetary disk, via dissipation of gravitational energy into heat. This additional source of energy is

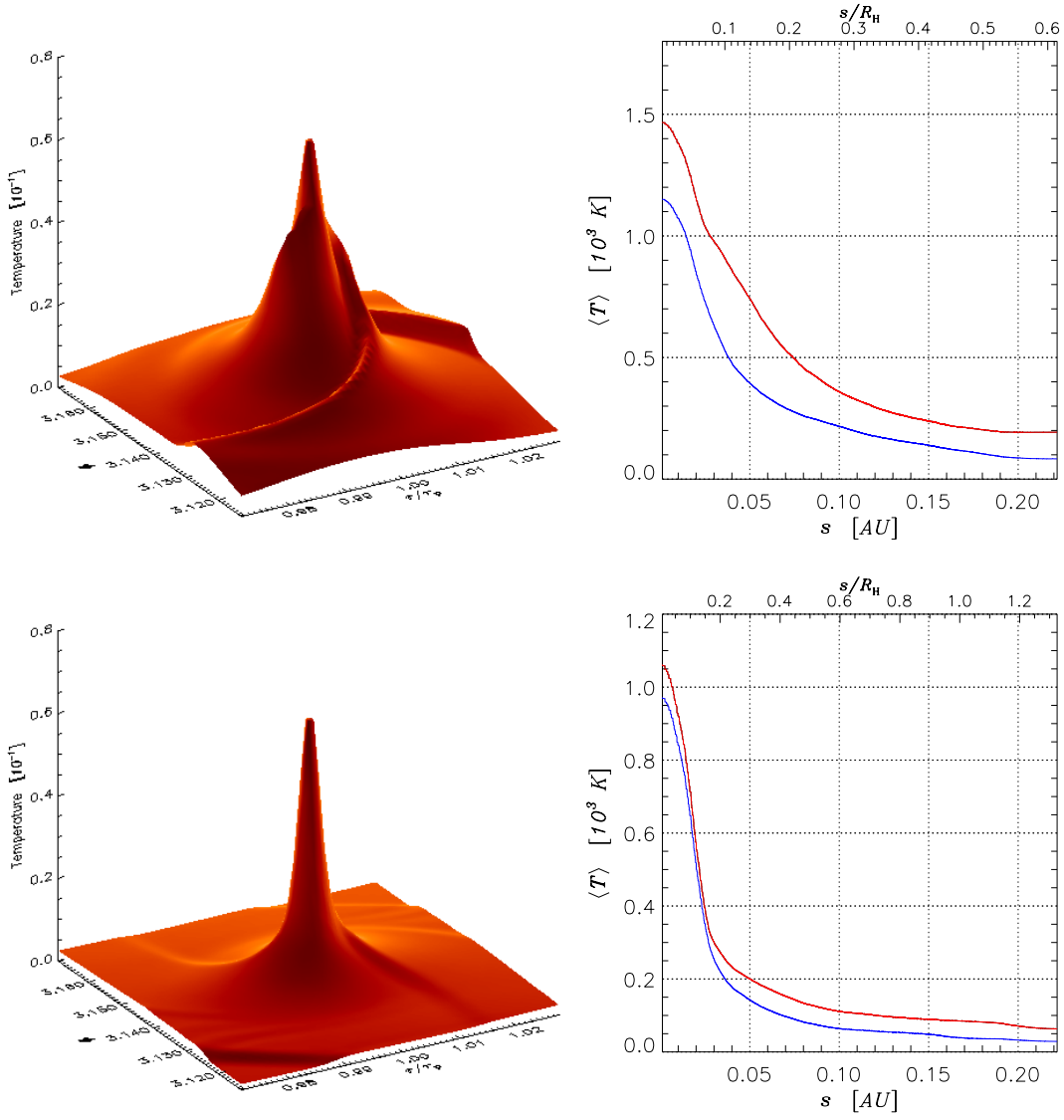

Figure 6.16: **Left Panels**. Two-dimensional distribution, inside of the Roche lobe, of the temperature around Jupiter-size (top) and 0.1 $M_{\oplus}$ (bottom) accreting C-models. The value $T = 0.1$ is equal to 1977 K. **Right Panels**. Since temperature distributions are quite symmetric with respect to the planet position for both planetary masses, they can be azimuthally averaged. In these two panels, red profiles (upper ones) refer to the H-models and blue (lower ones) to C-models.

not explicitly accounted for in these simulations [6]. In contrast, assuming this contribu-

[6]Yet, if the size of the protoplanet were larger than the accreting radius κ_{ac}, as probably is (see CHAPTER 5), accreted matter would come to rest, and release all of its energy content, before it had been actually removed

Table 6.4: Parameters that enter equation (6.40). This curve is a linear best-fit of the averaged temperature $\langle T \rangle$ computed inside of the Hill sphere. The column "RANGE" refers to the validity range of the fit.

$M_{\rm p}/M_{\star}$	C-MODELS			H-MODELS		
	$\langle T \rangle_{\bar{s}}$ [K]	ξ	RANGE	$\langle T \rangle_{\bar{s}}$ [K]	ξ	RANGE
1.0	5.405×10^2	0.97	$[0.05, 1.0]\, R_{\rm H}$	9.534×10^2	0.96	$[0.1, 1.0]\, R_{\rm H}$
0.5	5.304×10^2	0.96	$[0.05, 1.0]\, R_{\rm H}$	8.425×10^2	0.95	$[0.1, 1.0]\, R_{\rm H}$
0.2	5.713×10^2	1.12	$[0.05, 1.0]\, R_{\rm H}$	6.713×10^2	0.90	$[0.05, 1.0]\, R_{\rm H}$
0.1	4.395×10^2	1.03	$[0.05, 1.0]\, R_{\rm H}$	4.868×10^2	0.79	$[0.05, 1.0]\, R_{\rm H}$
0.06	4.634×10^2	1.07	$[0.05, 1.0]\, R_{\rm H}$			

tion as the only energy source around the planet, Tanigawa and Watanabe (2002) derived temperature profiles of sub-disks with different sound-speed regimes, performing local simulations with an isothermal equation of state. They found that the temperature would scale as $1/\sqrt{s}$, independently of the planetary mass.

We have to point out that, since radial transport of radiation is not taken into account here, one should expect large temperature gradients to be smoothed out. But temperature profiles are not extremely steep, at least in the range of distances covered by these models, hence correction by radial transfer should not be dramatically relevant, as we are going to demonstrate.

Radial Radiation Transfer in Circumplanetary Disks

Since the temperature gradient in the vicinity of a protoplanet may be quite steep, one of the hypothesis used in § 6.2.1 might break down locally. We refer to the assumption that the radiative flux in the vertical direction overwhelms those in the horizontal direction. With a semi-analytical, local analysis it is possible to make an *a posteriori* check of that hypothesis and shed some light over this matter. For simplicity we will suppose that the temperature distribution has a cylindrical symmetry around the planet, which is reasonable enough (see left panels in Fig. 6.16). Hence the total flux of energy transferred via radiation is

$$\Lambda \simeq \int_{-\infty}^{+\infty} \frac{\partial F_z}{\partial z}\, {\rm d}z + \int_{-\infty}^{+\infty} \frac{1}{s}\frac{\partial}{\partial s}[s\, F_s]\, {\rm d}z = \Lambda_z + \Lambda_s, \tag{6.41}$$

where s is the distance from the planet. The two terms on the right-hand side can be written as

$$\Lambda_z \simeq -\frac{128\, \sigma_{\rm R}}{3\, \kappa\, \rho}\, \frac{T^4}{H}, \tag{6.42}$$

and

$$\Lambda_s \simeq -\xi^2\, \frac{128\, \sigma_{\rm R}}{3\, \kappa\, \rho}\, H\, \frac{T^4}{s^2}. \tag{6.43}$$

from the system. Thus, also this energy source would have been implicitly considered in the computations.

Equation (6.42) was obtained by setting $\partial T/\partial z \approx T/H$ in equation (6.41), whereas equation (6.43) was derived by adopting equation (6.40), which we have checked to hold as long as $\bar{s} \lesssim s \leq R_{\rm H}$. The validity of the relation (6.9), used in § 6.2.1 (namely that $\Lambda \simeq \Lambda_z$) depends on the ratio of the left-hand sides of equations (6.42) and (6.43). Thus, this is the quantity that must be evaluated:

$$\frac{|\Lambda_s|}{|\Lambda_z|} = \xi^2 \left(\frac{H}{s}\right)^2 . \tag{6.44}$$

According to equation (6.44), only when $H < s$ the radiative cooling (eq. [6.15]) included in the energy equation is also locally a good approximation. To cast the above ratio in a more explicit form, one can use equation (6.20) in the limit $s \ll r$, which yields

$$\left(\frac{H}{s}\right)^2 = \frac{c_s^2}{\gamma} \left(\frac{s}{G\,M_{\rm p}}\right) . \tag{6.45}$$

By using the form of the sound speed in equation (6.5), one gets

$$\left(\frac{H}{s}\right)^2 = \left(\frac{k\,T}{\mu\,m_{\rm H}}\right) \left(\frac{s}{G\,M_{\rm p}}\right) . \tag{6.46}$$

Therefore, because of the position made above on the temperature profile, equation (6.44) becomes

$$\frac{|\Lambda_s|}{|\Lambda_z|} = \xi^2 \left(\frac{k\,\langle T\rangle_{\bar{s}}}{\mu\,m_{\rm H}}\right) \left(\frac{\bar{s}}{G\,M_{\rm p}}\right) \left(\frac{\bar{s}}{s}\right)^{\xi-1} . \tag{6.47}$$

Since the distance s is constrained by the applicability range of equation (6.40), the ratio given by equation (6.47) is supposedly meaningful roughly for $s \in [0.1\,R_{\rm H}, R_{\rm H}]$, for the models considered here. With the appropriate values the ratio 6.47 becomes

$$\frac{|\Lambda_s|}{|\Lambda_z|} = 0.145\,\xi^2 \left(\frac{\langle T\rangle_{\bar{s}}}{1000\,{\rm K}}\right) \left(\frac{M_{\rm \mathfrak{Y}}}{M_{\rm p}}\right)^{2/3} \left(\frac{\bar{s}}{s}\right)^{\xi-1} . \tag{6.48}$$

Note that with equation (6.48) we evaluate equation (6.47) at a distance s from the planet which shortens as ${M_{\rm p}}^{1/3}$. Since the squared sub-disk aspect ratio grows as $1/M_{\rm p}$, the flux ratio goes as ${M_{\rm p}}^{2/3}$. From Table 6.4, we see that $|\xi - 1|$ is between 0.03 and 0.12 in C-models and between 0.04 and 0.21 in H-models. Therefore, the right-most term in equation (6.47) can be considered as a unity term. Thus, around $s \approx \bar{s} = 0.1\,R_{\rm H}$, $|\Lambda_s|\,/\,|\Lambda_z| = 0.13$ for the Jupiter-mass H-model and a factor two smaller for the C-model. For the $M_{\rm p}/M_{\rm \mathfrak{Y}} = 0.1$, the ratio increases to 0.2 and 0.3, respectively. Thereby, apart from regions closer than $\sim 0.1\ R_{\rm H}$ to the accreting planet which cannot be investigated by these computations[7], radial radiation transport in the radial direction does not play a major role in the energy budget of circumplanetary disk material. This is in agreement with the standard scenario of the late stages of proto-Jovian disks (e.g., Coradini et al. 1989).

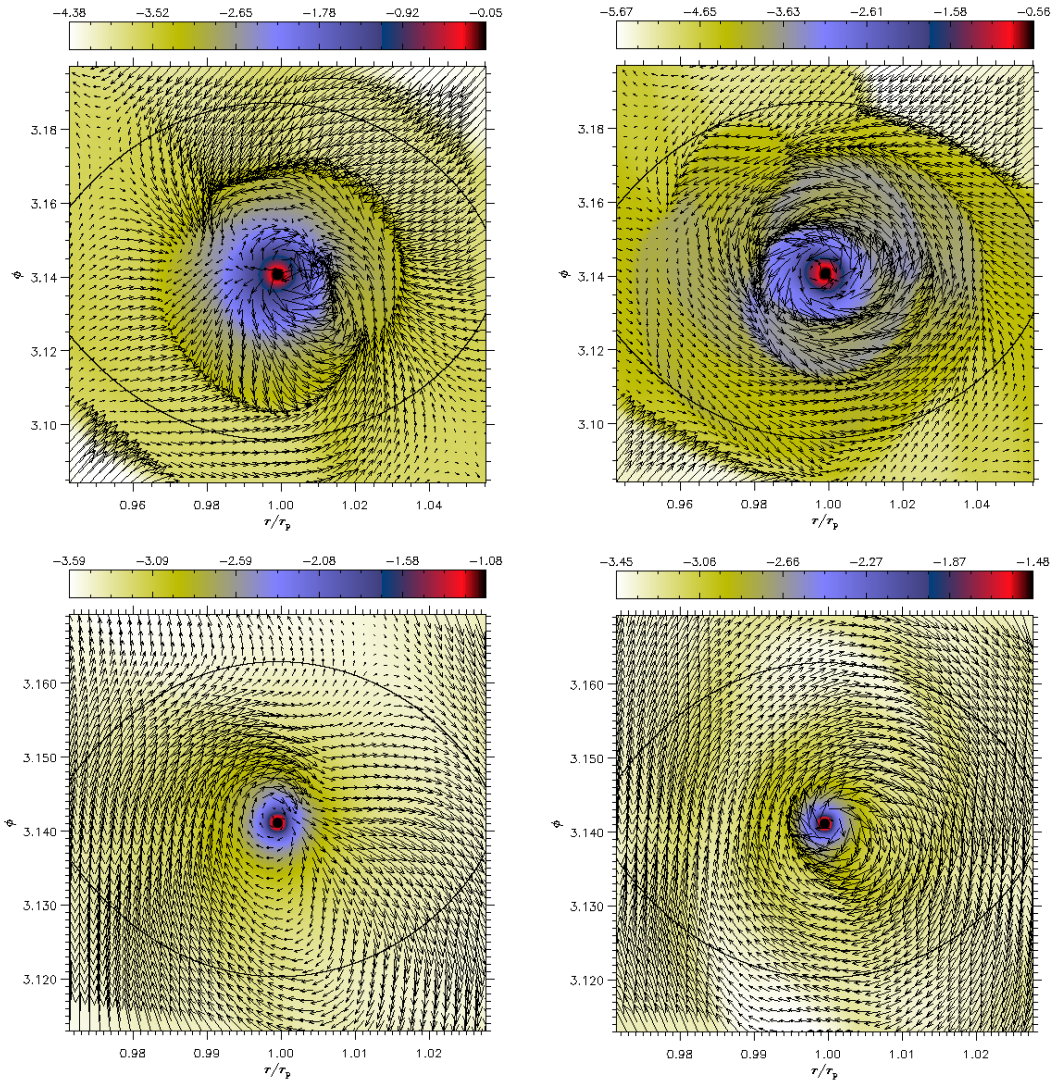

Figure 6.17: Density distribution and velocity field around $M_{\rm p} = 1\ M_{\oplus}$ (**upper panels**) and $M_{\rm p} = 0.1\ M_{\oplus}$ (**lower panels**) non-accreting models. Left panels show H-models while right ones show to C-models Colors scale logarithmically in all of the panels. In the units used in the color bar, -3 corresponds to $\Sigma = 328.7\ {\rm g\,cm^{-2}}$.

6.6.2 Non-accreting Models

The overall flow structure and density distribution of non-accreting protoplanets are drastically different from those of accreting ones. This can be clearly seen in Figure 6.17,

[7]The resolution limit of these simulations is $0.01\ R_{\rm H}$ in Jupiter-mass models and $0.03\ R_{\rm H}$ in $0.1\ M_{\oplus}$ models. Moreover, it must be pointed out that the actual size of protoplanets may extend beyond a tenth of the Hill radius, as stated in CHAPTER 5.

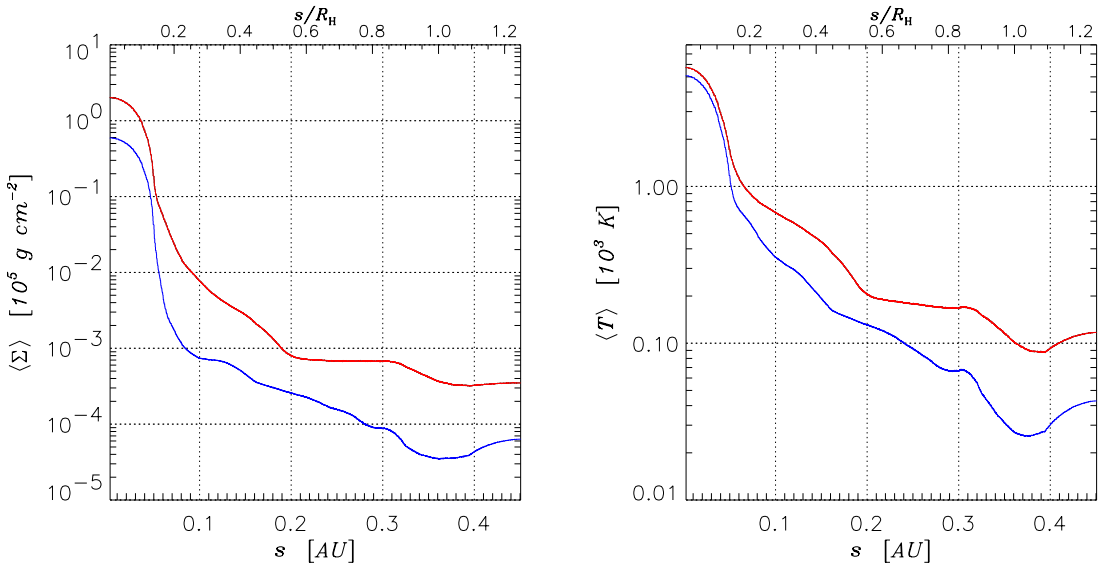

Figure 6.18: Average surface density (**left panel**) and temperature (**right panel**) around 1 M_{Jupiter} protoplanets. Red profiles refer to the H-models whereas blue ones to C-models.

where we show the surface density and the flow field for $M_{\rm p} = 1$ (upper panels) and $0.1\ M_{\mathrm{Jupiter}}$ (lower panels) objects. The standard scenario of a Keplerian-like sub-disk is completely altered. This is a consequence of the large pressure gradient, built up by the large density gradient, which allows matter to move on orbits not constrained by the centrifugal balance. Therefore, the two-arm spiral feature is replaced by a more complex system of multiple shock fronts across which material is first deflected toward the planet and then ejected outward, as also indicated by the sign of the in-fall velocity $w_{\rm in}$ within the region.

The flow strongly diverges in a zone that has a radius equal to $\approx 0.4\,R_{\rm H}$ in the upper-left panel (H-Jupiter model) and to $\approx 0.2\,R_{\rm H}$ in the upper-right panel (C-Jupiter model). The average surface density inside of $R_{\rm H}/3$ is between one and two and a half orders of magnitude larger than that measured accreting models. The mass collected in $s \leq 0.8\ R_{\rm H}$ is $1.97 \times 10^{-4}\ M_{\mathrm{Jupiter}}$ and $4.30 \times 10^{-5}\ M_{\mathrm{Jupiter}}$ for the Jupiter-mass H-model and the C-model, respectively. Curiously, the mass ratio of the Galilean satellites to Jupiter is 2.07×10^{-4}. The azimuthal average of the circumplanetary density, around Jupiter-size objects, can be approximated to $\langle\Sigma\rangle \simeq 1.2 \times 10^4\ (0.1\,R_{\rm H}/s)^{2.8}\ \mathrm{g\,cm^{-2}}$ (H-model) and to $\langle\Sigma\rangle \simeq 1.5 \times 10^3\ (0.1\,R_{\rm H}/s)^{2.7}\ \mathrm{g\,cm^{-2}}$ (C-model). The left panel of Figure 6.18 shows the averaged surface density profiles around $M_{\rm p} = 1\ M_{\mathrm{Jupiter}}$ objects.

A major difference can be also observed in the sub-disk circulation of low-mass models (Fig. 6.17, lower panels). In fact, the fluid rotates in a clockwise direction. In general, the direction of rotation in sub-disks is determined by the balance among the Coriolis force (which is proportional to the velocity and the mass of the planet), the pressure gradient, and the gravitational attraction by the planet. Basically, referring to the lower-right panel of Figure 6.17, the Coriolis deflects rightward fluid elements orbiting at $r \lesssim r_{\rm p}$. Therefore,

Table 6.5: Parameters that enter equation (6.40) when applied to non-accreting models.

$M_\mathrm{p}/M_\mathrm{\varsigma}$	C-MODELS			H-MODELS		
	$\langle T\rangle_{\bar{s}}$ [K]	ξ	RANGE	$\langle T\rangle_{\bar{s}}$ [K]	ξ	RANGE
1.0	1.187×10^3	1.29	$[0.05,1.0]\,R_\mathrm{H}$	1.909×10^3	1.11	$[0.05,1.0]\,R_\mathrm{H}$
0.5	1.132×10^3	0.81	$[0.05,1.0]\,R_\mathrm{H}$	1.458×10^3	1.00	$[0.05,1.0]\,R_\mathrm{H}$
0.2	9.256×10^2	1.18	$[0.05,1.0]\,R_\mathrm{H}$	9.335×10^2	0.76	$[0.05,1.0]\,R_\mathrm{H}$
0.1	7.570×10^2	0.70	$[0.05,1.0]\,R_\mathrm{H}$	6.242×10^2	0.59	$[0.05,1.0]\,R_\mathrm{H}$
0.06	6.103×10^2	0.60	$[0.05,1.0]\,R_\mathrm{H}$			

it forces matter to cross the gap and to reconnect to the other side, while still moving in a position upstream of the perturbed. In contrast, the term $-\mathrm{d}P/\mathrm{d}s$, supposedly positive, opposes to reconnection upstream of the planet's location but favors it downstream of the planet. The prograde rotation that has been encountered so far indicates that the Coriolis deflection overwhelms the pressure gradient, that's why reconnection across the gap always occurs upstream of the planet. Evidently, in the low-mass models displayed in Figure 6.17, the pressure gradient drives material, flowing from upstream, past the planet's position and forces it to circulate clockwise around the perturber. Consequently, matter entering the Hill sphere has an angular momentum anti-parallel (in the planet's frame) to that of the circumstellar disk. From 0.1 to 1 Hill radius, $|\langle w_\mathrm{rot}\rangle|$ increases roughly as $\sqrt{s}$. The behavior of $\langle\Sigma\rangle$ resembles that of a power-law, as in Jupiter-mass cases, with powers 0.9 and 0.5, respectively for the H- and C-model.

The high pressure gradient is also caused by the large temperature gradient. Parameters for an analytic approximations of the average temperature $\langle T\rangle$, according to equation (6.40), are reported in Table 6.5. Maximum temperatures, at $s=0.1\,R_\mathrm{H}$, reach 1900 K and 1200 K, in H- and C-models respectively (see also right panel in Fig. 6.18). At the limit of the Roche lobe the temperature is somewhat higher than that measured in accreting models and depends on the gap structure. They vary from ~ 100 to ~ 200 K. However, The resulting temperature profiles are not much steeper than the one shown in § 6.6.1. Actually, toward low planetary masses they appear less steep. Performing the same check as done in the previous section, it turns out that $|\Lambda_s|\,/\,|\Lambda_z|$ is at most 0.3. Hence, even in these circumstances the type of energy equation implemented here yields a reasonable description of the thermal structure of sub-disks, down to $\sim 0.1\,R_\mathrm{H}$.

6.7 Accretion and Migration

As done in the previous chapters for locally isothermal models, we estimate the mass accretion rate of protoplanets by reducing the surface density around the planet, according to a relation of the type $\Delta\Sigma/\Sigma=\Delta t/\tau_\mathrm{ev}$ (see § 4.3.2). This reduction process has a time scale τ_ev much smaller than the integration time step Δt. This is of course very important, for stability reasons. Figure 6.19 shows a comparison among the different types of simulations conducted during the course of this work. In order to compare the estimates of $\dot{M}_\mathrm{p}$ to those from the other chapters, outcomes from isothermal models have to be rescaled by

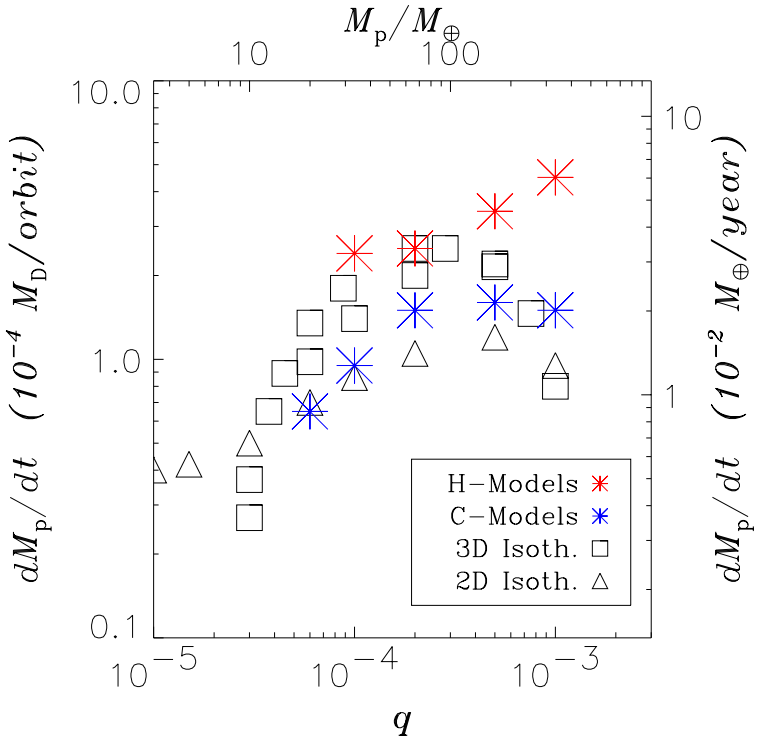

Figure 6.19: Comparison of the accretion rates obtained from different types of simulations. Red and blue asterisks indicate estimates provided by the non-isothermal models presented in this chapter. Triangles and squares represent the rates furnished by local isothermal computations in two (CHAPTER 4) and three (CHAPTER 5) dimensions, respectively. These last two sets of values are rescaled to match the disk mass $M_D = 4.8\times10^{-3}\ M_\star$, used in non-isothermal simulations.

the current disk mass (see § 6.4). In fact, here we are using a value of M_D slightly larger than that adopted in the other computations.

From Figure 6.19, one can see that C-models (blue asterisks) provide accretion rates quite similar to those obtained from models with a fixed temperature distribution. This occurrence is related to the quasi-Keplerian, circumplanetary flow observed in both kinds of computations. H-models provide values of $\dot{M}_p$ (red asterisks) that, in case of Jupiter-size planets, fall above the estimates from all of the other models. According to the accretion procedure (see § 4.3.2), the larger the amount of matter contained in the accretion region $s = \kappa_{ac}$, the larger the accretion rate is. Within $s = 0.1\ R_H$ of a Jupiter-mass planet the mean density computed in the H-model is roughly three times larger than that in the C-model (Fig. 6.14). This is likely due to the larger fluid viscosity.

Figure 6.20 shows the total gravitational torque $\mathcal{T}_D$ exerted by disk material onto accreting planets, as the inverse of the migration time scale ($\mathcal{T}_D \propto 1/\tau_M$), according to the procedure explained in § 4.4.5. The length β represents the radius of the circular region around the planet's position whose contribution is not accounted for. In the left panel of Figure 6.20, this length is set equal to R_H. Outcomes from C-models (and generally those from H-models) compare well to the local-isothermal computations[8]. This is a clear indication that, in these viscosity regimes, thermal effects do not significantly alter the locations of Lindblad resonances. Migration time scales in H-models differ by less than a factor two from those in C-models. Only for $M_p = 33\ M_{\oplus}$, τ_M is appreciably longer. One may at-

[8]We should note here that local-isothermal calculations presented in CHAPTER 4 have the same viscosity as C-models, which is a tenth of that adopted in H-models.

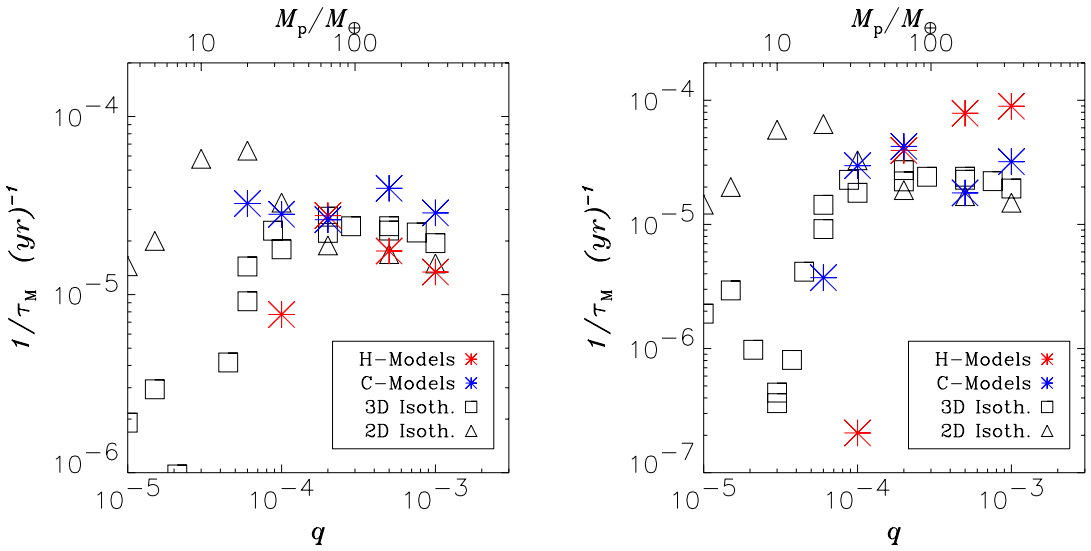

Figure 6.20: Migration time scales plotted against the planetary mass. Notations are the same as in Figure 6.19. Data points (asterisks) indicate the magnitude of the total gravitational torque when this is computed excluding the contributions of matter residing inside of the sphere $s = R_{\rm H}$ (**left panel**) and within $s = 0.5\,R_{\rm H}$ (**right panel**). Only accreting models are considered.

tribute this to the absence of a gap in this model (see Table 6.2), and thus to the onset of the Type I drifting regime.

In the right panel of Figure 6.20, we compute the total torque, reducing the value of β to $R_{\rm H}/2$. Estimates provided by C-models do not change much because of this choice, except for the 20 $M_{\oplus}$ model. H-models are more sensitive to β: Jupiter-mass objects migrate faster by slightly less than an order of magnitude; the 0.1 $M_{\oplus}$ body drifts at a rate 30 times smaller. Some more insight can be gained by examining the function $\mathcal{T}_{\rm D} = \mathcal{T}_{\rm D}(\beta)$, reported in Figure 6.21 for $M_{\rm p} = 1\ M_{\oplus}$ (upper-left panel), $M_{\rm p} = 0.1\ M_{\oplus}$ (upper-right), and $M_{\rm p} = 20\ M_{\oplus}$ (lower-left panel). For $M_{\rm p} = 1\ M_{\oplus}$ models, no significant net torque arises from within the Hill sphere in the C-model (blue line). The situation appears different for the H-model (red line) because $\mathcal{T}_{\rm D}$ decreases to a minimum, around $\beta = R_{\rm H}/2$, and then increases and changes sign around $\beta = 0.1\,R_{\rm H}$. At $M_{\rm p} = 0.1\ M_{\oplus}$, in either case, $\mathrm{d}\mathcal{T}_{\rm D}/\mathrm{d}\beta < 0$, because of the positive torques arising within the sub-disk. In the C-model, the total torque becomes positive when $\beta \lesssim R_{\rm H}/2$. In the 20 $M_{\oplus}$ model, positive torque are exerted down to $\approx 0.4\,R_{\rm H}$ and strong negative torques arise between $\approx 0.2\,R_{\rm H}$ and $\approx 0.4\,R_{\rm H}$.

It is worthy to stress that the protoplanet's volume may fill a fair fraction of the Hill sphere, especially in the highest temperature environments (i.e., H-models). Thereupon, migration rates plotted in the left panel of Figure 6.20 might be somewhat more meaningful than those in the right panel.

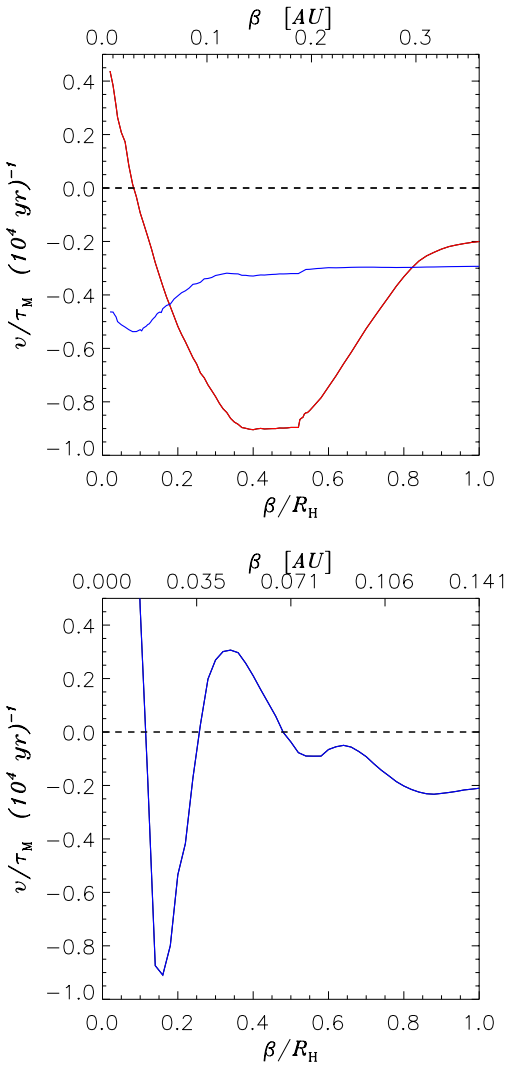

Figure 6.21: Inverse of the migration time scale versus the radius β of the region excluded from the torque calculation. The quantity $v = \dot{a}/|\dot{a}|$ indicates the direction of the planet migration. Red lines refer to H-models, blue lines to C-models. **Top-Left panel**: Jupiter-mass models; **top-right panel**: $M_{\rm p} = 0.1\ M_{\oplus}$ model; **bottom-left panel**: $M_{\rm p} = 20\ M_{\oplus}$ C-model.

6.8 Conclusions

In this chapter we presented two-dimensional simulations of disk-planet interaction in which, together with continuity and momenta equation, we solved also an energy equation that accounts for the major processes responsible for the energetic balance of fluid parcels. Therefore, these computations allow to investigate the thermal properties of the system. We restricted to the flat geometry in order to make some simplifying assumptions on the radiative part of the energy budget, i.e., by treating the radiation transfer as a cooling term. Two-dimensional approximation has been proved to work reasonably well as long as the planetary mass is larger than a tenth of the mass of Jupiter. Because of this, only planets more massive than $0.1\ M_{\rm p}$ have been simulated. We also considered different temperature regimes by choosing different values for the kinematic viscosity. Both accreting and non-accreting planets were investigated.

From the global point of view and generally speaking, we can conclude that models with a fixed temperature work decently well, though the details of the gap structure and the shape of the disk spirals may differ. In particular, only with low viscosities a wide and deep gap is carved in. Mean temperatures in the gap can be as low as 20–50 K, depending on the viscosity regime.

From the local point of view, we have obtained the temperature distribution in circumplanetary disks. These range from several hundred kelvin degrees, at distances $\lesssim 0.1 R_{\rm H}$ from the planet, to values between 50 and 100 K, at the border of the Hill sphere. Azimuthal averages yield profiles dropping as the inverse of the distance from the planet. As consequence of the thermal distribution in the sub-disk, the spiral features are weakened and wrap around the planet more loosely. The density, averaged around the planet, shows an exponential decay, which steepens as the planetary mass increases. Non-accreting models furnish a rather different scenario. Circulation in the Roche lobe is evidently not centrifugally supported because of the large pressure built up mainly by the density gradient and partly by the temperature gradient. Around $M_{\rm p} = 0.1\ M_{\rm J}$, clockwise rotation is achieved as a result of the weakening of the Coriolis force with respect to the pressure gradient term.

Accretion and migration rates are comparable to those evaluated with previous simulations. Once again we found that the material lying inside of the Roche lobe is able to exert strong torques on the planet. Since the density gap is usually filled in H-models (see Table 6.2), Type I migration regime might be valid starting from larger planetary masses (see Fig. 6.20).

BIBLIOGRAPHY

C. B. Agnor and W. R. Ward. Damping of Terrestrial-Planet Eccentricities by Density-Wave Interactions with a Remnant Gas Disk. *The Astrophysical Journal*, 567:579–586, 2002.

E. Agol, J. Krolik, N. J. Turner, and J. M. Stone. Two-dimensional Hydrodynamic Simulations of Convection in Radiation-dominated Accretion Disks. *The Astrophysical Journal*, 558:543–552, 2001.

M. D. Albrow, J.-P. Beaulieu, J. A. R. Caldwell, M. Dominik, B. S. Gaudi, A. Gould, J. Greenhill, K. Hill, S. Kane, R. Martin, J. Menzies, R. M. Naber, K. R. Pollard, P. D. Sackett, K. C. Sahu, P. Vermaak, R. Watson, A. Williams, H. E. Bond, and I. M. van Bemmel. Detection of Rotation in a Binary Microlens: PLANET Photometry of MACHO 97-BLG-41. *The Astrophysical Journal*, 534:894–906, 2000.

D. R. Alexander, G. C. Augason, and H. R. Johnson. An opacity-sampled treatment of water vapor. *The Astrophysical Journal*, 345:1014–1021, 1989.

P. J. Armitage, C. J. Clarke, and C. A. Tout. Accretion disc evolution in single and binary T Tauri stars. *Monthly Notices of the Royal Astronomical Society*, 304:425–433, 1999.

P. Artymowicz. Dynamics of binary and planetary-system interaction with disks - Eccentricity changes. *Publications of the Astronomical Society of the Pacific*, 104:769–774, 1992.

P. Artymowicz. Beta Pictoris: an Early Solar System? *Annual Review of Earth and Planetary Sciences*, 25:175–219, 1997.

S. V. W. Beckwith, T. Henning, and Y. Nakagawa. Dust Properties and Assembly of Large Particles in Protoplanetary Disks. *Protostars and Planets IV*, page 533, 2000.

S. V. W. Beckwith and A. I. Sargent. Circumstellar disks and the search for neighbouring planetary systems. *Nature*, 383:139–144, 1996.

K. R. Bell, P. M. Cassen, H. H. Klahr, and T. Henning. The Structure and Appearance of Protostellar Accretion Disks: Limits on Disk Flaring. *The Astrophysical Journal*, 486: 372–387, 1997.

K. R. Bell and D. N. C. Lin. Using FU Orionis outbursts to constrain self-regulated protostellar disk models. *The Astrophysical Journal*, 427:987–1004, 1994.

D. P. Bennett, S. H. Rhie, A. C. Becker, N. Butler, J. Dann, S. Kaspi, E. M. Leibowitz, Y. Lipkin, D. Maoz, H. Mendelson, B. A. Peterson, J. Quinn, O. Shemmer, S. Thomson, and S. E. Turner. Discovery of a planet orbiting a binary star system from gravitational microlensing. *Nature*, 402:57–59, 1999.

M. J. Berger and J. Oliger. Adaptive Mesh Refinement for Hyperbolic Partial Differential Equations. *Journal of Computational Physics*, 53:484–512, 1984.

P. Bodenheimer and J. B. Pollack. Calculations of the accretion and evolution of giant planets The effects of solid cores. *Icarus*, 67:391–408, 1986.

A. P. Boss. Formation of Extrasolar Giant Planets: Core Accretion or Disk Instability? *Earth Moon and Planets*, 81:19–26, 2000.

S. D. Brittain and T. W. Rettig. CO and H_3^+ in the protoplanetary disk around the star HD141569. *Nature*, 418:57–59, 2002.

G. Bryden, X. Chen, D. N. C. Lin, R. P. Nelson, and J. C. B. Papaloizou. Tidally Induced Gap Formation in Protostellar Disks: Gap Clearing and Suppression of Protoplanetary Growth. *The Astrophysical Journal*, 514:344–367, 1999.

A. Burkert and P. Bodenheimer. Multiple Fragmentation in Collapsing Protostars. *Monthly Notices of the Royal Astronomical Society*, 264:798–806, 1993.

R. P. Butler and G. W. Marcy. A Planet Orbiting 47 Ursae Majoris. *The Astrophysical Journal*, 464:L153–L156, 1996.

R. P. Butler, G. W. Marcy, D. A. Fischer, S. S. Vogt, C. G. Tinney, H. R. A. Jones, A. J. Penny, and K. Apps. Statistical Properties of Extrasolar Planets. In *IAU Symposium*, volume 202, 2000. In press.

R. P. Butler, G. W. Marcy, E. Williams, C. McCarthy, P. Dosanjh, and S. S. Vogt. Attaining Doppler Precision of $3\ \mathrm{m\,s^{-1}}$. *Publications of the Astronomical Society of the Pacific*, 108: 500–509, 1996.

N. Calvet, P. D'Alessio, L. Hartmann, D. Wilner, A. Walsh, and M. Sitko. Evidence for a Developing Gap in a 10 Myr Old Protoplanetary Disk. *The Astrophysical Journal*, 568: 1008–1016, 2002.

B. Campbell, G. A. H. Walker, and S. Yang. A search for substellar companions to solar-type stars. *The Astrophysical Journal*, 331:902–921, 1988.

D. Charbonneau, T. M. Brown, D. W. Latham, and M. Mayor. Detection of Planetary Transits Across a Sun-like Star. *The Astrophysical Journal*, 529:L45–L48, 2000.

P. Ciecieląg, T. Plewa, and M. Różyczka. High-resolution simulations and visualization of protoplanetary disks: structure of the flow in the vicinity of a massive planet. *Astronomische Nachrichten*, 321:171–174, 2000a.

P. Ciecieląg, T. Plewa, and M. Rózyczka. High-resolution simulations and visualization of protoplanetary disks. In *IAU Symposium*, volume 200, pages 199–201, 2000b.

P. Colella and P. R. Woodward. The Piecewise Parabolic Method (PPM) for Gas-Dynamical Simulations. *Journal of Computational Physics*, 54:174–201, 1984.

T. J. B. Collins, H. L. Helfer, and H. M. van Horn. Accretion Disk and Boundary Layer Models Incorporating OPAL Opacities. *The Astrophysical Journal*, 502:730–736, 1998.

A. Coradini, P. Cerroni, G. Magni, and C. Federico. Formation of the satellites of the outer solar system - Sources of their atmospheres. In *Origin and Evolution of Planetary and Satellite Atmospheres*, pages 723–762, 1989.

P. D'Alessio, J. Canto, N. Calvet, and S. Lizano. Accretion Disks around Young Objects. I. The Detailed Vertical Structure. *The Astrophysical Journal*, 500:411–427, 1998.

E. Dorfi and L. O. Drury. Single Adaptive Grids for 1-D Initial Value Problems. *Journal of Computational Physics*, 69:175–195, 1987.

C. P. Dullemond, G. J. van Zadelhoff, and A. Natta. Vertical structure models of T Tauri and Herbig Ae/Be disks. *Astronomy & Astrophysics*, 389:464–474, 2002.

J. Frank, A. King, and D. Raine. *Accretion Power in Astrophysics*. Accretion Power in Astrophysics, ISBN 0521408636, Cambridge University Press, 1992, 1992.

G. Gatewood. Lalande 21185. *Bulletin of the American Astronomical Society*, 28:885, 1996.

P. Godon. Accretion Disk Boundary Layers in Classical T Tauri Stars. *The Astrophysical Journal*, 463:674–680, 1996.

P. Godon, M. Livio, and S. Lubow. Spiral shocks in accretion discs. *Monthly Notices of the Royal Astronomical Society*, 295:L11–L14, 1998.

P. Goldreich and S. Tremaine. Disk-satellite interactions. *The Astrophysical Journal*, 241: 425–441, 1980.

T. Henning and R. Stognienko. Dust opacities for protoplanetary accretion disks: influence of dust aggregates. *Astronomy & Astrophysics*, 311:291–303, 1996.

W. B. Hubbard, A. Burrows, and J. I. Lunine. Theory of Giant Planets. *Annual Review of Astronomy and Astrophysics*, 40:103–136, 2002.

I. Hubeny. Vertical structure of accretion disks - A simplified analytical model. *The Astrophysical Journal*, 351:632–641, 1990.

J.-M. Huré, D. Richard, and J.-P. Zahn. Accretion discs models with the β-viscosity prescription derived from laboratory experiments. *Astronomy & Astrophysics*, 367:1087–1094, 2001.

H. H. Klahr, T. Henning, and W. Kley. On the Azimuthal Structure of Thermal Convection in Circumstellar Disks. *The Astrophysical Journal*, 514:325–343, 1999.

W. Kley. On the treatment of the Coriolis force in computational astrophysics. *Astronomy & Astrophysics*, 338:L37–L41, 1998.

W. Kley. Mass flow and accretion through gaps in accretion discs. *Monthly Notices of the Royal Astronomical Society*, 303:696–710, 1999.

W. Kley. On the migration of a system of protoplanets. *Monthly Notices of the Royal Astronomical Society*, 313:L47–L51, 2000.

W. Kley, G. D'Angelo, and T. Henning. Three-dimensional Simulations of a Planet Embedded in a Protoplanetary Disk. *The Astrophysical Journal*, 547:457–464, 2001.

D. N. C. Lin. Convective accretion disk model for the primordial solar nebula. *The Astrophysical Journal*, 246:972–984, 1981.

D. N. C. Lin and J. Papaloizou. On the dynamical origin of the solar system. In *Protostars and Planets II*, pages 981–1072, 1985.

D. N. C. Lin and J. C. B. Papaloizou. On the tidal interaction between protostellar disks and companions. In *Protostars and Planets III*, pages 749–835, 1993.

J. J. Lissauer. Planet formation. *Annual Review of Astronomy and Astrophysics*, 31:129–174, 1993.

B. F. Liu and E. Meyer-Hofmeister. The influence of new opacity data on the vertical structure of accretion disks. *Astronomy & Astrophysics*, 328:243–246, 1997.

S. H. Lubow. Vertically driven resonances in accretion disks. *The Astrophysical Journal*, 245: 274–285, 1981.

S. H. Lubow and J. E. Pringle. Wave propagation in accretion disks - Axisymmetric case. *The Astrophysical Journal*, 409:360–371, 1993.

S. H. Lubow, M. Seibert, and P. Artymowicz. Disk Accretion onto High-Mass Planets. *The Astrophysical Journal*, 526:1001–1012, 1999.

D. Lynden-Bell and J. E. Pringle. The evolution of viscous discs and the origin of the nebular variables. *Monthly Notices of the Royal Astronomical Society*, 168:603–637, 1974.

M. Makita, K. Miyawaki, and T. Matsuda. Two- and three-dimensional numerical simulations of accretion discs in a close binary system. *Monthly Notices of the Royal Astronomical Society*, 316:906–916, August 2000.

G. W. Marcy and R. P. Butler. A Planetary Companion to 70 Virginis. *The Astrophysical Journal*, 464:L147–L151, 1996.

G. W. Marcy and R. P. Butler. Detection of Extrasolar Giant Planets. *Annual Review of Astronomy and Astrophysics*, 36:57–98, 1998.

A. J. Markwick, M. Ilgner, T. J. Millar, and T. Henning. Molecular distributions in the inner regions of protostellar disks. *Astronomy & Astrophysics*, 385:632–646, 2002.

F. S. Masset. On the Co-orbital Corotation Torque in a Viscous Disk and Its Impact on Planetary Migration. *The Astrophysical Journal*, 558:453–462, 2001.

F. S. Masset. The co-orbital corotation torque in a viscous disk: Numerical simulations. *Astronomy & Astrophysics*, 387:605–623, 2002.

S. Matt, A. P. Goodson, R. M. Winglee, and K. Böhm. Simulation-based Investigation of a Model for the Interaction between Stellar Magnetospheres and Circumstellar Accretion Disks. *The Astrophysical Journal*, 574:232–245, 2002.

M. Mayor and D. Queloz. A Jupiter-Mass Companion to a Solar-Type Star. *Nature*, 378: 355–359, 1995.

T. Mazeh, Y. Krymolowski, and G. Rosenfeld. The High Eccentricity of the Planet Orbiting 16 Cygni B. *The Astrophysical Journal*, 477:L103–L106, 1997.

D. Mihalas and B. Weibel Mihalas. *Foundations of radiation hydrodynamics*. New York: Dover, 1999, 1999.

S. Miki. The gaseous flow around a protoplanet in the primitive solar nebula. *Progress of Theoretical Physics*, 67:1053–1067, 1982.

K. Miyoshi, T. Takeuchi, H. Tanaka, and S. Ida. Gravitational Interaction between a Protoplanet and a Protoplanetary Disk. I. Local Three-Dimensional Simulations. *The Astrophysical Journal*, 516:451–464, 1999.

G. E. Morfill, W. Tscharnuter, and H. J. Voelk. Dynamical and chemical evolution of the protoplanetary nebula. In *Protostars and Planets II*, pages 493–533, 1985.

R. P. Nelson, J. C. B. Papaloizou, F. Masset, and W. Kley. The migration and growth of protoplanets in protostellar discs. *Monthly Notices of the Royal Astronomical Society*, 318: 18–36, 2000.

H. Nomura. Structure and Instabilities of an Irradiated Viscous Protoplanetary Disk. *The Astrophysical Journal*, 567:587–595, 2002.

G. I. Ogilvie and S. H. Lubow. The Effect of an Isothermal Atmosphere on the Propagation of Three-dimensional Waves in a Thermally Stratified Accretion Disk. *The Astrophysical Journal*, 515:767–775, 1999.

J. Papaloizou and D. N. C. Lin. On the tidal interaction between protoplanets and the primordial solar nebula. I - Linear calculation of the role of angular momentum exchange. *The Astrophysical Journal*, 285:818–834, 1984.

J. C. B. Papaloizou, R. P. Nelson, and F. Masset. Orbital eccentricity growth through disc-companion tidal interaction. *The Astrophysical Journal*, 366:263–275, 2001.

J. C. B. Papaloizou and C. Terquem. Critical Protoplanetary Core Masses in Protoplanetary Disks and the Formation of Short-Period Giant Planets. *The Astrophysical Journal*, 521: 823–838, 1999.

M. A. C. Perryman. Extra-solar planets. *Reports of Progress in Physics*, 63:1209–1272, 2000.

T. Plewa and E. Müller. AMRA: An Adaptive Mesh Refinement hydrodynamic code for astrophysics. *Computer Physics Communications*, 138:101–127, 2001.

J. B. Pollack. Origin and History of the Outer Planets: Theoretical Models and Observational Contraints. *Annual Review of Astronomy and Astrophysics*, 22:389–424, 1984.

R. Popham, R. Narayan, L. Hartmann, and S. Kenyon. Boundary Layers in Pre-Main-Sequence Accretion Disks. *The Astrophysical Journal*, 415:L127–L130, 1993.

J. E. Pringle. Accretion discs in astrophysics. *Annual Review of Astronomy and Astrophysics*, 19:137–162, 1981.

S. Refsdal and J. Surdej. Gravitational Lenses. *Reports of Progress in Physics*, 57:117–185, 1994.

M. Ruffert. Collisions between a white dwarf and a main-sequence star. II - Simulations using multiple-nested refined grids. *Astronomy & Astrophysics*, 265:82–105, 1992.

W. Skamarock, J. Oliger, and R. L. Street. Adaptive Grid Refinement for Numerical Weather Prediction. *Journal of Computational Physics*, 80:27–60, 1989.

M. D. Snellgrove, J. C. B. Papaloizou, and R. P. Nelson. On disc driven inward migration of resonantly coupled planets with application to the system around GJ876. *Astronomy & Astrophysics*, 374:1092–1099, 2001.

L. J. Spitzer. The Dissipation of Planetary Filaments. *The Astrophysical Journal*, 90:675–688, 1939.

T. F. Stepinski and D. C. Black. Statistics of low-mass companions to stars: {} Implications for their origin. *Astronomy & Astrophysics*, 356:903–912, 2000.

D. J. Stevenson. Formation of the giant planets. *Planetary and Space Science*, 30:755–764, 1982.

J. M. Stone, D. Mihalas, and M. L. Norman. ZEUS-2D: A radiation magnetohydrodynamics code for astrophysical flows in two space dimensions. III - The radiation hydrodynamic algorithms and tests. *The Astrophysical Journal Supplement Series*, 80:819–845, 1992.

J. M. Stone and M. L. Norman. ZEUS-2D: A radiation magnetohydrodynamics code for astrophysical flows in two space dimensions. I - The hydrodynamic algorithms and tests. *The Astrophysical Journal Supplement Series*, 80:753–790, 1992a.

J. M. Stone and M. L. Norman. ZEUS-2D: A Radiation Magnetohydrodynamics Code for Astrophysical Flows in Two Space Dimensions. II. The Magnetohydrodynamic Algorithms and Tests. *The Astrophysical Journal Supplement Series*, 80:791–818, 1992b.

G. Suttner and H. W. Yorke. Early Dust Evolution in Protostellar Accretion Disks. *The Astrophysical Journal*, 551:461–477, 2001.

N. Tajima and Y. Nakagawa. Evolution and Dynamical Stability of the Proto-giant-planet Envelope. *Icarus*, 126:282–292, 1997.

H. Tanaka, T. Takeuchi, and W. Ward. Three-dimensional Interaction between a Planet and an Isothermal Gaseous Disk. I. Corotation and Lindblad Torques and Planet Migration. *The Astrophysical Journal*, 565:1257–1274, 2002.

T. Tanigawa and S. Watanabe. Gas Accretion Flows onto Giant Protoplanets: High-Resolution Two-dimensional Simulations. *The Astrophysical Journal*, 580:506–518, 2002.

J. Tassoul. *Theory of rotating stars*. Princeton Series in Astrophysics, Princeton: University Press, 1978, 1978.

D. E. Trilling, J. I. Lunine, and W. Benz. Orbital migration and the frequency of giant planet formation. *Astronomy & Astrophysics*, 394:241–251, 2002.

P. van de Kamp. The planetary system of Barnard's star. *Vistas in Astronomy*, 26:141–157, 1982.

B. van Leer. Towards the ultimate conservative difference scheme: IV. A new approach to numerical convection. *Journal of Computational Physics*, 23:276–299, 1977.

W. Ward. Density waves in the solar nebula - Differential Lindblad torque. *Icarus*, 67: 164–180, 1986.

W. Ward. Protoplanet Migration by Nebula Tides. *Icarus*, 126:261–281, 1997.

W. R. Ward. Disk-planet interactions: Torques from the coorbital zone. *New York Academy Sciences Annals*, 675:314–323, 1993.

A. J. Weinberger, E. E. Becklin, G. Schneider, B. A. Smith, P. J. Lowrance, M. D. Silverstone, B. Zuckerman, and R. J. Terrile. The Circumstellar Disk of HD 141569 Imaged with NICMOS. *The Astrophysical Journal*, 525:L53–L56, 1999.

K. A. Winkler and M. L. Norman, editors. *Astrophysical Radiation Hydrodynamics*, 1986.

S. Wolf, F. Gueth, T. Henning, and W. Kley. Detecting Planets in Protoplanetary Disks: A Prospective Study. *The Astrophysical Journal*, 566:L97–L99, 2002.

A. Wolszczan and D. A. Frail. A planetary system around the millisecond pulsar PSR1257 + 12. *Nature*, 355:145–147, 1992.

N. Woolf and J. R. Angel. Astronomical Searches for Earth-Like Planets and Signs of Life. *Annual Review of Astronomy and Astrophysics*, 36:507–538, 1998.

G. Wuchterl. Hydrodynamics of giant planet formation. II - Model equations and critical mass. III - Jupiter's nucleated instability. *Icarus*, 91:39–64, 1991.

G. Wuchterl. The critical mass for protoplanets revisited - Massive envelopes through convection. *Icarus*, 106:323–334, 1993.

G. Wuchterl, T. Guillot, and J. J. Lissauer. Giant Planet Formation. *Protostars and Planets IV*, page 1081, 2000.

H. W. Yorke, P. Bodenheimer, and G. Laughlin. The formation of protostellar disks. I - 1 $M_{\odot}$. *The Astrophysical Journal*, 411:274–284, 1993.

H. W. Yorke and M. Kaisig. Use of multiply nested grids for the solution of flux-limited radiation diffusion and hydrodynomics. *Computer Physics Communications*, 89:29–44, 1995.

H. W. Yorke and C. Sonnhalter. On the Formation of Massive Stars. *The Astrophysical Journal*, 569:846–862, 2002.

U. Ziegler. NIRVANA: An adaptive mesh refinement code for gas dynamics and MHD. *Computer Physics Communications*, 109:111–134, 1998.

U. Ziegler and H. W. Yorke. A nested grid refinement technique for magnetohydrodynamical flows. *Computer Physics Communications*, 101:54–74, 1997.

On the Cat, the Cow, and the Frenchman

I told about Louis Sixteenth that got his head cut off in France long time ago; and about his little boy the dolphin, that would a been a king, but they took and shut him up in jail, and some say he died there.

"Po' little chap."

"But some says he got out and got away, and come to America."

"Dat's good! But he'll be pooty lonesome – dey ain' no kings here, is dey, Huck?"

"No."

"Den he cain't git no situation. What he gwyne to do?"

"Well, I don't know. Some of them gets on the police, and some of them learns people how to talk French."

"Why, Huck, doan' de French people talk de same way we does?"

"No, Jim; you couldn't understand a word they said – not a single word."

"Well, now, I be ding-busted! How do dat come?"

"I don't know; but it's so. I got some of their jabber out of a book. S'pose a man was to come to you and say Polly-voo-franzy – what would you think?"

"I wouldn' think nuff'n; I'd take en bust him over de head – dat is, if he warn't white. I wouldn't 'low no nigger to call me dat."

"Shucks, it ain't calling you anything. It's only saying, do you know how to talk French?"

"Well, den, why couldn't he say it?"

"Why, he is a-saying it. That's a Frenchman's way of saying it."

"Well, it's a blame ridicklous way, en I doan' want to hear no mo' 'bout it. Dey ain' no sense in it."

"Looky here, Jim; does a cat talk like we do?"

"No, a cat don't."

"Well, does a cow?"

"No, a cow don't, nuther."

"Does a cat talk like a cow, or a cow talk like a cat?"

"No, dey don't."

"It's natural and right for 'em to talk different from each other, ain't it?"

"Course."

"And ain't it natural and right for a cat and a cow to talk different from us?"

"Why, mos' sholy it is."

"Well, then, why ain't it natural and right for a Frenchman to talk different from us? You answer me that."

"Is a cat a man, Huck?"

"No."

"Well, den, dey ain't no sense in a cat talkin' like a man. Is a cow a man? – er is a cow a cat?"

"No, she ain't either of them."

"Well, den, she ain't got no business to talk like either one er the yuther of 'em. Is a Frenchman a man?"

"Yes."

"Well, den! Dad blame it, why doan' he talk like a man? You answer me dat!"

MARK TWAIN,
THE ADVENTURES OF HUCKLEBERRY FINN,
1885